An Investigation on surface segregation of S in Fe and a Fe-Cr alloy using computational models and experimental methods

By

Pieter Egbert Barnard

M.Sc

A thesis presented in fulfilment of the requirements of the degree

DOCTOR PHILOSOPHIAE

in the Department of Physics

at the University of the Free State

Republic of South Africa

Supervisor: J.J. Terblans

Co-supervisor: H.C. Swart

November 2014

All glory and honour to Jesus Christ, my Lord and Saviour.

Acknowledgements

Although the study required hard work, patience and endurance on the part of the author, it would not have been possible without the help, advice and support of others. First of all, I would like to thank our **Lord Jesus Christ** for enabling me to complete this study. His grace and love has guided me along this path.

To my wife, **Johanné M. Barnard**, I truly appreciate all your love and support during this study. Thank you for the many sacrifices that you made, which you did with the greatest of understanding, in order for me to complete this study. Your drawings of the systems built in this study (SAM 600 heater and the annealing system) and the proof reading of this thesis is appreciated.

To my supervisor, **Prof. J.J. (Koos) Terblans**, thank you for mentoring me in the various facets of the project. You have truly been a good teacher, and your guidance as mentor has enabled me to handle the various challenges throughout the project and the eventual completion of this study. My co-supervisor **Prof. Hendrik C. Swart**, thank you for your advice and support during this study.

For the proof reading of this thesis, I would like to thank **Mrs. Annelize Prinsloo**. I appreciate the time you have taken to ensure the spelling and grammar is correct.

Apart from the above-mentioned persons, various others enabled me to complete this study. This includes **Mr. Adriaan B. Hugo** and **Mr. Inus Basson** from the department of electronics who assisted with maintenance on the control units of the various systems, especially the temperature control unit of the SAM 600. Also I would like to thank the personnel at the department of Instrumentation for their assistance with the equipment.

Then to the two people whom where always willing to help, even outside of office hours; **Mr. Albert van Eck** and **Mr. Fanie Riekert** from the High Performance Computer Center

(HPC). Thank you for your help and assistance in setting up the simulation software, it is greatly appreciated.

For financial aid that allowed me to conduct this study, I want to thank **SASOL** for providing me with a bursary. Also I would like to thank the **cluster program: Material Science and Nanotechnology** of the University of the Free State for financial support granted.

Keywords

Diffusion
Segregation
Surface analysis
Multi-scale modelling
Sulphur
Chromium
Iron
Fe(100)
Fe(110)
Fe(111)
Auger Electron Spectroscopy
Time-of-Flight Secondary Ion Mass Spectrometry
X-Ray Diffraction
Density Functional Theory
QUANTUM Espresso
Fick
Bragg-Williams
Modified Darken Model
Linear programmed heating
Diffusion mechanism
Schottky defect
Binding energy
Migration energy
Vacancy formation energy
Activation energy
Pre-exponential factor
Segregation energy
Surface effect

Opsomming

‘n In-diepte studie is uitgevoer om die invloed van die bcc Fe kristal se mikroskopiese eienskappe op die segregasie parameters, naamlik Q, D_0, ΔG en $\mathbf{\Omega}$, te ondersoek. Hierdie mikroskopiese eienskappe behels die invloed van die oppervlakoriëntasie op die aktiveringsenergie vir diffusie, Q, asook die lagie-afhanklikheid van die segregasieparameters in die oppervlaklaag (atomlaag 1) en naas-oppervlaklae (atoomlae 2-4) van die kristal.

Die vorming van leemtes in die lae-indeks oriëntasies van bcc Fe, naamlik die Fe(100), Fe(110) en Fe(111) oriëntasies, is beskou as die vorming van ‘n Schottky defek. Hierdie meganisme lei tot die oriëntasie-afhanlikheid van die leemte vormings energie en dus ook die aktiveringsenergie van diffusie. Die aktiveringsenergie vir swawel (S) in die bulk van die Fe(100), Fe(110) en Fe(111) oriëntasies, bereken deur gebruik te maak van Digtheids Funksionele Teorie (DFT), is 2.86 eV (276 kJ/mol), 2.75 eV (265 kJ/mol) en 1.94 eV (187 kJ/mol) onderskeidelik. Hierdie berekende oriëntasie-afhankliheid van die aktiveringsenergie is bevestig deur Auger Elektron Spektroskopie (AES) en Vlugtyd Sekondêre Ioon Massa Spektrometrie (“TOF”-SIMS) metings. Die data toon verder ook dat daar ‘n oriëntasie-afhanklikheid in die pre-eksponensiële faktor, D_0, die segregasie-energie, ΔG, asook die interaksieparameter, $\mathbf{\Omega}$, bestaan.

DFT berekeninge is aangewend om die lagie-afkankliheid van die segregasieparameters in atoomlagies 1 tot 4 van die Fe(100) oriëntasie te ondersoek. Hierdie verskynsel was vir die eerste keer in die betrokke studie ondersoek en is benoem as die “oppervlakverskynsel”. Resultate van die segregasieparameters vir beide S en Chroom (Cr) toon ‘n definitiewe lagie-afhankliheid. Die aktiveringsenergie vir elk van hierdie elemente vir segregasie van atoomlaag 2 na 1 is baie klein, met waardes van onderskeidelik 1.39 eV (134 kJ/mol) en 1.62 eV (156 kJ/mol) vir S en Cr. Dus, segregasie van beide S en Cr vanaf atoomlaag 2 na atoomlaag 1 vind teen ‘n baie hoë tempo plaas en dit kan beskou word dat die onderskeidelike elemente vanaf atoomlaag 2 na 1 “oorgestort” is, genoem die “oorstortingseffek”. Segregasie van S vanaf atoomlaag 3 na 2, ondervind ‘n aktiveringsenergie van 2.97 eV (287 kJ/mol), die grootste aktiveringsenergie van al die atoomlagies, en vorm dus die tempo-bepalende stap vir S segregasie in Fe(100). Cr segregasie in Fe(100) ondervind die grootste aktiveringsenergie met ‘n waarde van 4.16 eV

(401 kJ/mol) vir segregasie van Cr vanaf atoomlagie 4 na 3, wat tot gevolg het dat hierdie die tempo-bepalende stap vir Cr segregasie in Fe(100) is.

Daar is waargeneem dat die segregasie-energie van S toeneem vanaf 0.00 in atoomlaag 5 tot ‘n positiewe waarde van 0.07 eV (6.51 kJ/mol) in atoomlaag 3 en ‘n waarde van 0.21 eV (20.7 kJ/mol) in atoomlaag 2. Vanaf atoomlaag 2 na 1, daal die segregasie-energie egter dramaties na ‘n negatiewe waarde van -1.93 eV (-186 kJ/mol). Cr segregasie toon ‘n soortgelyke verskynsel waarby die segregasie-energie geleidelik toeneem vanaf die bulk en dan skerp afneem in die oppervlaklaag. Die segregasie-energie van Cr in atoomlaag 2 is 0.47 eV (45.3 kJ/mol) en daal dan skerp na ‘n waarde van 0.18 eV (17.6 kJ/mol) vir atoomlaag 1, die oppervlak atoomlaag. Hierdie data dui daarop dat S ‘n sterk segregerende element is, terwyl Cr segregasie nie sal plaasvind nie. Waardes vir die interaksieparameters bevestig die segregasie van S in Fe(100), asook die feit dat Cr segregasie in Fe(100) nie sal plaasvind nie.

Inkorporering van die DFT resultate in die “Modified Darken Model” (MDM) toon die segregasieprofiel van S segregasie in Fe(100), asook die desegregasieprofiel van Cr in Fe(100). AES segregasie metings van S in die Fe(100) en Fe(111) enkelkristalle toon ‘n oriëntasie-afhankliheid op elk van die segregasieparameters. Passings op die data was uitgevoer met die konvensionele MDM en daar word gemerk dat hierdie model nie die segregasieprofiel oor die hele temperatuurgebied akkuraat kan beskryf nie. Met inagneming van die lagie-afhanklikheid van elk van die segregasieparameters, die “oppervklakverskynsel”, is ‘n akkurate beskrywing van die eksperimentele segregasieprofiel van S in beide die Fe(100) en Fe(111) oriëntasies verkry.

Segregasie van S en Cr in die ternêre Fe-Cr-S allooi is ondersoek deur middel van TOF-SIMS en daar is gevind dat Cr segregasie wel plaasvind in die teenwoordigheid van S. Hierdie twee elemente ko-segregeer, met S wat weer desegregeer by hoër temperature (> 900 K) terwyl die Cr oppervlakkonsentrasie toeneem. Hierdie ko-segregasie is deur middel van DFT berekeninge verduidelik as die sterk positiewe interaksie tussen Cr en S in die bulk wat daartoe lei dat S die Cr uit die bulk trek na die oppervlak toe. In die oppervlaklaag is daar egter ‘n sterk afstotende interaksie tussen S en Cr wat lei tot die desegregasie van S. Hierdie resultate bied ‘n verduideliking vir die dubbelsinnigheid wat in die literatuur bestaan oor die segregasie van Cr in Fe, en verder bevestig dit ook die teenwoordigheid van die “oppervlakverskynsel”.

Abstract

A systematic investigation is conducted to determine the influence of the microscopic effects of the bcc Fe lattice on the segregation parameters, Q, D_0, ΔG and Ω. These microscopic effects include the dependence of the surface orientation on the activation energy of diffusion, Q, and the layer dependence of the segregation parameters in the surface (atomic layer 1) and near surface atomic layers (atomic layers 2-4).

The formation of vacancies in the low-index orientations of bcc Fe namely: Fe(100), Fe(110) and Fe(111) were considered to form via the Schottky defect mechanism. This mechanism resulted in an orientation dependence of the vacancy formation energy and also the activation energy of diffusion. Bulk activation energies for the segregation of Sulphur (S), as calculated by Density Functional Theory (DFT), for the Fe(110), Fe(100) and Fe(111) orientations are 2.86 eV (276 kJ/mol), 2.75 eV (265 kJ/mol) and 1.94 eV (187 kJ/mol) respectively. Experimental data obtained by Auger Electron Spectroscopy (AES) and Time-of-Flight Secondary Ion Mass Spectrometry (TOF-SIMS) confirmed the orientation dependence of the activation energy of diffusion. Furthermore, AES results revealed the orientation dependence of the pre-exponential factor (D_0), the segregation energy (ΔG) and interaction parameter (Ω).

DFT calculations are performed to investigate the layer dependence of the segregation parameters in the first 4 atomic layers of Fe(100), a phenomenon termed the “surface effect”. Results indicate that all the segregation parameters depend on the atomic layer in which either the S or Chrome (Cr) impurities reside. Both S and Cr have very small activation energies of respectively 1.39 eV (134 kJ/mol) and 1.62 eV (156 kJ/mol) for segregation from atomic layer 2 to 1. These low activation energies are responsible for the surface “dumping effect”, whereby S and Cr were “dumped” into the surface layer. S segregated from atomic layer 3 to 2 with an activation energy of 2.97 eV (287 kJ/mol), the highest activation energy value for the crystal and the rate limiting factor for S segregation in Fe(100). Cr had the highest activation energy for segregation from atomic layer 4 to 3 with a value of 4.16 eV (401 kJ/mol) forming the rate limiting step for Cr segregation in Fe(100).

Segregation energies of S are observed to increase from a 0.00 value in atomic layer 5 to a positive value of 0.07 eV (6.51 kJ/mol) in atomic layer 3 and a value of 0.21 eV (20.7

kJ/mol) in atomic layer 2. Atomic layer 1, the surface layer, has a negative segregation energy of -1.93 eV (-186 kJ/mol) indicating the favourable segregation of S to the Fe(100) surface. Cr segregation energies increase monotonically from the bulk up to atomic layer 2, with a value of 0.47 eV (45.3 kJ/mol), and then decrease to a value of 0.18 eV (17.6 kJ/mol) in the surface layer. Thus, segregation of Cr in Fe is observed to be unfavourable due to the positive segregation energies. The interaction energies obtained for S and Cr confirms the behaviour predicted by the segregation energies, with S being a strong segregant and Cr segregation being unfavourable.

Simulations incorporating the segregation parameters, calculated by DFT, in combination with the Modified Darken Model (MDM) reveals the macroscopic segregation of S in Fe(100) and the desegregation of Cr in Fe(100). Segregation experiments performed by AES on the Fe(100) and Fe(111) single crystals confirms the layer dependence of the segregation parameters. Fitting of the MDM to the segregation data of S in Fe(100) and Fe(111) shows that the conventional MDM fails to provide a truly accurate description of the segregation profile. Incorporation of the layer dependence, the “surface effect”, of the segregation parameters provides an accurate description of the observed segregation data.

Segregation of S and Cr is studied in the ternary Fe-Cr-S alloy by TOF-SIMS measurements. Results reveal the segregation of Cr as a result of Cr and S co-segregating towards the surface. At high temperatures (> 900 K) S desegregates into the bulk lattice while the concentration of Cr in the surface layer is observe to increase. This observed co-segregation of Cr and S in Fe is explained by the interaction parameters between Cr and S as calculated by DFT. In the bulk lattice Cr and S experience a strong positive interaction resulting in S “drawing” Cr from the bulk towards the surface. In the surface layer these two species however experience a strong negative interaction resulting in the desegregation of S. These results provide a possible explanation of the observed discrepancies that exist in literature concerning the desegregation of Cr in Fe. Furthermore it provides evidence for the presence of the “surface effect” responsible for the layer dependency of the segregation parameters.

Table of Contents

Chapter 4: Experimental techniques and measurements 63

Chapter 5: Sample preparation 105

Chapter 1

Introduction

1.1. Objectives of this study

Literature contains many sources where the diffusion parameters of different alloy systems are reported [1-10], but little information is available which describes the effect of the crystal's microscopic structure on segregation. This includes the influence of the surface orientation and the effect of surface relaxation on the segregation parameters. These factors are related to the first few atomic layers of the crystal, for this study the first 4 atomic layers were considered. Atomic layer 1 is the surface layer, with atomic layers 2-4 as the near surface layers and layer 5 being the first bulk layer. The study presented here performs a comprehensive investigation into the influence of the microscopic structure of the lattice on surface segregation in the Fe(100)-S, Fe(111)-S, Fe(100)-Cr and the Fe(100)-Cr-S alloys. This is achieved by utilising both experimental techniques and computational methods in order to provide a unique view of surface segregation in the respective alloys. The aim of this study is clearly set out in the following two points:

1. *Investigate the influence of the surface orientation on the segregation of S in the low-index orientations of Fe namely; Fe(100), Fe(110) and Fe(111).*
2. *Determine what the influence of surface relaxation is on the segregation parameters of the binary alloys Fe-S and Fe-Cr as well as for the ternary Fe-Cr-S alloy. This is the first known study which conducts a full scale investigation into the influence of the surface on all the segregation parameters and this phenomenon is termed the* ***"surface effect".***

The next section provides some background information concerning the motivation for this study and its significance to both the fundamental and applied scientist.

1.2. Motivation

The surface of a crystal is considered as a unique defect in the lattice which is caused by the abrupt termination in the periodicity of the lattice. Consequently, atoms in the surface region, the first 4 atomic layers of the surface (4 atomic layers were considered in this study), will experience a different chemical environment in comparison to bulk atoms. Firstly, due to the absence of nearest and second nearest neighbouring atoms, the atoms in the surface region will experience a reduction in their respective binding energies. Secondly, as a result of a reduced coordination, these atoms will experience different forces on the atoms, which will cause the surface to relax and in some cases reconstruct in an attempt to stabilise itself [11-13]. As a result of these microscopic effects in the lattice, solute atoms segregating to this region will experience a binding energy different to that of the solute atom in the bulk. Not only so, but the binding energy of the solute atom in the surface region will differ from one surface orientation to the next. The above mentioned microscopic changes in the surface region will result in the energetics and therefore the segregation parameters (activation energy, segregation energy, interaction parameter and the pre-exponential factor) being different in the surface region. The layer dependence of the segregation energy for Cr in bcc Fe has been reported independently by Yuan et. Al. [14] and Gupta et. Al. [15].

To the fundamental scientist, this provides a solid foundation by which other crystalline systems can be studied for similar microstructural effects. Adsorption studies could benefit from the information gained in this study, since the adsorption energy is determined by the surface region of the material. One area which has received a lot of interest lately is nanotechnology, although this subject is not considered in this work. Nanomaterials are excellent candidate materials in which the microstructural effects of the lattice can be harnessed in order to design functional materials.

To the applied scientist, the study presents answers to materials (Fe-S, Fe-Cr and Fe-Cr-S) that are of significant importance to industrial and technological applications. Most importantly is the known use of Fe-based alloys in high mechanical strength and low corrosion steels as well the use of Fe-based alloys as a catalyst in the Fischer-Tropsch process [16, 17]. This process utilises a Fe catalyst in order to convert syngas (H_2 + CO) into different hydrocarbon chains, depending on the reaction conditions and the catalyst composition.

Either of these applications for Fe, is negatively influenced by the presence of S on the surface. In the Fe catalyst, S occupies active sites on the surface which ultimately leads to deactivation of the catalyst [18, 19]. The presence of S in stainless steel results in grain boundary embrittlement of the alloys which leads to mechanical failure of the material [20-22]. Surface segregation of S in the Fe(100) and Fe(111) surface orientations were studied, both experimentally and computationally, in order to determine the influence of the surface orientation on surface segregation. Furthermore, the Fe(100) was studied to determine the influence of surface relaxation on the segregation parameters.

The presence of Cr on the surface of Fe provides a corrosion resistant Cr oxide layer. This prevents the corrosion of underlying atomic layers which is effectively shielded from the environment by the Cr oxide layer [7, 23]. Fe-Cr alloys are also promising candidates for materials in nuclear reactor vessels, since they are capable of long operating times despite high doses of radiation damage and being exposed to high temperatures [24, 25]. A number of studies have been carrier out to investigate diffusion of Cr in Fe [7, 8, 14, 15, 21, 26-32], but despite these many efforts, there is still ambiguity concerning the segregation of Cr in Fe. Some report the segregation of Cr [23, 28] while others present arguments to prove the contrary [7, 8, 14, 15, 33]. Of particular interest are the reports by [29, 34, 35] which states that the segregation of C, N, O and S in Fe-Cr is accompanied by the co-segregation of Cr. Thus, there exists a possibility that the segregation of Cr noted by some could have been caused by the presence of one or more of these non-metal impurities. Fe almost always contains one of these non-metal impurities; at least some concentration of S is always present in Fe as a trace impurity despite samples being of a high purity. Therefore, the observed segregation of Cr could well be caused by S segregation. This requires for a detailed study into the segregation of Cr in the ternary Fe(100)-Cr-S alloy.

1.3. Thesis layout

Presented in this section is a layout of the chapters in the thesis along with a short description of each chapter. In total the thesis consists out of 8 chapters plus 2 appendixes, appendix A and B.

Chapter 2: Diffusion and segregation theory

A theory chapter covering the fundamental concepts of diffusion and segregation in crystalline materials. This includes a description on the kinetics of diffusion using Fick`s two diffusion laws as well as an equilibrium description provided by the Bragg-Williams model. These models are used in future chapters to extract the segregation parameters form experimental segregation data.

Chapter 3: Simulation methods

The simulation methods are described here; firstly, an introduction to multi-scale modelling is provided to clarify the methods used in this study. Secondly, DFT is discussed, covering the most important theoretical concept required for calculations concerning segregation. Finally, the Modified Darken Model (MDM), a rate equation model describing segregation is discussed in detail.

Chapter 4: Experimental techniques and measurements

The main research techniques, namely: Auger Electron Spectroscopy (AES) and Time-of-Flight-Secondary Ion Mass Spectrometry (TOF-SIMS) as well as X-Ray Diffraction (XRD) is presented. Their basic principle of operation, set-up and configuration as well as quantification of AES and TOF-SIMS data is discussed.

Chapter 5: Sample preparation

All the sample preparation methods, techniques and equipment are described in this chapter along with results for the preparation of Fe-S and Fe-Cr-S samples.

Chapter 6: Dependence of the activation energy on the surface orientation

The dependence of the vacancy formation energy and consequently the activation energy of diffusion on the surface orientation in bcc Fe is explained by the combined efforts of DFT, AES and TOF-SIMS.

Chapter 7: Influence of the "surface effect" on the segregation of S in Fe(100) and Fe(111)

Simulations performed by DFT and the MDM are combined with Auger Electron Spectroscopy to investigate the "surface effect" in bcc Fe(100). The use of Fick`s laws in combination with the MDM was utilised to describe the "surface effect" in Fe(111). The results indicate a distinct layer dependence on the segregation parameters of S in both Fe(100) and Fe(111).

Chapter 8: Segregation of Cr in Fe(100) and Fe(100)-S alloys and the "surface effect"

The surface segregation of Cr in bcc Fe(100) is studied using DFT and the MDM. Similar to the Fe-S alloy, a layer dependence for the segregation parameters of Cr in Fe(100) is observed. Furthermore, the segregation of Cr in the ternary Fe(100)-Cr-S alloy is studied. The chapter attempts to clarify the discrepancies and disagreements found in literature concerning the segregation of Cr in Fe and the effect of S on Cr segregation in Fe.

Conclusion

This final chapter draws a conclusion outlining the results obtained in this study.

Appendixes

Appendix A: Computer codes

Appendix B: Publications and conferences attended

1.4. References

[1]. E.C. Viljoen, C. Uebing, Surf. Sci. 410 (1998) 123.

[2]. A. Rolland, M.M. Montagono, J. Cabané, Surf. Sci. 352-354 (1996) 206.

[3]. J. du Plessis, E.C. Viljoen Appl. Surf. Sci. 100-101 (1996) 222.

[4]. J.Y. Wang, J. du Plessis, J.J. Terblans, G.N. van Wyk, Surf. Sci. 423 (1999) 12.

[5]. J.K.O. Asante, J.J. Terblans, W.D. Roos, Appl. Surf. Sci. 252 (2005) 1674.

[6]. S. Choudhury, L. Barnard, J.D. Tucker, T.R. Allen, B.D. Wirth, M. Asta, D. Morgan, J. Nucl. Mater. 411 (2011) 1.

[7]. A. Kiejna, E. Wachowicz, Phys. Rev. B 78 (2008) 113403.

[8]. W.T. Geng, Phys. Rev. B 68 (2003) 233402.

[9]. S. Yamakawa, R. Asahi, T. Koyama, Surf. Sci. 622 (2014) 65.

[10]. M. Lin, X. Chen, X. Li, C. Huang, Y. Li, J. Wang, Appl. Surf. Sci. 297 (2014) 130.

[11]. P. Błonski, A. Kiejna, Vacuum 74 (2004) 179.

[12]. H. D. Shih, F. Jona, D. W. Jepsen, and P. M. Marcus, Phys. Rev. Lett. 46 (1981) 731.

[13]. T.K. Yamada, H. Tamura, M. Shishido, T. Irisawa, T. Mizoguchi, Surf. Sci. 603 (2009) 315.

[14]. X. -S. Yuan, C. Song, X.-S. Kong, Y.-C. Xu, Q.F. Fang, C.S. Liu, Physica B 425 (2013) 42.

[15]. M. Gupta, R.P. Gupta, J. Phys. Condens. Matter 25 (2013) 415502.

[16]. S. Li, S. Krishnamoorthy, A. Li, G. D. Meitzner, E. Iglesia, J. Catal. 206 (2002) 202.

[17]. Z. H. Chonco, A. Ferreira, L. Lodya, M. Claeys, E. Van Steen, J. Catal. 307 (2013) 283.

[18]. J. Oudar, Catal. Rev. 22 (1980) 171.

[19]. W. Arabczyk, D. Moszyński. U. Narkiewicz, R. Pelka, M. Podsiadńły, Catal. Today 124 (2007) 43.

[20]. J.S. Braithwaite, P. Rez, Acta. Mater. 53 (2005) 2715.

[21]. P. Rez, J.R. Alvarez, Acta. Mater. 47 (1999) 4069.

[22]. N.H. Heo, Scripta Mater. 51 (2004) 339.

[23]. S. Suzuki, T. Kosaka, H. Inoue, M. Isshiki, Y. Waseda, Appl. Surf. Sci. 103 (1996) 495.

[24]. J. M. Sampedro, E. del Rio, M. J. Caturla, M. Victoria, J. M. Perlado, J. Nucl. Mater. 417 (2011) 1050.

[25]. F.A. Garner, M.B. Toloczko, B.H. Sencer, J. Nucl. Mater. 276 (2000) 123.

[26]. B. Nonas, K. Wildberger, R. Zeller, P.H. Dederichs, Phys. Rev. Lett. 80 (1998) 4574.

[27]. M. Polak, C. Fadley, L. Rubinovich, Phys. Rev. B 65 (2002) 205404.

[28]. R. Idczak, K. Idczak, R. Konieczny, J. Nucl. Mater. 452 (2014) 141.

[29]. R. Franchy, J. Boysen, P. Gaßmann, C. Uebing, 119 (1997) 357.

[30]. P. Olsson, J. Nucl. Mater. 386-388 (2009) 86.

[31]. P. Olsson, I. Abrikosov, L. Vitos, J. Wallenius, J. Nucl. Mater. 321 (2003) 84.

[32]. E. Park, B. Hüning, M. Spiegel, Appl. Surf. Sci. 249 (2005) 127.

[33]. A.V. Ruban, H.L. Skriver, Comput. Mater. Sci. 15 (1999) 119.

[34]. B. Schiffmann, M. Polak, P.A. Dowben (eds.), A. Miller (eds.) Surface segregation phenomena, CRC Press Inc., Boca Raton, Florida, USA, 1990.

[35]. E. Clauberg, J. Janovĕc, C. Uebing, H. Viefhaus, H.J. Grabke, Appl. Surf. Sci. 161 (2000) 35.

Chapter 2

Diffusion and segregation theory

2.1. Introduction

Diffusion is the transfer of atoms from one part of a system to another as a result of the random motion of the individual atoms in the system [1]. This is illustrated by the following example: consider a large container filled with water, visible through the water volume is the container sides and bottom. Adding a small amount of a strongly concentrated dye to the water gives an illustrative example of diffusion. Initially the two liquids can be distinguished from one another, but as time passes the dye diffuses homogenously throughout the water volume. Should a similar experiment be carried out, with an increase in the water temperature, the time it takes for the dye to diffuse homogenously throughout the water would decrease. Consequently, an increase in thermal energy results in an increased diffusion rate.

Similar to the dye in water example, atoms in crystalline structures also diffuse and are said to “jump” from one atomic position to the next. Atoms diffusing from the bulk to the surface, be it the free surface of the material or the grain boundaries, are said to have ***segregated***. With this basic knowledge in mind the rest of this chapter will give a mathematical description of the rate (kinetics) and equilibrium behaviour (thermodynamics) of diffusion.

2.2. Kinetics of surface segregation and Fick`s model

The migration of atoms results in a flux, *J*, of atoms diffusing in a specific direction, figure 2.1.

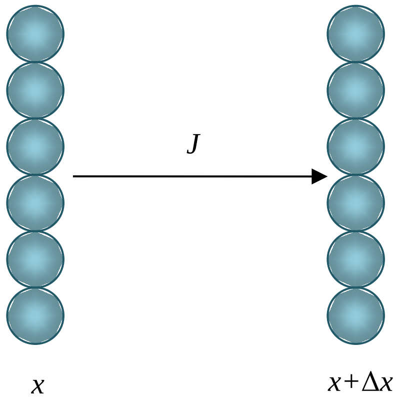

Figure 2.1: *Illustration of the atomic flux, J, as atoms diffuse between two atomic layers separated by a distance of Δx.*

This atomic flux is described by equation 2.1, known as Fick`s first diffusion law [2-4]

$$J = -D\frac{\partial C}{\partial x}. \tag{2.1}$$

Equation 2.1 describes diffusion as a change in concentration, *C*, with respect to position, *x*. The diffusion rate, *D*, is defined by equation 2.2,

$$D = \frac{1}{2}\Gamma(\Delta x)^2, \tag{2.2}$$

where Γ is the mean jump frequency depicting the average number of times an atom changes lattice sites per second. The factor of a half in equation 2.2 is incorporated to describe a 2 dimensional diffusion process. For the three dimensional case, the atomic flux and the diffusion rate is respectively described by equation 2.2 and 2.4

$$J = -D\nabla C. \tag{2.3}$$

$$D = \frac{1}{6}\Gamma(d)^2, \tag{2.4}$$

The symbol *d* in equation 2.4 is the distance over which atoms diffuse; the inter-lattice spacing.

Since it is not possible to obtain the atomic flux in all physical systems, a more useful description of diffusion is required to describe for example the diffusion of atoms in crystalline structures. Such a description is provided by Fick`s second diffusion law in the 2-dimensional case, equation 2.5, which describe the change in concentration as a time, *t*, varying process [2-5]

$$\frac{\partial C}{\partial t} = D\frac{\partial^2 C}{\partial^2 x}. \tag{2.5}$$

In three dimensions equation 2.5 becomes equation 2.6 [2- 5]

$$\frac{\partial C}{\partial t} = D\nabla^2 C. \tag{2.6}$$

Equation 2.6 can be solved for different initial and boundary conditions in order to describe the diffusion process at hand.

One such example is the segregation of atoms from the bulk to the surface of a material, where it is considered that the concentration in the material is uniform and that the surface is always free and open to accommodate the segregated atoms. These initial and boundary conditions are formulated in equation 2.7.

$$\begin{aligned} C &= C_0, \qquad x > 0, \qquad t = 0 \\ C &= 0, \qquad x = 0, \qquad t > 0 \end{aligned} \tag{2.7}$$

The following solution, equation 2.8, is obtained when solving Fick’s second law for the initial and boundary conditions provided by equation 2.7 [6].

$$C = C_0 \operatorname{erf}\left(\frac{x}{2\sqrt{Dt}}\right). \tag{2.8}$$

Equation 2.8 describes the concentration, *C*, of the segregating specie at position *x* in the material after time *t*. Using equation 2.8 and equation 2.1, the flux of atoms leaving an area *A* at *x* = 0 is derived as: [6]

$$J = D\left(\frac{\partial C}{\partial x}\right)_{x=0} = \frac{DC_0}{\sqrt{\pi D t}} \tag{2.9}$$

The total amount of the segregated specie, M_t, over the area *A* is obtained by multiplying equation 2.9 by the area, *A*, and then integrating over this area, resulting in equation 2.10.

$$M_t = 2AC_0\left(\frac{Dt}{\pi}\right)^{\frac{1}{2}}. \tag{2.10}$$

Dividing equation 2.10 by the volume of the segregated specie, results in the concentration of the segregated species segregated from area *A*, equation 2.11[6]

$$C_S = \frac{\left[2AC_0\left(\frac{Dt}{\pi}\right)^{\frac{1}{2}}\right]}{Ad} = \frac{2C_0}{d}\left(\frac{Dt}{\pi}\right)^{\frac{1}{2}}. \tag{2.11}$$

Equation 2.11 provides an expression for the total concentration of the segregating specie after time *t*. Recalling the boundary conditions provided by equation 2.7, the assumption made was that the surface is free and open. In order to be applicable to real systems the bulk concentration, C_B, needs to be taken into consideration, resulting in equation 2.12 [6]

$$C_S = C_B\left[1 + \frac{2}{d}\left(\frac{Dt}{\pi}\right)^{\frac{1}{2}}\right]. \tag{2.12}$$

Equation 2.12 is known as the semi-infinite solution to Fick`s second law, which effectively describes the surface segregation in materials under conditions of constant temperature heating.

Another method by which surface segregation in materials can be studied is the linear programmed heating method [7]. To derive an expression describing surface segregation under these conditions the surface enrichment factor, β, is defined by equation 2.13 [7, 8]

$$\beta = \frac{C_S - C_B}{C_B} = \left[\frac{2}{d} \left(\frac{Dt}{\pi} \right)^{\frac{1}{2}} \right]. \tag{2.13}$$

The time variation of β is provided by equation 2.14

$$\frac{d\beta}{dt} = \left[\frac{1}{d} \left(\frac{D}{\pi} \right)^{\frac{1}{2}} \left(\frac{1}{t_B} \right)^{\frac{1}{2}} \right] \tag{2.14}$$

where the increase in β is given as a function of t_B and not t, since the temperature was linearly increased resulting in a varying diffusion coefficient. From equation 2.13 the term t_B is given by equation 2.15

$$t_B = \left(\frac{\beta d}{2} \right)^2 \left(\frac{\pi}{D} \right). \tag{2.15}$$

To obtain an analytical solution for the surface enrichment, β, equation 2.15 is substituted into equation 2.14 to obtain equation 2.16

$$\partial\beta = \frac{1}{d} \left(\frac{D}{\pi} \right)^{\frac{1}{2}} \partial t \left(\frac{2}{\beta d} \right) \left(\frac{D}{\pi} \right)^{\frac{1}{2}}. \tag{2.16}$$

Where D is described by the well-known Arrhenius relation, equation 2.17 [9],

$$D = D_0 exp\left(\frac{-Q}{RT} \right) \tag{2.17}$$

with D_0 the pre-exponential factor, Q the activation energy and R the universal gas constant with a value of 8.314 J/K/mol. Since the temperature is linearly increased it is described in terms of time, t, and the heating rate, α, equation 2.18

$$T = T_0 + \alpha t. \tag{2.18}$$

Integration of equation 2.16 over the temperature range of the linear programmed heating run, $T_{final} - T_0$, results in equation 2.19 [7, 8]

$$\frac{1}{2}\beta^2 = \frac{2}{\pi}\left(\frac{D_0}{\alpha d^2}\right)\int_{T_0}^{T_{\mathrm{final}}} \exp\left(\frac{-Q}{RT}\right) dT \ . \tag{2.19}$$

The integral term in equation 2.19 can be approximated by the following expression, equation 2.20

$$\int_{T_0}^{T_{\mathrm{final}}} \exp\left(\frac{-Q}{RT}\right) dT = \left[\frac{RT^2}{Q}\exp\left(\frac{-Q}{RT}\right)\right] \tag{2.20}$$

which leads to equation 2.21 [8]

$$\beta^2 = \frac{4}{\pi}\frac{D_0}{\alpha d^2}\left[\frac{RT^2}{Q}\exp\left(\frac{-Q}{RT}\right)\right]. \tag{2.21}$$

Equation 2.19 and 2.21 effectively describes the kinetics of surface segregation in terms of the kinetic parameters Q and D_0, but fails to provide an accurate description of the equilibrium region. This is a consequence of the boundary condition which assumes a free and open surface. Figure 2.2 illustrates the use of equation 2.21 in order to describe the kinetics of S segregation in the Fe(100) surface orientation and obtain the kinetic parameters D_0 and Q. In order to obtain information concerning the equilibrium properties of segregation the Bragg-Williams model is described in the next section.

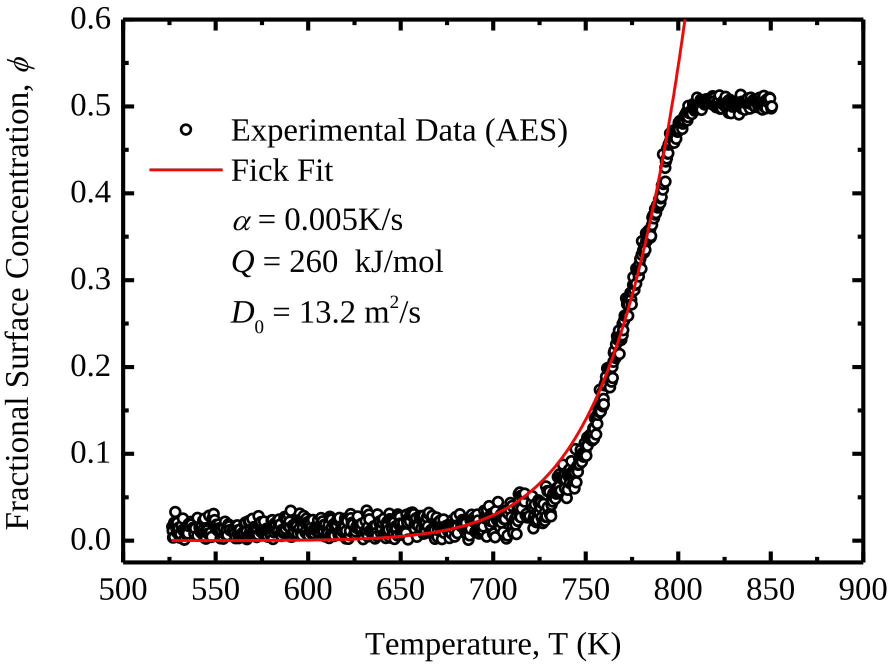

Figure 2.2: *Fick's model for linear programmed heating fitted onto the segregation data of S segregating to the surface of the Fe(100) orientation. The data was measured by Auger Electron Spectroscopy (AES).*

2.3. Equilibrium of surface segregation and the Bragg-Williams model

Equilibrium surface segregation in a closed thermodynamic system consisting of *p* phases can be considered as the lowering of the systems total energy, expressed by equation 2.22 [6]

$$(\delta E)_{S,V,n_i} = \sum_{\upsilon=1}^{p} \delta E^{\upsilon} \geq 0 \tag{2.22}$$

The term δE^{υ} is given by equation 2.23

$$\delta E^{\upsilon} = T^{\upsilon}\delta S - P^{\upsilon}\delta V + \delta G^{\upsilon} \tag{2.23}$$

where T is the temperature, S the entropy, V the volume and P the pressure of phase υ. If the pressure and temperature is the same for all the phases (constant T and P), equation 2.23 becomes equation 2.24

$$\delta E^{\upsilon} = \delta G^{\upsilon} . \tag{2.24}$$

This reduces equation 2.22 to:

$$\left(\delta E\right)_{n_i} = \delta G_{n_i} \geq 0 . \tag{2.25}$$

Thus, equilibrium segregation can be described in terms of the Gibbs free energy at constant P and T. Equation 2.26 provides and expression for the Gibbs free energy in terms of the chemical potential μ,

$$G = \sum_{\upsilon=1}^{p} \sum_{i=1}^{m} n_i^{\upsilon} \mu_i^{\upsilon} \quad , \tag{2.26}$$

where n_i^{υ} is the number of moles of specie i in phase υ. The chemical potential is thus a measure of the energy per mole of a substance. Previously diffusion/segregation was considered as the result of a concentration gradient (section 2.2), in this section the process is seen to be the result of the system tending to the lowest energy. In fact, the previous consideration obeys the energy minimization principle by decreasing the concentration gradient. Although, this only forms a special case where energy is minimized by a decrease in the concentration and cannot be considered as a general case as is evident in surface segregation. This concept is evident in the description of the Modified Darken Model in chapter 3, section 3.5.1. Using the product rule of differentiation, the variation in the Gibbs free energy is described by equation 2.27

$$\delta G = \sum_{\upsilon=1}^{p} \left[\sum_{i=1}^{m} \delta n_i^{\upsilon} \mu_i^{\upsilon} + \sum_{i=1}^{m} n_i^{\upsilon} \delta \mu_i^{\upsilon} \right] . \tag{2.27}$$

Thus, the equilibrium condition of surface segregation in a closed thermodynamic system can be written in terms of the chemical potential, equation 2.28

$$\sum_{\upsilon=1}^{p} \left[\sum_{i=1}^{m} \delta n_i^{\upsilon} \mu_i^{\upsilon} + \sum_{i=1}^{m} n_i^{\upsilon} \delta \mu_i^{\upsilon} \right] \geq 0 . \tag{2.28}$$

For a system of two phases, the bulk (B) and surface phase (ϕ), equation 2.28 becomes equation 2.29

$$\delta G = \left[\sum_{i=1}^{m} \delta n_i^{\phi} \mu_i^{\phi} + \sum_{i=1}^{m} \delta n_i^{B} \mu_i^{B} \right] + \left[\sum_{i=1}^{m} n_i^{\phi} \delta \mu_i^{\phi} + \sum_{i=1}^{m} n_i^{B} \delta \mu_i^{B} \right]. \tag{2.29}$$

The second square bracket is the well-known Gibbs-Duhem [6, 10] expression which is equal to zero and thus equation 2.29 reduces to equation 2.30

$$\delta G = \left[\sum_{i=1}^{m} \delta n_i^{\phi} \mu_i^{\phi} + \sum_{i=1}^{m} \delta n_i^{B} \mu_i^{B} \right]. \tag{2.30}$$

For a closed thermodynamic system, the number of atom remain constant as expressed in equation 2.31

$$\sum_{i=1}^{m} n_i^{\phi} = n^{\phi} \ . \tag{2.31}$$

The total change in the number of surface atoms is given by equation 2.32

$$\delta n_1^{\phi} + \delta n_2^{\phi} + \cdots + \delta n_{m-1}^{\phi} = -\delta n_m^{\phi} . \tag{2.32}$$

Substituting equation 2.32 into equation 2.30 results in equation 2.33

$$\sum_{i=1}^{m-1} \left(\mu_i^{\phi} - \mu_i^{B} - \mu_m^{\phi} + \mu_m^{B} \right) \delta n_i^{\phi} \geq 0 . \tag{2.33}$$

Since m-1 terms are independent of δn_i^{ϕ}, the term in brackets is equal to zero, equation 2.34 [6]

$$\left(\mu_i^{\phi} - \mu_i^{B} - \mu_m^{\phi} + \mu_m^{B} \right) = 0 . \tag{2.34}$$

Equation 2.34 describes the condition for surface-bulk equilibrium in terms of the chemical potential. In the case of a binary component system equation 2.34 becomes:

$$\mu_1^{\phi} - \mu_1^{B} - \mu_2^{\phi} + \mu_2^{B} = 0 . \tag{2.35}$$

In terms of the regular solution model, the chemical potential in equation 2.35 is described by equations 2.36 and 2.37 [6, 10]

$$\mu_i = \mu_i^0 + RT \ln a_i \,, \tag{2.36}$$

$$\mu_i = \mu_i^0 + RT \ln X_i + RT \ln f_i \,, \tag{2.37}$$

with the activity function, a_i, in terms of the activity coefficient, f_i, presented by [10]:

$$a_i = f_i X_i \,, \tag{2.38}$$

where X_i is the concentration of species i. The last term in equation 2.37 is expressed in terms of the interaction parameter for each component by equation 2.39 and 2.40 respectively [6, 10]

$$RT \ln f_1 = \Omega_{12} X_2^2 \,, \tag{2.39}$$

$$RT \ln f_2 = \Omega_{12} X_1^2 \,. \tag{2.40}$$

Where, Ω_{12}, is the regular solution interaction parameter described by equation 2.41 [6, 10]

$$\Omega_{12} = Z\left[\varepsilon_{12} - \frac{1}{2}\left(\varepsilon_{11} + \varepsilon_{22}\right)\right], \tag{2.41}$$

with ε being the interaction energy of the subscripted species. Inserting equations 2.39 and 2.40 into the definition of the chemical potential, equation 2.37, and using the result to solve equation 2.35 delivers the Bragg-Williams equation, equation 2.42 [6]

$$\frac{X_1^{\phi}}{1 - X_1^{\phi}} = \frac{X_1^{B}}{1 - X_1^{B}} \exp\left[\frac{\Delta G + 2\Omega_{12}\left(X_1^{\phi} - X_1^{B}\right)}{RT}\right] . \tag{2.42}$$

Equation 2.42 effectively describes the equilibrium of surface segregation in terms of the thermodynamic properties, ΔG and Ω, for a binary component system. This is illustrated in figure 2.3, where equation 2.42 was fitted to the segregation data of S segregating in the Fe(100) surface orientation.

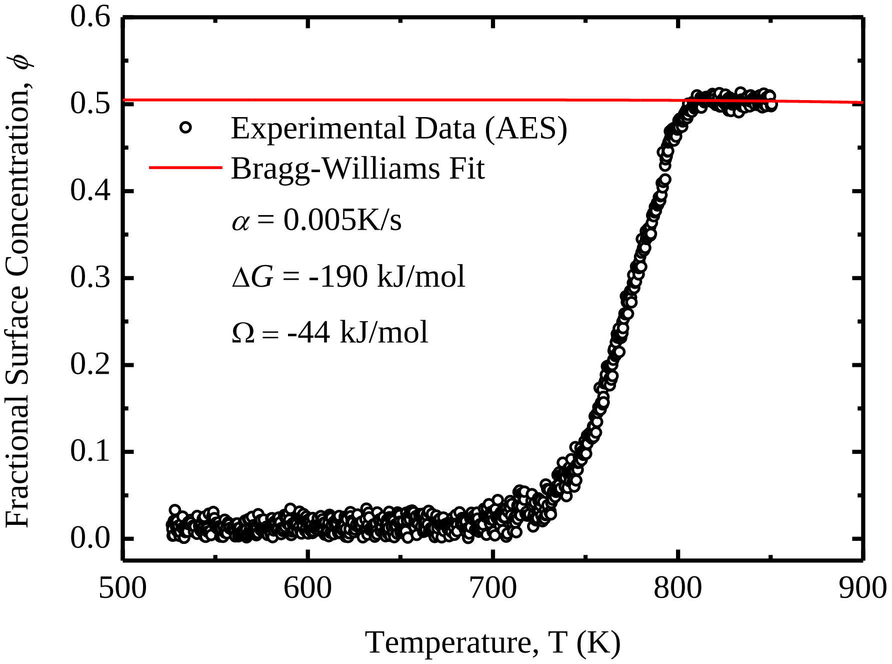

Figure 2.3: *Bragg-William model fitting to the Auger Electron Spectroscopy (AES) data of S segregation in the Fe(100) surface orientation.*

The Fick and Bragg-Williams models presented above were used as a first approximation to the fitting performed by the Modified Darken Model. This latter model is capable of describing both the kinetics and equilibrium of surface segregation and will be discussed in the next chapter, chapter 3.

2.4. Diffusion mechanisms/pathways

The undertaken study is focused on the diffusion of atoms favouring a substitutional lattice site. Thus, atoms which are large enough to occupy empty lattice sites within the host material are considered. There are a number of other mechanisms namely: interstitial, interstitialcy and the ring mechanism. However, these various mechanisms fall outside the scope of the present study; the interested reader is referred to references [2-4].

As mentioned above, atoms diffusing via a substitutional mechanism migrate into an empty lattice site located in a nearest neighbour lattice position. In order for this to occur, the creation of a lattice vacancy is required. The probability, *P*, for each of these processes, the creation of a vacancy and the migration of a solute atom into a vacancy is presented by equations 2.43 and 2.44 [4, 9, 11] respectively

$$P_{vac} = \exp\left(\frac{-E_{vac}}{RT}\right), \tag{2.43}$$

$$P_m = \exp\left(\frac{-E_m}{RT}\right), \tag{2.44}$$

where E_{vac} represents the vacancy formation energy and E_m the migration energy. To obtain the activation energy, Q, of the diffusion process these two energy terms are summed, giving rise to the diffusion probability, equation 2.45 [4].

$$P_{diffusion} = \exp\left(\frac{-(E_m + E_{vac})}{RT}\right) = \exp\left(\frac{-Q}{RT}\right). \tag{2.45}$$

Figure 2.4 illustrates the diffusion of a substitutional atom in a crystalline solid. The atom (grey atom) diffuses to a nearest neighbour vacant lattice site. This requires the lattice to distort, especially atoms 1 and 2, to allow for a path along which the atom can migrate.

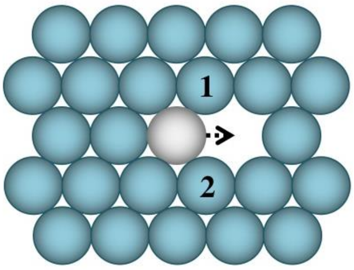

Figure 2.4: *Illustration of the substitutional diffusion mechanism for crystalline solids. For the atom in grey to diffuse into the nearest neighbour vacancy, the lattice needs to distort providing a diffusion path via atoms 1 and 2.*

The requirement of a vacancy makes this mechanism rather slow, compared to interstitial diffusion where atoms can diffuse freely without the need of a vacancy [3].

2.5. Diffusion rate and temperature

In the basic example of the dye diffusing in water, as referred to in section 2.1, an increase in temperature resulted in an increased diffusion rate. The influence of temperature on diffusion is evident in equations 2.43 – 2.45. This temperature relation to the diffusion rate, *D*, is provided by the Arrhenius equation, equation 2.46 [2; 4]

$$D = D_0 P_{diffusion} = D_0 \exp\left(\frac{-Q}{RT}\right), \tag{2.46}$$

where D_0 is a temperature independent quantity referred to as the pre-exponential factor. Equation 2.46 can be written in terms of the migration and vacancy formation energy terms, equation 2.47

$$D = D_0 \left\{ \left[\exp\left(-\frac{E_m}{RT} \right) \right]_{P_m} + \left[\exp\left(-\frac{E_{vac}}{RT} \right) \right]_{P_{vac}} \right\}. \tag{2.47}$$

The migration energy, vacancy formation energy and consequently the activation energy of diffusion was calculated in this study for both S and Cr in Fe using Density Functional Theory, with results presented in chapters 6, 7 and 8.

2.6. Summary

This chapter presented the most important concepts needed to understand the phenomena of diffusion and segregation. Two models were described, namely; Fick's model and the Bragg-Williams model. These two models can be used respectively to describe the kinetics and equilibrium of surface segregation. Each model was derived in full due to their significance to this study.

2.7. References

[1]. J. Crank, The mathematics of diffusion, Oxford university press, London, 1975.

[2]. P. Heitjans, J. Karger, (Eds.), Diffusion in condensed matter, Springer, Berlin, 2005.

[3]. P.G. Shewmon, Diffusion in solids, McGraw-Hill Book Company, New York, 1963.

[4]. R.J. Borg, G.J. Dienes, Introduction to solid state diffusion, Academic Press, New York, 1988.

[5]. D.A. Porter, K.E. Easterling, Phase transformations in metals and alloys, Chapman & Hall, 1981.

[6]. J. du Plessis, Surface segregation, Sci-Tech publications, Bloemfontein, 1990.

[7]. E.C. Viljoen, Lineêre verhittingstudie van oppervlaksegregasie in binêre allooie, Dissertation, Bloemfontein, 1995.

[8]. W.J. Erasmus, Die segregasie van Sb na die lae-indeksoppervlakke van Cu enkelkristalle, Dissertation, Bloemfontein, 1999.

[9]. D.R. Askeland, Material science and engineering, Stanley Thornes, Cheltenham, 1998.

[10]. C.H.P. Lupis, Chemical thermodynamics of materials, Elsevier Science Publishing Co., Inc., New York, 1983.

[11]. M.E. Glicksman, Diffusion in Solids: Fields theory solid state principles and applications, John Wiley & Sons Inc., New York, 2000.

Chapter 3

Simulation methods

3.1. Introduction

Computer aided simulations has added significant value to material science. The investigation of existing and the design of new materials can be achieved with the utilisation of computer aided simulations. Various techniques and methods have been developed over the years and together with the development of large supercomputer clusters, have resulted in the increased capabilities of computational material science. Computational methods range from the quantum mechanical methods, capable of describing the many-body interactions of electrons, to models that make use of rate equations. Figure 3.1 provides a schematic illustration of different computational methods and their respective spatial and temporal scales [1].

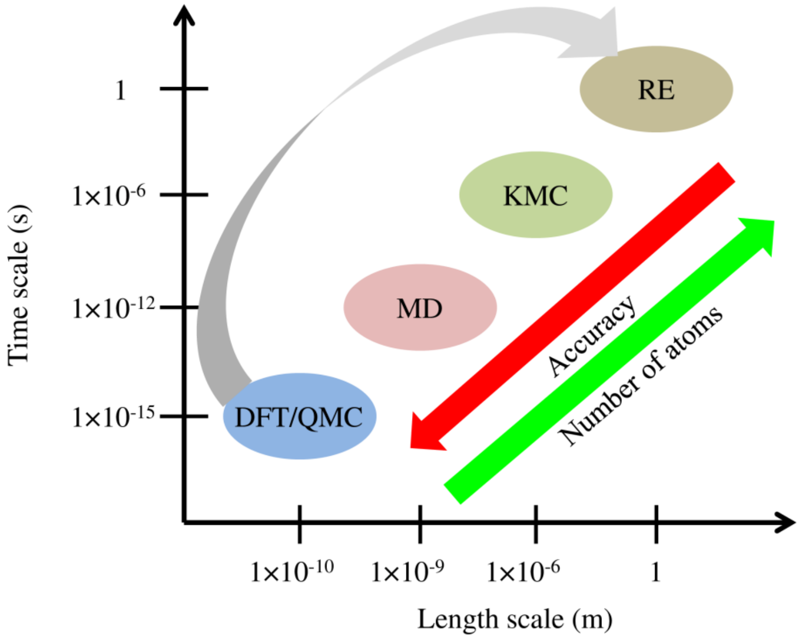

Figure 3.1: *Temporal and spatial scales that can be achieved with different computational methods namely; Density Functional Theory (DFT), Quantum Monte Carlo (QMC), Molecular Dynamics (MD), Kinetic Monte Carlo (KMC) and Rate Equation (RE) models.*

From figure 3.1 it is evident that computational tools are capable of probing the length and time scales ranging from the atomistic to the continuum regime. Density Functional Theory (DFT) is capable of describing the electron interactions in the system while Molecular Dynamics (MD) makes use of interatomic potentials to describe the atomic interactions using newton`s second law of motion. Kinetic Monte Carlo (KMC), as the name depicts, describes the system in terms of its kinetic rates. KMC is however incapable of determining the kinetic rates themselves and can only use the probabilities of a transition to predict certain properties of the material. The kinetic rates need to be obtained from another simulation method i.e. DFT or from empirical methods. Lastly, the use of rate equations significantly reduce the computational time, but is limited in terms of the information which they can provide since the material is treated as a continuum. However, if a rate equation model is combined with DFT a powerful computational tool is formed. The focus of this study will be on the combination of DFT and the Modified Darken Model (MDM), a rate equation model, to study surface segregation.

According to figure 3.1, each simulation method is capable of describing material properties in a certain temporal and spatial scale. On the one hand, the accuracy of DFT is always very desirable, although it comes at the expense of computational time and is therefore limited to small systems. On the other hand, rate equations are capable of describing very large systems in experimentally achievable time periods, although they are incapable of describing the electronic structure. These two methods are combined in this study using a bottom-up sequential ***multi-scale modelling*** approach in order to harness the advantages of accuracy, as well as both temporal and spatial scales. Two schemes exist for multi-scale modelling, namely; the sequential and the concurrent schemes [1, 2].

Sequential: Sequential multi-scale modelling, also called message passing or hierarchical multi-scale modelling, is the combination of two models which are computed independently. The first model is used to describe the properties of the system in a specific spatial and temporal region. Next, these properties are passed to the second model which uses these properties to obtain the final answer. An example of this scheme is the combined use of DFT and the KMC algorithm to study diffusion in materials. The activation energy barriers are calculated by DFT calculations, which are then passed to the KMC algorithm.

Concurrent: This multi-scale modelling approach, also known as the hybrid approach, uses two models when interdependency between the models exists. The first model is used to obtain the properties of the system. These properties are then passed on to the second model which performs further calculations on the system. Control is then again transferred to the first model and the cycle is repeated until the system converges or reaches an equilibrium point. In reality the two models execute almost simultaneously and the parameters of the system is said to be obtained on-the-fly by the first model. Using the same DFT and Kinetic Monte Carlo example as described for the sequential scheme, concurrently DFT will be used on-the-fly to calculate the activation energy barriers. Although this might lead to an increase in accuracy, since variations of the activation energy barriers are considered. The increase in computational time can make this implementation computationally very expensive.

DFT and the MDM were successfully used in a sequential multi-scale modelling approach in order to simulate the surface segregation of S in Fe and Cr in Fe. The results are presented in chapter 7, where S segregation in Fe(100) and Fe(111) is discussed and in chapters 8 which deal with Cr segregation in Fe(100) as well as both Cr and S segregation in Fe(100).

3.2. Density Functional Theory (DFT)

DFT uses the ground state electron density, $n(\bar{r})$, of the system under study to solve the Schrödinger-like Kohn-Sham equation self-consistently [3]. This allows for properties such as the force, energy and stress to be calculated. Since the electronic structure of the system is taken into account, DFT is capable of describing properties such as charge transfer and magnetism. This chapter covers the most important concepts of DFT that are required to perform calculations related to diffusion and segregation. Justification for using the electron density is outlined by the Hohenberg-Kohn theorems. The algorithm used for solving the Kohn-Sham equation is presented in the form of a diagram, outlining the important aspects of a DFT calculation. For an accurate description of the electron exchange and correlation, different functionals are available. Of these functionals the Local Density Approximation (LDA) and the Generalised Gradient Approximation (GGA) are the most common and will be discussed. Electronic wavefunctions are covered in the section on pseudopotentials, followed by the Climbing Image Nudged Elastic Band (CI-

NEB) algorithm for minimum energy path calculations. All DFT calculations presented in this study were performed by the Quantum ESPRESSO code [4], utilising plane waves and pseudopotentials to solve the Kohn-Sham equations.

3.2.1. Hohenberg-Kohn theorems

Density functional theory is based on two fundamental theorems formulated by Hohenberg and Kohn [5]. These theorems allow for any property of a many-body system to be described as a functional of the ground state electron density $n(\bar{r})$. This implies that in principle a function of position, $n(\bar{r})$, determines the ground state and all the excited states of the many-body wavefunction. The Hamiltonian to which these theorems apply is provided by equation 3.1 [5]

$$\hat{H} = -\frac{\hbar^2}{2m_e}\sum_i \nabla_i^2 - \sum_{i,I}\frac{Z_I e^2}{\left|\bar{r}_i - \bar{R}_I\right|} + \frac{1}{2}\sum_{i \neq j}\frac{e^2}{\left|\bar{r}_i - \bar{r}_j\right|} - \sum_I \frac{\hbar^2}{2M_I}\nabla_I^2 + \frac{1}{2}\sum_{I \neq J}\frac{Z_I Z_J e^2}{\left|\bar{R}_I - \bar{R}_I\right|}\,. \tag{3. 1}$$

where, $\frac{\hbar^2}{2m_e}\sum_i \nabla_i^2$, is the kinetic energy of the electrons, $\sum_{i,I}\frac{Z_I e^2}{\left|\bar{r}_i - \bar{R}_I\right|}$, is the potential acting on the electrons due to the nuclei and, $\frac{1}{2}\sum_{i \neq j}\frac{e^2}{\left|\bar{r}_i - \bar{r}_j\right|}$, is the electron-electron interaction. According to the Born-Oppenheimer approximation, the mass of the ions are large compared to the mass of the electrons and thus, $\frac{1}{M_I}$ is a negligible quantity which leads to a zero value for the fourth term. The final term, $\frac{1}{2}\sum_{I \neq J}\frac{Z_I Z_J e^2}{\left|\bar{R}_I - \bar{R}_I\right|}$, is the classical interaction of the nuclei with one another.

Theorem 1: For any system of interacting particles in an external potential, $V_{ext}(\bar{r})$, the potential $V_{ext}(\bar{r})$, is determined uniquely, except for a constant, by the ground state electron density $n(\bar{r})$.

Corollary 1: Since the Hamiltonian is fully determined, except for a constant shift in the energy, it follows that the many-body wavefunction for all states (ground and excited) are determined. Therefore, all the properties of the system are completely determined by the ground state electron density $n(\bar{r})$.

Theorem 2: A universal functional, $F(E[n])$ in terms of the energy, $E(n)$, which is a function of the electron density, *n*, can be defined which is valid for any external potential, $V_{ext}(\bar{r})$. For any particular external potential, $V_{ext}(\bar{r})$, the exact ground state energy of the system is the global minimum value of this functional, $F(E[n])$, and the electron density, $n(\bar{r})$, that minimises the functional is the exact ground state electron density $n(\bar{r})$.

Corollary 2: The functional $F(E[n])$ alone is sufficient to determine the exact ground state energy and electron density. Excited states of the electron must often be determined by other means.

[5 - 7].

3.2.2. The self-consistent loop for solving the Kohn-Sham equation

The Schrödinger-like Kohn-Sham equation with an effective potential, $V_{eff}^{\sigma}(\bar{r})$, is solved self-consistently in order to obtain the energy, force and stress of the system under study. Figure 3.2 [5] illustrates the self-consistent loop used in order to solve the Kohn-Sham equation. The symbols used in figure 3.2 are explained in table 3.1.

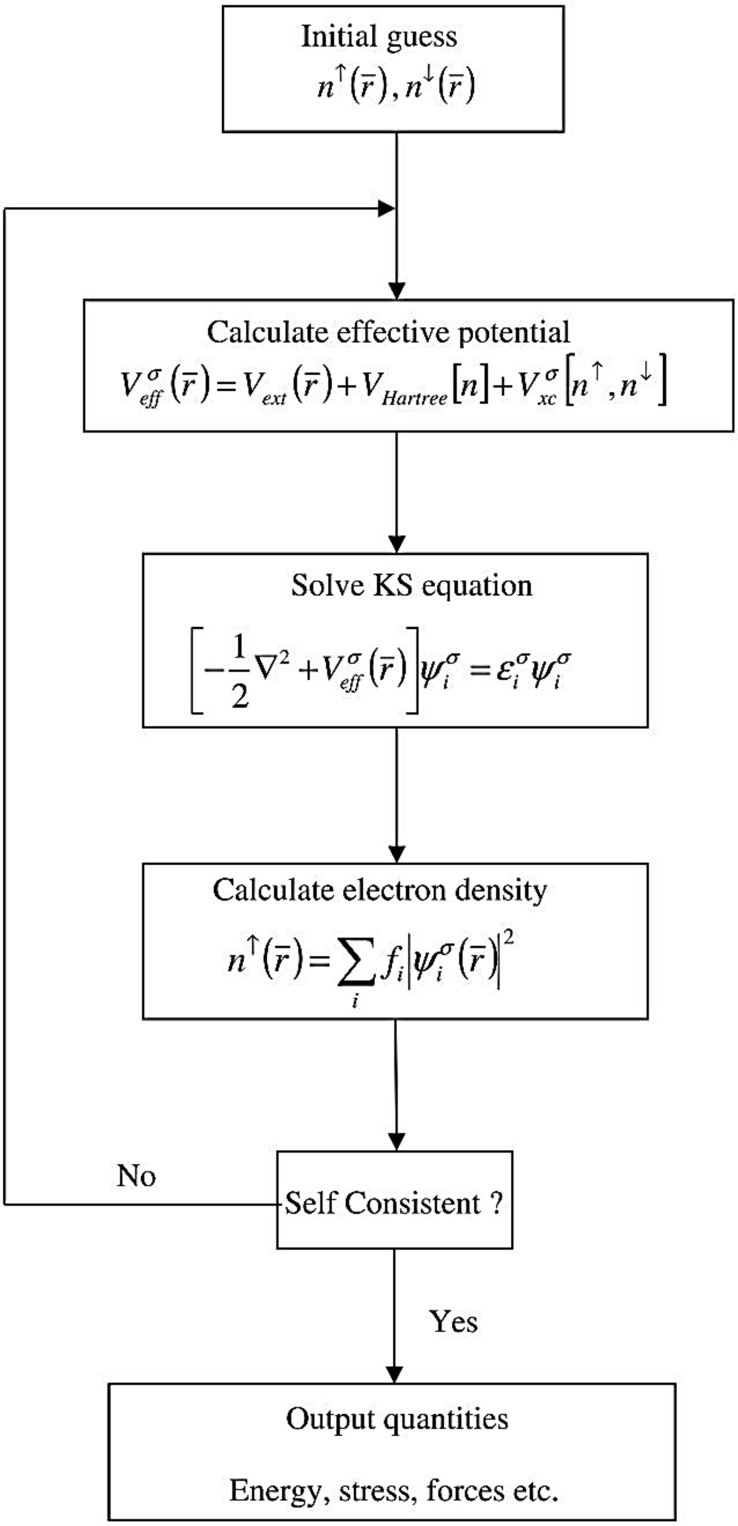

Figure 3.2: *Diagrammatic representation of the algorithm used in density functional theory for solving the Kohn-Sham equation self-consistently* [8].

The effective potential, V_{eff}, consisting of the external potential, V_{ext}, the Hartree potential, $V_{Hartree}$, and the exchange-correlation potential, V_{XC}, is calculated for a given electron density. Solving the Kohn-Sham equation for this effective potential, results in the total energy of the system. The total energy is used to calculate a new electron density, which is mixed in a specified ratio with the old electron density in order to obtain a new input value for the electron density. This step is repeated until convergence of the total energy is achieved according to a prescribed convergence criteria.

Table 3.1: *Symbols used in the Kohn-Sham loop of figure 3.2* [8]

$n^{\uparrow\downarrow}(\bar{r})$	Electron density with spin up ($\uparrow$) and spin down ($\downarrow$) electrons
$V_{eff}^{\sigma}(\bar{r})$	Effective potential of the Kohn-Sham equation, where σ refers to the spin of the electrons
$V_{ext}(\bar{r})$	External potential of electron-ion interactions
$V_{Hartree}[n]$	Hartree potential, that includes the electron-electron interactions
$V_{XC}^{\sigma}[n^{\uparrow},n^{\downarrow}]$	Exchange-correlation potential. Deals with the exchange and correlation effects of electrons in the system.
f_i	Smearing scheme for metallic systems (Methfessel-Paxton, Fermi etc.)

3.2.3. Exchange-Correlation energy functionals

To solve the Kohn-Sham equation, the exchange-correlation energy functional is determined self-consistently as it is a functional of the density. Different functionals have been derived, with the most common of these being the LDA and the GGA functionals.

3.2.3.1. Local Density Approximation (LDA)

This functional is based on the assumption of a solid having a charge density which closely resembles that of a homogeneous electron gas. In such a system the exchange and correlation effects are seen as being local in character. The functional integrates over all space where the exchange correlation energy density is assumed to be the same as that found in a homogeneous electron gas with that same density. Equation 3.2 provides the functional for a spin polarised system, with equation 3.3 where the exchange and correlation terms have been separated [5 - 7]

$$E_{XC}^{LSDA}[n\uparrow, n\downarrow] = \int d\bar{r}\; n(\bar{r})\varepsilon_{XC}^{\text{hom}}\left(n^{\uparrow}(\bar{r}), n^{\downarrow}(\bar{r})\right) \tag{3.2}$$

$$E_{XC}^{LSDA}[n\uparrow, n\downarrow] = \int d\bar{r}\; n(\bar{r})\varepsilon_{X}^{\text{hom}}\left(n^{\uparrow}(\bar{r}), n^{\downarrow}(\bar{r})\right) + \varepsilon_{C}^{\text{hom}}\left(n^{\uparrow}(\bar{r}), n^{\downarrow}(\bar{r})\right) \tag{3.3}$$

For the spin un-polarised case; the following simplification can be made to equations 3.2 and 3.3

$$n(\bar{r}) = \frac{n^{\uparrow}(\bar{r}) + n^{\downarrow}(\bar{r})}{2}. \tag{3.4}$$

Metals are a good example of where this functional provides an accurate description, as they closely resemble a homogenous electron gas. However, since the functional fails to include the self-interaction term care should be taken when applying the functional as it could lead to inaccurate results [5]. Additionally, the functional has been found to predict an inaccurate description of the ground state for bcc Fe [9] and was therefore not used in this study.

3.2.3.2. Generalised Gradient Approximation (GGA)

The GGA functional is similar to the LDA functional, but also includes the density gradient in the exchange-correlation energy term. This functional is expressed by equation 3.5 where the electron spin has been included [5 - 7]

$$E_{XC}^{GGA} = [n\uparrow, n\downarrow] = \int d\bar{r}\; n(\bar{r})\varepsilon_{XC}\left(n^{\uparrow}(\bar{r}), n^{\downarrow}(\bar{r}), \left|\nabla n^{\uparrow}\right|, \left|\nabla n^{\downarrow}\right|\right)$$

$$E_{XC}^{GGA} = [n\uparrow, n\downarrow] = \int d\bar{r}\; n(\bar{r})\varepsilon_{X}^{\text{hom}}(n)F_{XC}\left(n^{\uparrow}(\bar{r}), n^{\downarrow}(\bar{r}), \left|\nabla n^{\uparrow}\right|, \left|\nabla n^{\downarrow}\right|\right). \tag{3.5}$$

The term $F_{XC}\left(n^{\uparrow}(\bar{r}), n^{\downarrow}(\bar{r}), \left|\nabla n^{\uparrow}\right|, \left|\nabla n^{\downarrow}\right|\right)$ can further be divided into an exchange function, F_X, and a correlation function, F_C. The interested reader is referred to reference [5] for a more in-depth discussion on exchange correlation functionals. The GGA functional developed by Perdew and Wang (PW91) [10] has been used for all calculation presented in this study.

3.2.4. Pseudopotentials

Pseudopotentials are used to replace the all-electron potential, since they have fewer oscillations to account for and reduce the computational time. Outside of the core region, r_c, the pseudopotential, V_{pseudo}, resembles the shape of the all-electron potential, $V_{all\text{-}electron}$ and the pseudo wavefunction, Ψ_{pseudo}, resembles the shape of the all-electron wavefunction, $\Psi_{all\text{-}electron}$, as illustrated in figure 3.3. Since only the valence electrons in atoms, those electrons outside of the core region, are responsible for bond formation only these electrons are important in electronic structure calculations [11]. Two distinctions are made within the class of pseudopotentials, namely the “hard” potentials and the “soft” potentials. This refers to their smoothness, with the “hard” potentials having more oscillations and subsequently more Fourier components whilst the “soft” potentials are smoother with fewer oscillations and less Fourier components [11]. Depending on the parameters of interest a choice can be made between the two, with “hard” potentials being better suited for properties related to core interactions. Figure 3.3 illustrates the difference between the pseudo wavefunction and potential as compared to the all-electron wavefunction and potential. Outside the core region, r_c, it can be seen that there is no difference between the all-electron wavefunction and pseudo wavefunction as well as between the pseudo potential and the all-electron potential.

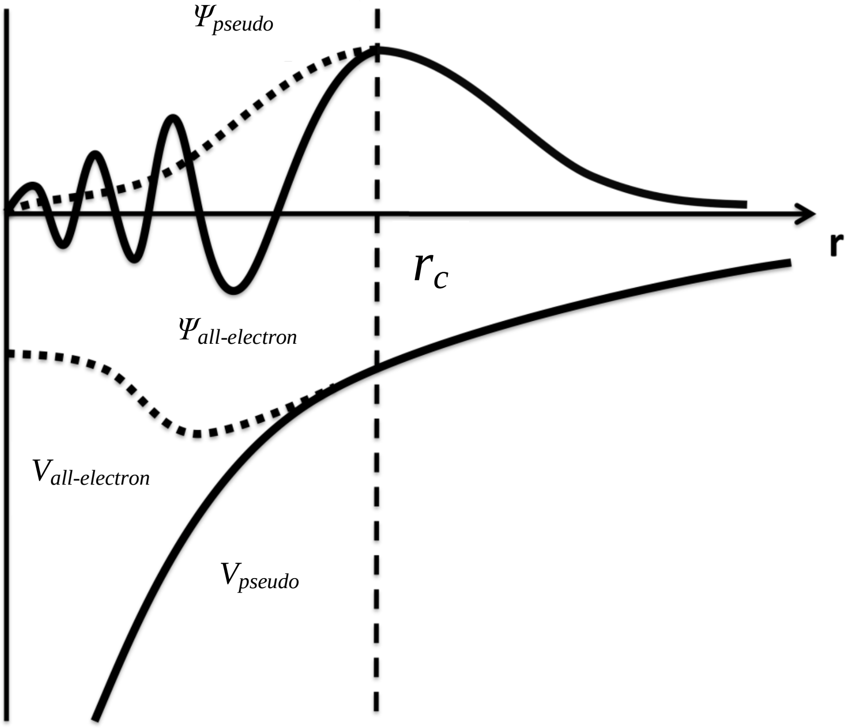

Figure 3.3: *Comparison between the all-electron potential, $V_{all\text{-}electron}$, and all-electron wavefunction, $\Psi_{all\text{-}electron}$, versus the pseudopotential, V_{pseudo}, and pseudo wavefunction, Ψ_{pseudo}. Outside of the core region, r_c, it is observed that the pseudo wavefunction and potential resemble that of the all-electron wavefunction and potential* [12].

3.2.5. Nudged Elastic Band (NEB)

Recalling the dependence of the diffusion rate on the temperature as described by the Arrhenius relation in chapter 2, presented here by equation 3.6 for completeness

$$D = D_0 \left\{ \left[\exp\left(-\frac{E_m}{RT} \right) \right]_{P_m} + \left[\exp\left(-\frac{E_{vac}}{RT} \right) \right]_{P_{vac}} \right\} , \tag{3.6}$$

where D is the diffusion rate and D_0 is the pre-exponential factor. In the exponent, E_m is the migration energy of diffusion, E_{vac}, the vacancy formation energy, R the universal gas constant and T the temperature in Kelvin. To obtain the migration energy of diffusion, the

Minimum Energy Path (MEP) is calculated by the Climbing Image Nudged Elastic Band (CI-NEB) method. This method and the ordinary Nudged Elastic Band (NEB) method are described.

The NEB method allows for a number of images along an elastic band to be chosen between an initial and a final state. Each image refers to a 3 dimensional coordinate of the atoms as they migrate from the initial to the final state. These images are then optimised according to the NEB force, $\overline{F}_i^{NEB}$, in order to obtain the MEP and consequently the equilibrium position of the atom along the path at each image. Figure 3.4 shows the diffusion of an atom along the initial NEB path and the MEP respectively [13]. When optimised, the initial NEB path is equal to the minimum energy path. The inset shows the NEB force with its parallel and perpendicular components.

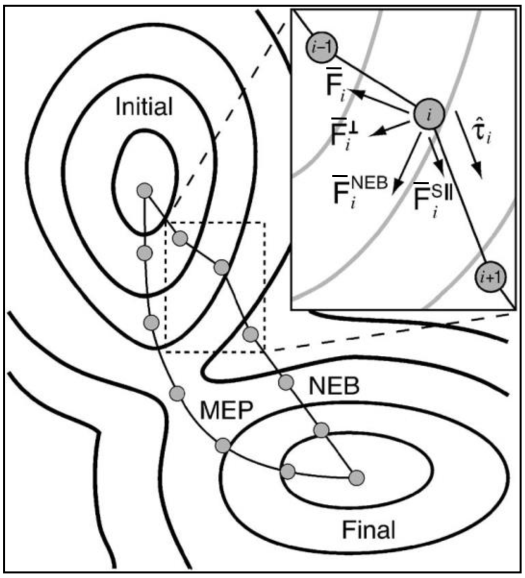

Figure 3.4: *Illustration of the NEB method for finding the minimum energy path of a diffusing atom, the NEB force,* $\overline{F}_i^{NEB}$, *with its parallel and perpendicular components are given in the inset* [13].

The NEB force is provided by equation 3.7 [11, 13, 14]

$$\overline{F}_i^{NEB} = \overline{F}_i^{\perp} + \overline{F}_i^{S\|} \tag{3.7}$$

where $\overline{F}_i^{\perp}$ is called the true force, the force projected perpendicular to the elastic band between two images. The true force is experienced by the atom as a result of the potential energy surface in which it is located, equation 3.8 [11, 13, 14]

$$\overline{F}_i^{\perp} = -\nabla E\left(\overline{R}_i\right) + \nabla E\left(\overline{R}_i\right) \bullet \hat{\tau}_i \hat{\tau}_i . \tag{3.8}$$

The force, $\overline{F}_i^{S\|}$, parallel to the elastic band is the force experienced by the images as a result of the elastic band itself, equation 3.9 [11, 13, 14]

$$\overline{F}_i^{S\|} = k\left(\left|\overline{R}_{i+1} - \overline{R}_i\right| - \left|\overline{R}_i - \overline{R}_{i-1}\right|\right)\hat{\tau}_i \tag{3.9}$$

where $\hat{\tau}_i$ is the tangent along the direction, $\overline{R}$, of the path from one image to a neighbouring image of higher energy and k is the elastic constant. Optimisation of the elastic band is obtained by minimising the NEB force in equation 3.7, resulting in the minimum energy path. The NEB method can be further modified by allowing the image of highest energy, image l, to climb up the saddle point via a reflection in the force along the tangent, $\hat{\tau}_l$. The force experienced by atom l is given by equation 3.10 [14]

$$\overline{F}_i^{\mathrm{CI}} = \overline{F}_l - 2\overline{F}_l \bullet \hat{\tau}_i \hat{\tau}_i . \tag{3.10}$$

Image, l, expressed in equation 3.10 does not experience any spring forces and can climb freely along the saddle point. This modified version of the NEB method is known as the Climbing Image Nudged Elastic Band Method (CI-NEB). The CI-NEB method as implemented in Quantum ESPRESSO was used to calculate the migration energies of both S in Fe(100) and Cr in Fe(100).

3.3. Rate equations

The first part of the bottom-up multi-scale model, consists of DFT calculations in order to obtain the segregation parameters. These parameters include the interaction parameter, Ω, segregation energy, ΔG, and the activation energy, Q. The second part of the sequential multi-scale scheme is the utilisation of the Modified Darken Model (MDM), a set of differential rate equations to simulate the segregation profiles in the binary Fe(100)-S and Fe(100)-Cr alloys. Apart from its simulation functionality, the MDM was also used in order to extract the segregation parameters from the experimental segregation data.

3.3.1. Modified Darken Model (MDM)

Darken [15] was the first to describe the diffusion process as the lowering of the system`s total energy, by considering the chemical potential of the system provided by equation 3.11

$$J_i = -M_i X_i^b \left(\frac{\partial \mu}{\partial x} \right)_{x=b}, \tag{3.11}$$

where J is the atomic flux, M the mobility given in terms of the diffusion rate D/RT, X the concentration and x the position of species, i. Du Plessis [16] modified Darken`s equation to be suitable for a discreet system of m components, composed of N+1 atomic layers parallel to the surface layer. Figure 3.5 illustrates the discreet system of layers with the surface layer , atomic layer 1, denoted by ϕ.

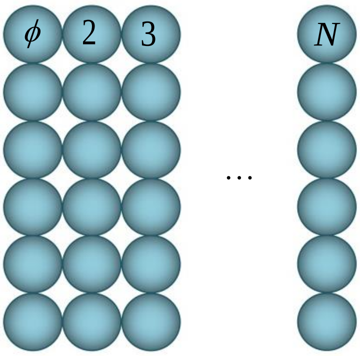

Figure 3.5: *A discreet system described by a set of atomic layers parallel to the surface layer,* ϕ.

The change in chemical potential with respect to position, for atoms diffusing from atomic layer j +1 to atomic layer j is described by equation 3.12

$$-\frac{\partial \mu}{\partial x} = \frac{\Delta \mu^{(j+1 \to j)}}{d}, \tag{3.12}$$

where d is the inter-lattice spacing of the crystal under consideration. For a substitutional system, $\Delta \mu^{(j+1 \to j)}$ is provided by equation 3.13 [16]

$$\Delta\mu^{(j+1\to j)} = \left(\mu_i^{(j+1)} - \mu_i^{(j)}\right) - \left(\mu_m^{(j+1)} - \mu_m^{(j)}\right). \tag{3.13}$$

Substituting equation 3.12 into equation 3.11 results in equation 3.14 which describes the flux of atoms from the j + 1-th layer to the j-th layer

$$J_i^{(j+1\to j)} = -M_i X_i^{(j+1)} \left(\frac{\Delta\mu_i^{(j+1\to j)}}{d} \right)_{x=b}, \tag{3.14}$$

with $X_i^{(j+1)}$ as the supply concentration for the diffusion process. A similar expression is obtained for the atomic flux of atoms from the j-th layer to the j + 1-th layer. The rate of increase in the number of atoms of specie i in the j-th layer is described by equation 3.15

$$\frac{\partial N_i^{(j)}}{\partial t} = d^2 \left(J_i^{(j+1\to j)} - J_i^{(j\to j-1)} \right). \tag{3.15}$$

Substitution of the expression for the atomic flux, equation 3.14, into equation 3.15 results in the general form of the MDM, equation 3.16 [16]:

$$\frac{\partial X_i^{(j)}}{\partial t} = \left[\frac{M_i^{(j+1\to j)}\alpha}{d^2} \Delta\mu_i^{(j+1\to j)} - \frac{M_i^{(j\to j-1)}\beta}{d^2} \Delta\mu_i^{(j\to j-1)} \right], \tag{3.16}$$

where

$$\alpha = X_i^{j+1} \text{ } if \text{ } \Delta\mu_i^{(j+1\to j)} > 0 \tag{3.17}$$

or $$\alpha = X_i^{j} \text{ } if \text{ } \Delta\mu_i^{(j+1\to j)} < 0 \tag{3.18}$$

and $$\beta = X_i^{j} \text{ } if \text{ } \Delta\mu_i^{(j\to j-1)} > 0 \tag{3.19}$$

or $$\beta = X_i^{j-1} \text{ } if \text{ } \Delta\mu_i^{(j\to j-1)} < 0 \tag{3.20}$$

and

$$\Delta\mu_i^{(j+1\to j)} = \mu_i^{(j+1)} - \mu_i^{(j)} - \mu_m^{(j+1)} + \mu_m^{(j)} \tag{3.21}$$

$$\Delta\mu_i^{(j\to j-1)} = \mu_i^{(j)} - \mu_i^{(j-1)} - \mu_m^{(j)} + \mu_m^{(j-1)}. \tag{3.22}$$

Equations 3.17 – 3.20 states that the supply concentrations, α and β, is determined by the sign of the term describing the change in chemical potential. This concept is illustrated in figure 3.6.

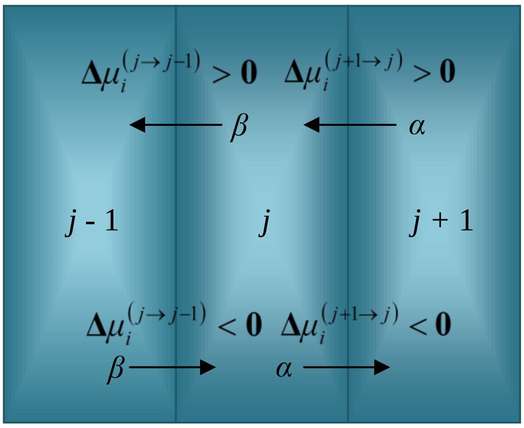

Figure 3.6: *Illustration of how the supply concentration for segregation between atomic layers is determined by the change in the chemical potential term,* $\Delta\mu$.

Considering the case of surface segregation, the following set of equations results from equation 3.16 [16]

$$\frac{\partial X_i^{(\phi)}}{\partial t} = \left[\frac{M_i^{(2\to\phi)} X_i^{(2)}}{d^2} \Delta\mu_i^{(2\to\phi)} \right], \tag{3.23}$$

$$\frac{\partial X_i^{(2)}}{\partial t} = \left[\frac{M_i^{(3\to2)} X_i^{(3)}}{d^2} \Delta\mu_i^{(3\to2)} - \frac{M_i^{(2\to1)} X_i^{(2)}}{d^2} \Delta\mu_i^{(2\to1)} \right], \tag{3.24}$$

$$\frac{\partial X_i^{(3)}}{\partial t} = \left[\frac{M_i^{(4\to3)} X_i^{(4)}}{d^2} \Delta\mu_i^{(4\to3)} - \frac{M_i^{(3\to2)} X_i^{(3)}}{d^2} \Delta\mu_i^{(3\to2)} \right], \tag{3.25}$$

$$\vdots$$

$$\frac{\partial X_i^{(j)}}{\partial t} = \left[\frac{M_i^{(j+1\to j)} X_i^{(j+1)}}{d^2} \Delta\mu_i^{(j+1\to j)} - \frac{M_i^{(j\to j-1)} X_i^{(j)}}{d^2} \Delta\mu_i^{(j\to j-1)} \right]. \tag{3.26}$$

Thus, there are (m-1)(N+1) rate equations for a m component system of N+1 atomic layers. These equations are valid for the segregation of solute atoms to the surface of crystalline materials. Due to the significance of this model in this study, the binary and ternary expressions for the change in chemical potential, $\Delta\mu_i^{(j+1\rightarrow j)}$ and $\Delta\mu_i^{(j\rightarrow j-1)}$, will be derived in full.

Derivation of the change in the chemical potential for segregation in binary alloys is performed next. The chemical potential of component *i*, expressed in terms of the standard chemical potential, μ^0, and the activity function, *a*, is described by equation 3.27 [17]

$$\mu_i = \mu_i^0 + RT\ln a_i = \mu_i^0 + RT\ln X_i + RT\ln f_i, \tag{3.27}$$

where f_i is the activity coefficient. The last term in equation 3.27 can be expressed in terms of the interaction parameter, Ω, for a regular solution model, resulting in equations 3.28 and 3.29 respectively [17]

$$RT\ln f_1 = \Omega_{12} X_2^2, \tag{3.28}$$

$$RT\ln f_2 = \Omega_{12} X_1^2. \tag{3.29}$$

Substitution of equations 3.28 and 3.29 into equation 3.27 for each component, leads to the expressions for the change in the chemical potential for a binary system, equations 3.30 and 3.31

$$\Delta\mu_1^{(j+1\rightarrow j)} = \left\{ \begin{array}{l} \mu_1^{0(j+1)} - \mu_1^{0(j)} - \mu_2^{0(j+1)} + \mu_2^{0(j)} + \left[RT\ln X_1 + \Omega_{12}\left(X_2^2\right)\right]^{(j+1)} - \left[RT\ln X_1 + \Omega_{12}\left(X_2^2\right)\right]^{(j)} \\ -\left[RT\ln X_2 + \Omega_{12}\left(X_1^2\right)\right]^{(j+1)} + \left[RT\ln X_2 + \Omega_{12}\left(X_1^2\right)\right]^{(j)}, \end{array} \right\} \tag{3.30}$$

$$\Delta\mu_1^{(j\rightarrow j-1)} = \left\{ \begin{array}{l} \mu_1^{0(j)} - \mu_1^{0(j-1)} - \mu_2^{0(j)} + \mu_2^{0(j-1)} + \left[RT\ln X_1 + \Omega_{12}\left(X_2^2\right)\right]^{(j)} - \left[RT\ln X_1 + \Omega_{12}\left(X_2^2\right)\right]^{(j-1)} \\ -\left[RT\ln X_2 + \Omega_{12}\left(X_1^2\right)\right]^{(j)} + \left[RT\ln X_2 + \Omega_{12}\left(X_1^2\right)\right]^{(j-1)}. \end{array} \right\}. \tag{3.31}$$

The standard segregation energy is expressed by equation 3.32[16], expressed in terms of the standard chemical potentials.

$$\Delta G_1^{0(j)} = \left(\mu_1^{0(j)} - \mu_1^{0(\phi)} - \mu_2^{0(j)} + \mu_2^{0(\phi)}\right). \tag{3.32}$$

Similar to the binary case, equations 3.27 together with the expressions of the activity coefficient term, equations 3.33 – 3.35 [16], results in the expressions for the change in the chemical potential of the tertiary component system, equations 3.36 and 3.37.

$$RT \ln f_1 = \Omega_{13}(1 - X_1)^2 + \Omega_{23} X_2^2 + \Omega' X_2 (1 - X_1), \tag{3.33}$$

$$RT \ln f_2 = \Omega_{23}(1 - X_2)^2 + \Omega_{13} X_1^2 + \Omega' X_1 (1 - X_2), \tag{3.34}$$

$$RT \ln f_3 = \Omega_{13} X_1^2 + \Omega_{23} X_2^2 + \Omega' X_1 X_2 \tag{3.35}$$

$$\begin{aligned}
&\Delta\mu_1^{(j+1\to j)} = \Delta G_1^{0(j)} + \left[RT \ln X_1 + \Omega_{13}(1 - X_1)^2 + \Omega_{23} X_2^2 + \Omega' X_2 (1 - X_1)\right]^{(j+1)} \\
&- \left[RT \ln X_1 + \Omega_{13}(1 - X_1)^2 + \Omega_{23} X_2^2 + \Omega' X_2 (1 - X_1)\right]^{(j)} - \left[RT \ln X_3 + \Omega_{13} X_1^2 + \Omega_{23} X_2^2 + \Omega' X_1 X_2\right]^{(j+1)} \\
&+ \left[RT \ln X_3 + \Omega_{13} X_1^2 + + \Omega_{23} X_2^2 + \Omega' X_1 X_2\right]^{(j)},
\end{aligned} \tag{3.36}$$

$$\begin{aligned}
&\Delta\mu_2^{(j+1\to j)} = \Delta G_2^{0(j)} + \left[RT \ln X_2 + \Omega_{23}(1 - X_2)^2 + \Omega_{13} X_1^2 + \Omega' X_1 (1 - X_2)\right]^{(j+1)} \\
&- \left[RT \ln X_2 + \Omega_{23}(1 - X_2)^2 + \Omega_{13} X_1^2 + \Omega' X_1 (1 - X_2)\right]^{(j)} - \left[RT \ln X_3 + \Omega_{13} X_1^2 + \Omega_{23} X_2^2 + \Omega' X_1 X_2\right]^{(j+1)} \\
&+ \left[RT \ln X_3 + \Omega_{13} X_1^2 + + \Omega_{23} X_2^2 + \Omega' X_1 X_2\right]^{(j)}.
\end{aligned} \tag{3.37}$$

$$\begin{aligned}
&\Delta\mu_1^{(j\to j-1)} = \Delta G_1^{0(j)} + \left[RT \ln X_2 + \Omega_{23}(1 - X_2)^2 + \Omega_{13} X_1^2 + \Omega' X_1 (1 - X_2)\right]^{(j)} \\
&- \left[RT \ln X_2 + \Omega_{23}(1 - X_2)^2 + \Omega_{13} X_1^2 + \Omega' X_1 (1 - X_2)\right]^{(j-1)} - \left[RT \ln X_3 + \Omega_{13} X_1^2 + \Omega_{23} X_2^2 + \Omega' X_1 X_2\right]^{(j)} \\
&+ \left[RT \ln X_3 + \Omega_{13} X_1^2 + + \Omega_{23} X_2^2 + \Omega' X_1 X_2\right]^{(j-1)},
\end{aligned} \tag{3.38}$$

$$\begin{aligned}
&\Delta\mu_2^{(j\to j-1)} = \Delta G_2^{0(j)} + \left[RT \ln X_1 + \Omega_{13}(1 - X_1)^2 + \Omega_{23} X_2^2 + \Omega' X_2 (1 - X_1)\right]^{(j)} \\
&- \left[RT \ln X_1 + \Omega_{13}(1 - X_1)^2 + \Omega_{23} X_2^2 + \Omega' X_2 (1 - X_1)\right]^{(j-1)} - \left[RT \ln X_3 + \Omega_{13} X_1^2 + \Omega_{23} X_2^2 + \Omega' X_1 X_2\right]^{(j)} \\
&+ \left[RT \ln X_3 + \Omega_{13} X_1^2 + + \Omega_{23} X_2^2 + \Omega' X_1 X_2\right]^{(j-1)},
\end{aligned} \tag{3.39}$$

To illustrate the use of the MDM for extracting the segregation parameters from experimental data, the model for a binary alloy is fitted to the Auger Electron Spectroscopy data of S segregation in Fe(100) in figure 3.7.

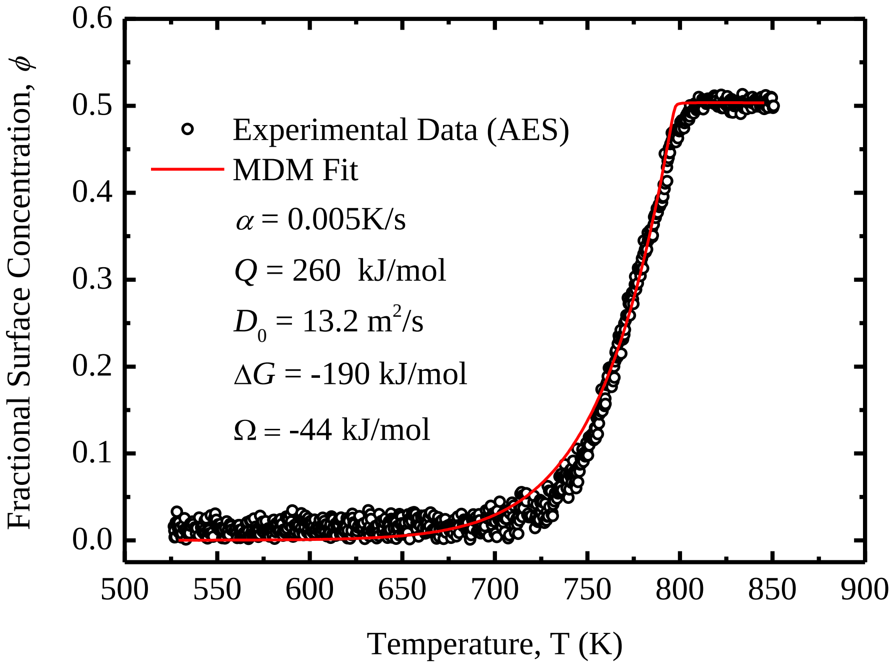

Figure 3.7: *The Modified Darken Model fitted to the experimental data of S segregation in bcc Fe(100).*

The Modified Darken Model was coded in the C++ programming language. Integration was performed using the forward difference Euler method with a variable time step in order to speed up the calculations. Apart from obtaining the appropriate time step, the majority of the computational time is spent on computing the chemical potential terms. To increase the speed of the calculations, these terms were computed in parallel by implementation of the OpenMP libraries within the Linux (Ubuntu) operating system. Appendix A contains sections of the computer code as well as the submission files required for submitting simulations.

3.4. Summary

This chapter provided the theoretical concepts necessary to understand the simulation methods used in simulating the surface segregation of S and Cr in bcc Fe. Included are the theoretical concepts of DFT namely the Hohenberg-Kohn theorems, the algorithm for solving the Kohn-Sham equations, a description of the exchange and correlation potentials, pseudopotentials and the NEB as well as CI-NEB methods. The Modified Darken Model, a rate equations model, was described in full for the case of a binary as well as a ternary component system. This model can be used to extract the segregation parameters from experimental data or to simulate surface segregation with segregation parameters obtained by DFT.

3.5. References

[1]. C.H. Claassens, Kinetic Monte Carlo Simulation of the Growth of Gold Nanostructures on a Graphite Substrate, Ph.D. Dissertation, Bloemfontein, 2006.

[2]. J.A. Elliot, Novel approaches to multi-scale modelling in materials science, Vol. 56 no 4, ASM International, 2011.

[3]. W. Kohn, L.J. Sham, Phys. Rev. B. 140 (1965) 1133.

[4]. P. Gianozzi, et al., J. Phys. Cond. Mat. 21 (2009) 1.

[5]. R.M. Martin, Electronic structure: basic theory and Practical applications, Cambridge University Press, Cambridge, 2004.

[6]. K. Burke, The ABC of DFT, Department of Chemistry, University of California Irvine, 2007.

[7]. P. Giannozzi, Density Functional Theory for electronic structure calculations, Italy: Pisa, 2005.

[8]. P. E. Barnard, Experimental and computational study of S segregation in Fe, M.Sc. Dissertation, Bloemfontein, 2012.

[9]. D.J. Singh, W.E. Pickett, H. Krakauer, Phys. Rev. B 43 (1991) 11628.

[10]. J.P. Perdew, Y. Wang, Phys. Rev. B. 45 (1992) 13244.

[11]. D.S. Sholl, J.A. Steckel, Density Functional Theory: A practical introduction, Wiley & sons, New Jersey, 2009.

[12]. S. Clark, pseudopotentials, Available from: http://cmt.dur.ac.uk/sjc/thesis_dlg/node21.html. (Accessed 26-11-2014).

[13]. D. Sheppard, R. Terrell, G. Henkelman, J. Chem. Phys. 128 (2008) 134106.

[14]. G. Henkelman, B.P. Uberuaga, H. Jonsson, J. Chem. Phys. 113 (2000) 9901.

[15]. L.S. Darken, Trans. AIME, 180 (1949) 430.

[16]. J. du Plessis, Surface segregation, Sci-Tech publications, Bloemfontein, 1990.

[17]. C.H.P. Lupis, Chemical thermodynamics of materials, Elsevier Science Publishing Co., Inc., New York, 1983.

Chapter 4

Experimental techniques and measurements

4.1. Introduction

The experimental techniques; X-Ray Diffraction (XRD), Auger Electron Spectroscopy (AES) and Time-of-Flight Secondary Ion Mass Spectrometry (TOF-SIMS) along with the settings used for the respective measurements is described. AES and TOF-SIMS are used to monitor the elements on the surface of Fe during a linear programmed heating segregation study. X-Ray Diffraction is used for analysing the crystal orientations of the different grains in a polycrystalline Fe sample. The existing SAM 600 Auger system is modified by the addition of a custom in-house built sample heater allowing the system to be used for surface segregation studies. This new sample heater is presented along with a software package for controlling the temperature. Quantification of AES data is discussed for both homogenous samples as well as for segregated layers. Since AES and TOF-SIMS are the primary research techniques used during the course of this study, a comparison between the techniques is drawn in order to highlight each techniques strengths and weaknesses with reference to surface segregation measurements.

4.2. X-Ray Diffraction (XRD)

X-Ray diffraction was utilised to obtain the orientations of the different grains in the polycrystalline Fe sample, see chapter 6 for results. The system used is the D8 Advance, manufactured by BRUKER. This section describes the principle of operation for XRD and provides the experimental settings used in this study.

4.2.1. Principle of operation

The technique is capable of identifying the crystal orientation of the sample under study. For the purpose of this study XRD was used to identify each of the grain orientations in the polycrystalline Fe sample. High energy X-Rays (up to 40 kV) bombard the sample, which are then diffracted from the atomic lattice planes in the sample. Since periodic structures have a well-defined crystal structure, diffracted X-Rays form an X-Ray peak from which the different orientations can be identified. For diffracted X-Rays differing with a whole number of wavelengths, as they arrive at the detector, constructive interference will occur since the X-rays are in phase. A resulting XRD peak with an amplitude equal to the sum of the interfering X-ray amplitudes will be observed. If the diffracted X-Rays are out of phase, destructive interference will occur resulting in a zero amplitude for the diffracted X-Rays. Figure 4.1 illustrates the diffraction of X-Rays from two parallel atomic planes. The angle of incidence is given by θ, where the angle 2θ, gives the experimentally measured angle.

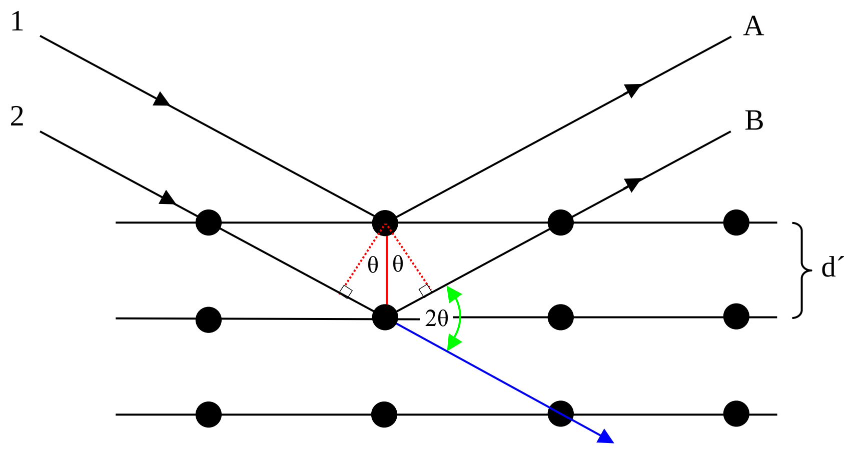

Figure 4.1: *Schematic representation of the principle of operation behind X-Ray diffraction. The sample is bombarded with X-Rays, which are diffracted off the sample to form either a constructive or destructive interference pattern, with constructive interference forming the XRD spectrum* [1].

From figure 4.1, the total path difference x, between the incident X-Rays 1 and 2 when they arrive at point A and B respectively is described by equation 4.1

$$x = 2d^{'} \sin\theta . \tag{4.1}$$

In order for constructive interference to occur, the path difference between two X-Rays has to be equal to a whole number of wavelengths, $n\lambda$, with n being a whole number. Inserting this condition into equation 4.1 results in equation 4.2 [2]

$$n\lambda = 2d^{'} \sin\theta \quad n = 1, 2, 3 \ldots \tag{4.2}$$

Equation 4.2 provides the condition required for constructive interference of the diffracted X-Rays, known a Bragg`s Law. Since different values of n can produce different $d^{'}$ values, it is more convenient to make use of equation 4.3 [2]

$$\lambda = 2d \sin\theta , \tag{4.3}$$

where

$$d = \frac{d^{'}}{n} . \tag{4.4}$$

4.2.2. XRD experimental settings

The optimised settings used for XRD analysis of the Fe sample is provided in table 4.1. These settings were obtained after a number of tests were performed in order to maximise the signal to noise ratio of the measured spectra.

Table 4.1: *Optimised parameters of the D8 ADVANCE X-Ray diffractometer used to determine the orientations of different grains in a polycrystalline Fe sample.*

	Parameter	**Value**
X-Ray source	Voltage	40 kV
	Current	40 mA
	Slit width	0.60 mm
	Rotary absorber	On
Detector	Filter	Nickel (Ni) 0.02 mm
Measurement settings	Time per step	1 s
	Step size	0.0085 °
	Mode	Coupled two theta
	Rotation	On

These settings were used to obtain the results presented in chapter 6, section 6.3.2.

4.3. Auger Electron Spectroscopy (AES)

4.3.1. Principle of operation

AES is a surface sensitive technique capable of detecting nearly all elements in the periodic table, except H, He and has difficulty detecting Li. This exclusion is due to the requirement of at least three electrons in the atoms of the element being analysed. Figure 4.2 illustrates the process whereby Auger electrons are generated. The technique’s surface sensitivity arises due to the inelastic mean free path of the emitted electron, which is limited to the first few atomic layers. Analysis of deeper layers can be achieved by “peeling” away the topmost layers using ion sputtering. The surface sensitivity of the technique makes it an ideal technique to study surface segregation, since segregated atoms occupy the first atomic layer of the host material.

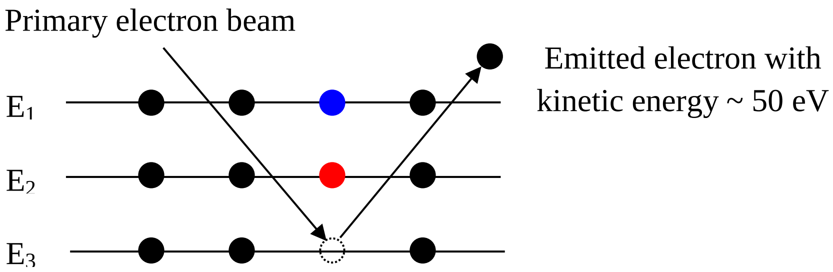

1. Ionisation of the core energy level

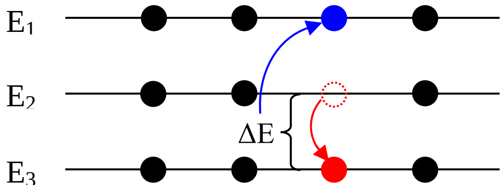

2. Electron fills the ionised energy level

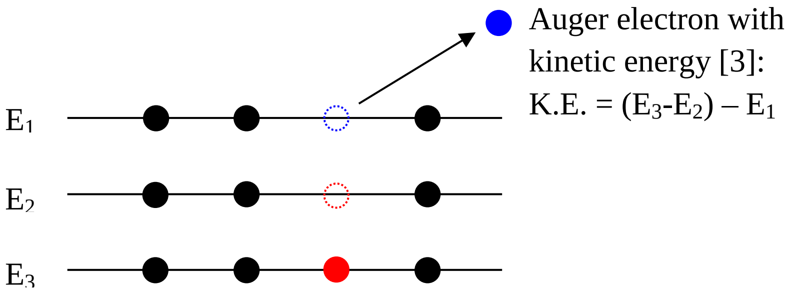

3. Emission of an Auger electron

Figure 4.2: *Illustration of the 3 step process whereby an Auger electron is generated upon high energy electron bombardment. The primary electron beam creates an ionised core level vacancy, which is subsequently filled by an electron from a higher energy level relaxing to this core level. The energy released during this relaxation is taken up by the Auger electron which enables it to be emitted with an energy characteristic to the element under investigation* [1].

4.3.2. AES apparatus

Auger Electron Spectroscopy measurements were conducted using both the SAM 600 and the PHI 700 Auger systems. Both systems are products of the Physical Electronics Company (PHI). The PHI 700 was used for depth-profiling analysis and SED imaging of samples. While the SAM 600 system was primarily used to study surface segregation of S in Fe. The experimental settings used for each of the systems are described in this section.

The accuracy of the measured data depends largely on the optimised settings and operation of the system. To ensure the system functions optimally, the control units were switched on and allowed to stabilise for 24 hours before use. If this step is neglected, drifting in the measured data can occur due to the progressive heating and thus optimum functioning of components. For the same reason the electron gun filament was switched on at least 3 hours before measurements were performed, while for the ion gun 1 hour was deemed sufficient. Tables 4.2 and 4.3 provide the optimised parameters used by each system in order to obtain the maximum signal to noise ratio.

Table 4.2: *Optimised settings used on the SAM 600 which allowed for a maximum signal to noise ratio.*

	Parameter	**Value**
Electron gun settings	Primary beam voltage	10.0 keV
	Primary beam voltage (elastic peak)	3.0 keV
	Emission current	35 µA
	Beam current	2.5µA
	Beam diameter	40 µm
Ion gun settings	Argon beam voltage	2.0 kV
	Beam current	32 nA
	Beam current (with raster on)	19.0 nA
	Raster size	1.5 × 1.5 mm
	Emission current	25 mA
	Ar Pressure	5.0 mPa
Measurement settings	eV/step	1 eV
	Time/step	200 ms
	Number of differentiation points	11
	Photomultiplier voltage (measurements)	1700 eV
	Photomultiplier voltage (elastic peak)	1400 eV

Table 4.3: *Optimised settings used on the PHI 700 Auger Nanoprobe which allowed for a maximum signal to noise ratio.*

	Parameter	**Value**
Electron gun	Primary beam voltage	25.0 keV
	Primary beam voltage (elastic peak)	1.0 keV
	Emission current	280 µA
	Beam current (depth profiling)	10 nA
	Beam current (SED imaging)	1 nA
	Beam diameter (SED imaging)	20 nm
Ion gun	Argon beam voltage	2.0 kV
	Beam current	2.0 µA
	Beam current (with raster on)	2.0 µA
	Emission current	12.5 mA
	Pressure	15 mPa
	Raster size	1 × 1 mm
Measurement settings	Energy per step	1 eV
	Time per step	50 ms
	Number of differentiation points	13
	Photomultiplier voltage (measurements)	2200 eV
	Photomultiplier voltage (elastic peak)	2200

4.3.3. AES segregation measurements

The segregation of S in bcc Fe was measured with the SAM 600. To enable the study of surface segregation, a custom in house built sample heater with an accompanying software package was utilised. This section elaborates on the design of the sample heater, the control unit for controlling the temperature as well as the accompanying software package.

4.3.3.1. Sample heater design

Figure 4.3 presents a 3D illustration of the sample heater and sample stage. Commercially no such sample heater could be found and one had to be designed and built in-house.

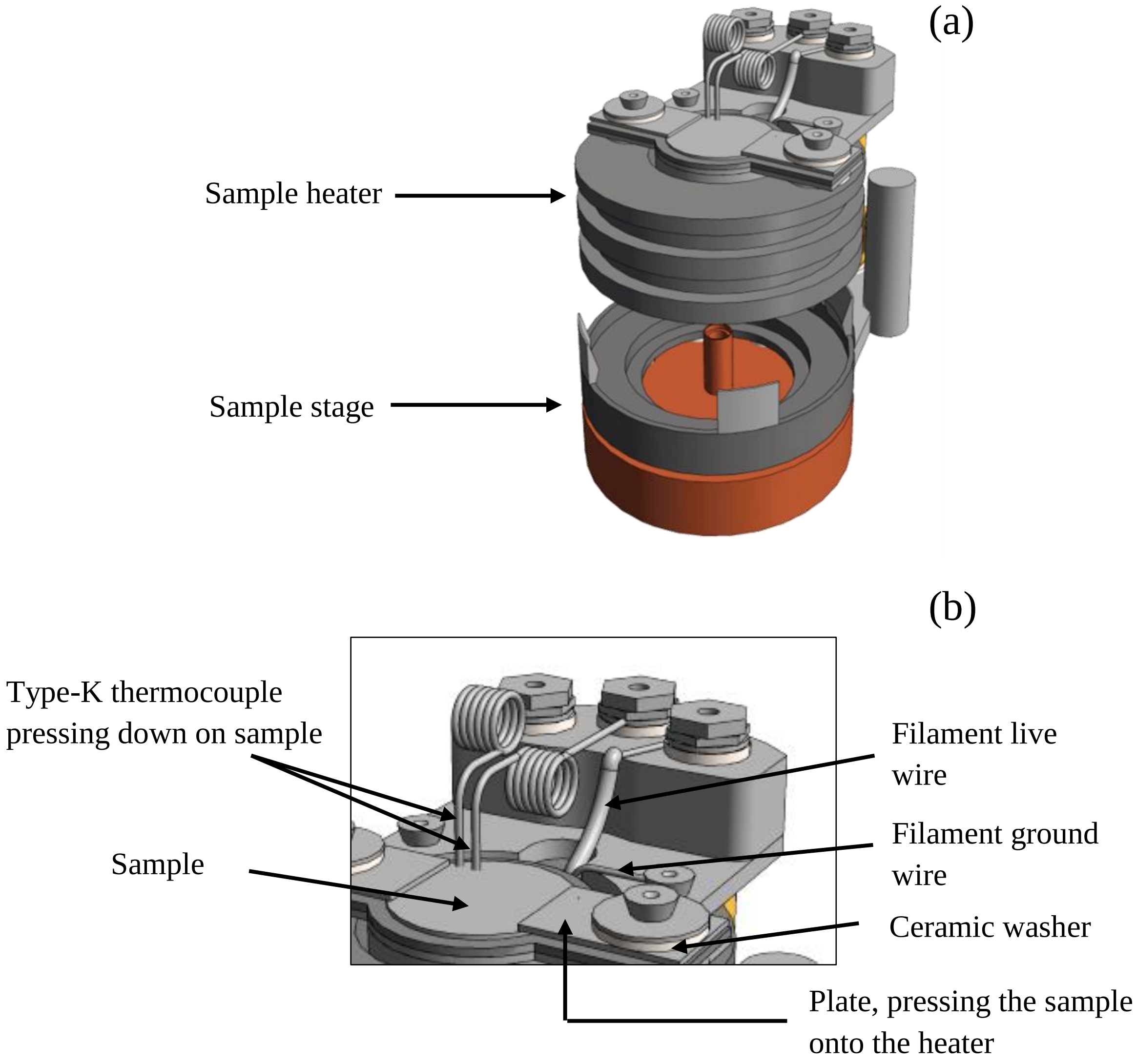

Figure 4.3: *(a) 3D drawing of the sample heater designed for surface segregation studies in the SAM 600 Auger system.(b) Detailed view of the sample heater showing the position of the thermocouple, the filament connections, ceramic washers and the plates for keeping the sample in positions .*

The sample itself is held in position by two small plates pressing the sample down onto the heater, figure 4.3 (b). The contact areas between the sample and these plates are made as small as possible to avoid heat conduction by the plates. This is also the reason for the use of ceramic washers between the part of the heater containing the filament and the rest of the sample heater (figure 4.3 (b)). The absence of these ceramic washers would cause the sample holder to act as a heat sink, removing large amounts of heat from the sample.

Provision is made for three points of electrical contact onto the sample heater; two of which are used for the thermocouple, and one for supplying a current to the heater filament. The ground connection for the filament is fixed onto the sample holder itself (figure 4.3 (b)) which in turn grounds onto the sample stage. The electrical connections between the sample holder and the sample stage are made of copper (Cu) clips. These clips, shown in figure 4.4, ensure effective electrical contact. The small and compact design of the sample heater allows for it to be loaded via the introduction or load lock chamber, since there are no fixed connections between the sample holder and sample stage.

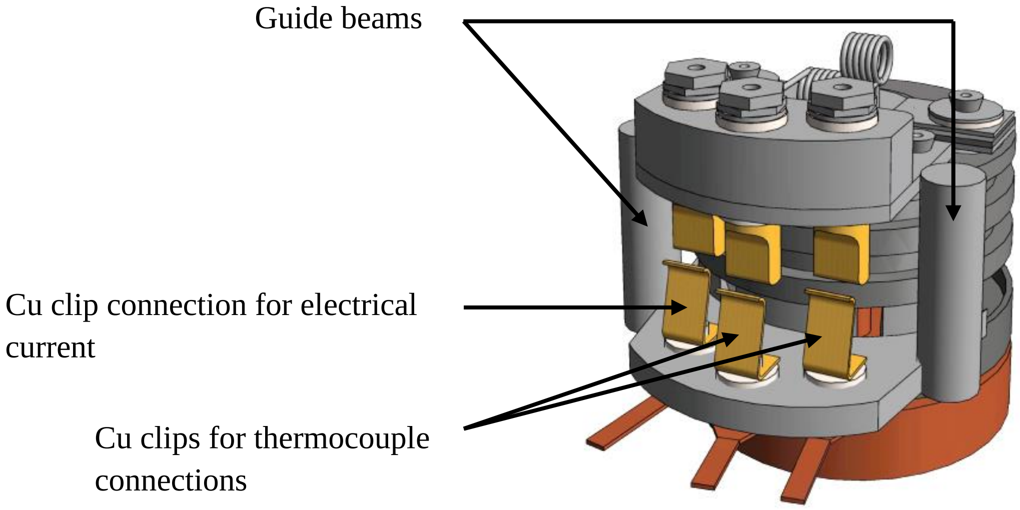

Figure 4.4: *Electrical connections of the sample heater, two connections are available for the thermocouple with a third connection for the heater filament. On either side of these connections a guide beam is present, used for guiding the sample heater into position.*

Two vertical "guide beams" (figure 4.4) are fitted onto the sample stage and is used to guide the sample heater into position. This makes sample loading easy and prevents possible damage to the heater and sample stage, since visibility inside the system is limited. The temperature was measured by a type-K thermocouple pressing down onto the surface of the sample as shown in figure 4.3 (b).

This position of the thermocouple provides the true surface temperature of the sample, after being corrected for the heat conduction of the thermocouple wires. The latter was achieved by simultaneously measuring the surface temperature with the thermocouple and an infrared temperature sensor. Figure 4.5 provides a graph of the infrared temperature versus the thermocouple temperature. The calibration curve was incorporated into the software in order to correct the measured thermocouple temperature and obtain the true surface temperature of the sample. Depending on the thickness of the sample there is a large temperature difference; a150 K difference was obtained for a 0.5 mm Fe sample with a surface temperature of 925 K. Since S segregation occurs from the surface, the segregation temperature should be the temperature measured on the surface and not that measured beneath the sample.

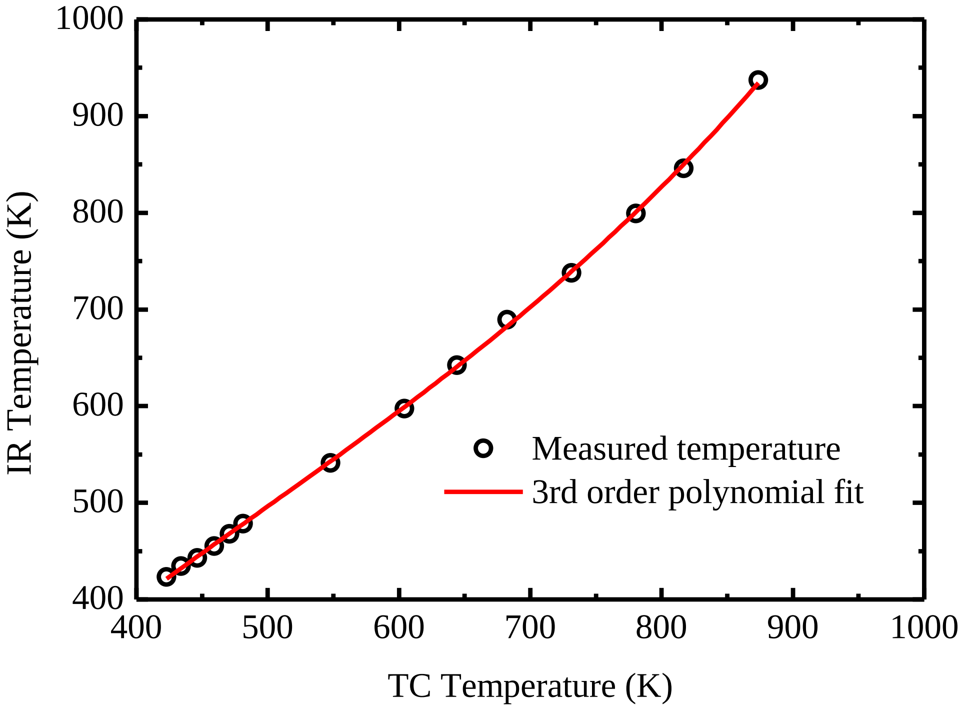

***Figure 4.5:** The temperature as measured by the infrared sensor (IR) versus the temperature measured by the thermocouple (TC).*

4.3.3.2. Control unit and software

Measurement of the surface temperature, T_m, is performed by the thermocouple pressing down onto the sample surface. The other end of the thermocouple is connected to the thermocouple reference block, kept at a constant temperature, T_{ref}. Amplification of the resulting voltage, by a factor of k, is performed with a difference amplifier, which apart from amplifying the voltage also ensures removal of electronic noise. Next, the output voltage from the difference amplifier and the reference temperature, T_{ref}, is summed by means of a summation amplifier. From the summation amplifier the output voltage is fed through an opto coupler to the measuring circuit, isolating it from the thermocouple circuit. This value is read by the PC in a sample size of 500 readings, which reduces the 50 Hz noise in the output voltage. Since the voltage read by the Analog-to-Digital converter is different from the actual thermocouple voltage, a voltage calibrator was used to construct a calibration curve to relate the read voltage to the true thermocouple voltage. Furthermore, the true thermocouple voltage is compared in the software to the thermocouple reference tables in order to obtain the corresponding temperature. With the above configuration and set-up it is capable of maintaining a stable temperature with a minimum variation of ±1 K. The temperature was controlled by comparing the set temperature to the measured temperature and then computing the appropriate filament voltage and current as determined by the PID controller. Figure 4.6 presents a schematic drawing of the measuring circuit.

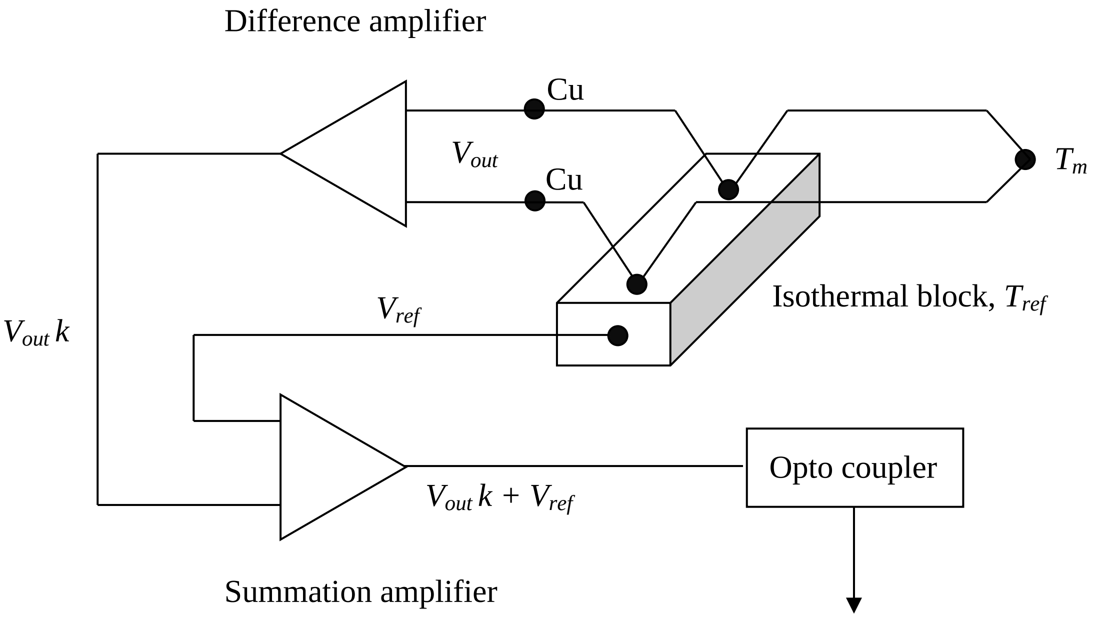

Figure 4.6: *Schematic drawing of the thermocouple circuit used to measure the sample temperature* [4].

Figure 4.7 provides an image of the temperature control unit`s front panel.

Figure 4.7: *The temperature control unit used for controlling the sample temperature in the SAM 600 AES system.*

On the front panel of the unit, the following settings are seen: A choice can be made between manual and PC control of the unit. If the manual option is preferred, the temperature can be set using the appropriate temperature dial. There is also an option for setting the voltage window, the maximum allowed voltage of the filament. Provision is also made for controlling the filament current internally or by the PC, and an option for controlling the temperature in a ramp mode or a constant temperature mode. Most important of these settings is the voltage window, which if set too large can cause an overshoot in the sample temperature; therefore, once the best value was determined the unit was kept unchanged.

Operation of the temperature control unit by PC is achieved by a software package coded in Visual Basic 6 Professional and forms part of the existing software package used for data capturing. In figure 4.8, the windows form of the temperature software is presented.

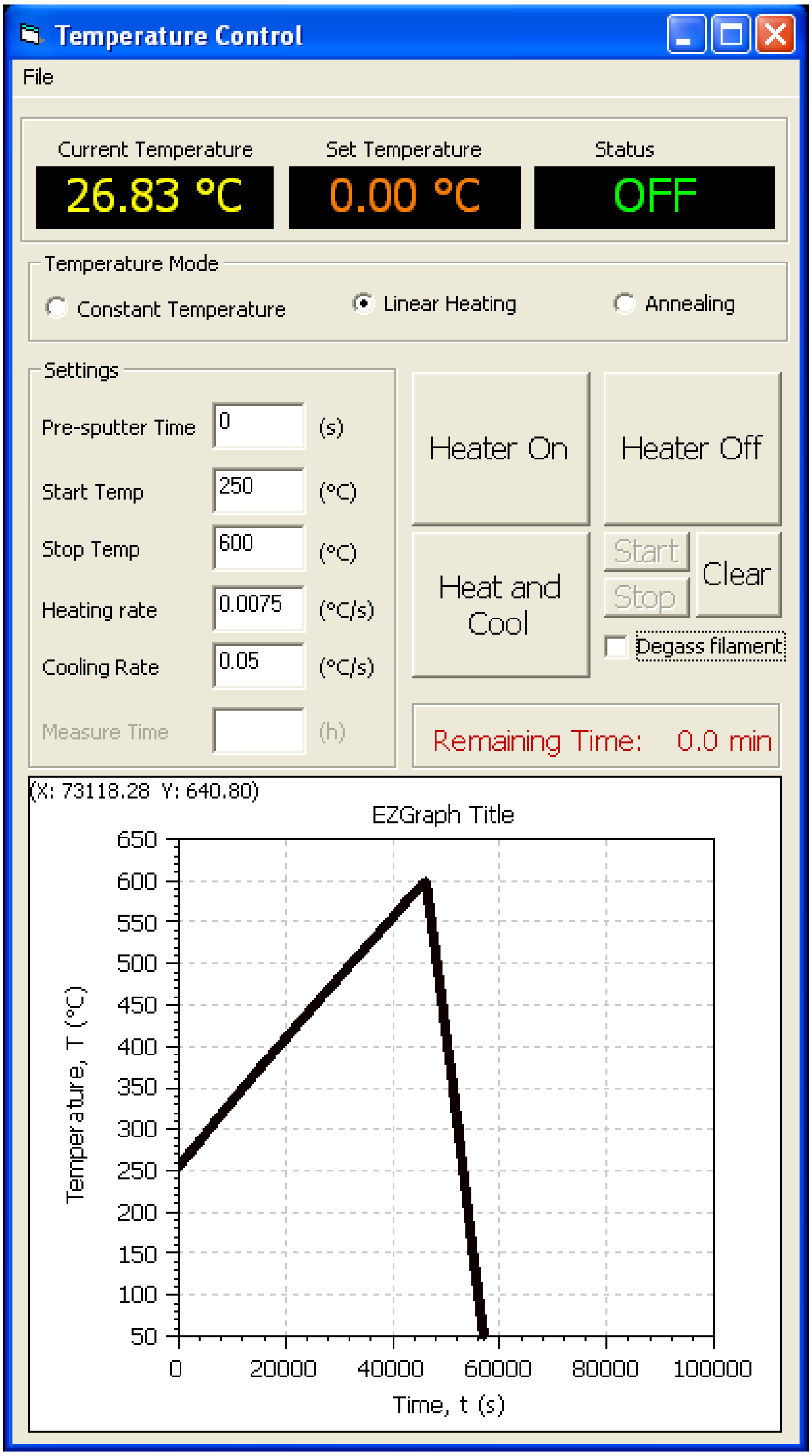

Temperature Control

Current Temperature: 26.83 °C

Set Temperature: 0.00 °C

Status: OFF

Temperature Mode

○ Constant Temperature

● Linear Heating

○ Annealing

Settings

Pre-sputter Time	0	(s)
Start Temp	250	(°C)
Stop Temp	600	(°C)
Heating rate	0.0075	(°C/s)
Cooling Rate	0.05	(°C/s)
Measure Time		(h)

Remaining Time: 0.0 min

(X: 73118.28 Y: 640.80)

Figure 4.8: *Windows form layout of the software used for surface segregation experiments on the SAM 600 AES system.*

The software allows the user to perform temperature measurements, by either the constant temperature or linear programmed heating (LPH) [5] methods. From the main window of the Auger software the user can open the temperature software window (figure 4.8). Three labels present the current state of the temperature functionality; the current temperature, the set temperature and the status. The current temperature is obtained from the thermocouple mounted onto the sample as described above. The set-temperature is the temperature the user has requested and the status, reports the current state of the heater (const. temp, LPH, Off, heating up). This status label will be updated during operation to indicate the choice of heating function that is currently being executed.

Once the user has selected the **temperature mode** option, the **Settings** panel becomes active and the user can provide the desired settings. This includes the pre-sputter time, start temperature, stop temperature, heating rate, cooling rate and the measuring time. If linear programmed heating is selected the measurement time is not available. For constant heating the experiment will run for the set measurement time and therefore the stop temperature is not an available choice.

When all the settings have been provided the user can switch on the heater by selecting the **Heater On** button. By default the heater will increase the temperature in increments of 1 K/s to the requested start temperature. If the heater is switched on for the first time since being placed into the system, either for sample loading or a new filament has been installed, the user is recommended to select the **Degas filament** check box. This will decrease the rate at which the temperature is increased to 0.2 K/s, allowing the heater to degas. Omitting to do this can cause rapid degassing of the sample heater, which can have a negative influence on the sample as well as on the filament lifetime.

If linear programmed heating was selected, the temperature run can only be started in the multiplexer section of the software, where Auger data is recorded. The **Heat and Cool** button is used for sample annealing, similar to constant temperature heating, a temperature, a measuring time and cooling rate is selected and the **Heater On** button can be selected. When the measuring time has expired, the temperature will decrease at the selected cooling rate, down to 323 K whereupon the heater switches off. The clear button is used to clear the temperature graph for the next measurement.

4.3.4. Experimental procedure for segregation measurements using linear programmed heating (LPH) with AES

The segregation of S in bcc Fe was studied by linear programmed heating in the temperature range 525-873/923K, performed at two different heating rates: 0.0075 K/s and 0.005 K/s. The single crystal samples (Fe100 and Fe111) were heated to only 873 K while the polycrystalline sample was heated to 923 K.

1. The sample was loaded into the system and allowed to pump down for 24 hours in order to remove the majority of surface contamination.
2. After pumping down for 24 hours, the sample was sputter cleaned using a raster size of 1.5 mm×1.5 mm. This ensured the removal of any O, N and C and other contaminants that might have been present on the surface.
3. Next, the sample temperature was slowly increased to allow the sample to degas. Once a temperature of 873/923K was reached, the temperature was maintained for 1 hour and then cooled at a controlled rate of 0.05K/s. This ensures that there are no depletion layers within the surface, which could originate during sample polishing.
4. Preheating of the sample was performed at 525 K until a stable temperature was obtained.
5. The sample surface was then sputter cleaned for 10 min using Ar^+ ions.
6. After sputter cleaning the surface, the recording of data was started immediately. Also the Ar gas was closed off and the system was pumped out removing any Ar^+ in the system.
7. Segregation profiles were recorded while the temperature was linearly increased at the specified rate.
8. Once the sample reached its maximum temperature of 873/923K, the sample was linearly cooled to 323 K at a rate of 0.05K/s.
9. Steps 3-8 were repeated for the next segregation run, this time the annealing of 1 hour ensured that there were no depletion layers as a result of the previous segregation run.

4.3.5. Auger quantification

Auger quantification is essential in order to perform model fittings from which the segregation parameters can be extracted. Apart from this essential requirement for this study, quantification also reveals important quantitative information of the sample under study. For each of the different samples; segregated layers and homogenous samples, there is a unique method by which the data can be quantified. Three different methods of AES quantification will be discussed next: The basic Palmberg method, the quantification of segregated layers and the quantification of homogenous samples.

4.3.5.1. Palmberg method

The most basic form of AES quantification is provided by Palmberg's relation in equation 4.5 [3; 6]. The concentration, *C*, of element *i* is expressed as the ratio of the measured intensity, *I*, in the sample under consideration to the intensity of an elemental standard, I^*, (intensity of pure *i*) divided by this same ratio for all elements (*n*) in the system.

$$C_i = \frac{\frac{I_i}{I_i^*}}{\sum_j^n \frac{I_j}{I_j^*}} \tag{4.5}$$

Equation 4.5 provides a good first approximation to AES quantification, but since it neglects the matrix factors it fails to provide a truly accurate quantitative description of data. Therefore, equation 4.5 was only used to obtain initial values for the concentrations of elements which were then used in the more accurate methods of AES quantification, described in the next sections.

4.3.5.2. AES quantification of segregated layers

For quantification of segregated layers, the system under study is considered as an infinite number of atomic layers, enabling the quantification of elements as a function of their escape depth [7]. Consider the quantification of a binary system, with element A as the segregant in the matrix material, element B. The Auger intensity for element A is provided by equation 4.6 [6, 7]

$$I_{\mathrm{A}} = I_0\, T\left(E_{\mathrm{A}}\right) D\left(E_{\mathrm{A}}\right) \sigma_{\mathrm{A}}\left(E_P\right) R_{\mathrm{A}} \sum_{n=0}^{\infty} N_A(nd) \exp\left[-nd / \lambda_{\mathrm{A}} \cos\theta\right] \tag{4.6}$$

where I_0 is the primary electron beam current, $T(E_{\mathrm{A}})$ is the transmission efficiency of the electron spectrometer and $D(E_{\mathrm{A}})$ is the efficiency of the electron detector. The ionisation cross section of the core level responsible for the Auger transition with an electron energy of E_p, is given by $\sigma_{\mathrm{A}}(E_p)$. To account for the backscattering of electrons the term R_{A} is included. The atomic density of element A at a distance of *nd* from the surface is given by the symbol $N_{\mathrm{A}}(nd)$, with *d* as the segregated layer thickness of element A and *n* the atomic layer of interest. The distance travelled by an Auger electron from where it is generated in the material, to the surface of the material is given by: $\lambda_{\mathrm{A}} \cos\theta$, where λ_{A} is the inelastic mean free path and θ is the angle of emission relative to the surface normal. For the pure element A, the Auger intensity is given by an expression similar to equation 4.6, equation 4.7

$$I_{\mathrm{A}}^{*} = \mathrm{const}\ \sigma_{\mathrm{A}}\left(E_P\right) R_{\mathrm{A}}^{*} \sum_{n=0}^{\infty} N_{\mathrm{A}}^{*}\left(nd^{*}\right) \exp\left[-nd_{\mathrm{A}}^{*} / \lambda_{\mathrm{A}}^{*} \cos\theta\right] \tag{4.7}$$

where the symbol * indicates the use of a pure element. The primary electron beam current, the transmission efficiency of the spectrometer and the efficiency of the electron detector were taken as constants (const) in equation 4.7. The Auger yield for element A in the binary alloy is provided by equation 4.8

$$I_{\mathrm{A}} = \mathrm{const}\, \sigma_{\mathrm{A}}\left(E_P\right) R_{\mathrm{A}}^{M} N^{M} \left[X_{\mathrm{A}}^{\phi} + \sum_{n=1}^{\infty} X_{\mathrm{A}}^{bulk} \exp\left(-nd^{M} / \lambda_{\mathrm{A}}^{M} \cos\theta\right) \right], \tag{4.8}$$

where X_{A}^{ϕ} is the surface concentration of element A and X_{A}^{bulk} is the bulk concentration of element A. Solving equation 4.7 for σ_{A} and substituting the result into equation 4.8 delivers equation 4.9 [7]

$$I_{\mathrm{A}} = \frac{I_{\mathrm{A}}^{*} R_{\mathrm{A}}^{*} N_{\mathrm{B}}^{M}}{R_{\mathrm{A}}^{*} N_{\mathrm{A}}^{*} \sum_{n=0}^{\infty} \exp\left(-nd_{\mathrm{A}}^{*} / \lambda_{\mathrm{A}}^{*} \cos\theta\right)} \left[X_{\mathrm{A}}^{\phi} + \sum_{n=1}^{\infty} X_{\mathrm{A}}^{bulk} \exp\left(-nd^{M} / \lambda_{\mathrm{A}}^{M} \cos\theta\right) \right]. \tag{4.9}$$

For element B a similar expression is obtained, equation 4.10

$$I_{\mathrm{B}} = \frac{I_{\mathrm{B}}^{*} R_{\mathrm{B}}^{*} N_{\mathrm{A}}^{M}}{R_{\mathrm{B}}^{*} N_{\mathrm{B}}^{*} \sum_{n=0}^{\infty} \exp\left(-nd_{\mathrm{B}}^{*} / \lambda_{\mathrm{B}D}^{*} \cos\theta\right)} \left[X_{\mathrm{B}}^{\phi} + \sum_{n=1}^{\infty} X_{\mathrm{B}}^{bulk} \exp\left(-nd / \lambda_{\mathrm{B}} \cos\theta\right) \right]. \tag{4.10}$$

Taking the ratio of the Auger yields for the two elements in the alloy (equation 4.9 and equation 4.10), delivers equation 4.11 [7]

$$\frac{I_{\mathrm{A}}}{I_{\mathrm{B}}} = \frac{I_{\mathrm{A}}^{*} R_{\mathrm{A}}^{M} R_{\mathrm{B}}^{*} N_{\mathrm{B}}^{M}}{I_{\mathrm{B}}^{*} R_{\mathrm{B}}^{M} R_{\mathrm{A}}^{*} N_{\mathrm{A}}^{M}} \frac{\sum_{n=0}^{\infty} \exp\left(-nd_{\mathrm{B}}^{*} / \lambda_{\mathrm{B}D}^{*} \cos\theta\right)}{\sum_{n=0}^{\infty} \exp\left(-nd_{\mathrm{A}}^{*} / \lambda_{\mathrm{A}D}^{*} \cos\theta\right)} \times \frac{\left[X_{\mathrm{A}}^{\phi} + \sum_{n=1}^{\infty} X_{\mathrm{A}}^{bulk} \exp\left(-nd^{M} / \lambda_{\mathrm{A}}^{M} \cos\theta\right) \right]}{\left[X_{\mathrm{B}}^{\phi} + \sum_{n=1}^{\infty} X_{\mathrm{B}}^{bulk} \exp\left(-nd^{M} / \lambda_{\mathrm{B}}^{M} \cos\theta\right) \right]}. \tag{4.11}$$

The first term of equation 4.11 is provided by equation 4.12

$$\alpha_{\mathrm{AB}} = \frac{I_{\mathrm{A}}^{*} R_{\mathrm{A}}^{M} R_{\mathrm{B}}^{*} N_{\mathrm{B}}^{M}}{I_{\mathrm{B}}^{*} R_{\mathrm{B}}^{M} R_{\mathrm{A}}^{*} N_{\mathrm{A}}^{M}} \frac{\sum_{n=0}^{\infty} \exp\left(-nd_{\mathrm{B}}^{*} / \lambda_{\mathrm{B}}^{*} \cos\theta\right)}{\sum_{n=0}^{\infty} \exp\left(-nd_{\mathrm{A}}^{*} / \lambda_{\mathrm{A}}^{*} \cos\theta\right)}, \tag{4.12}$$

with the second terms of equation 4.7 being represented respectively by β_{A} and β_{B} in equations 4.13 and 4.14.

$$\beta_{\mathrm{A}} = \sum_{n=1}^{\infty} \exp\left(-nd^{M} / \lambda_{\mathrm{A}}^{M} \cos\theta\right), \tag{4.13}$$

$$\beta_{\mathrm{B}} = \sum_{n=1}^{\infty} \exp\left(-nd^{M} / \lambda_{\mathrm{B}}^{M} \cos\theta\right). \tag{4.14}$$

Equation 4.11 can thus be written in a more simplistic form using equations 4.12 – 4.14, resulting in equation 4.15 [7]

$$\frac{I_{A}}{I_{B}} = \alpha_{AB} \frac{X_{A}^{\phi} + \beta_{A} X_{A}^{bulk}}{X_{B}^{\phi} + \beta_{B} X_{B}^{bulk}} \; . \tag{4.15}$$

Equation 4.15 can be expanded to m-1 expressions in X^{ϕ} for a system consisting of m components. The backscattering coefficients, R, were calculated using the expression of Shimizu [3, 8], equation 4.16

$$R = 1 + \left(0.462 - 0.777Z^{0.2}\right)U^{-0.32} + \left(1.15Z^{0.20} - 1.05\right). \qquad (4.16)$$

Z is the atomic number for the element of interest and U is the ratio of the primary electron beam voltage over the binding energy of the core electron responsible for the Auger transition. For the calculation of the inelastic mean free path, the TPP-2 method proposed by Tanuma, Powell and Penn [9], equation 4.17, was used

$$\lambda = \frac{E}{\left\{E_p^2\left[\xi \ \ln(\gamma E) - \left(\frac{\chi}{E}\right) + \left(\frac{\kappa}{E^2}\right)\right]\right\}} \ , \qquad (4.17)$$

where E is the primary electron beam energy and E_p is the free-electron plasmon energy. Each of the symbols used in equation 4.17 are defined by the expressions below:

$$E_p = 28.8 \ \left(\frac{N_v \rho}{M}\right)^{\frac{1}{2}}$$

$$\xi = -0.0216 + \frac{0.944}{E_p} + 7.39 \times 10^{-4} \rho$$

$$\gamma = 0.191 \rho^{-0.50}$$

$$U = \frac{N_v \rho}{M}$$

$$\chi = 1.97 - 0.91\ U$$

$$\kappa = 53.4\ - 20.8\ U$$

In the above equations, ρ is the density (g.cm^{-3}), M the molecular mass (amu) and N_v the number of valance electrons of an element. The values for the matrix, denoted by the superscript M, are calculated as a weighed sum of all the elements. For an alloy consisting of n elements the matrix values are calculated by:

$$\rho^M = \sum_i^n X_i^{bulk} \rho_i$$

$$M^M = \sum_i^n X_i^{bulk} M_i$$

$$Z^M = \sum_i^n X_i^{bulk} Z_i$$

$$d^M = \sum_i^n X_i^{bulk} d_i$$

In order to obtain the elemental concentrations of the species that segregated to the surface equation 4.15 needs to be solved to obtain X_A^ϕ and X_B^ϕ simultaneously. This is achieved by utilising the Nelder-Meads [10] optimisation algorithm, implemented in a Visual Basic 6 software package developed in house. Initial values for the optimisation procedure is obtained from Palmberg`s relation, equation 4.5.

4.3.5.3. AES Quantification of homogenous samples

If the sample under consideration is composed of a homogenous composition the quantification of data can be achieved with the method described next. For element A, distributed homogenously throughout the host material B, the Auger intensity is described by equation 4.18 [6]

$$I_\mathrm{A} = I_0 T(E_\mathrm{A}) D(E_\mathrm{A}) \sigma_\mathrm{A}(E_P) R_\mathrm{A} N_\mathrm{A} \lambda_\mathrm{A} \cos\theta \tag{4.18}$$

Similarly for the pure element A, the Auger intensity is provided by equation 4.19

$$I_\mathrm{A}^* = I_0 T(E_\mathrm{A}) D(E_\mathrm{A}) \sigma_\mathrm{A}(E_P) R_\mathrm{A}^* N_\mathrm{A}^* \lambda_\mathrm{A}^* \cos\theta \tag{4.19}$$

Solving equation 4.19 for the ionisation cross section, $\sigma_\mathrm{A}(E_P)$, and substituting the result into equation 4.18 delivers equation 4.20

$$\frac{I_\mathrm{A}}{I_\mathrm{A}^*} = \frac{R_\mathrm{A} N_\mathrm{A} \lambda_{\mathrm{A}D} \cos\theta}{R_\mathrm{A}^* N_\mathrm{A}^* \lambda_{\mathrm{A}D}^* \cos\theta} \tag{4.20}$$

A similar expression, equation 4.21, is derived for element B [6].

$$\frac{I_\mathrm{B}}{I_\mathrm{B}^*} = \frac{R_\mathrm{B} N_\mathrm{B} \lambda_{\mathrm{B}D} \cos\theta}{R_\mathrm{B}^* N_\mathrm{B}^* \lambda_{\mathrm{B}D}^* \cos\theta} \tag{4.21}$$

The ratio of equations 4.20 and 4.21 results in equation 4.22

$$\frac{I_{\mathrm{A}}}{I_{\mathrm{B}}}=\frac{I_{\mathrm{A}}^{*}R_{\mathrm{B}}^{*}N_{\mathrm{B}}^{*}N_{\mathrm{A}}\lambda_{\mathrm{B}}^{*}}{I_{\mathrm{B}}^{*}R_{\mathrm{A}}^{*}N_{\mathrm{A}}^{*}N_{\mathrm{B}}\lambda_{\mathrm{A}}^{*}}. \tag{4.22}$$

This equation provides the relation between the intensities of elements A and element B. Using equation 4.23 [6]

$$\frac{N_{\mathrm{B}}^{\infty}N_{\mathrm{A}}}{N_{\mathrm{A}}^{\infty}N_{\mathrm{B}}}=\frac{X_{\mathrm{A}}}{X_{\mathrm{B}}}\left(\frac{a_{A}}{a_{B}}\right)^{3}, \tag{4.23}$$

where N_A is Avogadro’s number with the value of 6.022×10^{-23} [11]. The final expression for the quantification of homogenous samples is obtained, equation 4.24

$$\frac{I_{\mathrm{A}}}{I_{\mathrm{B}}}=\frac{I_{\mathrm{A}}^{*}R_{\mathrm{B}}^{*}\lambda_{\mathrm{B}}^{*}}{I_{\mathrm{B}}^{*}R_{\mathrm{A}}^{*}\lambda_{\mathrm{A}}^{*}}\frac{X_{\mathrm{A}}}{X_{\mathrm{B}}}\left(\frac{a_{A}}{a_{B}}\right)^{3}. \tag{4.24}$$

The matrix factors can be grouped together, described by the term α, equation 4.25 [6]

$$\alpha_{AB}=\frac{I_{A}^{*}R_{B}^{*}\lambda_{B}^{*}}{I_{B}^{*}R_{A}^{*}\lambda_{A}^{*}}\left(\frac{a_{A}}{a_{B}}\right)^{3}. \tag{4.25}$$

The atomic diameter, a, is provided by equation 4.26

$$1000\ \ \rho N_{A}a^{3}=M, \tag{4.26}$$

Using equation 4.25, equation 4.24 can thus be written in a more simplified form, equation 4.27

$$\frac{I_{\mathrm{A}}}{I_{\mathrm{B}}}=\alpha_{\mathrm{AB}}\frac{X_{\mathrm{A}}}{X_{\mathrm{B}}}\ . \tag{4.27}$$

Equation 4.27 was derived above for the case of a binary system, but can be expanded to m-1 equations for an m component system.

The backscattering factor, R, is described by equation 4.16 and the inelastic path, λ is provided by equation 4.17.

Equation 4.27 was solved in order to produce the concentrations of elements A and B simultaneously. This was achieved by the Nelder-Meads [10] optimization algorithm, implemented in a custom software package developed in house.

4.4. Time-of-Flight Secondary Ion Mass Spectrometry (TOF-SIMS)

TOF-SIMS was used to obtain both qualitative and quantitative information on the S doped Fe samples and was also used for qualitative measurements on the Fe-Cr-S sample. This technique is capable of detecting dilute concentrations of elements [12] and served as an important tool for the quantification of S in Fe. AES is less sensitive for the detection of dilute concentrations and was incapable of detecting the low S concentrations in the Fe sample used in this study. Other advantages of the technique include the fast analysis times made possible by the time-of-flight analysis of secondary ions. [13]. AES analysis occurs at a much slower rate, due to the fact that less elements can be analysed in a given time period. At the end of this chapter, table 4.3 draws a comparison between the two techniques, AES and TOF-SIMS, outlining their strengths and weaknesses with respect to segregation measurements.

4.4.1. TOF-SIMS principle of operation

Samples are bombarded with a pulsed primary beam of Bi ions, Bi^{+}, Bi^{2+} or Bi^{3+} depending on the mode of operation. This results in the emission of secondary ions, neutrals and some electrons. Figure 4.9 illustrates this process of secondary particles being emitted upon Bi bombardment. Secondary ions with a specific polarity are extracted by the extraction electrode kept at a constant potential, U. Ions then move along a field-free flight path where ions with different mass-to-charge ratios (m/q) arrive at the detector after time t, figure 4.10.

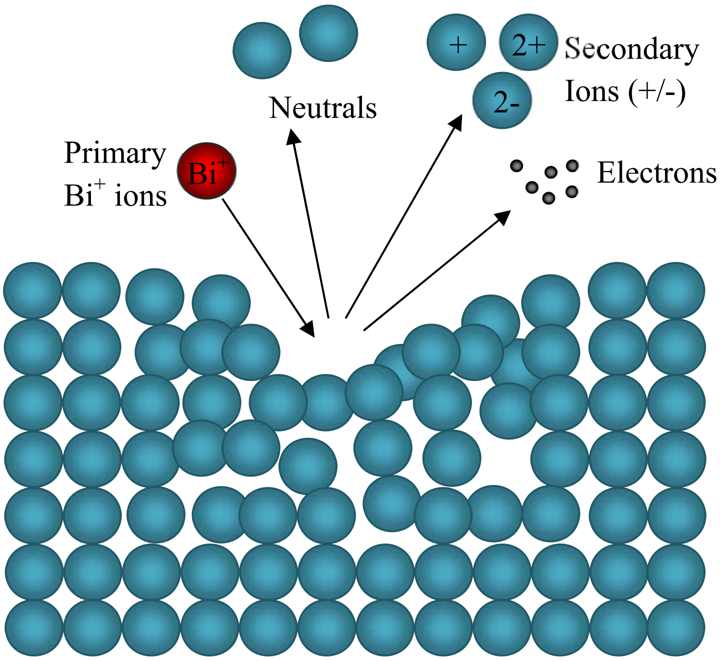

Figure 4.9: *Illustration of the Time-of-Flight Secondary Ion Mass Spectrometry (TOF-SIMS) technique, whereby the sample surface is pulsed with primary Bi-ions which cause the emission of secondary ions from the sample. These secondary ions are then analysed by a time-of-flight mass analyser, from which their ionic masses are deduced.*

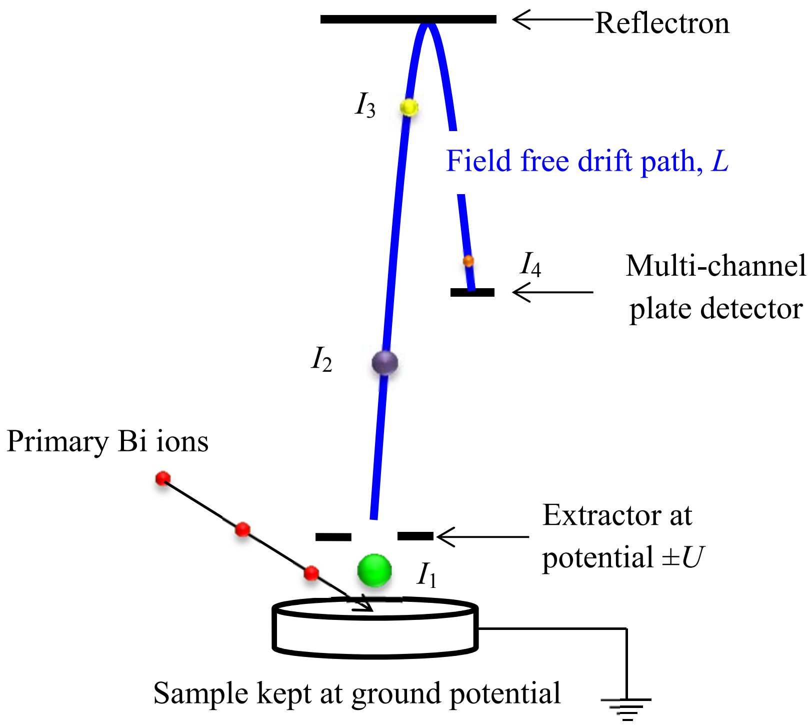

Figure 4.10: *Time-of-Flight analysis of secondary ions is performed by separating the ions based on their time-of-flight along a path of equal distance, L. Since the flight time can be related to the mass of an ion, their atomic masses can be determined. The ion denoted I_1 is located in an electric field with an applied extraction voltage U.*

Ions are accelerated into the analyser by the extraction electrode kept at a constant voltage, U, for the experiments performed in this study the potential U was set at ± 2000 Volts. For species forming positive ions, a negative extractor voltage is preferred, while a positive extraction voltage is best suited for negatively charged ions, such as S^-. Since Fe is abundant in the samples studied, the use of a positive extractor voltage was sufficient to produce a high intensity of Fe^- ions. These Fe^- ions are formed in the ionisation process which allows Fe to become negatively charged due to an excess of electrons being available during the ionisation process. The ions have an energy, E_p, described by equation 4.28, which is the potential energy for a charged particle, q, in an electric field [14] (figure 4.10).

$$E_p = qU \, . \tag{4.28}$$

Due to the extraction voltage the particle is accelerated with kinetic energy, E_k, provided by equation 4.29 [14]

$$E_k = \frac{1}{2} m v^2 \, . \tag{4.29}$$

The potential energy of the particle is converted into kinetic energy as a result of the applied voltage and therefore the kinetic energy is equal to the potential energy, resulting in equation 4.30.

$$qU = \frac{1}{2} m v^2 \, . \tag{4.30}$$

The velocity of the particle entering the field-free drift path, L, is the same as the velocity of the particle when it reaches the multi-channel plate detector. The applied potential U only ensures the ions enter the flight path, L, where after the ions no longer experience the potential U. Using this knowledge allows for the velocity to be expressed in terms of the flight path, L, by equation 4.31

$$qU = \frac{1}{2} m \left(\frac{L}{t} \right)^2 , \tag{4.31}$$

where t is the flight time for the ion of interest. Considering the flight time as the subject of the equation and rearranging the terms, delivers the final equation relating the flight time to the mass-to-charge ratio (m/q), equation 4.32 [13]

$$t = K\sqrt{\frac{m}{q}}\,, \tag{4.32}$$

The symbol K was used to group together the constant terms, provided by equation 4.33

$$K = \frac{L}{\sqrt{2U}}\,. \tag{4.33}$$

All the ions will experience the same potential; U, and the same flight path, L, and these terms are therefore considered as constant. Equation 4.32 relates the measurable quantity, the flight time, to the mass-to-charge ratio of the ions. Since different masses of ions will have different velocities and therefore different flight times, the flight time can be used to obtain the correct ionic mass. Since the two are balanced by the factor K, the measured spectrum needs to be calibrated to a number of known ionic masses.

The accuracy and therefore reliability of TOF-SIMS data lies in the correct calibration of the mass spectra. As a first approximation, H and H_2 can be used for calibrating the mass spectra. This calibrates the spectra sufficiently, in order for a more detailed calibration to be performed. This detailed calibration depends on whether ions or compounds are of interest. As a general rule of thumb, if compounds are of interest, compounds should be used for calibration, and the same rule applies for ions. The reason for this is that the peaks produced by ions are more defined and sharp as compared to that of compounds. If compounds are used for the calibration when ions are of interest, a less accurate calibration is obtained. This is especially important when quantification of data is performed, since even the smallest variation in mass can result in incorrect data interpretation. Another important point to note is that calibration needs to be performed for a range of different ionic masses, with the largest mass used for calibration exceeding the mass of interest, recommended to be double that of the mass of interest.

4.4.2. TOF-SIMS apparatus

All TOF-SIMS measurements were performed on the SIMS 5 TOF-SIMS instrument from Ion-TOF. The system is equipped with a primary Bi ion gun (Inactive source), and a dual column Caesium (Cs^+) and Oxygen (O^+) sputter source, serving as the two active ion sources. They are referred to as being active since they are capable of forming compounds with ions in the sample. Bi is considered as an inactive source since it does not regularly form compounds with the ions in the sample. Apart from these sources, the system also contains an Ar cluster gun, which is primarily used as a sputter source on organic samples. Samples charging can be reduced by the use of an oxygen flood gun, to remove negative charge build-up on the sample, while an electron flood gun is used to compensate for positive charging of the sample. Detection of secondary electrons to from a SED image is made possible by a secondary ion detector (photomultiplier). Figure 4.11 shows the orientation of the different sources inside of the system, not visible from the figure is the secondary electron detector and the argon cluster gun, these two sources are located behind the analyser with their tips in the same vicinity as the other sources.

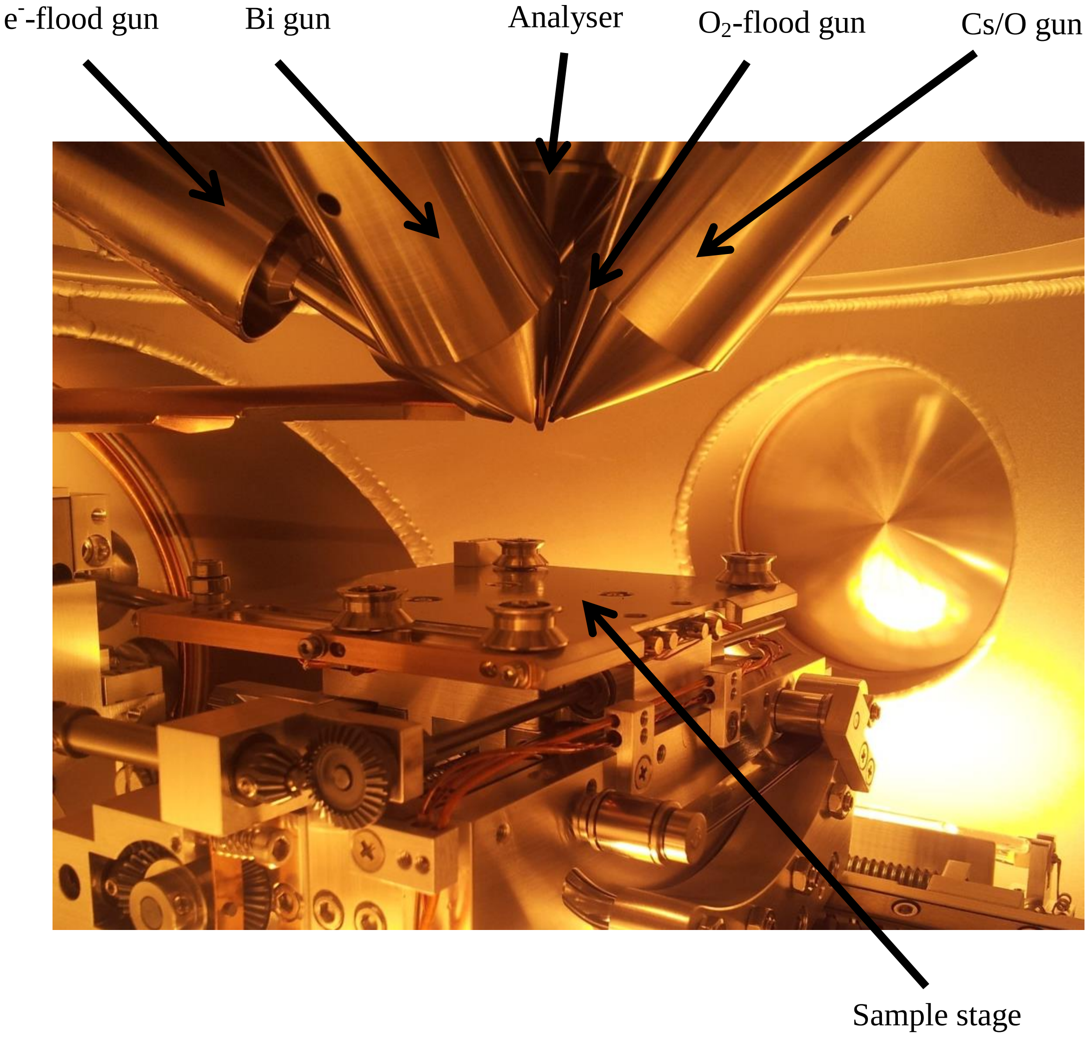

Figure 4.11: *Picture on the inside of the SIMS 5 TOF-SIMS system, identifying the various sources (Bi,Cs/O,* O_2*-flood gun,* e^-*- flood gun), the analyser and the sample stage.*

Bi was used for analysis of samples in this study, although Ga and Au have been used for TOF-SIMS analysis until recently, before Bi became the popular choice [15]. Figure 4.12 presents a picture of the Bi liquid metal ion source emitter.

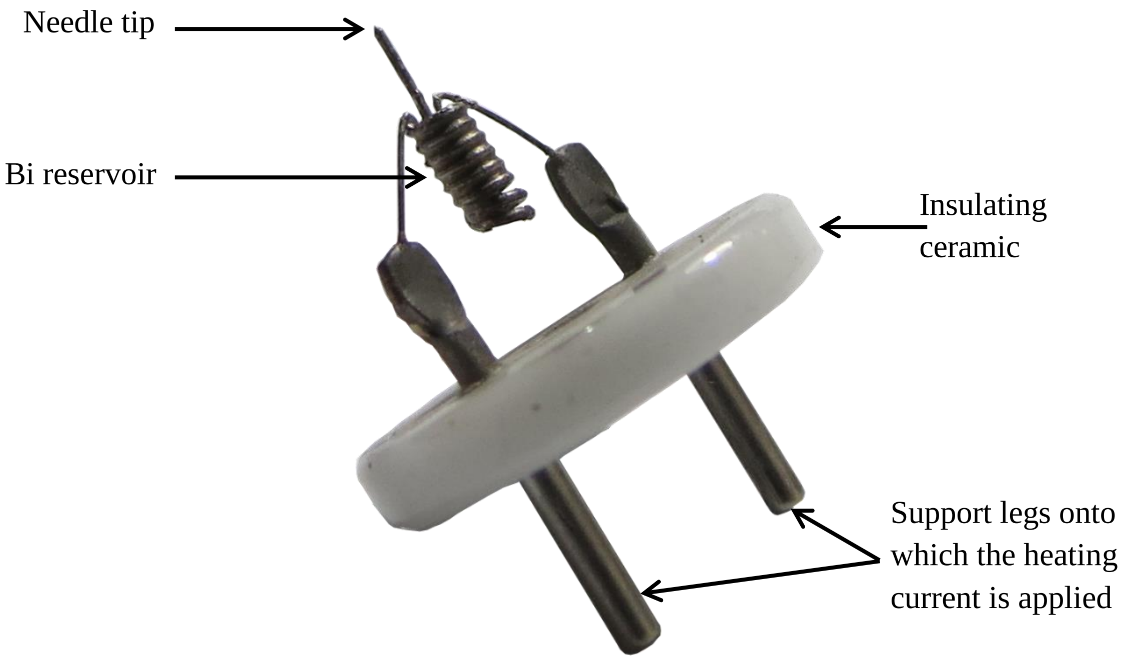

Figure 4.12: *Picture of the Bi liquid metal ion source emitter of the SIMS 5 TOF-SIMS system. When heated, the Bi forms a cone like shape (Taylor cone) on the needle tip, from where the Bi ions are extracted by the extractor voltage.*

The Bi is melted into a liquid form with the application of a heating current to the support legs (figure 4.12). With the applied extractor voltage an electric field is generated. This electric filed causes electrons to retract from the needle tip while causing positive Bi ions to migrate towards the tip, where a Bi cone, called the Taylor cone is formed [15]. After sufficient time an equilibrium state is obtained producing a stable Bi ion current from the needle tip. This process is not without fault and often the cone does not form as it should towards the needle tip. This results in Bi ions being extracted on the side of the tip, instead from the tip itself. A consequence of this is a reduced beam current and a poorly defined beam. This undesirable phenomenon is known as side emission. Most of the time this can be corrected by flashing the suppressor voltage, which increases the extraction of Bi ions from the needle tip (see figure 4.14).

The Bi beam is pulsed, in cycles of a few µs (95 µs for analysis of samples in this study). Pulsing of the beam is required in order to allow time-of-flight analysis of the secondary ions created by the pulsed Bi beam. This procedure whereby the sample is pulsed with Bi and the secondary ions analysed in an alternating fashion is illustrated in figure 4.13

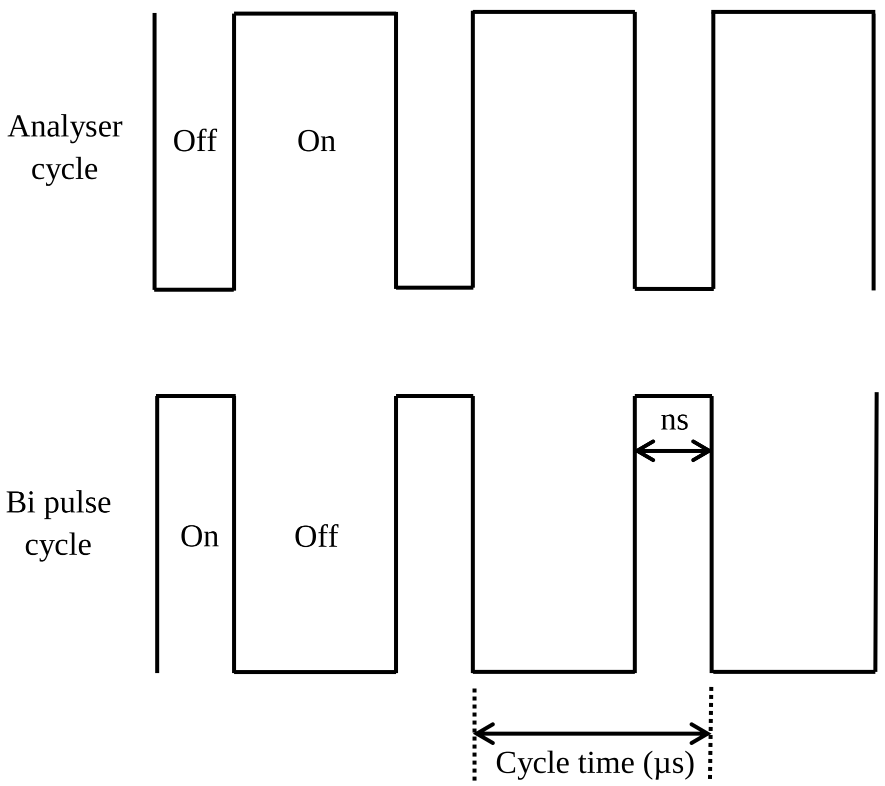

Figure 4.13: *illustration of how the analyser and Bi source is operated in an alternating fashion. The Bi source produces pulses for a given time (ns), resulting in the generation of secondary ions from the sample. Following this, the analyser is given a time window (µs) in which to analyse the secondary ions based on their time-of-flight.*

Figure 4.14 provides a schematic drawing of the Bi gun`s optical column.

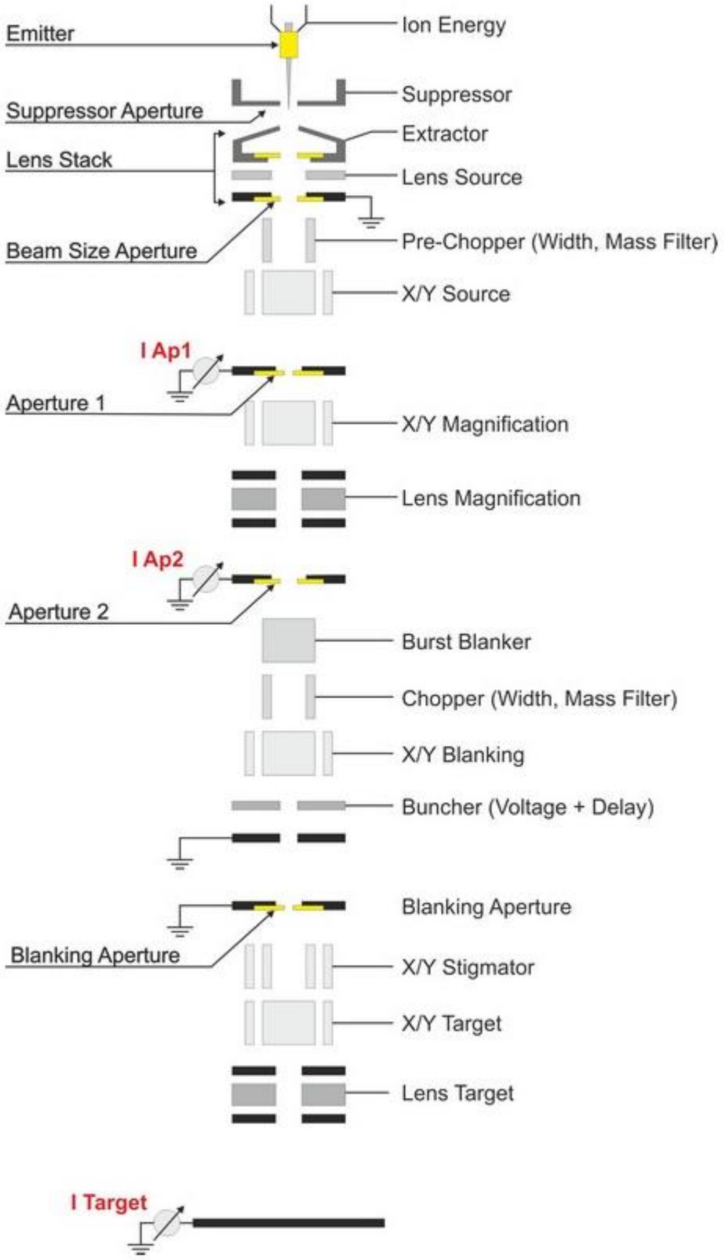

Figure 4.14: *Optical column of the Bi ion gun. The various components can be set to the appropriate voltages in order to obtain an ion beam with a certain pulse width, size and ion current depending on the operation mode which is required for sample analysis* [16].

The Bi ion gun can be operated in different modes, depending on the information required from the sample under study. Table 4.4 provides an outline of the different operation modes, with their respective applications and beam characteristics.

Table 4.4: *Different operating modes of TOF-SIMS. Depending on the information required, the appropriate operating mode can be selected* [16].

	Beam size	**Application**	**Characteristics**
Spectroscopy	5 µm	Spectroscopy, depth profiling, imaging on areas of 500 × 500 μm^2	High mass resolution, poor lateral resolution
800 nm mode	800 nm	Imaging on areas of 250 × 250 μm^2	High mass resolution, low secondary ion intensity
Fast imaging mode	150 nm	Imaging, 3 dimensional depth-profiling	High lateral resolution, poor mass resolution
Burst-mode	300 nm	Imaging on 50 × 50 μm^2 areas	Good mass resolution, poor intensity
Ultimate Imaging mode	80 – 100 nm	Imaging of 15 × 15 μm^2 area	High lateral resolution, low intensity of secondary ions
High current imaging mode	300 nm	Imaging on areas exceeding 50 × 50 μm^2, 3 dimensional depth-profiling	High lateral resolution, poor mass resolution

The last column of table 4.4 describes the characteristics of the beam. It is noted that the characteristics of the beam is a trade-off between; mass resolution, secondary ion intensity and lateral resolution. These three properties can be represented in an isosceles triangle as illustrated in figure 4.15.

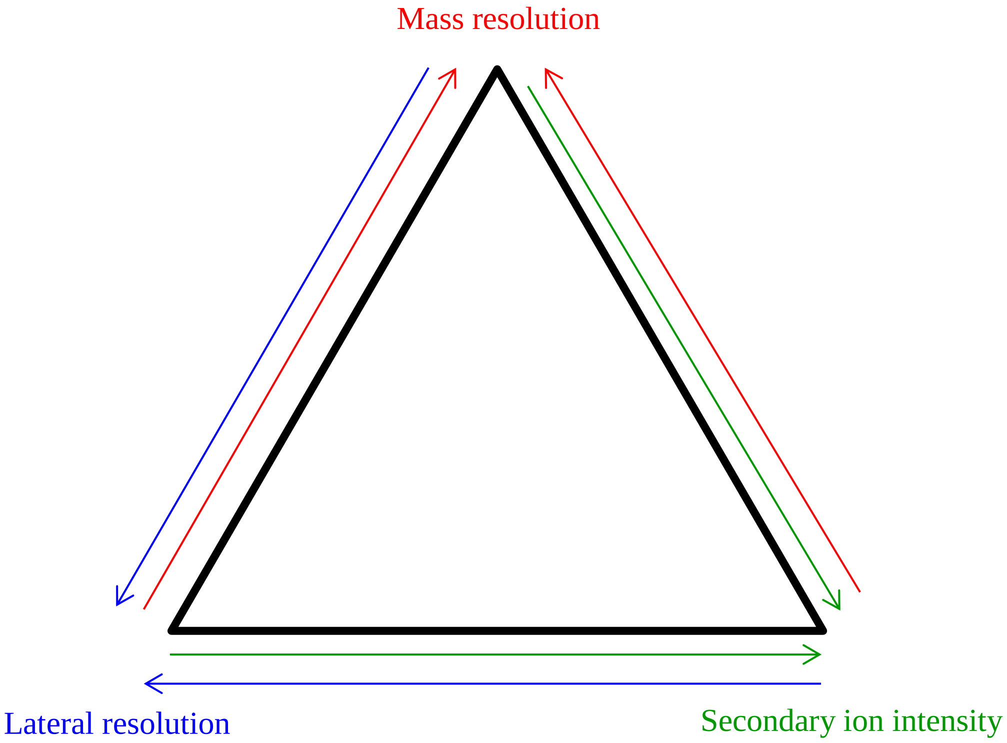

Figure 4.15: *Illustration of the trade-off that exists between the mass resolution, secondary ions intensity and lateral resolution for different operation modes. The three angles of the triangle represent each of these properties. Choosing one of these properties comes at the expense of the other two.*

TOF-SIMS is performed with the primary goal of being an analytical technique; therefore the mass resolution is a highly desirable property. This quantity is the degree with which the ionic mass of interest can be distinguished from other interfering masses, with a high value indicating a good distinction. It forms the primary reference to use in order to accurately assign masses, if the mass resolution is insufficient, then the mass of interest cannot be assigned with certainty. Ignoring the mass resolution can lead to false identification of ionic masses resulting in misinterpretation of data. S^- and O_2^- are two masses which are very close on the mass scale and is a common problem in other mass spectrometry techniques such as ICP-MS [17]. Figure 4.16 provide the mass spectra of S^- and O_2^-, measured in spectroscopy mode in order to illustrate the concept of mass resolution.

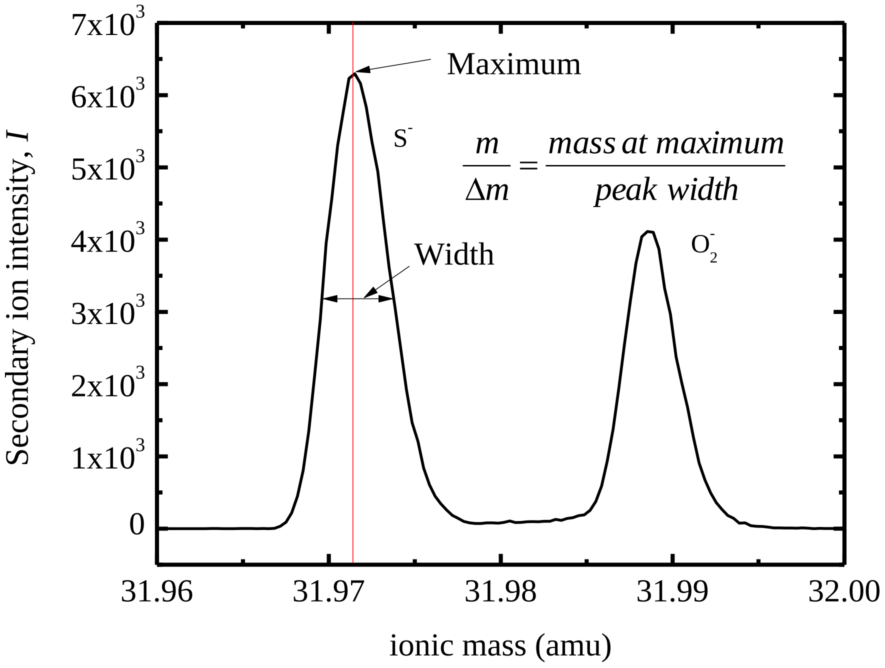

Figure 4.16: *Mass spectra of S^- and O_2^-, as a result of a high mass resolution with a value of 9100 measured at the mass of S^-, these two peaks are clearly distinguishable despite a mass difference of only 0.01703 amu. The calculation of the mass resolution is given as the ratios of the mass to peak width.*

Despite the small mass difference of only 0.01703 amu, S^- and O_2^- can be distinguished unambiguously, since both of these species have a high mass resolution. The mass resolution is calculated as the mass obtained at the highest peak intensity divided by the peak width at full width half maximum (FWHM), expressed by equation 4.34.

$$\frac{m}{\Delta m} = \frac{mass\ at\ higest\ energy}{peak\ width}, \tag{4.34}$$

The mass resolution for the Fe-S sample analysed in figure 4.16, is 9100, which exceeds the value required for the distinction between S^- and O_2^-, 1800 [13]. Thus, TOF-SIMS is capable of distinguishing between ionic species such as S^- and O_2^- which have very little mass difference due to the high mass resolution achievable in spectroscopy mode.

4.4.3. TOF-SIMS configuration and calibration

The Cs sputter source was used for all measurements on the Fe-S samples. An hour before measurements were started, the Cs source was switched on to allow the liquid metal ion source (LMIS) to stabilise. For the same reason the Bi ion source was switched on 30 minutes prior to performing measurements. The Bi source has a short lifetime of 500 µAh, and the use of half an hour to reach equilibrium was deemed sufficient. Once the sources were ready for measurements the desired settings were loaded and the sources were optimised with respect to their optical columns. Using a Silicon (Si) wafer the two sources were aligned with respect to one another. To ensure accurate analysis of the samples, a number of elemental masses were used to calibrate the mass spectra. This depended largely on the species of interest and therefore varied from one experiment to the next. Similarly, the settings depended on the information required and is provided along with the ionic masses used for calibration in chapter 6.

4.4.4. TOF-SIMS temperature measurements

Both S segregation in Fe and S segregation in Fe-Cr were studied by linear programmed heating. The sample holder used for heating is shown in figure 4.17.

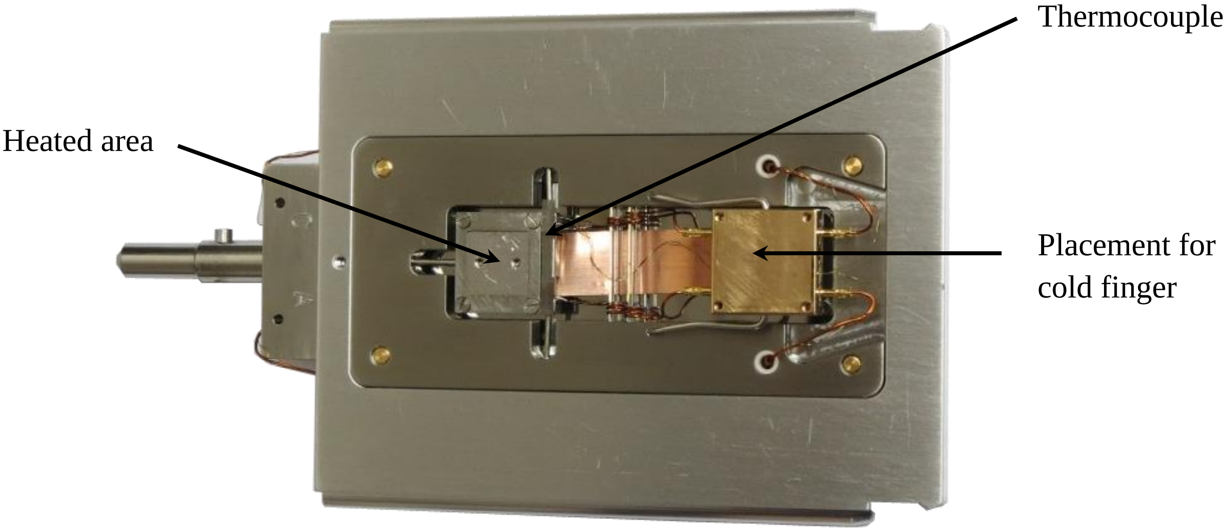

Figure 4.17: *Sample heater used in the SIMS 5 TOF-SIMS spectrometer to study the segregation of S and Cr in bcc Fe.*

The cold finger removes excess heat, using liquid nitrogen, from the sample holder and consequently also from the system stage. The steps listed below were used to perform segregation experiments by linear programmed heating.

1. The sample was placed into the TOF-SIMS system and allowed to reached a pressure of $<1\times10^{-8}$ Torr, before measurements were started.
2. The sample was cleaned using Cs^+ sputtering on a 1000×1000 µm area to remove any surface contaminants.
3. Next, the system was slowly heated to a maximum temperature of 923 K to allow the sample to degas. Once the desired temperature was reached, the sample was linearly cooled at a rate of 0.1K/s to 273 K using the cold finger.
4. The sample was heated to a starting temperature of 525 K and kept at that temperature long enough to ensure stable operation of the temperature control unit.
5. The surface was sputter cleaned to ensure that the surface was free from any segregates or adsorbents.
6. Immediately after switching off the Cs sputter gun, the sample temperature was linearly increased to 923 K in increments of 0.1 K/s while the data was recorded.
7. Once the sample reached the temperature of 923 K it was allowed to cool linearly to 323 K, before switching off the filament.

The experimental results obtained using the above experimental procedure is described in chapters 6 and 8 for the segregation of S in Fe and the segregation of both Cr and S in Fe.

4.4.5. TOF-SIMS quantification

Secondary ions emitted from the sample can either have a positive or negative charge. The formation of positive ions is strongly influenced by their ability to be ionised within the matrix material. Formation of negatively charged ions depends on the electron affinity of the ions. The ionisation probability of positive ions and the availability of electrons to negative ions are influenced by the surrounding chemical environment in the material [12, 13]. This is referred to as the “matrix effects” of the material under study. Since the environment can vary dramatically from material to material, similar elements in different host materials will have different ionisation probabilities or availability of electrons and thus have different sensitivities. This complicates the quantification of TOF-SIMS data significantly. For homogenous samples of dilute concentrations, quantification can be achieved by using a standard sample with a matrix resembling that of the analysed samples [12, 13]. In the current study, dilute concentrations of S in Fe was quantified with the use of a standard sample. Care was taken to analyse the standard sample under exactly the same experimental conditions as the measured samples to ensure reliable results.

In order to quantify the data, the measured intensity, *I*, for the element of interest was divided by the measured intensity of the matrix material, Fe [12, 13]. This normalises, and reduces possible drifts in the data. Normalisation of the data is better explained by using the mathematical expression for the secondary ion intensity provided by equation 4.35 [12]

$$I_m = I_p Y_m \alpha_m^{+/-} \theta_m \eta \,, \tag{4.35}$$

where, I_m is the secondary ion intensity, I_p, is the primary ion density, Y_m, is the sputter yield for specie *m*, $\alpha_m^{+/-}$ is the ionisation probability of specie *m*, θ_m is the concentration of specie *m* at the sample surface and η is the transmission rate of the instrument and detector. Dividing the secondary ion intensity of specie *m* by the secondary ion intensity of the matrix material, *n*, delivers equation 4.36

$$\frac{I_m = I_p Y_m \alpha_m^{+/-} \theta_m \eta}{I_n = I_p Y_n \alpha_n^{+/-} \theta_n \eta} = \frac{Y_m \alpha_m^{+/-} \theta_m}{Y_n \alpha_n^{+/-} \theta_n} \;. \tag{4.36}$$

Therefore, any factors brought about by a change in primary ion current density or the transmission of the instrument and detector cancels out. Using a standard with a known S concentration, the S concentration in the unknown sample can be determined. The intensity of the reference sample is provided by an expression similar to equation 4.35, equation 4.37.

$$I_m^* = I_p Y_m \left(\alpha_m^{+/-}\right)^* \theta_m^* \eta \,, \tag{4.37}$$

Where the superscript * refers to the use of a standard sample. If the unknown sample has a similar composition to that of the standard then they would have the same probability of ionising the species in the sample and therefore these terms are equal as described by equation 4.38

$$\alpha_m^{+/-} = \left(\alpha_m^{+/-}\right)^* . \tag{4.38}$$

By making the ionisation probability in equation 4.35 the subject of the equation and substituting the result into equation 4.37 delivers the relation between intensity and concentration, equation 4.40 [12, 13]

$$\frac{I_m^*}{\theta_m^*} = \frac{I_m}{\theta_m} \ . \tag{4.39}$$

Equation 4.39 describes a linear relationship between the concentration of an unknown sample and a reference sample. This linearity is only valid when the concentration of the unknown sample closely resembles that of the standards sample. Dilute samples in the concentration region <1 at. % abides to this linearity [12]. If the concentration of the unknown sample exceeds the 1 at. % value, the ionisation probabilities of the two samples are no longer equal and therefore equation 4.39 is no longer valid. The quantification of S in Fe samples of different S concentrations, within the dilute limit, was performed using the above procedure, see chapter 5 for results.

4.5. Comparison between AES and TOF-SIMS analysis for surface segregation studies

AES and TOF-SIMS are the primary research techniques used in this study and knowledge concerning their strengths and weaknesses are important in order to obtain the desired information. Some of these characteristics have already been mentioned earlier in this chapter. Below table 4.5 contains a more detailed comparison of the two techniques.

Table 4.5: *Comparison between AES and TOF-SIMS, outlining their respective strengths and weaknesses in surface segregation studies.*

	AES	**TOF-SIMS**
Ease of use	Moderate • Few settings are required • Primary electron beam is easy to operate • Data analysis is relatively easy, since a handbook with reference spectra is available.	Difficult • Requires the optimisation of a number of settings • The liquid metal ion source can be troublesome, with effects such as side emission occurring. • Data analysis needs to be performed with great care.
Elemental information	All elements except H, He and even Li	All elements
Chemical information	Limited	Capable of detecting different ions, compounds and isotopes
Detection limit	Typically in the at.% range	ppm to ppb range
Analysis time	Slow – Fewer elements can be scanned at a specific time.	Fast - Secondary ions are analysed in time-of-flight mode allowing rapid analysis of ions
Imaging	• Smaller beam size allows for increased image quality. • Elemental mapping is very slow	• Image quality is limited, due to the larger Bi ion beam • Fast elemental mapping due to time-of-flight analysis
Quantification	• Semi-quantitative – elemental standards required and matrix effects need to be considered.	• Semi-quantitative - requires standards. Matrix effects are more complex than in AES

4.6. Summary

The surface analytical techniques, AES and TOF-SIMS were discussed and a comparison was drawn between the two techniques to highlight their respective strengths and weaknesses in segregation studies. Their respective principles of operation, the systems themselves and the optimised settings used in the experiments were described. AES quantification for the case of segregated layers as well as for homogenous solids was discussed. Additionally TOF-SIMS quantification was described for the case of dilute homogenous alloys. A brief description along with the experimental settings used in this study is also provided for XRD.

4.7. References

[1]. P. E. Barnard, Experimental and computational study of S segregation in Fe, M.Sc. Dissertation, Bloemfontein, 2012.

[2]. B.D. Cullity, S.R. Stock, Elements of X-Ray diffraction, Prentice Hall, New Jersey, 2001.

[3]. D. Briggs, J.T. Grant, (Eds.), Surface analysis by Auger and X-Ray Photoelectron Spectroscopy, IM Publications and Surface Spectra Limited, United Kingdom, 2003.

[4]. J.J. Terblans, Modellering en eksperimentele ondersoek van Sb-oppervlak segregasie in Cu-enkelkristalle, Ph.D dissertation, Bloemfontein, 2001.

[5]. E.C. Viljoen, J. du Plessis, Surf. Sci. 468 (2000) 27.

[6]. D. Briggs, M.P. Seah, (Eds.), Practical surface analysis by Auger and Photoelectron spectroscopy, John Wiley & Sons, New York, 1983.

[7]. J. du Plessis, Surface Segregation, Sci-Tech Publications, Bloemfontein, 1990.

[8]. R. Shimizu, JPN. J. APPL. PHYS. 22 (1983) 1631.

[9]. S. Tanuma, C.J. Powell, D.R. Penn, Surf. Interface Anal. 20 (1993) 77.

[10]. J.A. Nelder and R. Mead, A simplex method for function minimization, Computer Journal 7 (1965) 308–313.

[11]. K.J. Laidler, J.H. Meiser, B.C. Sanctuary, Physical chemistry, Houghton Mifflin Company, 2003.

[12]. M. Py, A study of interfaces and nanostructures by time of flight mass spectrometry: towards a spatially resolved quantitative analysis, 2011.

[13]. T. Stephan, TOF-SIMS in cosmochemistry, Planet. Space Sci. 49 (2001) 859–906.

[14]. D. Halliday, R. Resnick, J. Walker, Fundamentals of physics, John Wiley & Sons. Inc., USA, 2001.

[15]. J.C. Vickermann (eds.), D. Briggs (eds.), TOF-SIMS: Materials analysis by mass spectrometry, IM Publications, UK, 2013.

[16]. Unpublished documentation from Ion-TOF.

[17]. G. Holland, S.D. Tanner, Plasma source Mass Spectrometry: Applications and emerging technologies, Royal Society of Chemistry, USA , 2003.

Chapter 5

Sample preparation

5.1. Introduction

This chapter describes the methods and equipment used in order to prepare Fe samples doped with Sulphur (S) and Chromium (Cr) respectively. The samples are prepared in order to investigate the segregation of both Cr and S in the Fe matrix (refer to chapters 6, 7 and 8 for results). A considerable part of this chapter is focussed on the equipment designed specifically for the preparation of high purity samples: The S doping chamber and the high temperature annealing furnace. The preparation of Fe-S samples are carried out by custom in-house built equipment and the sample quality is evaluated by Auger Electron Spectroscopy (AES) and Time-of-Flight Secondary Ion Mass Spectrometry (TOF-SIMS). The latter technique is also used to evaluate the surface composition of samples annealed in the high temperature annealing furnace.

5.2. Doping Fe crystals with S

The method described below was developed in previous work [1] in order to prepare Fe samples doped with S. Further modification to the system was made in this work by fitting a Ti (Titanium) filament into the system to act as a getter for oxygen and other impurities. A qualitative and quantitative analysis of the method was performed in this study in order to emphasise its effectiveness. Another widely used method [2-5]; to pass a mixture of H_2S/H_2 over the Fe sample, was not considered due to the unwanted diffusion of H into the sample along with the S. The presence of H can negatively influence the thermodynamic and kinetic properties of S during surface segregation runs, resulting in less accurate results for the segregation parameters of S. Figure 5.1 provides an image of the doping system used for doping Fe with S.

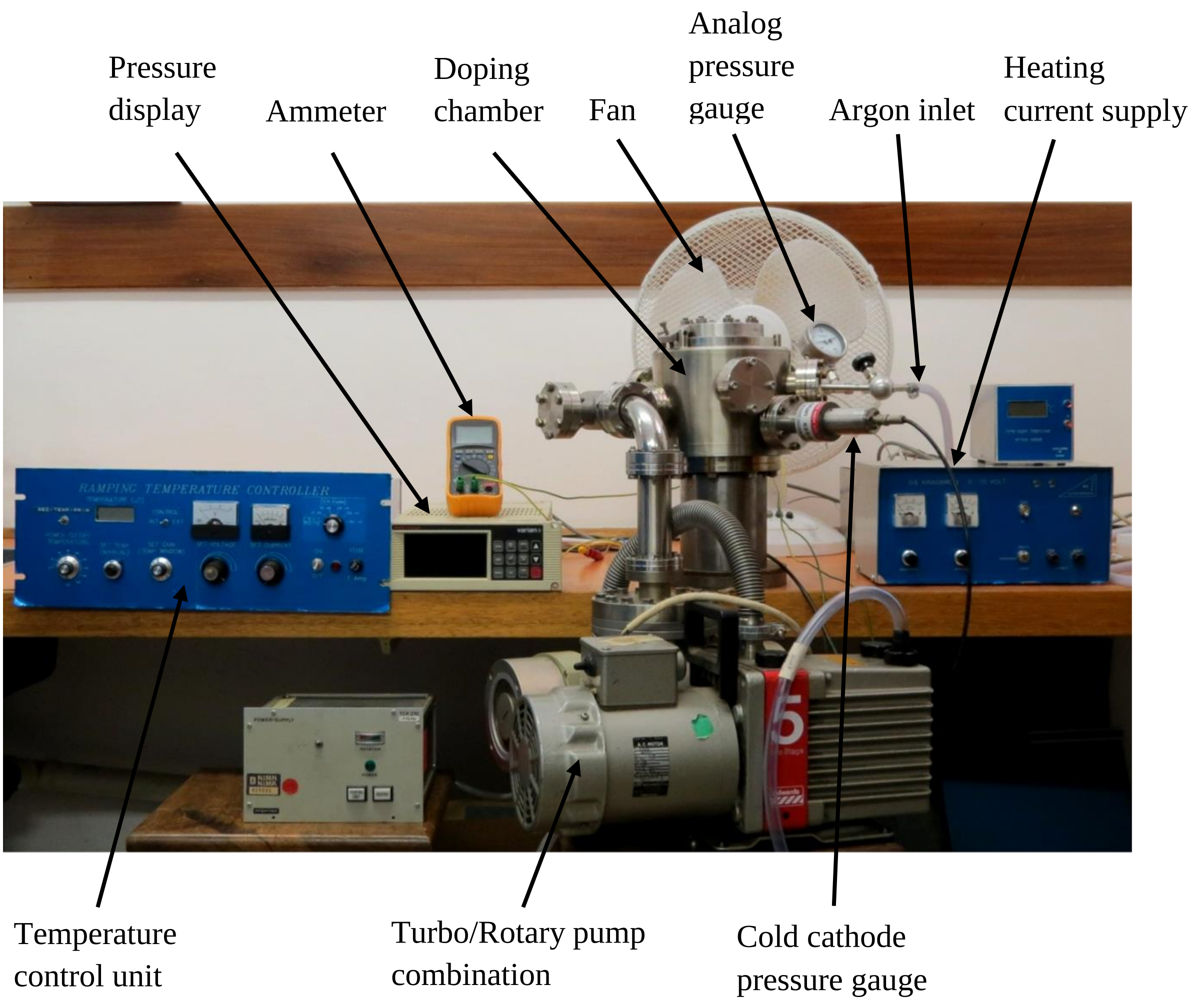

Figure 5.1: *Custom in-house built doping system for the preparation of S doped Fe samples* [1].

The system consists of a doping chamber which is pumped by a rotary and turbo pump combination, capable of reaching vacuum pressures down to $<2.0\times10^{-6}$ Torr as measured by the cold cathode gauge. Argon gas is allowed to fill the system via the Ar inlet to a pressure of 1500 Torr as measured by the analogue pressure gauge. Electrical current to the two filaments, the one for heating the Fe sample and the one for heating S are respectively supplied by the temperature control unit and the heating current supply. The current supply to the Fe sample from the temperature control unit is measured by an ammeter. During sample preparation the glass window of the doping chamber heats up due to heat being transferred from the two heaters. To prevent damage to this window, a fan is used to ensure cooling thereof.

The basic principle of the sample preparation method is the deposition of S onto a Fe sample kept at an elevated temperature, which results in the formation of a FeS surface phase. When the sample is annealed at a high temperature the FeS phase, which has a melting point of 1185 K [6], compared to that of S, 385 K [6], allows for the sufficient high temperature necessary to be used. If the FeS phase is absent, a very low annealing temperature has to be used to avoid evaporation of the deposited S. This would require extremely long annealing times, making sample preparation using this method impractical.

5.2.1. Experimental procedure

S was heated by means of resistive heating which created a vapour of S to be deposited onto Fe. During deposition of the S vapour, the Fe sample was kept at a high temperature (660 K) to ensure the formation of a FeS phase. The detailed procedure used in doping Fe with S is listed below:

1. The Fe host was mounted onto the top heater and S flakes were placed in the cup mounted onto the bottom heater, see figure 5.2.
2. The system was then closed off from atmosphere and pumped down to $<2.0\times10^{-6}$ Torr.
3. This was followed by backfilling the system with Ar gas to a pressure of 1500 Torr, and subsequently pumping it down to a pressure of $<2.0\times10^{-6}$ Torr.
4. Step 3 was repeated 5 times to ensure that most impurity gasses were removed from the system.
5. A final backfilling of the system with Ar gas to a pressure of 1500 Torr ensured an inert atmosphere under which Fe could be doped with S.
6. The heater containing the Fe sample was heated to 660 K. This temperature allowed diffusion of the S vapour into Fe within a reasonable time period.
7. The system was allowed to stabilise for 2 minutes, to ensure that the Fe host was thoroughly heated and that a stable temperature was obtained.
8. After the 2 min preheating of the Fe host, the S was slowly heated to allow degassing of the S flakes.
9. The Fe host was then exposed to the S vapour (T>718 K) until the desired doping time was reached.

10. As soon as the desired doping time was reached the electrical current of the two filaments was switched off and the system was pumped down to remove the S vapour.
11. The sample was removed from the preparation chamber after it was allowed to cool down to room temperature, and subsequently cleansed in an ultrasonic bath of ethanol.

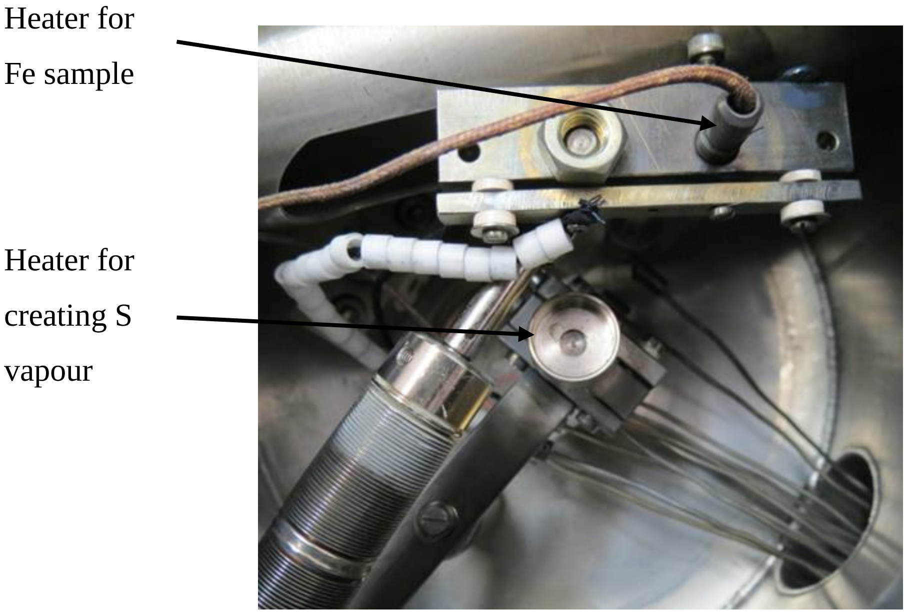

Figure 5.2: *Internal view of the S doping chamber, showing the two heaters used respectively for heating of the Fe sample and the formation of the S vapour* [1].

To confirm the repeatability and reproducibility of the sample preparation method, two sets of samples were prepared. The first set of samples, consisting of four samples, were analysed by AES and TOF-SIMS depth profile analysis in order to confirm the diffusion of S into Fe. Three of these samples were doped each for 25 s and the fourth sample was doped for 12.5 s.

The second set of samples, three samples in total, were doped and then annealed at 1073 K for a total of 60 days in order to obtain a homogenous S concentration. Two of the samples were each doped for 61 s, a third sample was doped for 25 s and a fourth sample was doped for 100 s. TOF-SIMS was used to quantify the S concentration in the respective samples using a standard sample with a known S concentration.

5.2.1.1. Time-of-Flight Secondary Ion Mass Spectrometry (TOF-SIMS) analysis

TOF-SIMS analysis was performed using the TOF-SIMS 5 Ion-TOF system, described in chapter 4, section 4.4.2. The samples were analysed in spectroscopy mode with a positive extractor current (negative mode), using a Bi^+ primary ion beam operated at 30 kV with a target current of 1 pA. The beam was rastered over an area of 100×100 µm with a scanning resolution of 512×512 pixels. For depth profiling, a Cs^+ liquid metal ion source (LMIS) with an ion current of 130 nA was operated at 2 kV. The Cs^+ source was used to erode away the sample on an area of 300×300 µm in 20 s intervals. To ensure accurate analysis of the samples, the mass spectra was calibrated to the following mass peaks: H^-, C^-, CH^-, CH_2^-, CH_3^-, O^-, OH^-, F^-, Si^-, P^-, Cl^-, SiO^-, SO^-, Fe^-, S_2^-, FeO^-, FeS^-, Fe_2^-, S_3^-, Cs^- and Br^-. The analysis was conducted with a mass resolution of >7000 obtained for S (31.9686 amu), ensuring that the S^- and O_2^- mass peaks are clearly separated. A detailed description of the mass resolution is provided in chapter 4, section 4.4.2.

5.2.1.2. Auger Electron Spectroscopy (AES) Analysis

AES depth profiling was performed with the PHI 700 Auger Nanoprobe, described in chapter 4, section 4.3.2. The samples were analysed with a 25 kV 10 nA primary electron beam. The ion source used for sputtering was an Ar^+ ion gun, operated at 2kV and 2µA. Analysis was performed by allowing scanning of the electron beam and sputtering by Ar^+ to be carried out in an alternating fashion; Firstly, the sample was scanned by the electron beam on an area of 4 μm^2 for all elements selected. Secondly, the sample was sputtered by the Ar^+ beam on an area of 1×1 mm^2 for 2 min. During analysis the base pressure in the UHV chamber rose to $<5\times10^{-8}$ Torr as a result of the Ar^+ gas in the chamber.

5.2.2. Results and discussion

The diffusion of S into Fe and the formation of the desired FeS phase were confirmed by AES depth profiling, performed on the first set of samples. Figures 5.3 and 5.4 present the quantified depth profiles of the sample doped for 25 s and the one doped for 12.5 s respectively. The measured Auger-peak-to-peak height (APPH) data was converted to fractional concentrations using the method described by Du Plessis [7]. With the backscattering factors, *R*, obtained with the method described by Shimizu [8] and the inelastic mean free path obtained using the TPP2 method described by Tanuma et. al. [9]. A detailed description of AES quantification is provided in chapter 4, section 4.3.5.3. Depth scale calibration was performed by analysing a Fe standard of known thickness (85 nm) which resulted in a sputter rate of 8.2 nm/min.

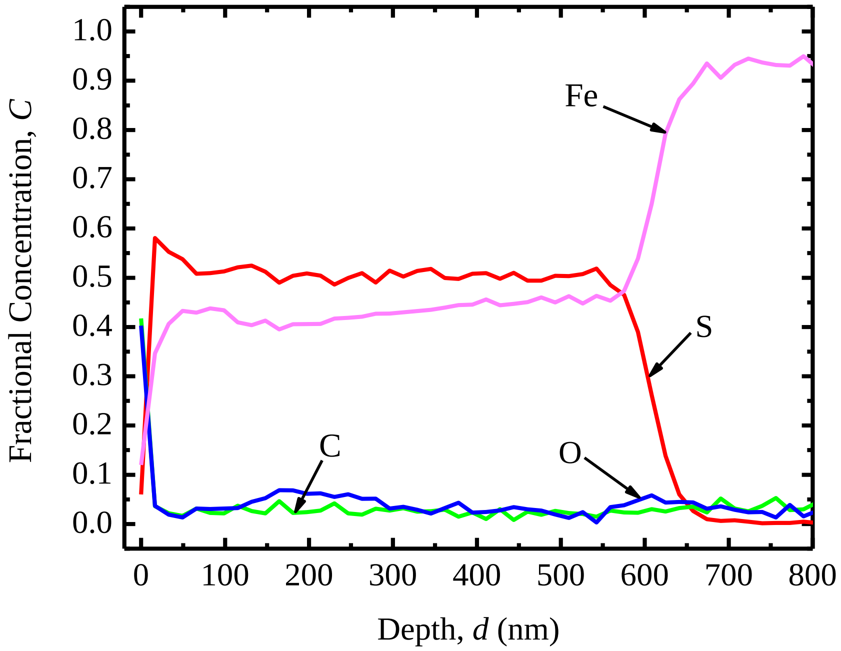

Figure 5.3: *Quantified AES depth profile of the Fe sample doped for a total of 25 s with S. The formation of a FeS phase is visible by the plateau regions of both Fe and S.*

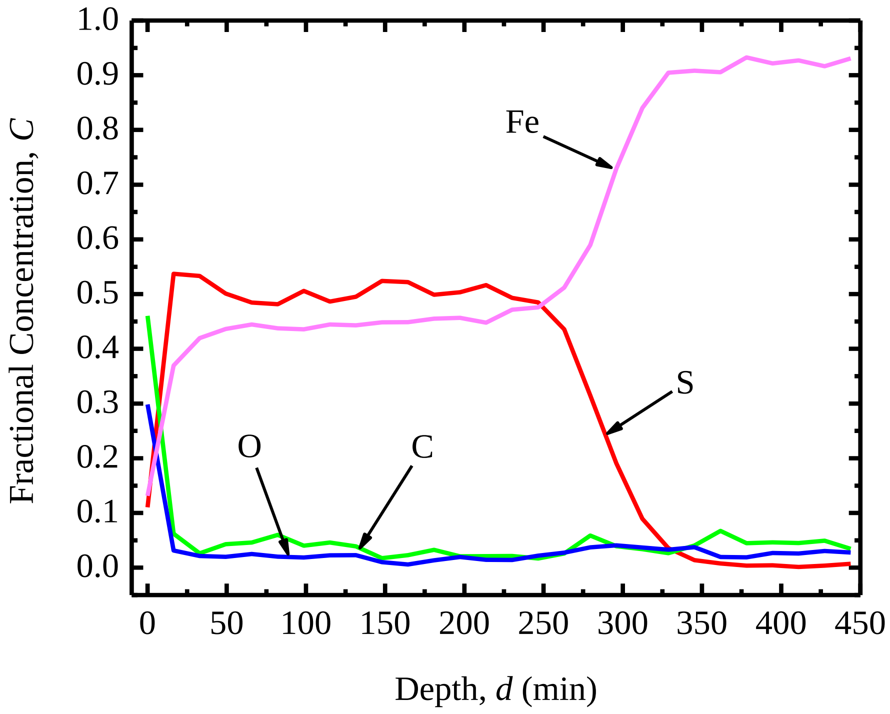

Figure 5.4: *Quantified AES depth profile of the Fe sample doped for a total of 12.5 s with S.*

The depth profiles in figures 5.3 and 5.4 show the elements S and Fe, both C and O were detected as contaminants on the surface. C and O originated from atmosphere as a result of the samples being transferred to the PHI 700. Both S and Fe formed a plateau region indicating that a FeS (S and Fe within experimental error ~ 50%) phase has formed in the Fe sample. Indicated by the plateau areas of Fe and S, the FeS layer of the samples doped for 25 s has a thickness double that of the sample doped for 12.5 s. Figure 5.3 show a slight increase in the O concentration at ~200 nm and likewise a slight increase in the C concentration is observed in figure 5.4 at ~100 nm. Possible reasons for the appearance of these slight increases are: Impurities coming from the S flakes or it could also be caused by local effects, such as a grain boundary in the Fe crystal. In an effort to minimise local effects two an analysis area of 20×20 µm was chosen. Despite these slight increases in concentrations of C and O, the concentrations of the contaminants remain low throughout the crystal indicating a clean sample. Depth profiling was also performed by TOF-SIMS, with the data presented in figure 5.5 and 5.6.

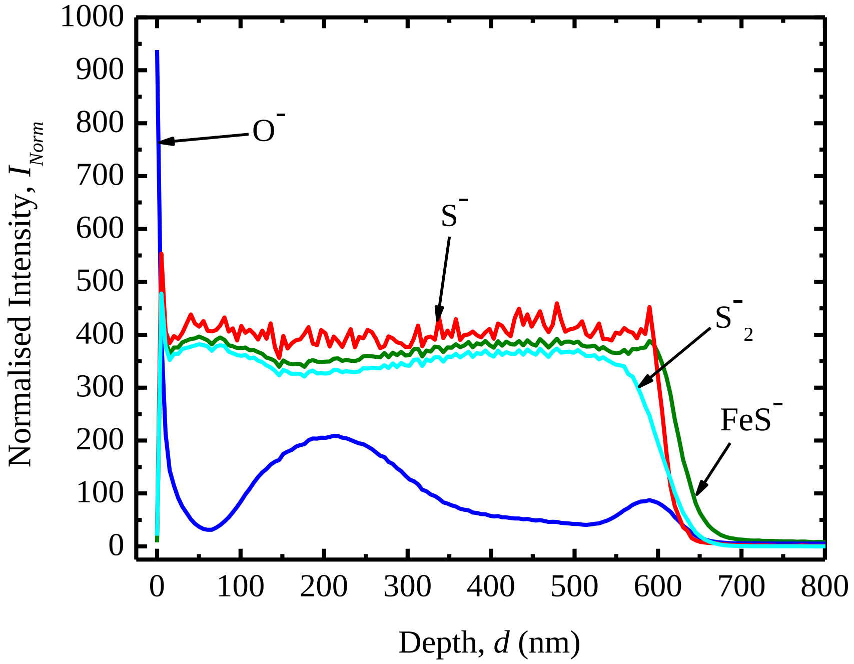

Figure 5.5: *TOF-SIMS depth profile of the Fe sample doped for a total of 25 s with S, where the presence of the FeS phase is evident.*

Figure 5.5 provides the depth profile of the sample doped for 25 s. The sputtering time was converted into a depth scale using the same Fe standard previously used for AES depth scale calibration. A sputter rate of 15nm/min was obtained for the Fe standard with a thickness of 85 nm. The data measured on the FeS samples was normalised with respect to Fe to ensure the removal of any drift that may be present in the data. Formation of the FeS phase in the surface region is clearly visible as indicated by the presence of the FeS^- ion in figure 5.5. Also noted in figure 5.5 is a presence of O on the surface and again the presence of a slight increased O intensity is observed at ~200 nm. The presence of oxygen at 200 nm corresponds to the oxygen detected in the AES depth profile of figure 5.3.

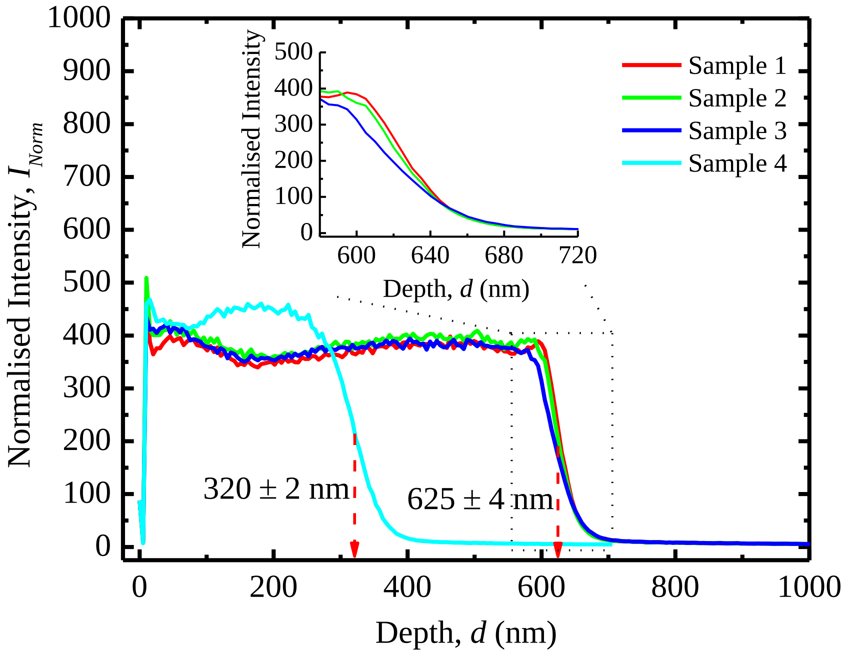

Figure 5.6: *TOF-SIMS FeS profiles of the samples doped with S, forming the FeS phase. The inset provides a clear view of the profile on the FeS/Fe interface.*

From figure 5.6 the samples doped for 25 s is seen to have a FeS thickness of 625±4 nm compared to the 320±2 nm thickness of the sample doped for 12.5 s. This shows a 49% increase in concentration when the doping time is doubled. There is however a limit of 330 ppm which samples can be prepared with and still remain within the α-phase limit of Fe [10].

The final step in obtaining pure, binary Fe-S alloys is the annealing of the doped samples; sample set two. The samples were placed into the annealing system (section 5.4) and annealed at 1073 K for a total of 60 days. The samples were then loaded into the SIMS 5 TOF-SIMS system and the bulk concentration of S in each sample was determined using a sample with a known S concentration of 5 ppm as the reference material. Concentrations below 1 atomic percentage (at.%) shows a linear relationship with respect to intensity [11]. Since the concentrations of S in Fe is far below 1 at.% this linear relationship was used to determine the concentration of the prepared samples using the obtained Relative Sensitivity Factor (RSF) of 51 ppm. Figure 5.7 shows the concentration of the respective samples as a function of the normalised intensity. For a description on the quantification of TOF-SIMS data in dilute systems refer to chapter 4, section 4.4.5. The repeatability of the doping method is also evident in the data presented in figure 5.7, where two samples, doped for the same time has concentrations which vary by no more than 2 ppm.

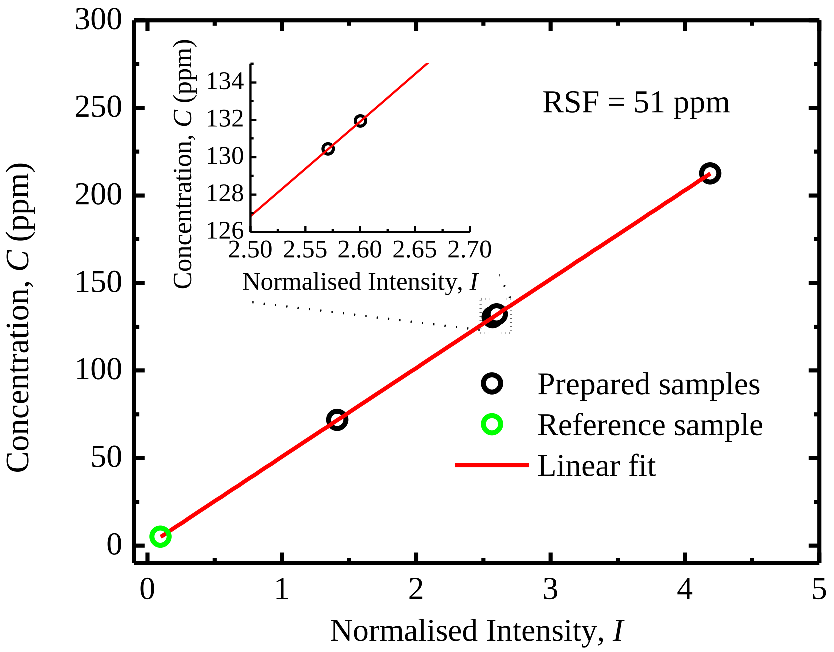

Figure 5.7: *Relation of the S concentration with respect to the normalised intensity of S in Fe, as measured by TOF-SIMS. The quantification was done using a standard sample with a known S concentration of 5 ppm.*

For the samples used in segregation studies, the bulk concentrations were determined using the same approach. Since the measurement of these samples was done at a later time period than the samples used in the method evaluation step, a new standard measurement had to be performed. The quality and hence the reliability of quantification depends on using the same conditions for all samples measured, including the standard. Therefore, the analysis of samples and the standard should be done within the shortest time period to avoid variation in measurement conditions. An un-doped sample, of the same batch as the samples used for doping, with a known bulk concentration of 5 ppm was used as the standard. A Relative Sensitivity Factor (RSF) of 51 ppm was also obtained for the standard sample. All Fe-S samples were quantified using this RSF value with the results presented in table 5.1.

Table 5.1: *Bulk concentration values of S in the Fe samples used in surface segregation studies. A Relative Sensitivity Factor (RSF) value of 51 ppm was obtained for the standard sample.*

Sample	Secondary ion intensity	Concentration, *C* (ppm)	RSF
Standard	0.098	5	51
Fe(100)	3.62	184	-
Fe(111)	5.32	271	-
poly Fe	5.07	258	-

All samples have successfully been doped with S, evident in the increased concentration of S in the samples. The Fe(100) and the polycrystalline sample have concentrations which corresponds to their respective doping times of 65 s and 100 s. The Fe(111) sample have a concentration higher than expected, due to a filament failure which occurred during the sample preparation step. Therefore the sample had to be doped for a second time, with only an estimate of the amount of S diffused into the sample during the first doping opportunity. Despite this larger than expected concentration for the Fe(111) orientation, all samples are within the solid solution region (S < 330 ppm) of the Fe-S phase diagram. These samples were studied for their respective segregation parameters with results presented in chapters 6 and 7.

5.3. Doping Fe with Cr

Deposition of a thin layer of Cr onto a polycrystalline Fe sample was performed by electron beam evaporation. The technique utilises electrons to bombard the element to be deposited, for this study this element was Cr, up to the point where sufficient energy has been transferred to the element to cause it to evaporate. Electrons are generated by applying a heating current to a tungsten filament, resulting in the generation of thermal electrons. These electrons are then accelerated onto the material (Cr) using a high voltage (4kV). Steering of these electrons is achieved by the use of a magnetic field, which ensures a sufficient electron flood to cause evaporation of the material (Cr).

By controlling the exposure time of the samples to the Cr vapour, the desired thickness of Cr was deposited onto Fe. The thickness of the evaporated layer was monitored by a thickness monitor inside the vacuum chamber, which uses the density of the dopant and the Z-ratio of the evaporation system to determine the thickness of the deposited layer.

The sample was weighed before and after evaporation of Cr in order to obtain the mass of the deposited Cr layer. To calculate the mass needed to obtain a desired bulk concentration, equation 5.1 was used

$$m_{Cr} = \frac{m_{Fe} X_{Cr} M_{Cr}}{(1 - X_{Cr}) M_{Fe}}, \tag{5.1}$$

where *m* is the mass of the Fe sample and deposited Cr layer respectively, *X* is the desired Cr concentration and *M* the molecular mass of the elements. With the mass of the dopant known, the thickness of the evaporated layer, *d*, could be calculated using the sample area, A_{Fe}, and the density of the dopant material, ρ_{Cr}, described by equation 5.2.

$$d_{Cr} = \frac{m_{Cr}}{A_{Fe} \rho_{Cr}}. \tag{5.2}$$

Table 5.2 presents the respective mass and concentration value of Cr in the Cr doped Fe sample.

Table 5.2: *Mass of Cr deposited onto the Fe sample along with the corresponding bulk concentration.*

weight (before) mg	**weight (after) mg**	**weight diff (Cr mass) mg**	**at. % Cr in bulk**
302.03	302.47	0.44	0.16

The following experimental procedure was performed in order to deposit Cr onto the Fe surface using electron beam evaporation:

1. The Fe sample was mounted inside of the evaporation chamber. To ensure that the sample is free from dust particles, it was cleaned with nitrogen gas beforehand.
2. The evaporation chamber was then pumped down to a pressure of ~10^{-5} Torr.

3. Iron (Fe) was evaporated in the chamber to act as a getter, trapping oxygen and other impurities. Fe was used since this minimises the risk of contamination by other elements.
4. The crucible containing Cr was positioned in front of the electron gun and the current of the electron gun was slowly increased.
5. As soon as the desirable evaporation rate of Cr was achieved the Fe sample was placed in front of the Cr vapour until the desired thickness of Cr was obtained.

The sample deposited with Cr was subsequently annealed at a temperature of 1173 K for a total of 30 days in order to obtain a homogenous bulk concentration of Cr in Fe. The annealing process is described in the next section, section 5.4.

5.4. High temperature annealing

As mentioned in section 5.2, after the desired amount of dopant is deposited onto the Fe surface, the sample has to be annealed at a high temperature for a long period of time. The purity of the samples will directly affect the results of the segregation measurements. If any impurity has diffused into the sample during annealing, this impurity could potentially influence the diffusion mechanism of the system under study. This is of particular concern when a metallic sample such as Fe is the material under study due to its affinity for O. Therefore, the need arose for a system capable of annealing samples at high temperatures for time periods of up to 90 days, without affecting the purity of the samples. The annealing system presented in the next section, section 5.4.1, was designed and built in-house in order to prepare Fe samples, doped with S/Cr.

5.4.1. Design of the annealing system

The main focus of this system entails the annealing of metallic samples which are highly sensitive to oxidation. The system was designed with this in mind and these features are discussed next. The system is capable of reaching vacuum pressures of ~10^{-5} Torr, which effectively removes the majority of impurity gasses from the system. After pumping down, the system is backfilled with Ar gas to a pressure of 700 mmHg above atmosphere. The choice of Ar backfilling ensures that an inert environment is created; free of contaminants such as O. Vacuum annealing poses the threat of sample damage in case of equipment or a power failure. A 3-dimensional drawing of the annealing system is presented in figure 5.8, with the front, rear and top views of the system illustrated in figures 5.9, 5.10 and 5.11 respectively.

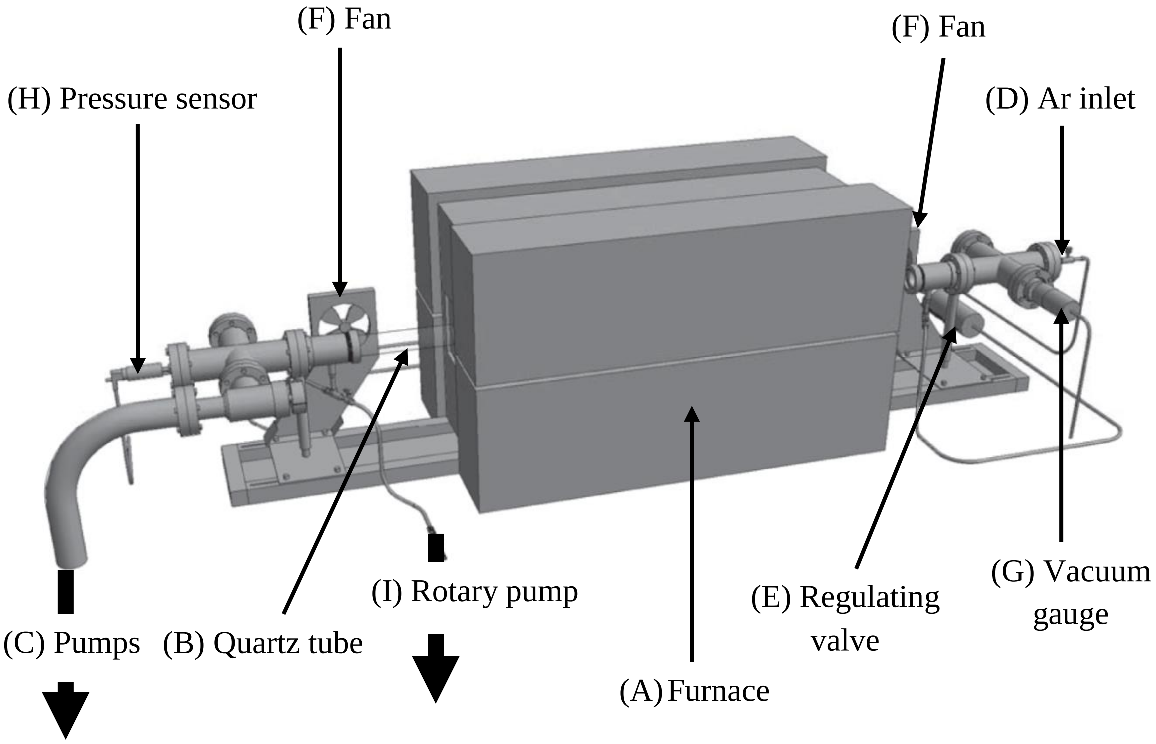

Figure 5.8: *3D drawing of the annealing system: The image shows the main components of the annealing furnace excluding the control units. Each of the components is briefly described in the text.*

The annealing system consists of the following components:

A. Lindberg tube furnace capable of reaching temperatures up to 1473 K.
B. Quartz tube in which the Fe samples are placed for annealing.
C. Turbo and rotary vane pump combination capable of reaching vacuum pressures of 10^{-5} Torr.
D. Ar gas inlet providing Ar gas to obtain an inert atmosphere for annealing.
E. Pressure regulating valve to maintain a constant Ar pressure in the small chamber between the outside of the quartz tube and the inside of the metal coupling (see figure 5.12).
F. 12 V DC fan to prevent the quartz tube connected to the metal couplings, containing Viton O-ring seals, from overheating.
G. Cold cathode/pirani pressure gauge combination, capable of measuring pressures in the range 10^{2}-10^{-9} Torr.
H. Positive pressure gauge capable of measuring pressures above atmosphere.
I. Rotary pump capable of reaching pressure down to 10^{-2} Torr.

Figure 5.9: *Front view of the annealing system where the letter* ***A*** *indicates the adjustable support legs of the quartz tube which are used in the horizontal alignment of the quartz tube. This ensures the tube is in a stable position without excess forces on either side of the tube.*

Figure 5.10: *Rear view of the annealing system with the letter* ***B*** *indicating the 12 V DC fans that are positioned in-line with the connections made to the quartz tube. The use of the fans prevents the metal coupling connections from overheating which would result in damage of the Viton O-ring seals.*

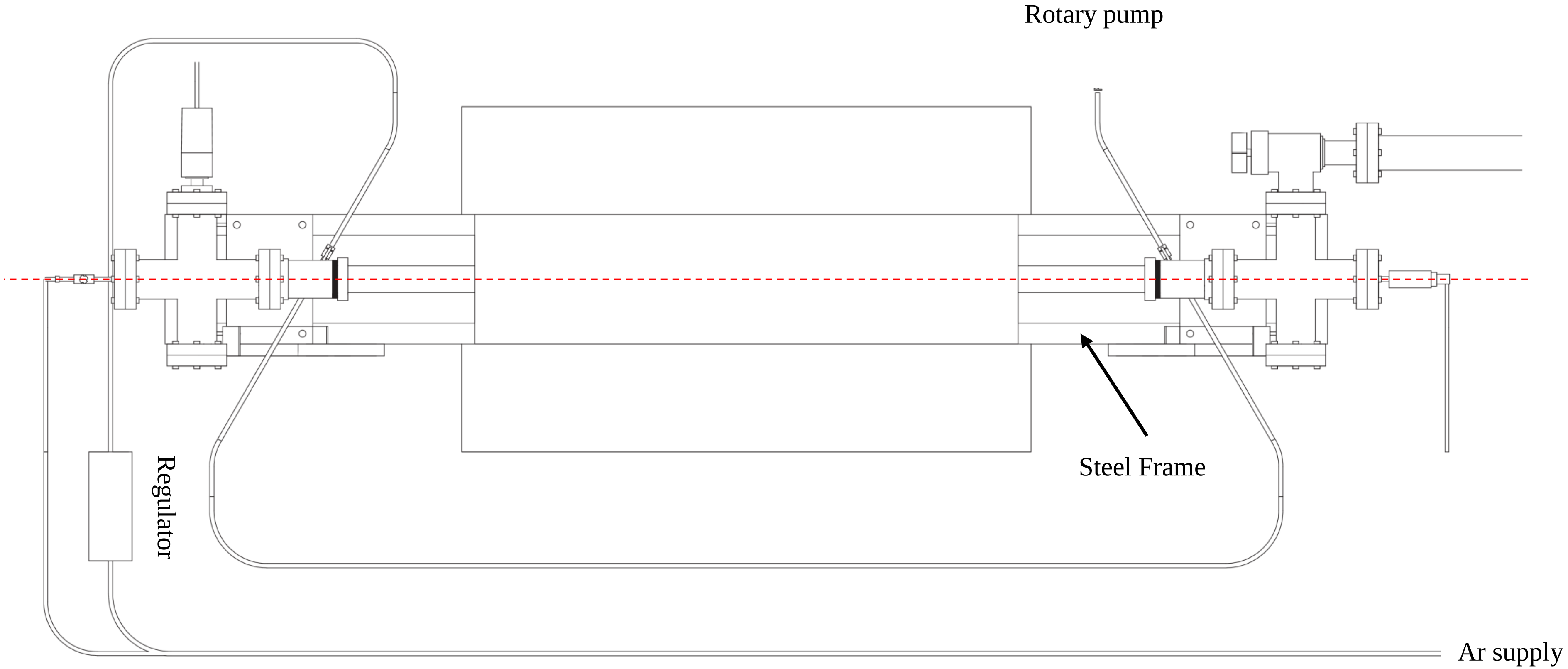

Figure 5.11: Top view of the annealing system. It illustrates how the design of the system ensures that the quartz tube is kept in a fixed position, and is always aligned in this direction. Not only is the two sides of the tube aligned with respect to each other, but also the position of the tube with respect to the furnace centreline (indicated by the red dotted line).

The ability of the system to anneal samples which are sensitive to oxidation over long periods of time and at high temperatures is made possible by the unique design of the system. The flange connections on the system are all made using copper gaskets and the possibility of leakage occurring there is minimal. The greatest possibility of leakage is where the quartz tube is connected to the metal couplings on either side of the tube, with a Viton O-ring to provide a seal as shown in figure 5.12.

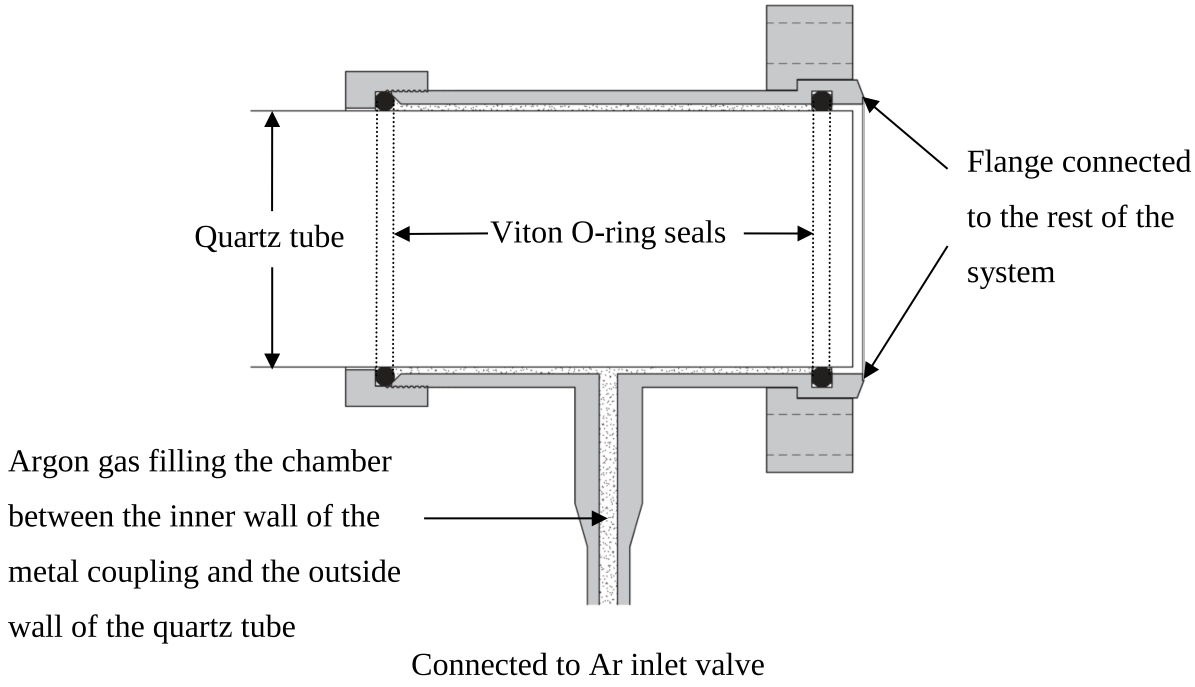

Figure 5.12: *Cross sectional view showing the connection of the quartz tube to the metal couplings, made on either side of the quartz tube. A small "chamber", kept at a constant Ar pressure through a regulating valve, is formed between the two viton O-ring seals.*

The chamber created between the inner wall of the metal coupling and the outside wall of the quartz tube is kept at a constant Ar pressure through a regulating valve. The use of Ar prevents air from flowing into the chamber; a high to low pressure environment is created, with the high pressure inside the small chamber. This prevents O and other contaminant from entering the system, since Ar will always flow from the inside of the chamber to the outside, in the case of a leak.

The abovementioned set-up depends on the correct positioning of the tube inside the metal couplings. If the two couplings, resting on their respective support legs (see Figure 5.9) are not aligned with one another, this could result in a leak since it will cause a displacement in the O-rings. Of bigger concern is the fact that any force on the tube could result in the tube cracking/breaking which would cause damage to the samples. Therefore, it is ensured that the tube is aligned horizontally as viewed from the front of the system. The support legs on either sides of the tube are adjustable in a vertical direction and by setting them to the appropriate height the tube is correctly aligned with respect to the couplings as well as the centre of the furnace. The tube only rests inside of the metal couplings with the O-rings and the metal couplings in turn being supported by the support legs, ensuring the tube is free of excess forces. To ensure that the tube is correctly aligned as viewed from the top, the furnace is fixed to the base, a solid steel frame (figure 5.10, 5.11), preventing any movement. This ensures that the tube is aligned with respect to both the furnace and the metal couplings on either side, forming one centreline.

The tube has a fixed length to ensure the couplings are far removed from the furnace and limits heat transfer from the furnace to the couplings. To aid in limiting heat transfer, both side of the tube was also fitted with a 12 V DC fan (see Figure 5.10) in order to remove heat from the couplings.

5.4.2. Validation of the system

Before the Fe samples were annealed various tests were conducted to ensure optimum working conditions of the system. The most important of these tests were to test for possible leaks in the system. Figure 5.13 presents the data of the pressure inside the quartz tube as a function of the room temperature and time (number of days), monitored aver a 17 day time period.

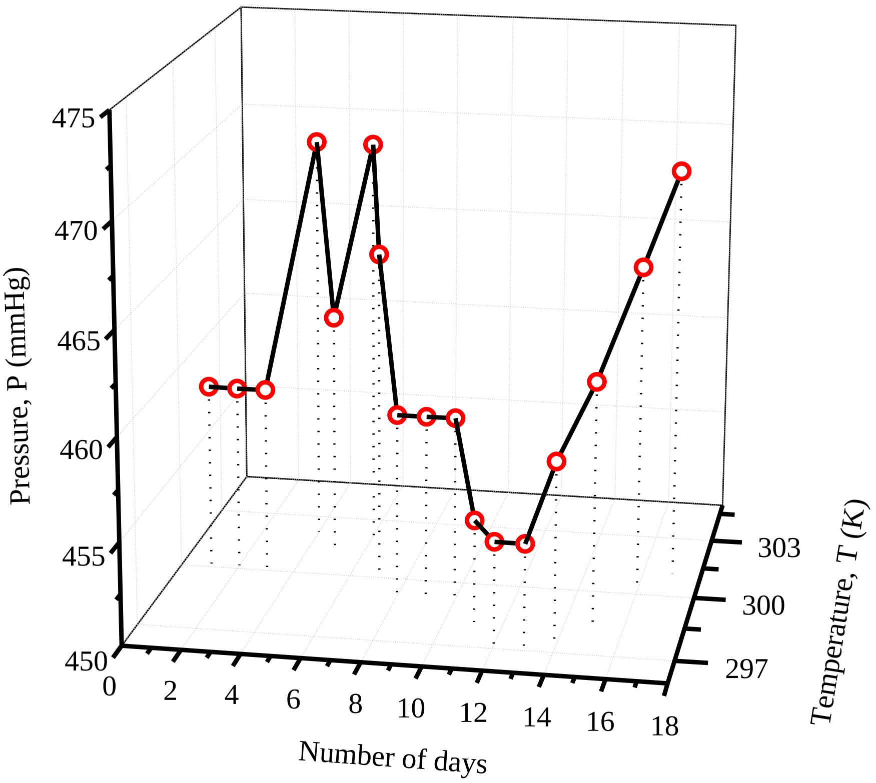

Figure 5.13: *3D plot of the pressure inside the quartz tube as a function of time and temperature, monitored over a period of 17 days.*

From figure 5.13 it is evident that the only variation in pressure was caused by a variation in the room temperature. During the 17 days in which the system was monitored, no visible leakage could be observed. Next, Fe samples doped with S were placed into the furnace and annealed at 1133 K for a total of 90 days. This ensures a homogenous concentration of S in the Fe samples, which is required for segregation studies to be performed on the samples.

5.4.3. Experimental procedure

5.4.3.1. Annealing

The following procedure was followed in the annealing of the S doped Fe samples:

1. The samples, supported on small boats made of quartz, were carefully placed inside the quartz tube. The use of ceramic boats could potentially contaminate the system with O and other impurity gasses.

2. The quartz tube was closed off from atmosphere and pumped down to a pressure of ~10^{-5} Torr, and kept there for 24 hours.
3. The pipeline connected to the metal couplings, the Ar gas bottle and the Ar feed of the quartz tube itself were pumped out. Once this was done the pipeline was backfilled with Ar to a pressure of 500 Torr above atmosphere. This procedure was repeated 10 times to ensure that most impurity gasses were removed from the Ar pipeline.
4. Once the vacuum pressure of ~10^{-5} Torr was reached, the tube was backfilled with Ar to a pressure of 600 Torr above atmosphere. To ensure that most of the impurity gasses where removed, the pumping and subsequent backfilling of the tube was repeated 10 times. Each time the tube was allowed to reach the pressure of ~10^{-5} Torr before being backfilled with Ar.
5. The temperature was increased slowly to 1133 K and maintained at this temperature for a total of 90 days.
6. Once the 90 day time period expired the furnace was switched off and allowed to cool to room temperature before the samples were removed.

5.4.3.2. Time-of-Flight Secondary Ion Mass Spectrometry (TOF-SIMS) analysis

TOF-SIMS depth profiling was performed using the TOF-SIMS 5 Ion-TOF system (chapter 4). The samples were analysed in spectroscopy mode with a positive extractor current (negative mode) using a Bi^+ primary ion beam operated at 30 kV with a target current of 2 pA. To ensure accurate analysis of the samples the mass spectrum was calibrated to the following mass peaks: H^-, C^-, CH^-, CH_2^-, CH_3^-, O^-, OH^-, F^-, C_2^-, Si^-, P^-, Cl^-, Fe^-, S_2^-, FeO^- and B^-. The analysis was done by analysing an area of 200×200 µm at a scanning resolution of 256×256 pixels.

5.4.4. Results and discussion

Two samples, sample 1 and 2, that were annealed together for the period of 90 days were analysed by TOF-SIMS in order to determine their surface composition. Both samples experienced the same temperature, but were placed in slightly different locations of the annealing furnace. To take into account the presence of C and O, which was adsorbed onto the sample surface during sample transfer, a standard sample un-annealed was also analysed. The profiles obtained for each of the samples were normalised with respect to Fe^- to eliminate any drift that could have occurred during the analysis. Figures 5.14 – 5.17 presents the data for the ions: H^-, C^- and O^- detected on the surface of the respective Fe samples.

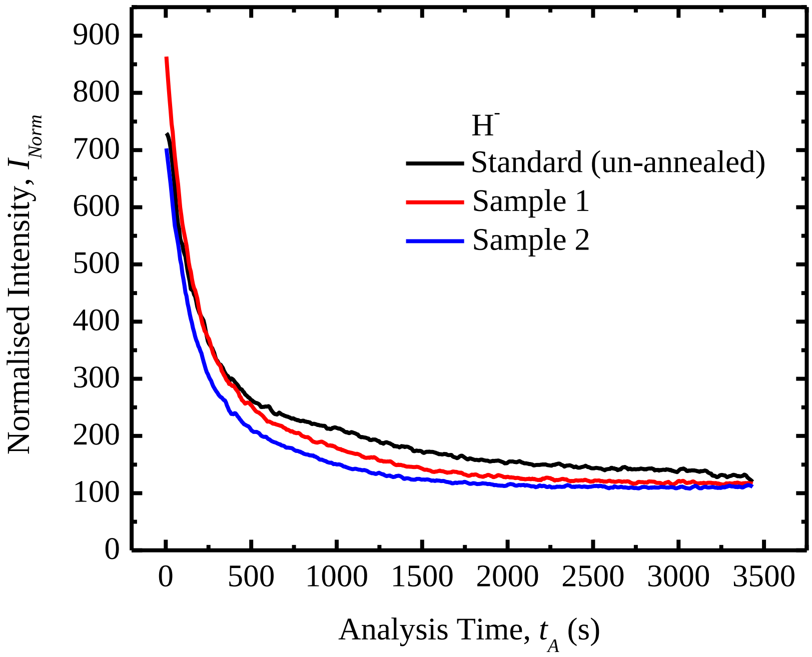

Figure 5.14: *TOF-SIMS profile of* H^- *on the respective surfaces of the two samples annealed for 90 days at a temperature of 1133 K, as well as the standard sample.*

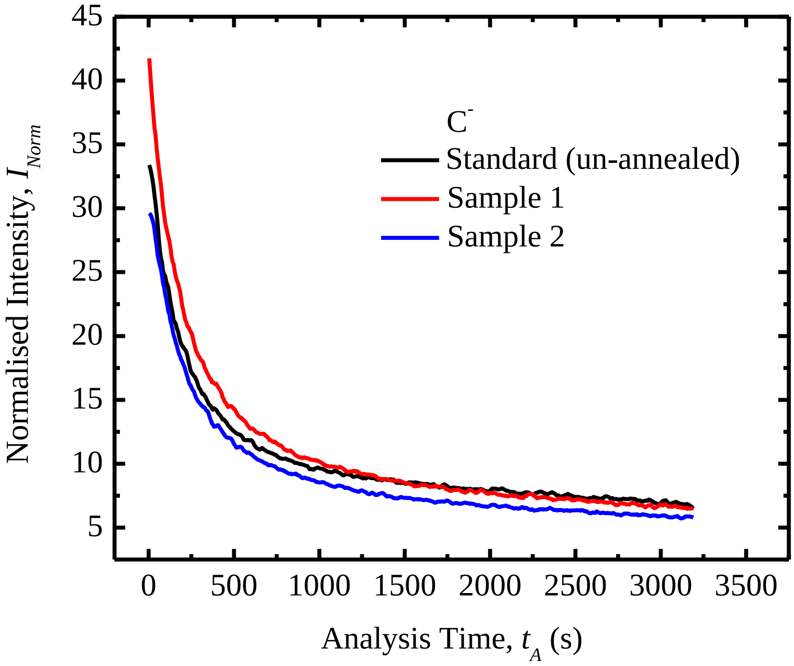

Figure 5.15: *C^- measured by TOF-SIMS on the respective surfaces of the samples annealed for a period of 90 days at a temperature of 1133 K.*

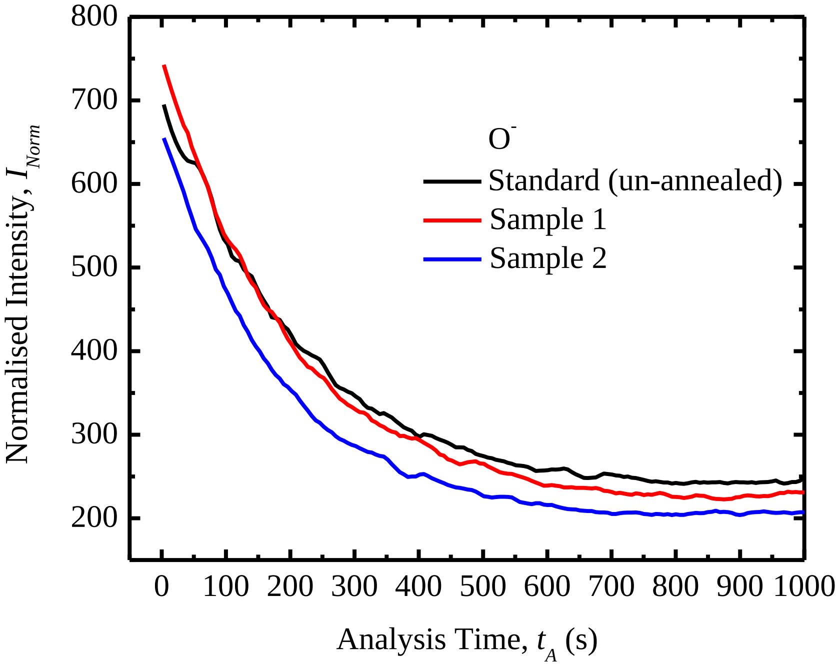

Figure 5.16: *Comparison of O^- between the different samples annealed for 90 days at a temperature of 1133 K, as measured by TOF-SIMS.*

Figure 5.14-5.16 indicates that the samples have not obtained any contaminants during annealing. For the ions H^- and C^-, the measured secondary ion intensities of the two annealed samples are comparable to that measured on the standard un-annealed sample. The standard sample was not stored in vacuum or an inert gas environment and consequently a small O layer had time to form on the surface as a result of native O adsorbing onto the Fe surface. If the annealing chamber had any O inside, the formation of an oxide layer is expected to be more prominent especially with the annealing temperatures and annealing times used. Thus the annealing system is capable of preparing samples of high purity, free from any contaminants such as O and C.

5.5. Summary

The chapter gave an in-depth description of the equipment used and the methods followed in order to prepare Fe samples doped with S and Cr respectively. This includes the custom in-house built S doping chamber for the preparation of Fe-S samples as well as the custom in-house built annealing system that allowed for the annealing of Fe samples at high temperatures for long time periods (90 days). AES and TOF-SIMS confirmed the successful operation of the S doping chamber and the effectiveness of the doping method. Data obtained by TOF-SIMS for the Fe samples after annealing confirmed the preparation of high purity Fe samples without the presence of surface contaminants. The samples prepared in this section were used in segregation studies of which the results are presented in chapters 6, 7 and 8.

5.6. References

[1]. P. E. Barnard, Experimental and computational study of S segregation in Fe, M.Sc Dissertation, Bloemfontein, 2012.
[2]. M.M. Montagono, J. Cabané, Surf. Sci. 285 (1993) L468.
[3]. Y. Niu, G.Y. Fu, P. Catello, F. Gesmundo, W.T. Wu, F. Viani, Corros. Sci. 39 (1997) 1811.
[4]. T. Rosenqvist, B.L. Dunicz, Jom-J. Min. Met. Mat. S. June (1952).
[5]. M.F. Pillis, L.V. Ramanathan, Mater. Res. 5 (2002) 349.
[6]. R.C. Weast, M.J. Astle, W.H. Beyer, (Eds.), Handbook of chemistry and physics, CRC Press, Inc., Boca Raton, Florida, 1983-1984.

[7]. J. du Plessis, Surface segregation, Sci-Tech Publications, Bloemfontein, South Africa. 1990.

[8]. R. Shimizu, Jpn. J. Appl. Phys. 22 (1983) 1631.

[9]. S. Tanuma, C.J. Powell, D.R. Penn, Surf. Interface Anal. 21 (1993) 165.

[10]. T.B. Massalski, H. Okamoto, P.R. Subramanian, L. Kacprzak, (Eds.), Binary alloy phase diagrams, ASM International. 1990.

[11]. T. Stephan, Planet. Space Sci. 49 (2001) 859.

Chapter 6

Dependence of the activation energy on the surface orientation in bcc Fe

6.1. Introduction

In this chapter the influence of the surface orientation on the activation energy of diffusion is investigated, by considering the segregation of Sulfur (S) in bcc Fe. In chapter 2 the diffusion rate, D, is given in terms of the migration energy, E_m, and the vacancy formation energy, E_{vac}. This expression is again included in this chapter for completeness, equation 6.1,

$$D = D_0 \left\{ \left[\exp\left(-\frac{E_m}{RT} \right) \right]_{P_m} + \left[\exp\left(-\frac{E_{vac}}{RT} \right) \right]_{P_{vac}} \right\} \ , \tag{6.1}$$

where the P_m and P_{vac} subscripts respectively refer to the probability of an atom migrating in the lattice and the probability of forming a vacancy. The activation energy of diffusion, Q, is described by equation 6.2 as the sum of the migration energy, E_m, and vacancy formation energy, E_{vac}

$$Q = E_m + E_{vac} \, . \tag{6.2}$$

Equation 6.2 indicates a direct relationship between the activation energy and the vacancy formation energy as well as between the migration energy and the activation energy. The focus of this chapter is to determine whether the activation energy of diffusion is dependent on the surface orientation in bcc Fe as a result of vacancies forming via the Schottky defect mechanism [1, 2]. The orientation dependence of the activation energy of diffusion was observed by Terblans [3, 4], who studied the formation of Schottky defects in the low-index orientations of both Cu and Al. Recently a Molecular Dynamic study was performed by Van Der Walt et. Al. [5] in order to investigate the formation of vacancies via the Schottky defect mechanism as a function of temperature in fcc metals (Al, Ni, Cu, Pd, Ag and Pt). Figure 6.1 provides a simplistic illustration of how a Schottky defect is formed: An atom (labelled 1) is removed from a lattice site, forming a vacancy, and this atom is then subsequently adsorbed onto the surface. This is a simplistic view on the Schottky defect mechanism providing only the initial and final crystal structures for the formation of a vacancy. In section 6.2.2 the formation of a Schottky defect is described in more detail, where it is considered as a multi-step process.

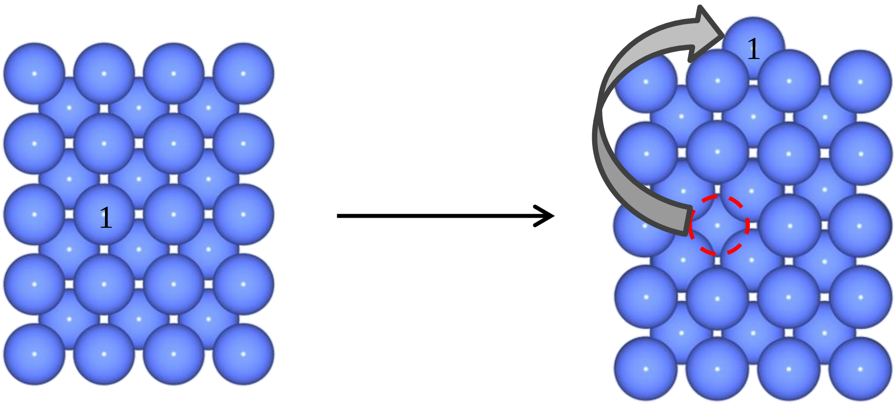

Figure 6.1. *Simplistic illustration of the Schottky defect mechanism by which vacancies are proposed to form in bcc Fe. An atom is removed from the lattice and subsequently adsorbed onto the surface. The newly formed vacancy is presented by the red dotted circle.*

Formation of vacancies in the low-index orientations of bcc Fe namely; Fe(100), Fe(110) and Fe(111) will be investigated by considering them to be of the Schottky type. The energy required to form a vacancy in the bulk for each of these orientation is calculated by utilising DFT modelling. Subsequent confirmation of the calculations is obtained by AES and TOF-SIMS segregation measurements of S segregating in bcc Fe. The calculations presented in sections 6.2.2 form part of previous work [6] conducted. However, the previous results were expanded and refined for greater accuracy in the present study.

6.2. Calculating the formation of vacancies.

6.2.1. Computational details

All calculations contained in this chapter were performed using DFT as implemented in the Quantum ESPRESSO code [7]. The code makes use of plane waves (PW) and pseudpotentials (PP) to obtain an effective potential to solve the Schrödinger-like Kohn–Sham equation [8] self-consistently. The effective potential was calculated within the generalised-gradient approximation (GGA) using the functional of Perdew and Wang (PW91) [9]. The electronic wave functions were expanded as linear combinations of plane waves, truncated to include only plane waves with kinetic energies below the energy cutoff, E_{cut}, of 381 eV. This and other parameters of bcc Fe were obtained by converging the total energy of a single bcc unit cell to $<2 \times 10^{-3}$ eV/atom with respect to each of the parameters. Core electrons were replaced by ultrasoft pseudopotentials (USPP) [10] in order to simulate the effect of electrons in the material. k-Space sampling was performed using a Monkhorst-Pack mesh [11] of dimension 8×8×8 for all unit cell (1×1×1) calculations and a mesh of dimension 3×3×3 for all calculations on the 3×3×3 bulk supercell. For the calculation of the surface structures, the size of the k-point mesh was reduced to 3×3×1, where the smallest dimension is in the direction of the surface. To take into account the continuous distribution of electrons across the Fermi level, a fictitious temperature, the smearing scheme of Methfessel and Paxton [12] with a smearing width of 0.54 eV was used. A fractional electron spin-up state of 0.4 was used for the starting magnetisation of the ferromagnetic Fe system which resulted in the ground state energy of the bcc unit cell. The calculated ground state properties of the bcc Fe (1×1×1) unit cell are summarised in table 6.1.

Table 6.1: *Ground state properties of bcc Fe, calculated using the GGA functional of Perdew and Wang (PW91).*

Parameter	This work	Experimental [13]	Theory (PW91) [14]
Lattice parameter, *a* (Å)	2.861	2.866	2.869
Bulk modulus, B_0 (GPa)	149.5	168.0	140.0
Magnetic moment, *B* (µB)	2.48	2.22	2.37

For all surface structures a vacuum spacing of 14.81 Å was used, which was obtained by determining the minimum distance required to prevent interaction between two Fe atoms in a rectangular cell of dimension 43.32 Å×10.58 Å. This vacuum spacing prevents the interaction of periodically repeated cells while effectively simulating the surface of the material. The vacuum spacing of 14.81 Å corresponds well with literature values which range from 10 to 14 Å [14 - 19]. All of the Fe surfaces used in the calculations consisted in total of 9 atomic layers along the depth axis of the crystal structure. Of these 4 atomic layers forms the surface of the crystal structure and the remaining 5 atomic layers forms the bulk of the crystal structure. The choice for using 9 atomic layers was based on literature information [14 - 19], where depending on the information required structures had layers ranging from 4 to17 atomic layers. For relaxation of the surface structures, the damped dynamics algorithm was used to remove any kinetic energy from the system and minimise the total force on the system. The equilibrium positions of the atoms were obtained by converging the total energy to $<2\times10^{-4}$ eV/atom and the total force to $<2\times10^{-2}$ eV/Å. The migration energy of diffusion was calculated by the CI-NEB algorithm [20] as implemented in the Quantum EPRESSO code. Images were optimised until the force perpendicular to the NEB path had value less than 0.05 eV/A. Elastic constants were allowed to relax in order to provide a high definition around the saddle point.

6.2.2. DFT results

Figure 6.1 gave an idea of what the formation of a Schottky defect entails, but this is a simplified description. The actual process is more complex, involving a number of steps and is considered as a multi-step process. Such a multi-step description closely reflects the behaviour of atoms in real systems. Figure 6.2 presents an illustration of the multi-step process for the formation of a Schottky defect, with the initial step being the diffusion of a surface atom to a position onto the Fe surface, forming an adatom. An atom from the second atomic layer, the subsurface layer, then fills this newly formed vacancy within the surface. This process of atoms from atomic layers beneath the vacated lattice site filling the newly formed vacancy will continue until a vacancy is located within the bulk of the material. Therefore, it can be considered that vacancies are formed in the surface layer and then subsequently diffuse into the bulk of the crystal.

Firstly, it should be taken into consideration that the surface constitutes a unique defect in the crystal. As a consequence the atoms within the surface region have less second and third nearest neighbouring atoms which contribute to long range interactions. Secondly, due to the relaxation of the surface, the energetics of these atoms undergo change due to either an increase or decrease in the bond length between neighbouring atoms. This is confirmed by the binding energies of the respective atoms from the surface layer up to the 5th atomic layer (Bulk) for Fe(100), presented in table 6.2. Thus, given enough thermal energy, atoms within the first atomic layer would have the highest probability of vacating their lattice positions. With the temperature of the system below its evaporation temperature, atoms have allowed positions only on the surface where it occupies an adatom site.

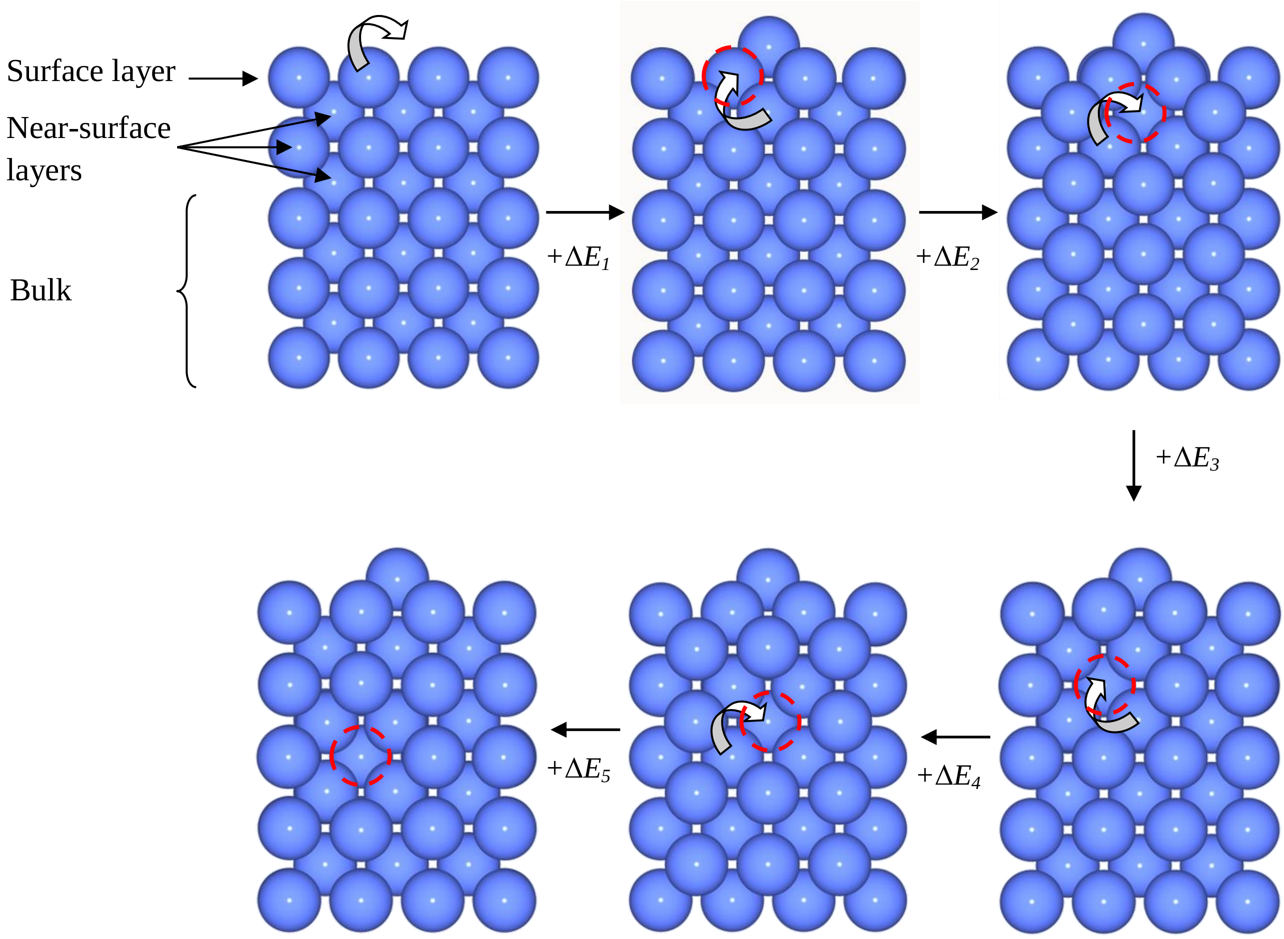

Figure 6.2. *Illustration of the formation of a Schottky defect in Fe(100). Part of the crystal was cut away in order to provide a clear view of the atoms involved in forming a vacancy (red dotted circle) in the surface and near surface layers of Fe(100).*

Table 6.2: *Binding energies of Fe in the first 5 atomic layers of bcc Fe(100)*

Atomic layer	**E_B(eV)**
1	-3.50
2	-4.64
3	-4.85
4	-4.99
5 (bulk)	-4.86

Mathematically figure 6.2 is described by equation 6.3

$$E_{vac} = \Delta E_1 + \Delta E_2 + \cdots + \Delta E_5 , \tag{6.3}$$

where the ΔE_i terms are the differences in binding energies between the respective atomic layers, i. Equation 6.3 corresponds to figure 6.2, where only the first 4 atomic layers of the respective surface orientations were considered to relax. Summation of all the ΔE_i terms results in the vacancy formation energy of a bulk atom. This is illustrated for the Fe(100) surface orientation, where each of the ΔE_i terms were calculated with results presented in table 6.3.

Table 6.3: *Binding energy difference between the different atomic layers of the Fe(100) surface orientation .*

Atomic layer	**ΔE_i (eV)**
1→On surface	1.28
2→1	1.14
3→2	0.21
4→3	0.14
5→4	-0.14
Bulk	0

Table 6.3 shows that an energy difference of 1.28 eV exists between the first atomic layer and the adatom layer. The value between the second and first atomic layer is slightly smaller and decreases to 0 in the bulk of the crystal. An exception is observed for the ΔE_i term of atomic layer 5 to 4 having a negative value. This is caused by a stronger binding energy of Fe in the 4th atomic layer as opposed to the 5th atomic layer of the Fe lattice as a result of the surface relaxing, see chapter 7 for a description of surface relaxation. If all the values presented in table 6.3 are summed, a value of 2.64 eV is obtained, which is the value reported in table 6.4 for the bulk vacancy formation energy in bcc Fe(100).

To calculate the vacancy formation energies of the different surface orientations, the Schottky defect mechanism can be considered as the removal of a bulk atom which is then placed onto the surface of the crystal structure. This provides a description of the thermodynamic parameter, E_{vac}, in terms of the initial, $E_{initial}$, and final states, E_{final}, of the crystal, equation 6.4

$$E_{vac} = E_{final} - E_{initial}. \tag{6.4}$$

Equivalently, the Schottky defect mechanism can be considered as the amount of energy removed from the system when an atom is removed from the bulk of the crystal and the energy gained by the system when the atom is adsorbed onto the surface of the crystal. In terms of this description the vacancy formation energy is the energy difference between an atom bound in the bulk of the material as opposed to an atom bound onto the surface of the material as expressed by equation 6.5 [3, 4].

$$E_{vac} = E_{B(Surf)} - E_{B(Bulk)} \tag{6.5}$$

Equation 6.5, provides the answer to the orientation dependence of the Schottky defect mechanism. Different crystal orientations will have different values for the binding energy of the surface adatom. This is due to the number of available atoms with which the adatom can bind and the strength of these bonds. To obtain the surface binding energy of a Fe adatom on the respective surfaces, the equilibrium position of a Fe adatom were determined for each orientation. The most stable position for an atom placed onto the Fe(100) surface was found to be the four fold hollow site while and adatom on the Fe(111) surface was found to bind most favourably in the three fold hollow site. For the Fe(110) crystal orientation it was found that the surface adatom binds most favourably in the long bridge site. These stable positions of the atoms on each of the surfaces are shown in figure 6.3.

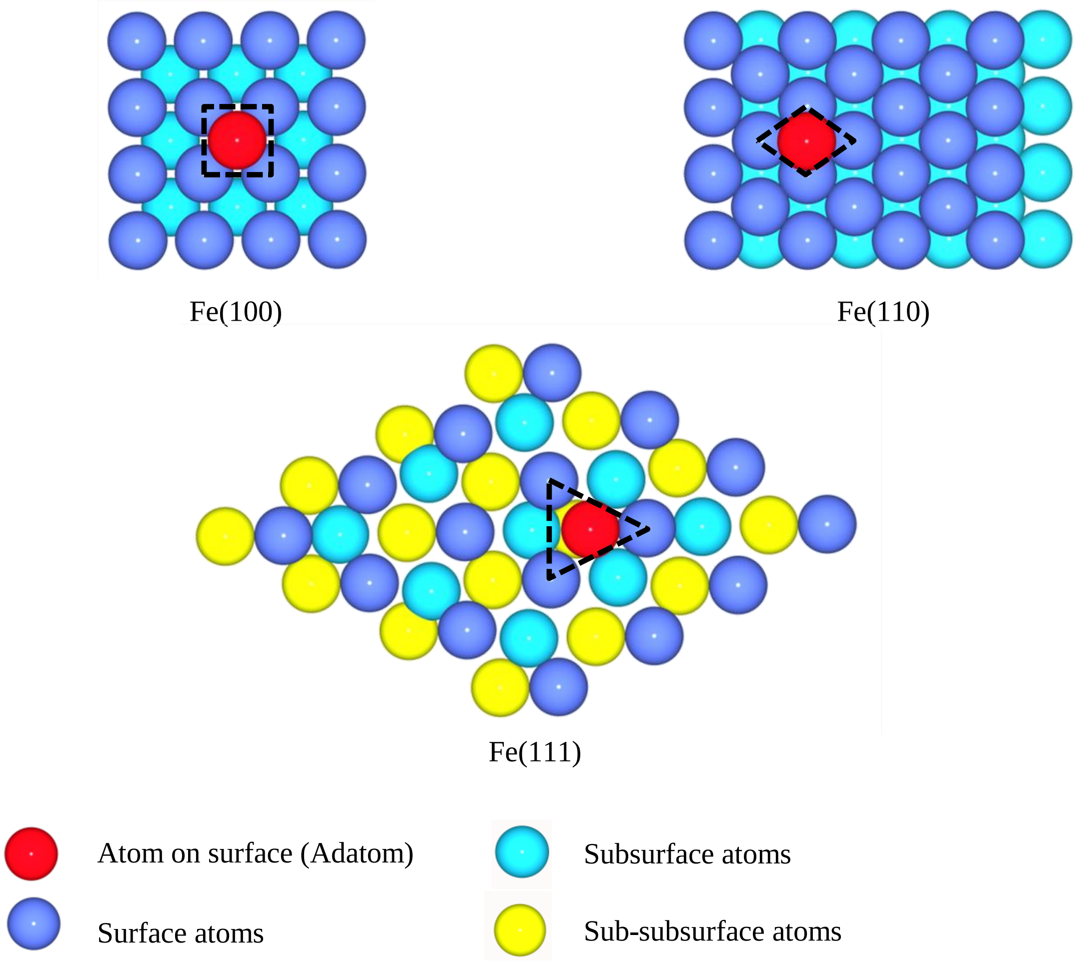

Figure 6.3. *Illustration of the surface adatom on each of the low-index orientations of bcc Fe. For Fe(100) and Fe(111) the equilibrium positions are the four and three fold hollow sites respectively while for Fe(110) surface the most stable position is the long bridge site.*

The surface binding energy of a Fe adatom in the stable position on each of the respective surfaces is given in table 6.4.

Table 6.4: *Surface binding energy of a Fe adatom on each of the three low-index orientations of bcc Fe*

Crystal orientation	**Surface binding energy, $E_{B(Surf)}$ (eV)**
Fe(110)	-2.11
Fe(100)	-2.22
Fe(111)	-3.03

The binding energy of a bulk Fe atom is independent of the surface orientation under consideration and was calculated as -4.86 eV using equation 6.6

$$E_{bind} = \frac{E_{Total} - \left(N \times E_{Fe}\right)}{N}, \qquad (6.6)$$

where E_{Total} is the total energy of a bulk Fe structure (3×3×3 supercell) and E_{Fe} is the energy of a single Fe atom calculated in a cubic cell of length 14.81 Å. Vacancy formation energies calculated using equation 6.4, for each of the three low-index orientations of bcc Fe, are tabulated in table 6.5.

Table 6.5. *Vacancy formation energy values calculated for the three low-index surfaces of bcc Fe, by considering the formation of vacancies to occur via the Schottky defect mechanism.*

Crystal orientation	**Calculated vacancy formation energy, E_{vac} (eV)**
Fe(110)	2.75
Fe(100)	2.64
Fe(111)	1.83

The different values of the crystal orientations in table 6.5 indicate the dependence of the vacancy formation energy on the surface orientation of the crystal structure under study. Arranged from highest to lowest vacancy formation energy, the surface orientations can be arranged as: Fe(110)>Fe(100)>Fe(111). According to equation 6.2, the values in table 6.5 predict that the activation energy of diffusion is therefore dependent on the surface orientation under consideration. As a consequence, the rate at which S atoms segregate in Fe will be dependent on the surface orientation of the host material in which they segregate, as described by equation 6.1.

The CI-NEB algorithm described in chapter 3, section 3.5, was utilised to obtain the minimum energy path and thus the migration energy for S diffusing in the bulk of the bcc Fe crystal. This value is independent of the surface orientation and is the same for all surface orientations considered. To obtain a well-defined path, 12 images were used in the calculation. Also a variable elastic constant was used to allow for a high resolution around the saddle point. Figure 6.4 presents the migration energy barrier for S migrating in the bulk of bcc Fe.

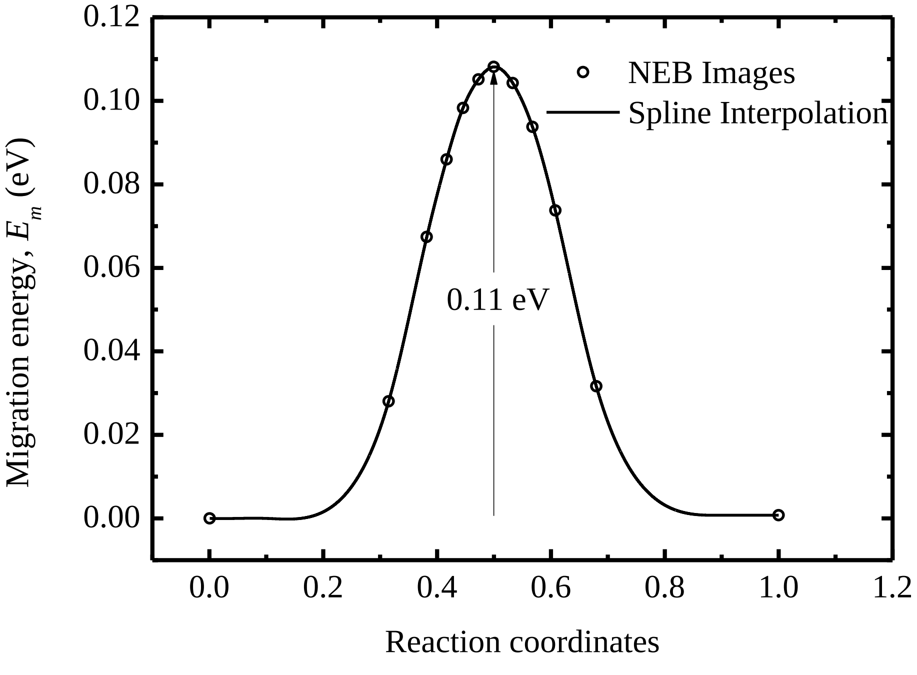

Figure 6.4: *Migration energy barrier of S in bulk bcc Fe with a height of 0.11 eV.*

Summation of each of the vacancy formation energies for the respective orientations in table 6.5, with the migration energy barrier of 0.11 eV, results in the activation energy of diffusion for the respective surface orientations, table 6.6.

Table 6.6: *Activation energy of diffusion values calculated for the three low-index orientations of bcc Fe.*

Crystal orientation	Calculated activation energy, E_{vac} (eV)	Calculated activation energy, E_{vac} (kJ/mol)
Fe(110)	2.86	276
Fe(100)	2.75	265
Fe(111)	1.94	187

The activation energies in table 6.6 indicate the expected variation of the activation energy of diffusion on the surface orientation. A macroscopic description of the surface enrichment and thus the segregation rate is found by simulating the obtained results using Fick`s model described in chapter 2, section 2.2 and provided here by equation 6.7.

$$\frac{1}{2}\beta^2 = \frac{2}{\pi}\left(\frac{D_0}{\alpha d^2}\right)\int_{T_0}^{T_{\text{final}}} \exp\left(\frac{-Q}{RT}\right) dT \qquad (6.7)$$

were β is the surface enrichment, described in terms of the surface, C_ϕ, and bulk, C_B, concentrations, equation 6.8

$$\beta = \frac{C_\phi - C_B}{C_B}\,. \qquad (6.8)$$

Equation 6.7 performs an integration of the diffusion probability over the temperature range, T_{final} -T_0, and effectively performs a summation of the S atoms segregated onto the Fe surface. It provides an accurate description of the segregation kinetics but fails to describe the equilibrium of segregation. The latter topic falls outside the scope of this chapter, with the kinetics of segregation being the subject of interest here. The heating rate of 0.1 K/s used in the simulation is denoted by the symbol α and the inter-lattice spacing of the respective surfaces by the symbol d. A pre-exponential factor value of 0.16 m^2/s was taken from the work of Reichl et. al. [21]. Figure 6.5 presents the simulated segregation profiles of the kinetic region for S segregating in Fe(100), Fe(110) and Fe(111) respectively.

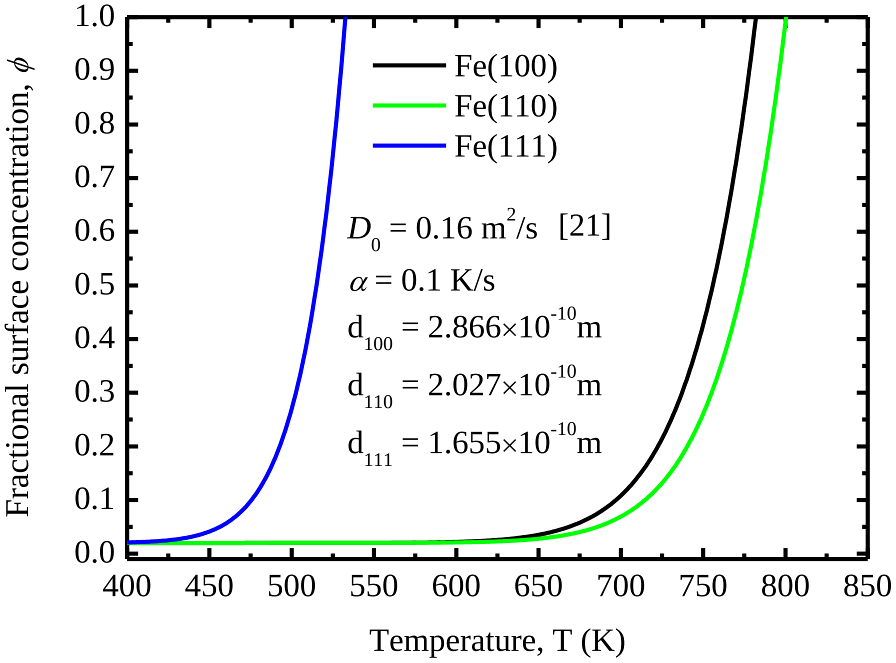

Figure 6.5: *Simulated segregation profiles of the kinetic part of S segregating in the low-index orientations of bcc Fe namely: Fe(100), Fe(110) and Fe(111).*

Figure 6.5 shows that a distinct difference can be expected between the segregation rates of different Fe orientations. This will be investigated experimentally in the next section, using two different experimental techniques.

6.3. Confirming the Schottky defect mechanism by experiments

The previous sections presented calculations for the formation of vacancies via the Schottky defect mechanism in the low-index orientations of bcc Fe. Results from these calculations predicted that the activation energy of diffusion is dependent on the surface orientation under study. This dependency on the surface orientation is caused by the formation of vacancies via the Schottky defect mechanism. According to the calculations, there should be a rate difference for S segregating in different orientated crystals. In order to validate the calculations the next section studies the segregation of S in different orientated Fe crystals, which all form part of the same polycrystalline Fe sample, using two different experimental techniques, namely: AES and TOF-SIMS. Thus the same grains studied by AES are also studied by TOF-SIMS in order to make a direct comparison between the segregation results obtained by the two techniques.

6.3.1. Auger Electron Spectroscopy (AES)

Surface segregation of S was monitored on three separate grains of a polycrystalline Fe sample using AES. The electron beam was positioned onto one of the grains to analyse for a specific element. Once this was completed, the electron beam was placed onto the next grain, to analyse for the same element as for the first grain. This process was repeated for all 3 grains until all the elements selected were analysed. During this time the temperature was allowed to increase and thus it can be considered that the segregation of S from the three different grains was monitored simultaneously. The experimental settings used for analysis of the samples is covered in chapter 4, section 4.3.4. Figure 6.6, provides a Secondary Electron Image of the polycrystalline Fe sample surface, where the three grains are numbered 1-3. An additional grain, numbered 4, was analysed by TOF-SIMS.

Due to shifting of the sample during heating, the beam scans across and area of the sample. Therefore, the additional grain, grain 4, was unsuitable for AES analysis since the segregation of S from the grain boundaries are likely to be detected from such a small grain. During analysis it was ensured that the beam remained a minimum of 5 µm away from the grain boundaries to prevent detection of grain boundary segregation. In order for the grains analysed to be comparable, they have to be located next to one another. This is required to minimise artefacts in the measured intensities caused by a variation in the z-distance, the distance from the sample to the Cylindrical Mirror Analyser (CMA). If the beam has to scan two areas which are far removed from one another, the measured intensities are expected to be different as a result of the exposure to the analyser view. Thus, the measurements have two limitations, the size of the grains that can be measured and the relative distance between the different grains analysed. As a result of these limitations, only grains 1-3 were suitable for AES analysis.

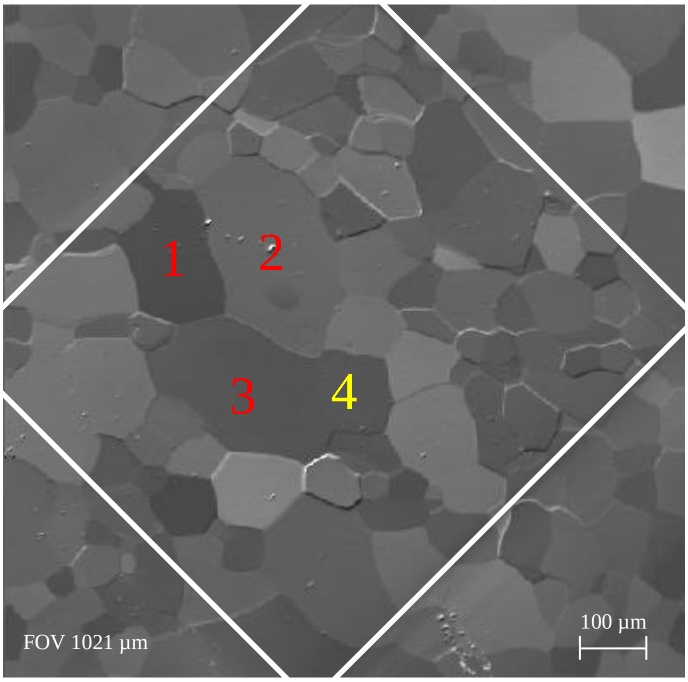

Figure 6.6: *Secondary electron image of the three grains selected for AES and TOF-SIMS segregation measurements. The grain numbered 4 was an additional grain analysed by TOF-SIMS. The area (indicated by white lines) sputtered by the Cs gun during TOF-SIMS analysis provided a clear marker for the analysed area.*

The segregation profiles measured on the three grains are presented in figure 6.7

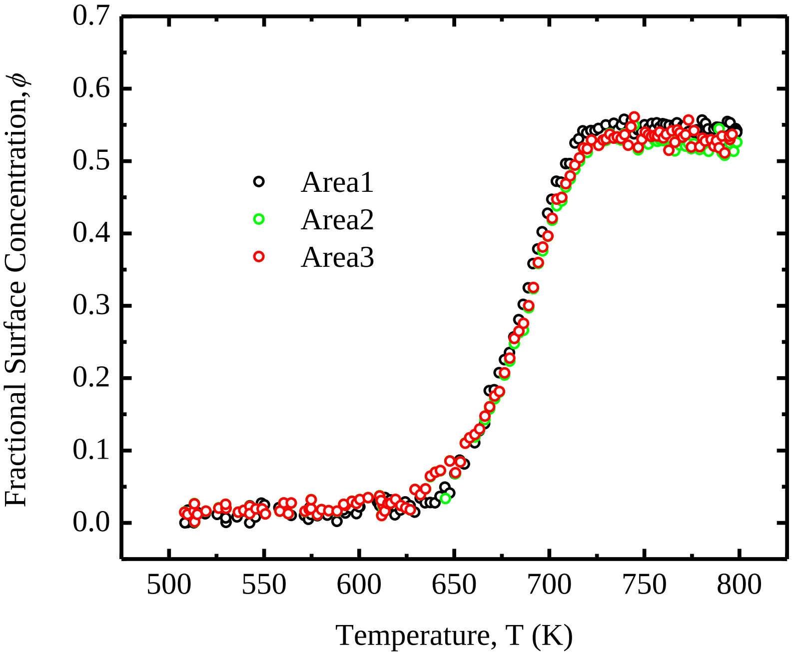

Figure 6.7: *Linear programed heating segregation profile of S from three different grains of a polycrystalline Fe sample heating at a rate of 0.005K/s.*

Apart from minor deviation between the segregation profiles presented in figure 6.7, there is no definite variation. This indicates that the measured grains all have the same crystal orientations and therefore the same vacancy formation energy and activation energy of diffusion. Next, TOF-SIMS was utilised to study the surface segregation of S in the polycrystalline Fe sample.

6.3.2. Time-Of-Flight Secondary Ion Mass Spectrometry (TOF-SIMS)

TOF-SIMS was used to study the segregation of S in four different grains of the polycrystalline Fe sample, shown in figure 6.6. Results were obtained using the following settings: TOF-SIMS analysis was performed in spectroscopy mode with a positive extractor current (negative mode). Bi^+ was used as the primary ion beam operated at 30 kV with a target current of 1 pA. To ensure accurate analysis of the samples the mass spectra was calibrated to the following mass peaks: H^-, C^-, OH^-, F^-, Si^-, P^-, S^-, O_2^-, Cl^-, Fe^- and S_2^-. A mass resolution of 8900 was obtained for S on the clean Fe surface. This value changed slightly as the surface concentration of S increased, with the mass resolution always exceeding a value of 6300. These values are above the minimum criteria of 1800, which is required to distinguish S^- from the O_2^- peak according to the work of Stephens [22]. The analysis was done by analysing an area of 500×500 µm at a scanning resolution of 256×256 pixels. The procedure for segregation studies is described in chapter 4, section 4.4.4.

Since the sample shifted during analysis, the data was analysed afterwards to correct for this shift. A circle of diameter 60 µm was selected on each grain for data analysis, figure 6.8. This area was sufficient to ensure a high intensity of secondary ions while at the same time avoiding the detection of grain boundary segregation. Figure 6.8 presents a TOF-SIMS image of the analysed area identifying the areas analysed on the different grains. The segregation profiles of S from the 4 different grains are presented in figure 6.9.

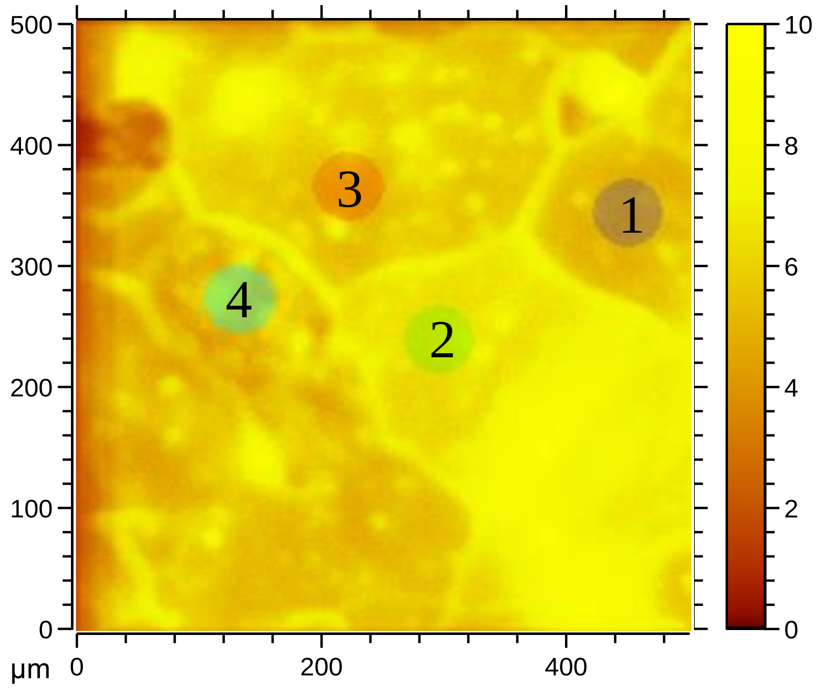

Figure 6.8: *TOF-SIMS image of S$^-$ on the Fe$^-$ surface with the four grains analysed numbered 1-4. The analysis areas, with a diameter of 60 µm, on each of the grains are identified by the coloured circles.*

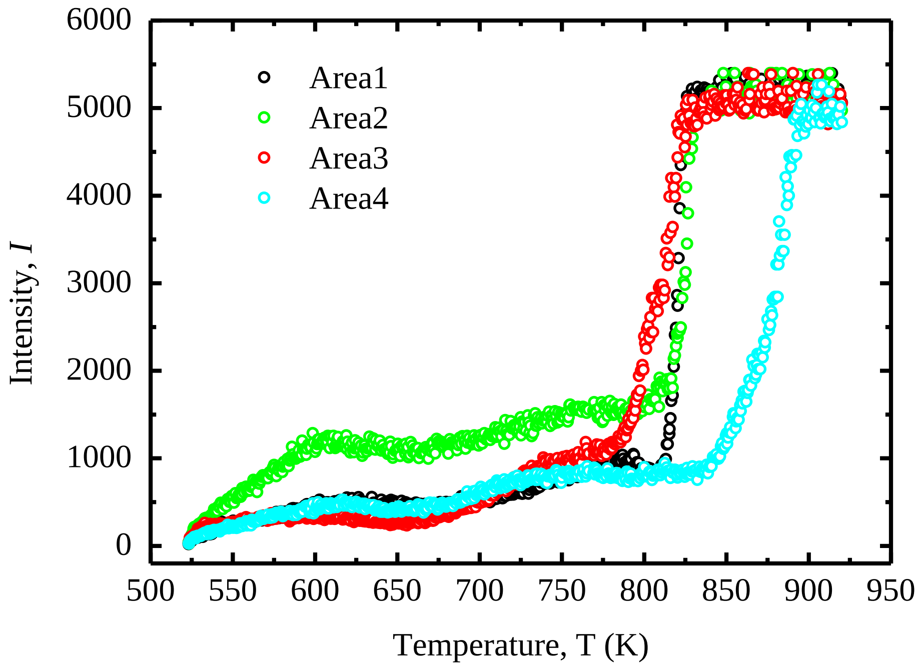

Figure 6.9: *Segregation profiles of S$^-$ from four different grain orientations of a polycrystalline Fe sample.*

Grains 1 to 3 exhibit the same segregation rate of S, which is in agreement with the results obtained by AES, figure 6.7. The rate of S segregation from grain 4 is distinctly different from the other grains measured, with a shift towards the higher temperature scale. This corresponds to grain 4 having a higher activation energy as that of grains 1 to 3. To obtain the grain orientations in the sample, XRD analysis of the sample was performed. To avoid contributions from grains outside of the analysed area of the crystal, the analysed area was shielded off from the rest of the sample. This was achieved by using a double layer of carbon tape to carefully isolate the analysed area from the remainder of the sample. Cs sputtering on an area of 1000 × 1000 mm during surface segregation studies performed by TOF-SIMS provided a definite identification of the analysed area (see figure 6.6). The XRD results of the analysed area are presented in figure 6.10. The details of the analysis, including the settings used are provided in chapter 4, section 4.2.2.

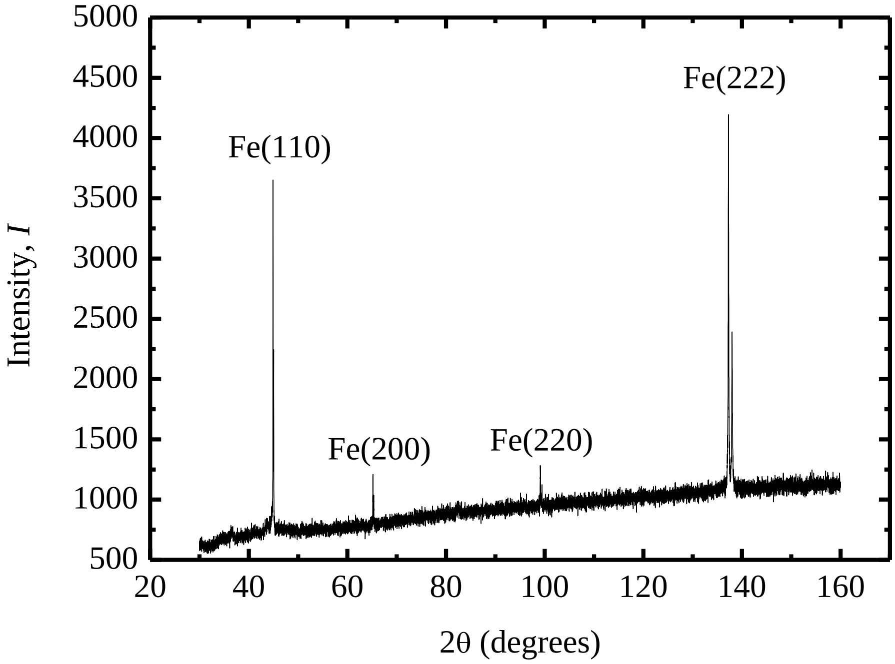

Figure 6.10: *XRD spectra of the area analysed by AES and TOF-SIMS. The presence of the three low-index orientations of bcc Fe can be identified as the only crystal orientations in the analysed area.*

Figure 6.10 shows that only the low-index orientations of Fe, namely Fe(100), Fe(110) and Fe(111) are present in the area analysed by AES and TOF-SIMS. Diffraction from the Fe(220) orientation is caused by diffraction from the Fe(110) crystal plane and similarly diffraction from the Fe(200) and Fe(222) orientations is due to the Fe(100) and Fe(111) planes respectively. This indicates that the segregation profiles presented in figures 6.7 and 6.9 could only be as a result of S segregating from these three low-index orientations. Grains 1-3, analysed by TOF-SIMS and AES have the lowest activation energy of diffusion and could therefore be assigned to the Fe(111) orientation (table 6.6). Segregation measured on the fourth grain, is shifted towards the higher temperature scale which indicate a higher activation energy of diffusion. This segregation profile could be the result of segregation from either the Fe(110) or the Fe(100) crystal orientations. Further analysis is thus required to obtain the orientation of grain 4. Nevertheless, comparing figure 6.9 to figure 6.5, a striking resemblance is observed between the simulated segregation kinetics and the experimentally observed segregation kinetics of S. In figure 6.5 a large variation is observed between the segregation profile of the Fe111 and the Fe100 orientation as well as between the Fe111 and the Fe110 orientations. Figure 6.9 confirms the separation in the segregation profiles between the Fe111 and the Fe100 or Fe110 orientation as a result of the activation energy variation between different orientations. In this chapter the influence of the pre-exponential factor has been neglected and is discussed in the next chapter, chapter 7. The results presented here, provides evidence for the formation of vacancies in bcc Fe to occur via the Schottky defect mechanism. A result of this mechanism is the orientation dependence of the vacancy formation energy and therefore the activation energy of diffusion. Furthermore, the segregation rate of S is observed to depend on the surface orientation as a consequence of the activation energy dependence on the surface orientation.

6.4. Summary

The formation of vacancies in the low-index orientations of bcc Fe were shown to be the result of a Schottky defect forming in the lattice. This mechanism is described in detail, with the initial step being the diffusion of a surface atom onto the surface where it forms an adatom. The binding energy of atoms in the surface layer is only -3.50 eV compared to the binding energy of a bulk atom which is -4.86 eV. Consequently, surface atoms can diffuse with relative ease to occupy a lattice position on the surface in an adatom position. Since different surface orientations have different equilibrium positions for an adatom, they will each bind with a different energy onto the respective surface orientations. This was shown to result in an orientation dependence of the vacancy formation energy and consequently also on the activation energy of diffusion. Values for the activation energy of diffusion for the Fe(110), Fe(100) and Fe(111) orientations were calculated as 2.86 eV, 2.75 eV and 1.94 eV respectively. This variation in activation energies was shown to cause a variation in the kinetics of S segregating to each of the low-index surfaces of Fe. AES and TOF segregation results of S segregating to the surface of different grains in a polycrystalline Fe sample confirmed this variation in segregation kinetics. The results presented provides evidence for the formation of vacancies to occur via the Schottky defect mechanism which results in a dependence of the activation energy of diffusion on the surface orientation of the crystal under study.

6.5. References

[1]. M.A. Omar, Elementary solid-State physics: Principles and applications, Addison-Wesley publishing company, Philippines, 1975.

[2]. N.W. Ashcroft, N. D. Mermin, Solid-State Physics, Saunders College, USA; Philadelphia, 1976.

[3]. J. J. Terblans, Surf. Interface Anal. 33 (2002) 767.

[4]. J. J. Terblans, Surf. Interface Anal. 35 (2003) 548.

[5]. C. van der Walt, J. J. Terblans, H.C. Swart, Comp. Mater. Sci. 83 (2013) 70.

[6]. P. E. Barnard, Experimental and computational study of S segregation in Fe, M.Sc Dissertation, Bloemfontein, 2012.

[7]. P. Giannozzi et. al., J. Phys. Condens. Matter 21 (2009) 395502.

[8]. W. Kohn, L.J. Sham, Phys. Rev. B 140 (1965) 1133.

[9]. J.P. Perdew and Y. Wang, Phys. Rev. B 45 (1992) 13244.

[10]. D. Vanderbilt, Phys. Rev. B 41 (1990) 7892.

[11]. H.J. Monkhorst, J.D. Pack, Phys. Rev. B 13 (1976) 5188.

[12]. M. Methfessel, A.T. Paxton, Phys. Rev. B 40 (1989) 3616.

[13]. H.C. Herper, E. Hoffman, P. Entel, Phys. Rev. B 60 (1999) 3839.

[14]. A. Hung, I. Yarovsky, J. Muscat, S. Russo, I. Snook, R.O. Watts, Surf. Sci. 501 (2002) 261.

[15]. N. Todorova, M.J.S. Spencer, I. Yarovsky, Surf. Sci. 601 (2007) 665.

[16]. P. Błoński, A. Kiejna, Vacuum 74 (2004) 179.

[17]. M.J. Spencer, A. Hung, I.K. Snook, I. Yarovsky, Surf. Sci. 513 (2002) 389.

[18]. P. Błoński, A. Kiejna, Surf. Sci. 601 (2007) 123.

[19]. S.G. Nelson, M.J.S. Spencer, I.K. Snook, I. Yarovsky, Surf. Sci. 590 (2005) 63.

[20]. G. Henkelman, B.P. Uberuaga, H. Jónsson, J. Chem. Phys. 113 (2000) 9901.

[21]. B.M. Reichl, M.M. Eisl, T. Weis, H. Hutter, H. Störi, Fresen. J. Anal. Chem. 353, (1995) 762.

[22]. T. Stephan, Planetary and Space Science. 49 (2001) 859.

Chapter 7

Influence of the “surface effect” on the segregation of S in Fe(100) and Fe(111).

7.1. Introduction

In the previous chapter the influence of the surface orientation on the activation energy of diffusion was investigated, with results revealing a dependence of the activation energy of diffusion on the surface orientation under study. In this chapter the influence of the crystals microscopic structure on the segregation parameters is investigated by considering the presence of a “*surface effect*”. This effect entails the layer dependence of the segregation parameters (segregation energy, activation energy, interaction parameter, and pre-exponential factor) in the surface and near surface layers, the first 4 atomic layers of the crystal.

Firstly, by considering the surface relaxation data of the Fe(100) and Fe(111) surfaces presented in table 7.1, a variation is observed in the inter-lattice spacing for the surface and the near surface layers. Secondly, the surface should be viewed as a unique defect in the lattice caused by the abrupt termination of the lattice periodicity and would therefore have a reduction in the number of next nearest neighbouring atoms for the surface and near surface layers. Consequently, atoms within the surface and near surface layers experience different forces on the atoms which influence the binding energies of the atoms and therefore the segregation parameters in these atomic layers. To the authors best knowledge, the layer dependency of all the segregation parameters referred here to as the “surface effect” has not been researched in literature and this chapter serves as the first study carried out to investigate the effect of the surface on all of the segregation parameters. Literature reported results for the layer dependency of the segregation energy [1, 2], but no study could be obtained where the influence of all the segregation parameters were investigated, as performed in this study.

Table 7.1: *Surface relaxation data for the Fe(100) and Fe(111) orientations, showing the contraction and expansion of the surface and near surface layers as a percentage value, Δ_{ij}, between subscripted atomic layers. The relaxation values were determined from the inter-lattice spacing values, d, for the respective atomic layers.*

Fe(100)	**Δ_{12} (%)**	**Δ_{23} (%)**	**Δ_{34} (%)**	**Δ_{45} (%)**	
	-2.60	+2.96	+1.51	+1.20	Theory [3]
	-3.06	+2.83	+1.93	-	Theory [4]
	-1.89	+2.59	+0.21	-0.56	Theory [5]
	-3.60	+2.30	+0.40	-0.40	Theory [6]
	-5±2	-5±2	-	-	Exp. (LEED) [7]
	-1.40±3	-	-	-	Exp. (LEED) [8]
Fe(111)	**Δ_{12} (%)**	**Δ_{23} (%)**	**Δ_{34} (%)**	**Δ_{45} (%)**	
	-5.12	-18.33	+12.48	+3.32	Theory [3]
	-6.47	-16.9	+12.4	-	Theory [4]
	-13.3	-3.60	+13.3	-1.20	Theory [5]
	-17.7	-8.40	+11.0	-1.00	Theory [6]
	+16.90±3	-9.80±3	+4.20±3.60	-2.20±3.60	Exp. (LEED) [9]

Various studies have been performed to investigate segregation and diffusion in a range of different systems, but little is known about the influence of the surface on the thermodynamic and kinetic parameters of segregation. These parameters include the interaction parameter, Ω, the segregation parameter, ΔG, the migration energy, E_m, the vacancy formation energy, E_{vac}, and consequently also the activation energy of diffusion, Q. It is usually considered that these parameters are independent of the atomic layer in which the segregating atom resides. However, due to the reduction in the number of nearest neighbour atoms in the surface region as well as the variation in the inter-lattice spacing values, this study predicts a layer dependency on the segregation parameters from the surface layer, atomic layer 1, up to atomic layer 4. Atomic layer 1 is referred to as the surface layer and atomic layers 2 to 4 as the near surface layers in the remainder of this study.

Yuan et. al. [1] have conducted a computational study on the segregation for each of the 3d metals Sc, Ti, Mn, Ni, Zn, V, Cr and Co as impurities in bcc Fe, with results revealing a layer dependency of the segregation energy. This dependence, although distinct for each element, was shown to extend to the 4th atomic layer of Fe(100). Yuan et. al. [1] found that the segregation of especially Cr in Fe(100) was determined by the energy barrier of the second atomic layer and not the first atomic layer as expected. These results were explained by looking at the magnetism of each of the 3d metals in the Fe matrix. The unexpected behaviour of Cr was explained by its antiferromagnetic properties. Gupta et al. [2] obtained results which resembled the findings of Yuan et. al. [1], which shows a layer dependence for the segregation energy of Cr in Fe(100).

The presence of a “surface effect” was investigated for the Fe(100) surface orientation as S segregates to the surface in a combined Density Functional Theory (DFT), Modified Darken Model (MDM) and Auger Electron Spectroscopy (AES) study. Calculations performed by DFT delivered values for each of the segregation parameters. These parameters were used in the MDM simulations to obtain a fit onto the experimental (AES) segregation data of S in Fe(100). The model effectively describes the experimental data and thus also the presence of the “surface effect”

Furthermore, this concept of layer dependency is also investigated for the Fe(111) surface orientation by fitting of the MDM onto AES data. The use of Fick`s model and the Bragg-Williams model, described in chapter 2, were used to extract the segregation parameters for S segregating in Fe(111). These models provided initial values for the MDM to be fitted to the experimental data. The MDM adapted to describe the “surface effect” is compared to the conventional method whereby the MDM is applied. A distinct difference is observed as a result of the “surface effect”. The findings of this chapter show the importance of taking the “surface effect” into account when studying surface segregation. It is suggested to play an important role in the study of nano-structured materials and catalysis, where microscopic variations in the surface can have a significant influence on the properties of the material under consideration.

7.2. Theory

The computational details for the Fe-S system was described in chapter 6, section 6.2.1. Theoretical concepts and equations for the study of the "surface effect" in Fe are described in this section. It is well known that S diffuses in bcc Fe via a vacancy-mediated mechanism, that is S diffuses from one substitutional lattice site to a nearest neighbour vacancy site [10]. According to the findings of chapter 6, the vacancies are formed via the Schottky defect mechanism. In chapter 6, equation 6.4 was used to calculate the vacancy formation energy. This expression is provided by equation 7.1 for the sake of completeness.

$$E_{vac}^{j} = E_{final}^{j} - E_{initial} \tag{7.1}$$

where $E_{initial}$ and E_{final}^{j} is the binding energies of the initial state (perfect lattice) and the final state (lattice containing the Schottky defect) for each of the atomic layers, *j*. Equation 7.2, similar to equation 6.5 presented in chapter 6, can be used to obtain the binding energy of an atom in the surface and each of the near surface layers, $E_B^{(j)}$,

$$E_B^{(j)} = E_B^{(Surf)} - E_{vac}^{j} \ . \tag{7.2}$$

$E_B^{(Surf)}$ describes the binding energy of a surface atom and E_{vac}^{j} describes the vacancy formation energy in a specific atomic layer. Equations 7.1 and 7.2 were respectively used to calculate the vacancy formation energies and the binding energies of an Fe atom in each of the Fe(100) surface and near surface layers.

The segregation of an impurity atom is considered as the migration of the impurity atom from the bulk of the material towards the surface layer, atomic layer 1. In this work this definition is expanded to include also the near surface layers (2-4) and the segregation energy is defined in this work as the migration of an impurity atom from the bulk to the surface layer or one of the near surface layers. Therefore, the segregation energy is calculated as the energy difference between an atom bound in the bulk material and an atom bound in the surface or one of the near surface layers [1, 11]. Equation 7.3, was used to obtain the segregation energy of S towards the first 4 atomic layers of Fe(100) as well as to the first true bulk layer, atomic layer 5

$$\Delta G^{(j)} = E_{B(imp)}^{(j)} - E_{B(imp)}^{bulk} = E_{final}^{imp} - E_{initial}^{imp} \ . \tag{7.3}$$

To investigate the interaction of Fe and S as a function of the atomic layer, the interaction parameter, as defined by the regular solution model, was calculated by equation 7.4 [12, 13]

$$\Omega_{12}^{j} = Z^{j}\left[\varepsilon_{12}^{j} - \frac{1}{2}\left(\varepsilon_{11} + \varepsilon_{22}\right)\right]. \tag{7.4}$$

The symbol Z refers to the coordination number or number of nearest neighbouring atoms of a S atom and ε to the interaction energy between subscripted species. For the pure components 1 and 2, the interaction energies ε_{11} and ε_{22} are considered to be that of the respective bulk structures.

The segregation parameters, Q, ΔG and Ω obtained from DFT calculations were used in the MDM to obtain a fit onto the experimental data of S segregation in Fe(100). The MDM consists of a set of coupled differential rate equations which is solved to obtain the segregation profile of S in bcc Fe(100). The model effectively describes both the kinetic and equilibrium regions of the segregation profile and has been used with great success to describe surface segregation in alloys [14, 15]. The MDM was described in detail in chapter 3, and only the final result is presented here by equation 7.5 [12].

$$\frac{\partial X_1^{(\phi)}}{\partial t} = \left[\frac{M_1^{(2\to\phi)} X_1^{(2)}}{d^{2(\phi)}} \Delta\mu_1^{(2\to\phi)}\right] \qquad [\phi = 1],$$

$$\frac{\partial X_1^{(2)}}{\partial t} = \left[\frac{M_1^{(3\to2)} X_1^{(3)}}{d^{2(2)}} \Delta\mu_1^{(3\to2)} - \frac{M_1^{(2\to\phi)} X_1^{(2)}}{d^{2(2)}} \Delta\mu_1^{(2\to\phi)}\right],$$

$$\vdots$$

$$\frac{\partial X_1^{(j)}}{\partial t} = \left[\frac{M_1^{(j+1\to j)} X_1^{(j+1)}}{d^{2(j)}} \Delta\mu_1^{(j+1\to j)} - \frac{M_1^{(j\to j-1)} X_1^{(j)}}{d^{2(j)}} \Delta\mu_1^{(j\to j-1)}\right], \tag{7.5}$$

where X refers to the concentration of the specie indicated in the subscript and the atomic layer indicated in the superscript. The symbol M refers to the mobility of atoms described by equation 7.6 [12]

$$M_0^j = \frac{D_0^j \exp\left(-Q^j / RT\right)}{RT}. \tag{7.6}$$

The inter-lattice spacing is described by the symbol d. The segregation of S in Fe(100) was simulated by allowing the temperature to increase linearly at a constant rate, α, according to equation 7.7;

$$T(t) = T_0 + \alpha t, \tag{7.7}$$

where $T(t)$ describes the temperature of the system after time t, with the initial temperature given by T_0. This method is known as the linear programmed heating method, described in the work of Du Plessis et. al. [15].

7.3. Results and discussion

7.3.1. Activation energy of diffusion

According to chapter 6, the activation energy of diffusion, Q, is comprised of the migration energy, E_m, and the vacancy formation energy, E_{vac}. The migration energy is defined as the amount of energy needed for the impurity atom to jump from a substitutional lattice site to a vacant nearest neighbour site. Utilising the Climbing Image Nudged Elastic Band (CI-NEB) algorithm [16], as implemented in Quantum ESPRESSO [17], the migration energy of S was calculated in each of the first four atomic layers and the bulk of Fe(100) respectively. Figure 7.1 presents the migration energies as a function of the diffusion path length, L. The migration energy, vacancy formation energy and activation energy values are tabulated in table 7.2.

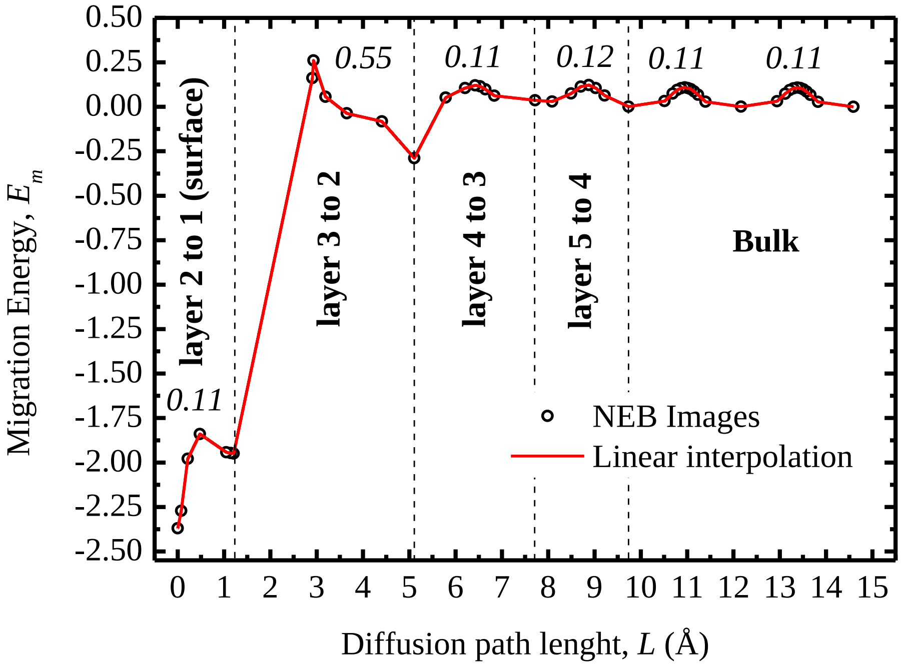

***Figure 7.1**. Migration energy, E_m, of S as a function of the diffusion path length, L, as S segregates from the bulk to the surface of the Fe(100) orientation.*

***Table 7.2:** Migration energy, E_m, vacancy formation energy, E_{vac}, and activation energy, Q, values for each of the respective near surface layers, surface layer and the bulk of Fe(100) as S segregates towards the Fe(100) surface.*

Layer, *n*	**Migration Energy, E_m (eV)**	**Vacancy formation Energy, E_{vac} (eV)**	**Activation Energy, *Q* (eV)**	**Activation Energy, *Q* (kJ/mol)**
2→1	0.11	1.28	1.39	134
3→2	0.55	2.42	2.97	287
4→3	0.11	2.63	2.74	264
5→4	0.12	2.77	2.89	279
bulk	0.11	2.64	2.75	265

From the results presented in table 7.2, a distinct layer dependence is observed for the activation energy of S as it segregates toward the surface. The smallest activation energy is observed for segregation of S from the second to the first atomic layer (surface layer), indicating a rapid diffusion rate of S from atomic layer 2 to 1. This would result in the almost immediate "dumping" of S into the surface layer. Since the activation energy determines the segregation rate of S towards the surface, segregation from atomic layer 2 to 1, with the largest activation energy, forms the rate limiting step for S segregation in Fe(100).

7.3.2. Segregation energy, ΔG

The segregation energy will account for a change in the total energy of the crystal structure when an atom is removed from one position in the bulk lattice and placed within one of the first 4 atomic layers, described by equation 7.3. Negative segregation energies indicate a decrease in the total energy (exothermic reaction). A positive value means that the total energy has increased (endothermic reaction). Endothermic reactions predict that the impurity atom is unlikely to segregate, while an exothermic reaction predicts the segregation of an impurity atom. The standard segregation energies for the surface and near surface layers are presented in table 7.3. For illustrative purposes the results are also given graphically in figure 7.2.

Table 7.3: *Segregation energies of a single S atom in the surface and near surface layers of Fe(100).*

Layer, *n*	**Segregation energy, ΔG (eV)**	**Segregation energy, ΔG (kJ/mol)**
Bulk →1(surface)	-1.93	-186
Bulk →2	0.21	20.7
Bulk →3	0.07	6.51
Bulk →4	-0.01	-1.40
Bulk →5	0.00	0.00

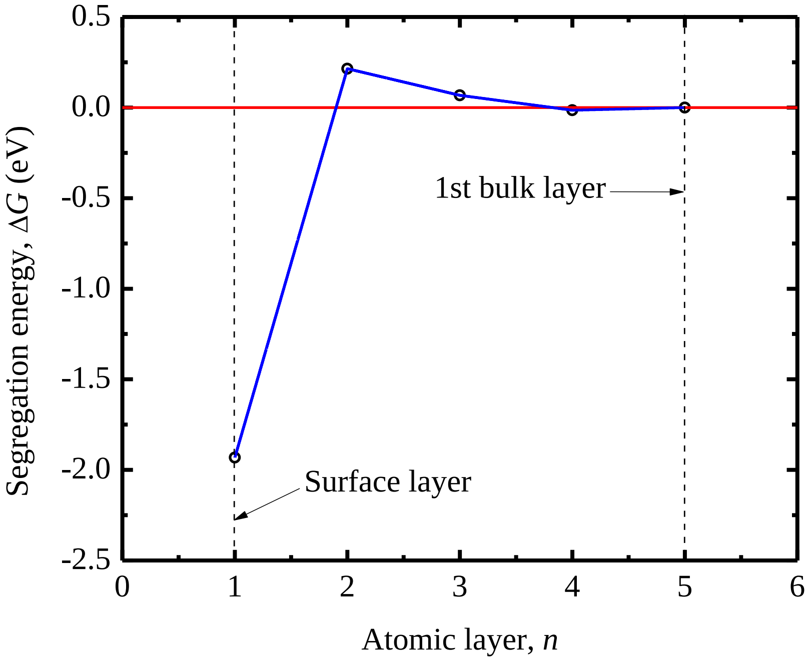

Figure 7.2: *Layer dependence of the segregation energy for S segregating in bcc Fe(100).*

Figure 7.2 shows a distinct layer dependence of the segregation energy. Atoms from the second atomic layer are shown to segregate towards the surface layer with a large negative segregation energy. Atomic layers 2 and 3 have positive segregation energies which indicate that S does not prefer to segregate from the bulk to these layers. A small negative segregation energy is observed for atomic layer 4, showing favourable segregation of S from the bulk towards this layer. Once again, similar to the activation energy of diffusion, a large energy barrier is seen from atomic layer 3 to atomic layer 2. The segregation energy value of -1.93 eV, for atoms segregating from the bulk towards the surface, compares well to the experimental value of -1.97 eV found in literature [18]. Thus, the energy barrier preventing the segregation of S toward the surface layer is provided by the positive segregation energy of layer 2 (0.21eV), from there on atoms freely segregate towards the surface layer. Furthermore, during the desegregation of S from the surface into the bulk, S experiences a high energy barrier of 2.14 eV. This high energy barrier predicts a very slow desegregation rate of S into the bulk material.

7.3.3. Interaction parameter, Ω

The interaction parameter, Ω, describes the attractive or repulsive interaction between the various components in the system (equation 7.4). If S and Fe are strongly attracted towards one another, a positive interaction parameter will be obtained, while a negative value would suggest a strong repulsion between the two species. Impurity atoms with a strong repulsive interaction parameter are more likely to segregate toward the surface as opposed to impurity atoms with a strong attractive interaction parameter. The regular solution model [12, 13] describes the interaction parameter as a pair-wise interaction between two species under consideration. There is an inherent error in such a description, since the long range interactions of next nearest neighbouring atoms are neglected. Nevertheless, the model gives acceptable results and has been used to effectively describe the interaction between atoms in alloys [14, 15].

The interaction energies, ε, are considered as the energy per single bond in the respective components. Therefore, the binding energy for each of the atoms in Fe, S and Fe-S were calculated and divided amongst the numbers of bonds for that particular atom. For Fe and S this value was calculated for the bulk system, while for Fe-S it was determined for each atomic layer. Thus, the regular interaction parameter describes the likelihood that atoms would prefer to remain in their respective bulk structures or if they are going to form a mixture. Table 7.4 presents the interaction energies of the respective atoms and the interaction parameters of S in the first 5 atomic layers of Fe(100). The symbol *Z* denotes the number of nearest neighbour atoms.

Table 7.4: *Regular solution interaction energy, ε, of Fe and S in their respective bulk structures and the regular solution interaction energies and interaction parameters of Fe-S in the first 5 atomic layers of Fe(100). The number of nearest neighbour atoms is denoted by the symbol Z.*

Layer, *n*	***Z***	ε_{Fe-Fe} **(eV)**	ε_{S-S} **(eV)**	ε_{Fe-S} **(eV)**	Ω_{Fe-S} **(eV)**	Ω_{Fe-S} **(kJ/mol)**
1	4	-	-	0.42	-0.46	-44.4
2	8	-	-	0.44	-0.32	-30.9
3	8	-	-	0.45	-0.23	-22.2
4	8	-	-	0.45	-0.26	-25.1
bulk	8	0.61	0.36	0.45	-0.26	-25.1

All atomic layers show a favourable segregation of S towards the surface layer, with the interaction parameter decreasing monotonically from atomic layer 1 into the bulk. These results are in good agreement with the segregation data of table 7.3, which indicate that S segregates with a large endothermic segregation energy into the surface layer, atomic layer 1.

7.3.4. MDM simulations and fittings of S segregation in Fe(100) and Fe(111)

The segregation parameters calculated above by DFT were used in the MDM to simulate the segregation of S in Fe(100) and perform fittings to experimental data. One more parameter is required in order to completely describe the segregation of S in Fe(100), the pre-exponential factor, $D_{0.}$ Equation 7.8 describes the pre-exponential factor for the bcc crystal lattice [19, 20];

$$D_0 = a^2 f \nu_0 \exp\left(\frac{\Delta S_v^f + \Delta S_m}{k_B}\right), \tag{7.8}$$

where a is the equilibrium lattice parameter, f is the correlation factor and ν_0 is the attempt frequency for the jump of a S atom to a nearest neighbour vacancy. The exponential term provides the entropy for vacancy formation, ΔS_v^f, and the entropy of migration, ΔS_m. The pre-exponential factor was not calculated by DFT calculations, but was instead extracted from the experimentally obtained segregation profile of S in Fe(100) by implementing the MDM. Equation 7.8 presents a complicated equation to be used in a fitting procedure with all the quantities, except the lattice parameter, presented on the right hand side of equation 7.8 being unknown. Fitting of such an equation would require the simultaneous optimisation of four different parameters, a task requiring large computational resources and time. Apart from the computational requirements the values for these parameters are not required and only the final value for D_0 is required. To simplify this complicated expression of many variables, to a first approximation, the correlation factor, the jump frequency and the exponential term are considered to be independent of the atomic layers. This of course is not true since the entropy for vacancy formation is layer dependant. However, the variation between different layers is expected to be small. Using this first approximation and using the ratios of D_0 for each of the atomic layers with respect to the bulk D_0 value, results in equation 7.9

$$\frac{D_{0_i}}{D_{0bulk}} = \frac{\left[a^2 f\nu_0 \exp\left(\frac{\Delta S_v^f}{k_B}\right)\right]_i}{\left[a^2 f\nu_0 \exp\left(\frac{\Delta S_v^f}{k_B}\right)\right]_{bulk}}$$

$$D_{0_i} = D_{0bulk}\frac{a_i^2}{a_5^2}. \qquad (7.9)$$

Equation 7.9 presents a simple equation whereby the D_0 value for the different atomic layers can be obtained, with only the lattice parameter that is needed. It should be noted that this expression, equation 7.9, is only valid to obtain the initial values of D_0 for each atomic layer. In order to obtain the final values, the MDM was fitted to the experimental data of S segregation in Fe(100) and the D_0 values were obtained from the best fit.

The experimental data for the segregation of S to the surface of Fe(100) obtained by AES measurements are presented in figure 7.3, with the MDM fitted onto the data providing a description of the "surface effect". All the segregation parameters for this fit were obtained from DFT calculations, except for the D_0 values that were extracted from the data. Table 7.5 presents the D_0 values for each of the first 5 atomic layers of Fe(100).

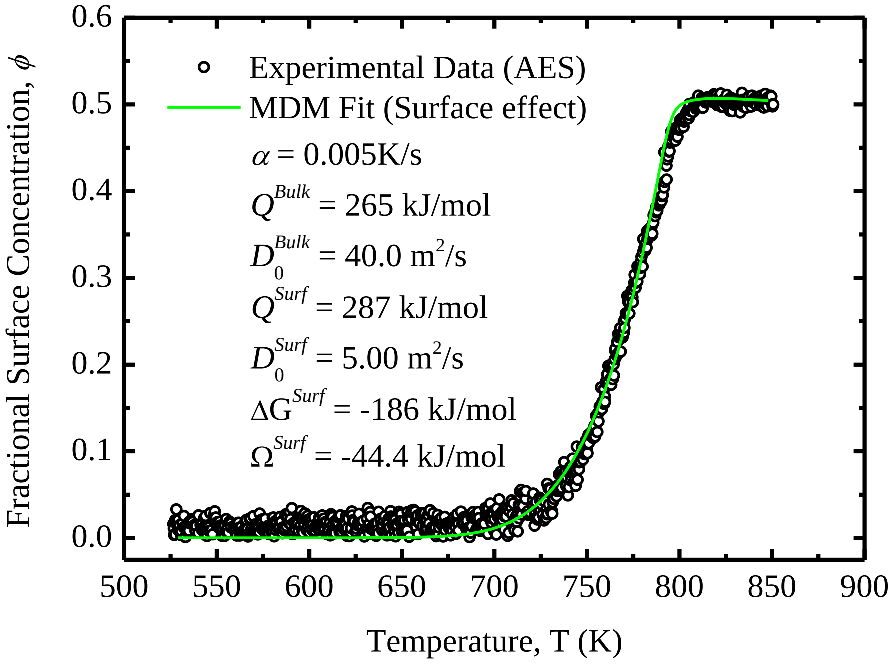

Figure 7.3: *Fitting of the MDM which describes the presence of a "surface effect" whereby the surface and bulk are described by a different set of kinetic parameters, Q and* D_0*. The bulk lattice has parameters; Q = 265 kJ/mol,* D_0 *= 40.0 m*^{2}*/s and the surface has parameters; Q = 287 kJ/mol,* D_0 *= 5.00 m*^{2}*/s. The equilibrium parameters* ΔG *= -186 kJ/mol and* Ω *= -44.4 kJ/mol is obtain from the surface layer, atomic layer 1.*

Table 7.5: *Values for the pre-exponential factors of the first 4 atomic layers and the bulk lattice for S segregating in the Fe(100) surface. These values were obtained by the best fit of the MDM to experimental data obtained by AES.*

Layer, *n*	D_0 (m^2/s)
1	26.3
2	5.00
3	30.7
4	31.0
bulk	40.0

From figure 7.3 it is observed that the MDM incorporating the "surface effect" provides an accurate description of the experimental data obtained by AES. Small deviations are observed as the S concentration approaches the equilibrium region, region where S reaches a plateau concentration.

All the pre-exponential factor values for the first 4 atomic layers are smaller than that for the bulk layer, with atomic layer 2 having the smallest value. This indicates that the exponential terms, correlation factors and vibrational frequencies for the different atomic layers described in equation 7.8 are indeed different as a result of the "surface effect". This confirms that equation 7.9 can only be used to obtain the initial values of D_0 for the fitting procedure and not to provide a final answer to the values of D_0. The final answer is obtained from the fit of the MDM. Since layer 2 is the rate limiting step for the segregation of S to the surface, the pre-exponential factor from this layer is responsible for the surface region of the segregation profile in figure 7.3. The bulk value for D_0 dominates the remainder of the kinetic region of the segregation profile. Simulations were performed to determine the influence of the D_0 values of the other atomic layers. The results showed that the segregation profile is described by only the D_0 values of atomic layer 2 and the bulk, with little influence by D_0 values from any of the other layers.

This implementation of the MDM differs from the conventional method whereby the surface effect was not taken into consideration, resulting in only one set of segregation parameters. This conventional method is illustrated in figure 7.4 where it is fitted onto the segregation data of S in Fe(100). Initial values for the segregation parameters were obtained by fitting of Fick`s model and the Bragg-Williams model to the experimental data (see chapter 2 for a description of these two models).

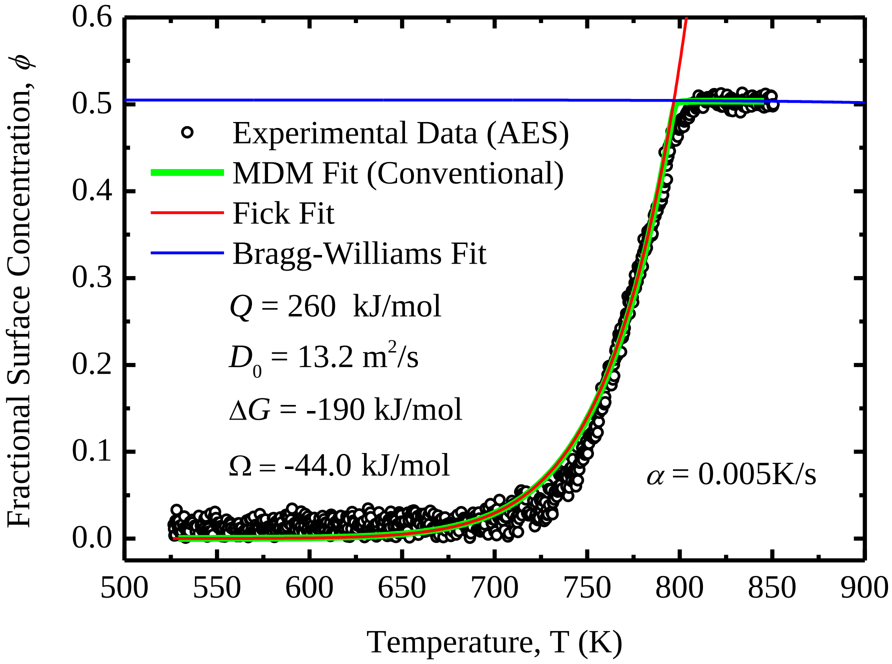

Figure 7.4: *Fit of Fick` s model to the kinetic region and the Bragg-Williams model to the equilibrium region of the S segregation profile in Fe(100). These two models supplied the initial values for the MDM model, implemented in the conventional way, which describes both the kinetic and equilibrium regions of S segregation in Fe(100).*

The MDM fit in figure 7.4 delivered segregation parameters that are in good agreement to the values calculated by DFT. The bulk value for the activation energy of diffusion obtained by DFT calculations is in agreement with the activation energy of diffusion extracted by the MDM. The equilibrium parameters, the interaction parameter and segregation energy for the 1st atomic layer (surface layer) is in good agreement with the values obtained by the MDM. Table 7.6 draws a comparison between the segregation parameters obtained by the conventional MDM and DFT.

Table 7.6: *Comparison of the segregation parameters extracted by the conventional implementation of the MDM, neglecting the surface effect, to the segregation parameters calculated by DFT.*

Layer, *n*	**MDM (kJ/mol)**	**DFT (kJ/mol)**
Q	260	265
ΔG	-190	-186
Ω	-44	-44.4

This indicates that the conventional method of utilising the MDM provides accurate results for the bulk value of the activation energy of diffusion and for the segregation energy and interaction parameter of the surface layer. However, if fails to provide information on the activation energies in the near surface layers and therefore deviates from the experimental data in the region dominated by the surface effect at temperatures between ~675 – 762 K.

In order to draw an accurate comparison between the MDM incorporating the surface affect and the conventional implementation which neglects the surface effect, the two are plotted onto the same graph, figure 7.5.

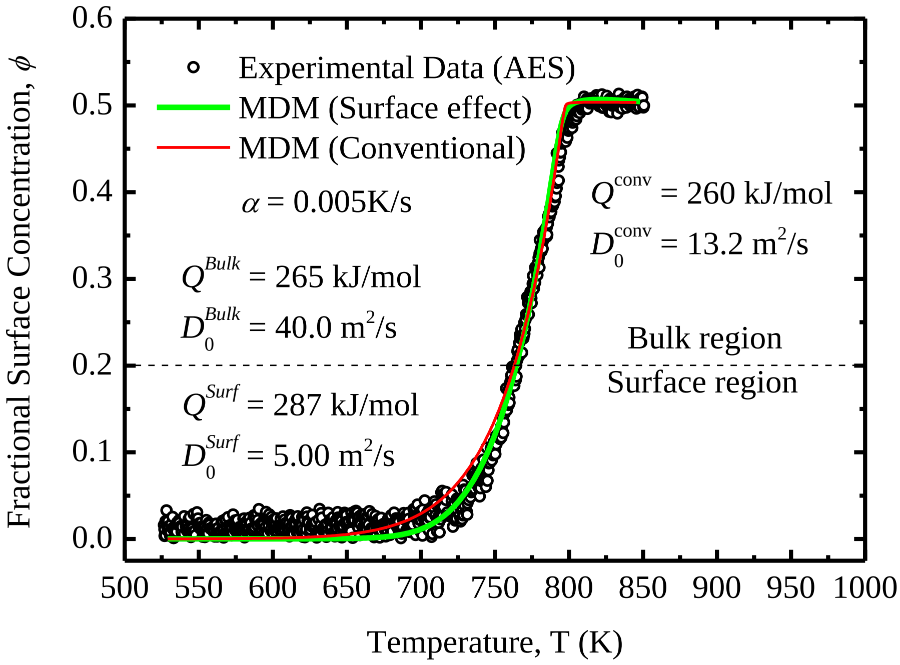

Figure 7.5: *The presence of a surface effect is evident in a comparison of the two curves both simulated by the Modified Darken Model (MDM). The green curve incorporates a description of the surface effect, while the red curve is the conventional implementation of the MDM. The results indicate that the segregation profile can be divided into two regions the surface and bulk regions, each described by a different set of kinetic parameters Q and* D_0.

Figure 7.5 shows that the model incorporating the surface effect effectively describes the segregation of S in Fe(100) by taking the layer dependence of the segregation parameters into account. The conventional method whereby the MDM is applied, fails to provide an accurate description of S segregation in Fe(100). This is especially prominent for temperatures in the range ~675 – 762 K, which can be attributed to the surface effect. Above 762 K the two curves, for the remainder of the kinetic region, are similar with slight deviations visible. As the S concentration approaches the equilibrium region, the MDM taking the surface effect into account is observed to have a more gradual transition from the kinetic to the equilibrium region, which is in agreement with the observed experimental data. The conventional method of the MDM shows a very sharp transition in contradiction to the experimental data. The equilibrium region is also described more accurately by the model incorporating the surface effect in comparison to the conventional method. The D_0

value obtained by the conventional method can be considered as an average value of the D_0 values obtained by the MDM which considers the surface effect.

An important factor to take into consideration is that the MDM as implemented in this study, makes use of the full 15 000 atomic layers chosen for the calculation and thus 15 000 differential equations were solved for each temperature instance. Other sources made certain approximations to decrease the number of differential equations to allow for a speedup in the calculation time. These approximations include interpolation between the different atomic layers as well as increasing the inter-lattice spacing value. Both of these methods result in a number of atomic layers being grouped together in one equation and thus effectively reduce the total number of equations that needs to be solved. Both of these methods were tested against the current MDM implementation, and were observed to deliver inaccurate results. These approximations are suggested to be better suited for higher impurity concentrations, but should be avoided for the concentrations studied in this work. The use of 15 000 equations resulted in the calculations becoming computationally very expensive. To speed up the calculation time, the software incorporated the OpenMPI libraries allowing parallel execution of the code resulting in almost linear speedup of the calculations. Using 4 CPU cores resulted in a 350 % speed increase in comparison to running the calculation on only 1 CPU core, measured in Wall time (actual calculation time).

Figure 7.3 describes the concentration increase of S in the surface layer of the Fe(100) surface as the temperature is linearly increased. Thus, the result of the diffusion processes which occurred in the near surface layers and the bulk is now evident on the surface. A picture of what occurred in the near surface layers and bulk during the segregation process is therefore of great significance. AES is incapable of providing such a picture, but detailed information of the near surface and bulk layers are well described by the MDM model incorporating the surface effect. The validity of the model is evident in figure 7.3, and therefore provides an accurate description of S segregation in the system as a whole. The combined utilisation of DFT, MDM and AES forms an efficient "probe" by which the segregation of S in Fe(100) could be studied from the bulk up to the surface layer. This is evident in figure 7.6 which provides a 3-dimensional image of the S concentration from atomic layer 2 up to atomic layer 15 000. The concentration in the surface region is illustrated from atom layer 2 to 10 in figure 7.7. A corresponding contour plot of figure 7.7 is provided in figure 7.8.

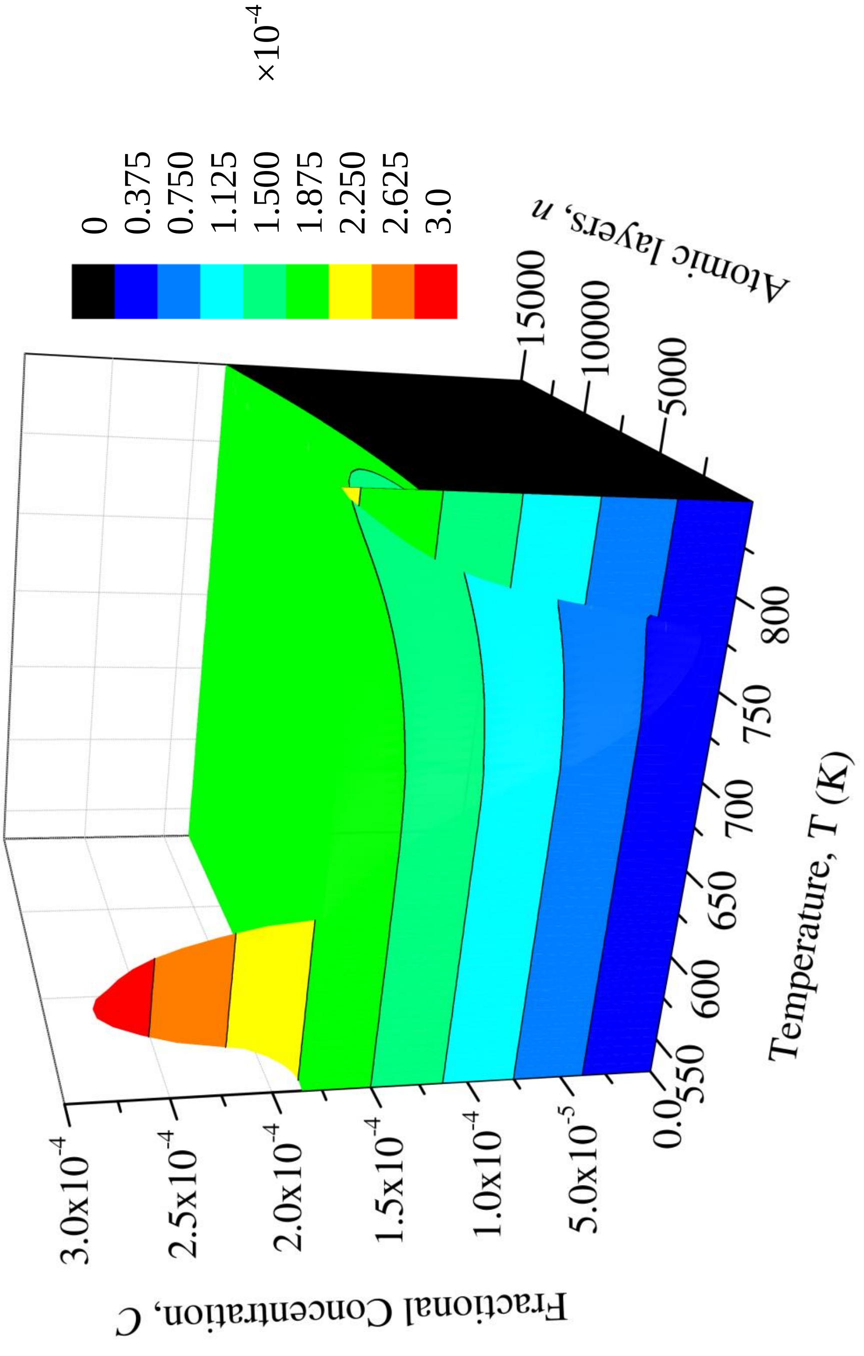

Figure 7.6: *3-dimensional plot of the S concentration in the surface region and bulk of the Fe(100) crystal during a linear programmed heating segregation run at a heating rate of 0.005K/s. The decrease in S concentration at higher temperatures is a result of S segregating to the surface layer, atomic layer 1.*

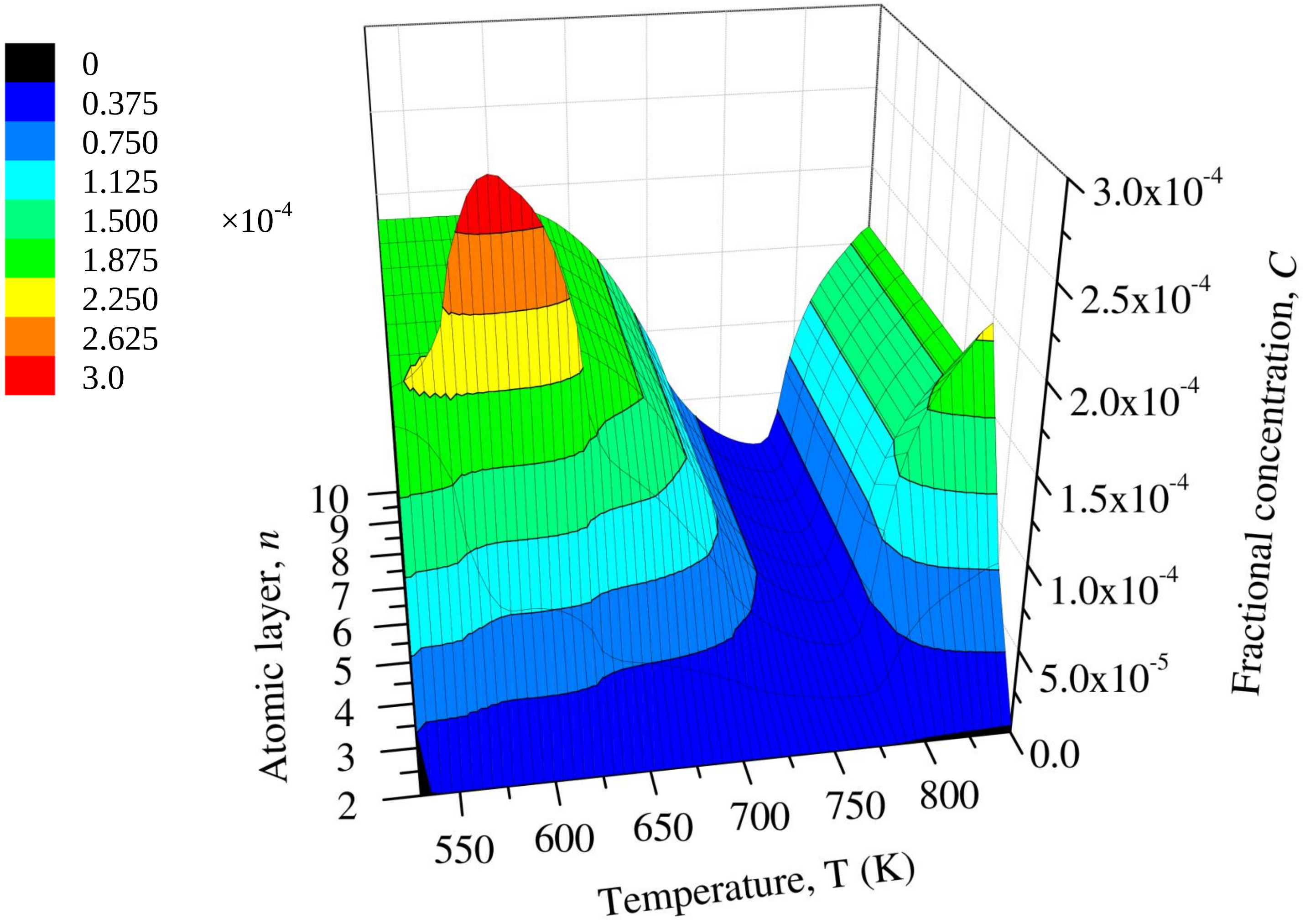

Figure 7.7: *3-dimensional plot of the concentration in the subsurface layers and a portion of the bulk crystal as a function of temperature during linear programmed heating segregation at a heating rate of 0.005K/s. The dependence of the segregation parameters on the atomic layers is evident in the concentration variation of especially the subsurface*

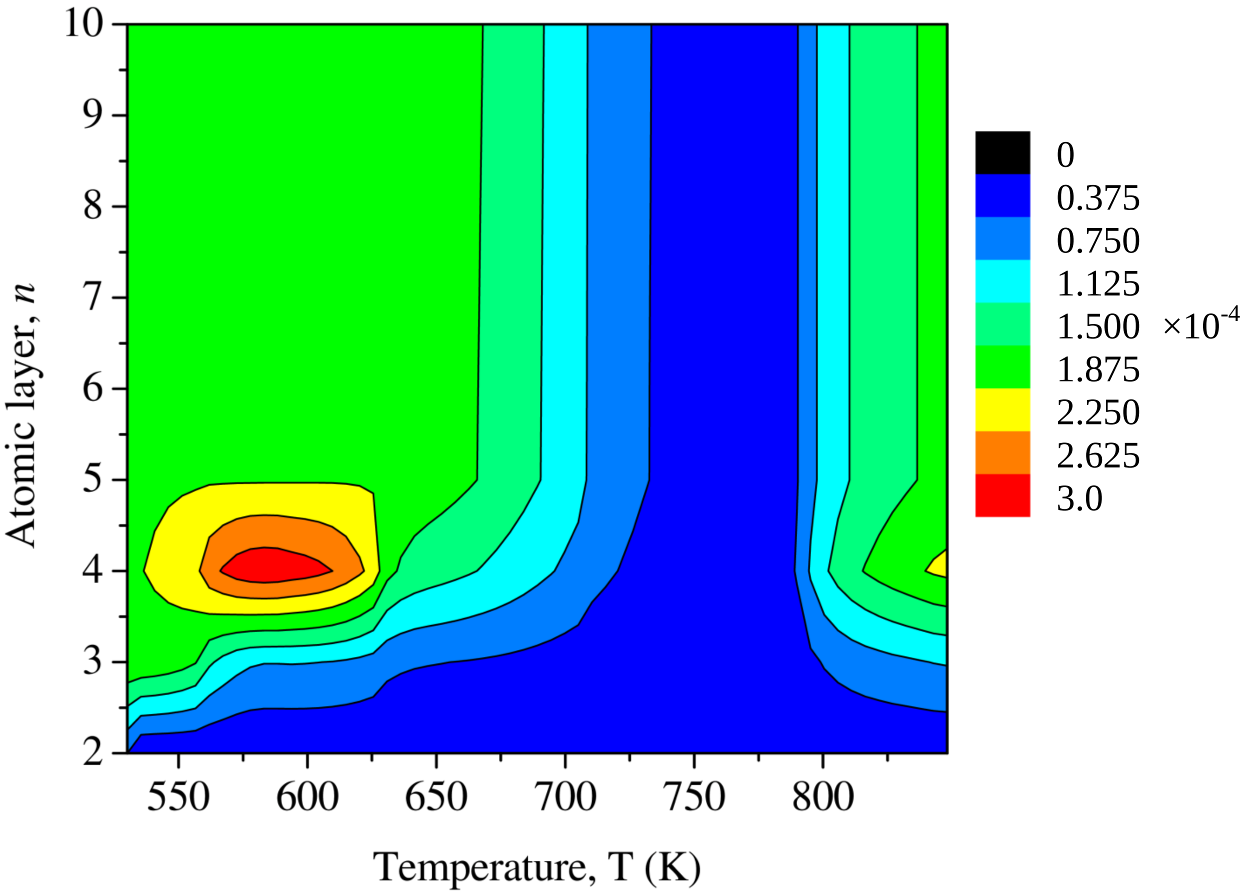

***Figure 7.8:** Contour plot of atomic layers 2 to 10 of the Fe(100) surface orientation during surface segregation. The sample was heated linearly at a rate of 0.005K.s*

From figures 7.7 and 7.8 it is evident that the subsurface layers, atomic layers 2 to 4, undergoes a dramatic change in concentration during segregation. The S concentration in each of these atomic layers (1-10) is plotted as a function of the temperature in figure 7.9.

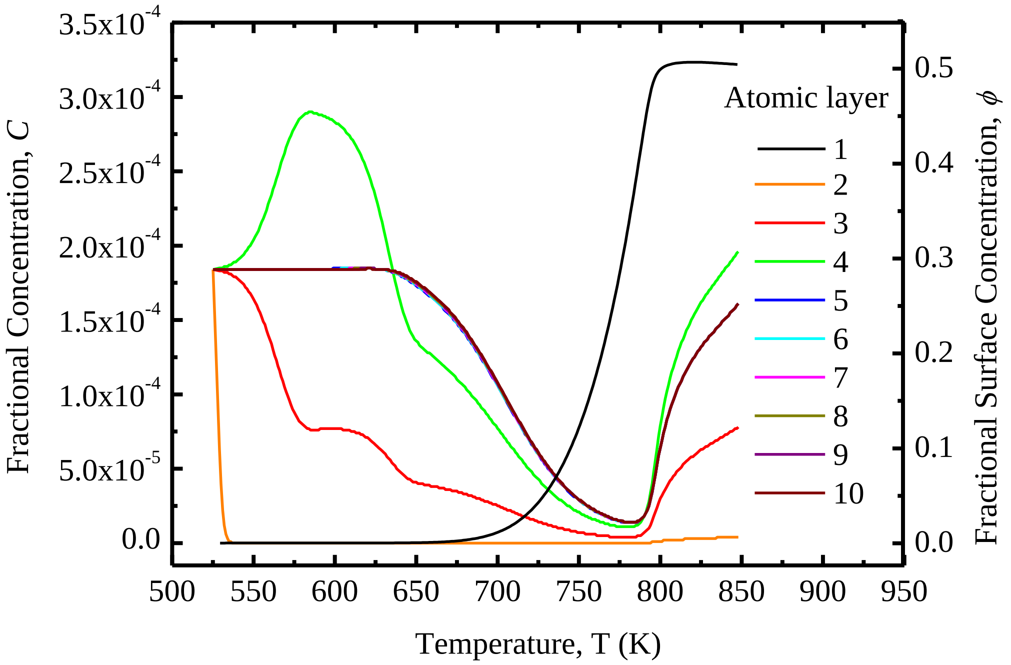

Figure 7.9: *S concentration in the surface and each of the near surface atomic layers as well as in the first 5 bulk layers (atomic layers 1 to 10).*

Figure 7.9 indicates a clear layer dependence of the segregation parameters in the first 4 atomic layers. For an explanation of the observed phenomena, consider tables 7.2 – 7.4. The rapid decrease in S from atomic layer 2 is caused by a combined effect of having a large negative segregation energy, a large negative interaction parameter and a low activation energy barrier. As previously mentioned (section 7.3.1), S is effectively "dumped" into the surface layer, atomic layer 1, from atomic layer 2. This dumping of S is observed in the rapid decrease of S in atomic layer 2.

Atomic layer 3 experiences a high activation energy for diffusion of S to atomic layer 2. Instead of segregating to atomic layer 2, S is observed to desegregate from atomic layer 3 into atomic layer 4 which requires less energy than diffusion into atomic layer 2. This desegregation of S is accommodated by the segregation energy of atomic layer 4 being more negative than that of atomic layer 3. Atomic layer 4 thus experiences an increase in concentration to a value of 0.00029 at.%, before S segregates from this layer towards the surface layer. At this point, the system has acquired sufficient thermal energy for S to segregate from the bulk into the surface layer. All the near surface layers are observed to decrease in concentration as S now segregates into the surface layer. Once the surface has reached a concentration of 50 at.%, the system is said to be in an equilibrium state. S no longer segregates into the surface layer, but instead fills up the subsurface layers as is evident at temperatures above 775 K.

The same segregation trend is observed for the segregation of S in the Fe(100) orientation when heated a slightly increase heating rate of 0.0075 K/s. The results for this heating rate is presented in figure 7.10, with Fick`s model describing the kinetic region and Bragg-Williams model describing the equilibrium region of the data. Along with these two models, is a fit of the MDM performed by the conventional method.

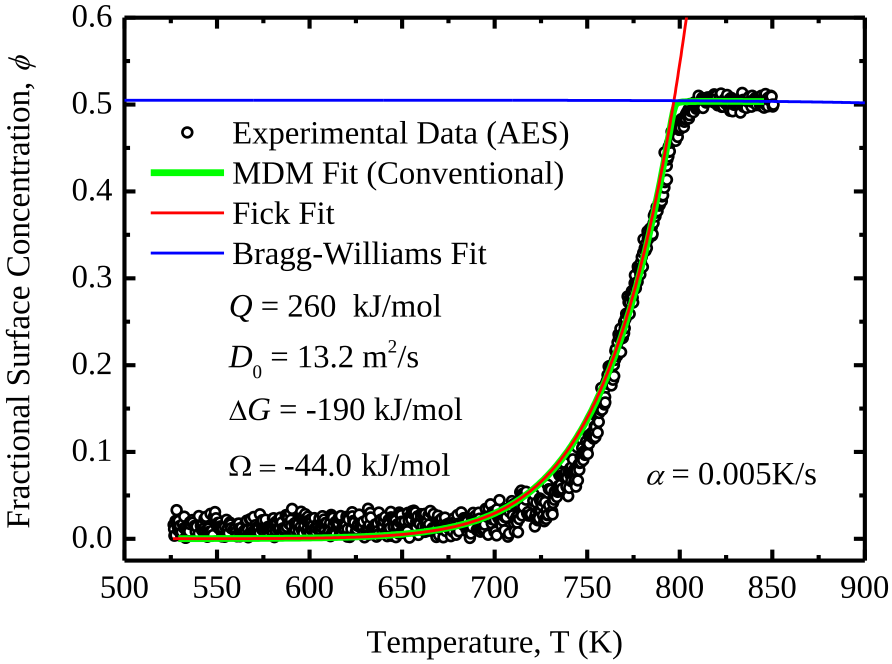

Figure 7.10: *Surface segregation of S in Fe(100) studied by the linear programmed heating method with a heating rate of 0.0075K/s. The models of Fick and Bragg-Williams are fitted onto the data to provide the initial segregation parameters for the MDM fit as implemented by the conventional method.*

The MDM which considers the presence of the surface effect is fitted onto the segregation data of S in Fe(100) obtained at a heating rate of 0.0075K/s in figure 7.11.

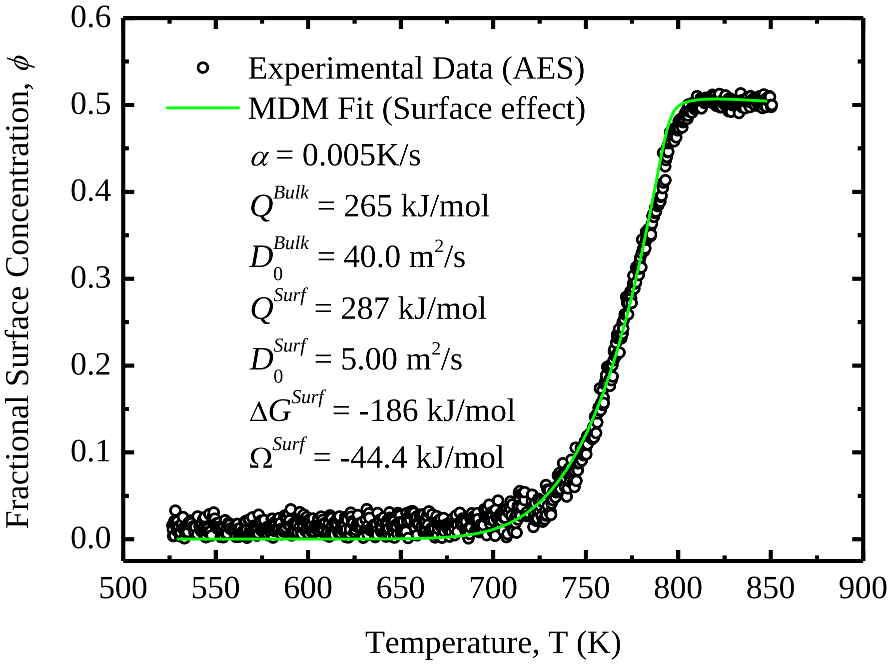

Figure 7.11: *Fit of the MDM which describes the surface effect present in the Fe(100) crystal orientation. The segregation profile is divided into two regions, the surface region and the bulk region. Each is described by a different set of kinetic parameters. The equilibrium parameters,* ΔG *and* Ω *are obtained for the surface layer, atomic layer 1.*

In comparison to the segregation profile obtained at a heating rate of 0.005 K/s, the same trend is observed in both the kinetic and equilibrium regions of the profile. The segregation parameters obtained by both implementations of the MDM is in good agreement with the MDM fits to the data obtained at a heating rate of 0.005 K/s (figure 7.4). The similarities in the two segregation profiles obtained at respectively 0.005 K/s and 0.0075 K/s predicts similar behaviour would be observed in the near surface layers for the two heating rates. The combined efforts of DFT, the MDM and AES provides conclusive evidence for the presence of a "surface effect" in the Fe(100) orientation. This effect is observed to cause a variation in the segregation parameters of the surface and near surface layers of Fe(100), the first 4 atomic layers.

Previously it has been said that the effect is caused by two factors; the relaxation of the lattice and the reduction in the number of nearest neighbouring atoms for the surface and near surface layer atoms. In comparison to the Fe(111) surface orientation, the surface relaxation of the Fe(100) orientation is less dramatic. As a consequence it is expected that the “surface effect” in the Fe(111) orientation would be more prominent as was observed for the Fe(100) orientation.

In order to investigate the presence of the surface effect in the Fe(111) orientation an experimental study was carried out combined with the models of Fick, Bragg-Williams and the MDM to extract the segregation parameters. DFT calculations were not performed to obtain each of the segregation parameters in the surface and near surface layers as was performed for the Fe(100) orientation due to the time constraints of the DFT calculations. DFT calculations of the migration energies of S in Fe(100) has proven to be computationally very expensive. A CI-NEB calculation needs to be optimised for each image by taking all the possible atomic positions into account, as a result of relaxation, and this all within a self-consistent convergence for the electronic structure of the system. Calculations for the migration energy of S in the Fe(100) surface ranged from 500 Wall hours to 4000 Wall hours, this is equal to a time period in days of between 20 days to ~160 days for a single calculation running on a high performance computer cluster of 60 CPU`s. Although the use of DFT was essential in order to study the Fe(100) surface in depth, it is not required to investigate the presence of the surface effect in Fe(111). Recalling from figures 7.5 and 7.11 that the surface effect is predominantly visible in the kinetic region of the segregation profile, this effect can effectively be described by the use of Fick`s model in combination with the MDM. However, there is a key point to take into consideration; Fick`s model is incapable of describing a dynamic process as the MDM is capable of doing. Fick`s equation describes segregation for a single set of segregation parameters, while the MDM is dynamic in the sense that it can incorporate multiple sets of segregation parameters. Thus, there exists a “linking” problem between going from Fick`s static description of segregation to the MDM `s dynamic description in a system composed of multiple sets of segregation parameters. The use of the term “linking” refers to the link that is required to take a static description composed of a single segregation process into a dynamic description where various segregation processes are involved.

The segregation data of S in the Fe(111) orientation is presented in figure 7.12, along with Fick`s model and the Bragg-Williams model fitted to the data.

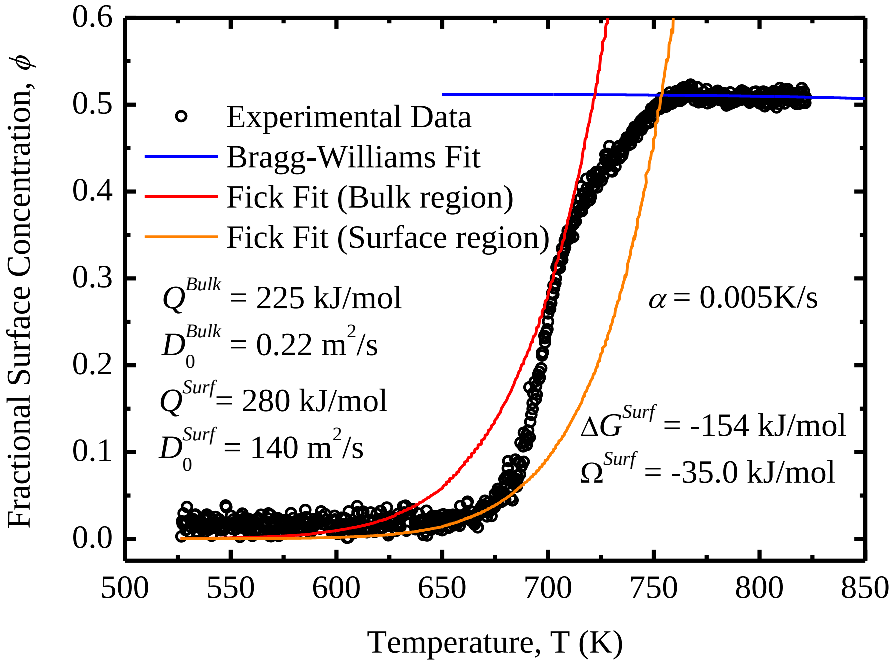

Figure 7.12: *Surface segregation of S in the Fe(111) orientation studied at a heating rate of 0.005 K/s. Two different fittings of Fick`s model is performed on the data in order to describe the "surface effect".*

In order to effectively describe the surface effect in the Fe(111) orientation heated at a rate of 0.005 K/s, two different fittings of Fick`s model was performed to the data. One of the fits describes the bulk region (red) of the segregation profile, while the other describes the surface region (orange). From these two fits, the presence of the surface effect is evident and as expected is more prominent as observed for the Fe(100) orientation. The same deviation is observed for the Fe(111) orientation as was observed for the Fe(100) orientation, but for the Fe(111) orientation the deviation is larger. This confirms the earlier statement made that the surface effect is expected to be more prominent in the Fe(111) orientation as a result of the surface relaxing to a greater extend than the Fe(100) orientation.

The segregation parameters obtained from the two fits of Fick`s model in figure 7.12 were used as initial values in the MDM to obtain a single model that can describe the surface effect in Fe(111). Figure 7.13 illustrates the fitting of the MDM to the segregation data of S in Fe(111).

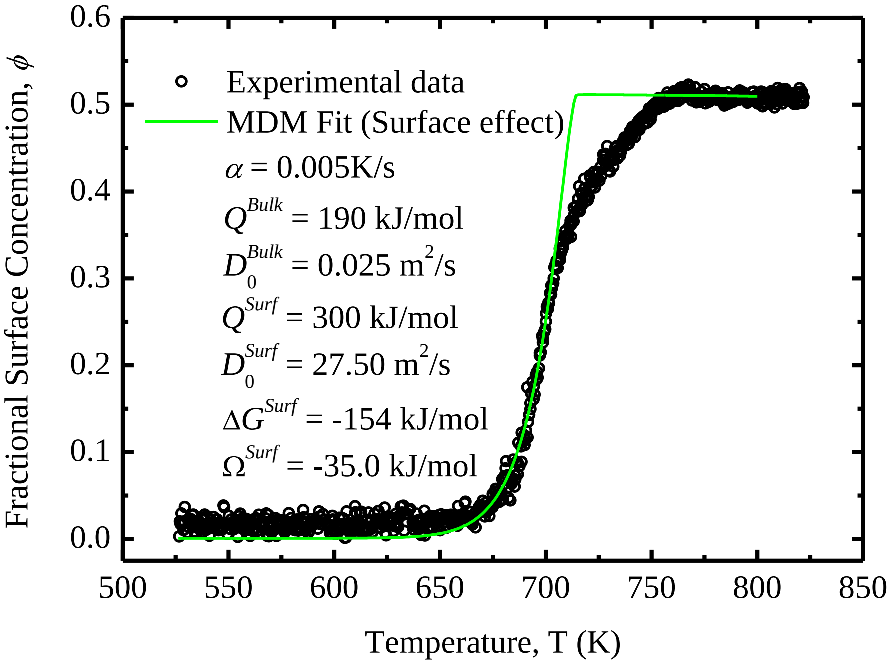

Figure 7.13: *MDM fitting to the segregation data of S in Fe(111). The model incorporates two different sets of kinetic parameters in order to effectively describe the surface effect during S segregation in Fe(111).*

The segregation parameters describing the kinetics of segregation, Q and D_0, obtained by the MDM are different from the values obtained by Fick`s model. Reasons for the observed deviation are ascribed to the linking problem mentioned earlier. Since the model of Fick only considers the segregation of S atoms having a single set of segregation parameters, Q and D_0, the model does not consider the presence of other processes in the crystal. Therefore, the two fits of Fick each describe the segregation of S with a single Q and D_0 value without considering the influence of the other. Linking the static Fick model to the dynamics of the real system is achieved by optimising the parameters obtained by Fick`s two fits in the MDM to obtain the best fit to the experimental data. The segregation energy and interaction parameter obtain by the Bragg-Williams equation accurately describes the equilibrium region of the segregation profile. Knowledge gained from the Fe(100) orientation showed that the parameters delivered by the Bragg-Williams model is that of the surface layer, the first atomic layer.

Deviations between the experimental data and the MDM in the temperature range 700-750 K is caused by the reconstruction of the Fe(111) orientation. The segregation of S to the surface causes the surface to reconstruct to lower the systems total energy. In doing so the surface allows for more S to occupy the surface layer. Reconstruction of the Fe(111) surface has been observed by Błoński et. Al. [4], Shih et. Al. [21] and Yamada et. Al. [22]. The current model is not capable of describing this surface reconstruction that occurs during surface segregation. Nevertheless, the MDM provides an accurate description of the kinetic region which reveals the presence of the surface effect as well as describing the equilibrium region of surface segregation.

The segregation of S from the Fe(111) orientation at a heating rate of 0.0075K/s is provided by figure 7.14, with the Models of Fick and Bragg-Williams fitted onto the data.

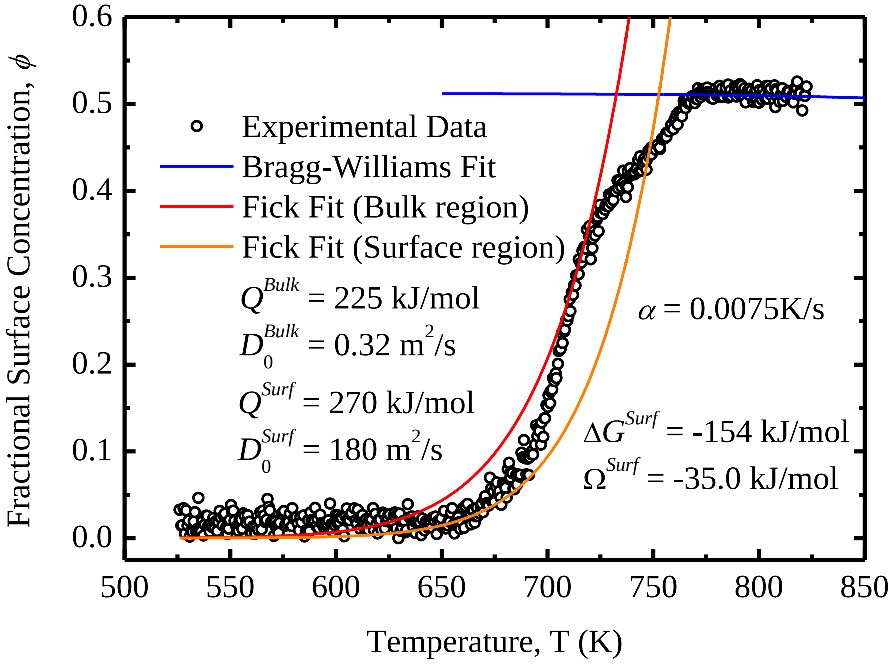

Figure 7.14: *Fittings of Fick`s model and the Bragg-Williams models to the segregation data of S in the Fe(111) orientation obtained at a heating rate of 0.0075K/s. The use of two fits of Fick`s model allows for a description of the surface effect.*

The segregation parameters obtained from the fittings of Ficks model and Bragg-Williams model were used as initial values for the fitting of the MDM. Optimisation of these parameters in the MDM resulted in a final description of S segregating in the Fe(111) orientation heated at a rate of 0.0075 K/s, figure 7.15.

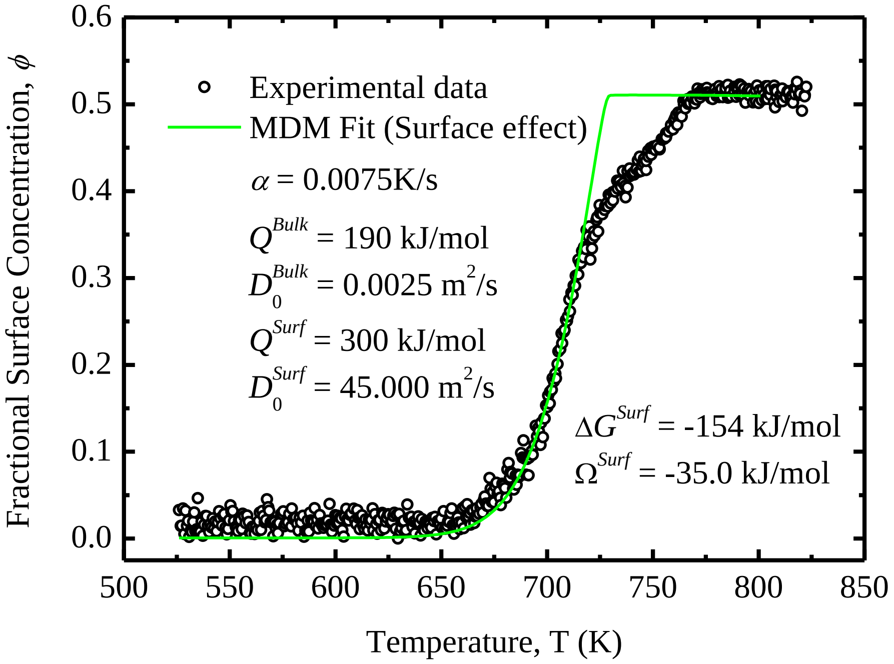

Figure 7.15: *MDM Fit onto the experimental segregation profile of S segregating in the Fe(111) orientation heated at a rate of 0.0075K/s.*

The segregation parameters obtained for the two heating rates of 0.005 K/s (figure 7.13) and 0.0075 K/s (7.15) are in good agreement with one another, with only the D_0 values that are observed to deviate. The surface effect was successfully explained in the Fe(111) orientations by using two different Fick fits to describe respectively the surface and the bulk regions. The equilibrium segregation parameters; ΔG and Ω as described by the Bragg-Williams model were used in the MDM, resulting in the same values.

Apart from confirming the presence of a surface effect, the data obtained for the segregation of S in the Fe(100) and Fe(111) orientations also confirm the influence of the surface orientation on the activation energy of diffusion. This topic was discussed in chapter 6 for the segregation of S in different grain orientations in a polycrystalline Fe sample. Figure 7.16 and 7.17 compares the segregation profiles of the Fe(100) to that of the Fe(111) orientations for the heating rates of 0.005K/s and 0.0075K/s respectively.

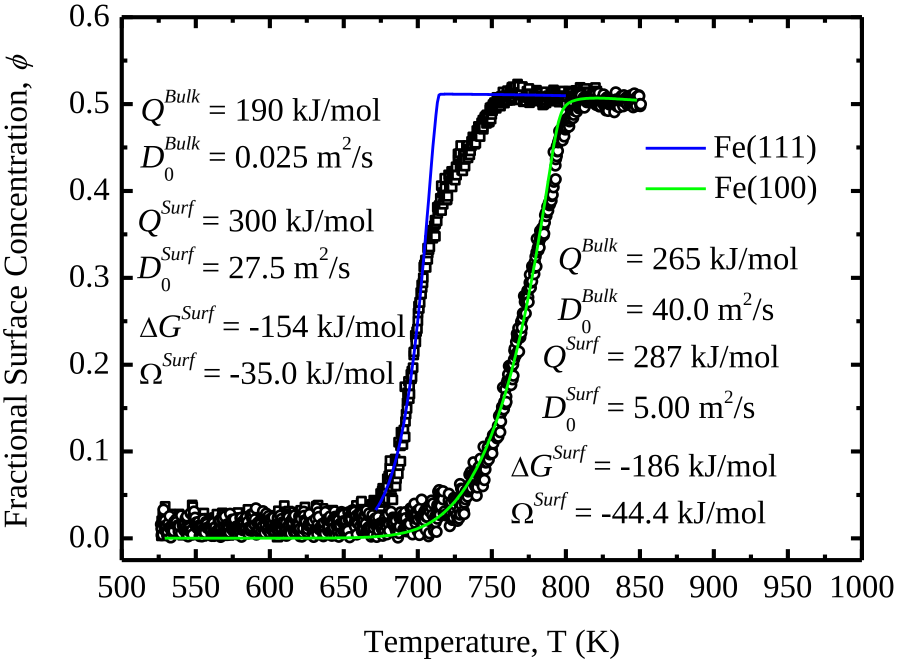

Figure 7.16: *Comparison of the segregation profiles of S obtained at a heating rate of 0.005K/s for the Fe(100) and Fe(111) orientations. The dependence of the surface orientation on the activation energy of diffusion is evident in the large variation in the kinetic regions of the two profiles. The equilibrium segregation parameters are also observed to vary between the two orientations of Fe.*

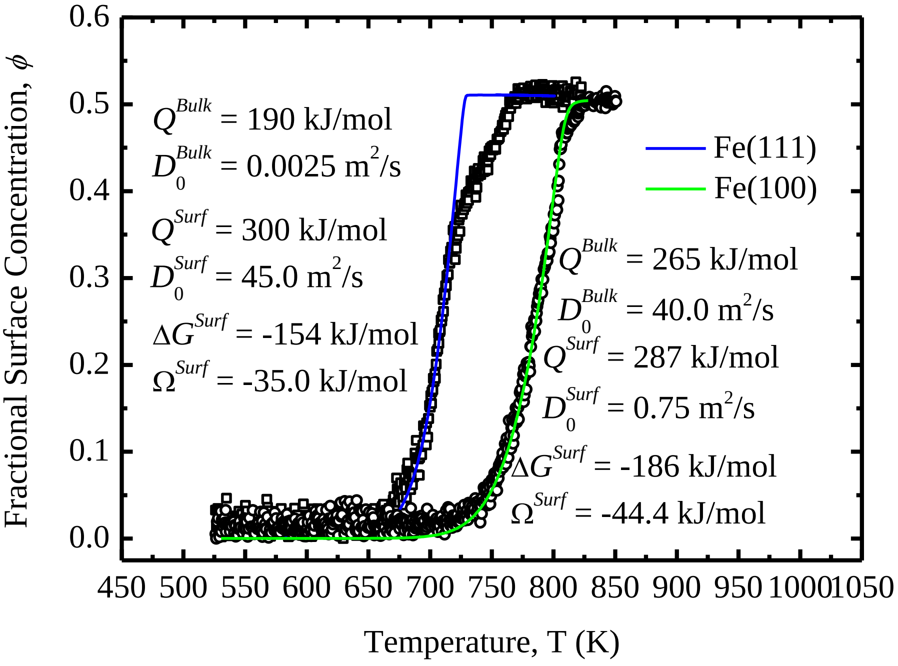

Figure 7.17: *Comparison between the segregation profiles of S for the Fe(100) and Fe(111) orientations obtained at a heating rate of 0.0075K/s.*

A comparison of the segregation parameters obtained for the Fe(100) and Fe(111) crystal orientations is presented in table 7.7.

Table 7.7: *Segregation parameters for the Fe(100) and Fe(111) orientations obtained by AES.*

Parameter	**Fe(100)**	**Fe(100)**	**Fe(111)**	**Fe(111)**	**Fe(100)**	**Fe(111)**
Rate (K/s)	0.005	0.0075	0.005	0.0075	**Average**	**Average**
Q^{Bulk} (kJ/mol)	265	265	190	190	265	190
Q^{Surf} (kJ/mol)	287	287	300	300	287	300
D_0^{Bulk} (m^2/s)	40.0	40.0	0.025	0.0025	40.0	0.0138
D_0^{Surf} (m^2/s)	5.00	0.75	27.5	45.0	2.88	36.3
ΔG^{Surf} (kJ/mol)	-186	-186	-154	-154	-186	-154
Ω^{Surf} (kJ/mol)	-44.4	-44.4	-35.0	-35.0	-44.4	-35.0

From the knowledge gained in chapter 6, a variation in the kinetic rates of the two different Fe orientations; Fe(100) and Fe(111) is expected as is presented in figure 7.16 and 7.17. Furthermore, a variation is also observed in the pre-exponential value as well as for the equilibrium parameters; the segregation energy (ΔG) and the interaction parameter (Ω) and like the activation energy, these parameters are also dependent on the surface orientation. In chapter 6, the surface orientation dependence was described as being the result of atoms on the surface (adatom) having a different number of bonds (Equation 6.5 in chapter 6). Similarly the variation in the equilibrium parameters from one orientation to the next is the result of S having a different binding energy in the surface layers of Fe(100) and Fe(111). This can be explained in more detail by considering the equations used in order to calculate the respective parameters. The pre-exponential factor (D_0) is described by equation 7.8, provided here for completeness by equation 7.10

$$D_0 = a^2 f \nu_0 \exp\left(\frac{\Delta S_v^f + \Delta S_m}{k_B}\right). \tag{7.10}$$

It was shown in chapter 6 that the vacancy formation energy and therefore the activation energy of diffusion are dependent on the surface orientation. Similarly the entropy for vacancy formation is dependent on the surface orientation. Also the relaxation of the surface layers causes a variation in the lattice parameter, *a*, as well as in the correlation factor, *f*, between different atomic layers. These differences caused by the surface relaxation and the orientation dependence of the entropy of vacancy formation results in the observed orientation dependence of the pre-exponential factor, D_0.

In the theory section of this chapter the segregation energy was described by equation 7.3, also provided here by equation 7.11 for atomic layer 1

$$\Delta G^{(1)} = E_{B(imp)}^{(1)} - E_{B(imp)}^{bulk}, \tag{7.11}$$

where $E_{B(imp)}^{(1)}$ is the binding energy of a S impurity in the surface layer and $E_{B(imp)}^{bulk}$ is the binding energy of S in the bulk lattice. The bulk binding energy is the same, irrespective of the surface orientation. Since the Fe(100) and Fe(111) orientation have a different number of nearest neighbouring atoms for S in the respective surfaces, the binding energy of an atom in the respective surface layers of Fe(100) and Fe(111) are different. This gives rise to the segregation energy being dependant on the surface orientation of the crystal under investigation. The interaction energy is described by equation 7.4 in the theory section of this chapter, and is provided here by equation 7.12 for atomic layer 1

$$\Omega_{12}^{1} = Z^{1}\left[\varepsilon_{12}^{1} - \frac{1}{2}\left(\varepsilon_{11} + \varepsilon_{22}\right)\right], \tag{7.11}$$

with the interaction energy between different species is provided by ε, and the number of nearest neighbouring atoms is described by *Z*. For the surface layer the number of nearest neighbouring atoms is half of what a bulk atom would experience, with Z = 4. The interaction energies for S (ε_{22}) and Fe (ε_{11}) in the bulk is the same and the only variation between the different orientations is the interaction energy, ε_{12}, for S in the respective surface layers of Fe(100) and Fe(111). This variation results in the interaction parameter being dependent on the surface orientation of the crystal under investigation.

7.4. Summary

The chapter describes the "surface effect", observed in the segregation data of S segregating in the Fe(100) and Fe(111) crystal orientations. This effect is caused by the relaxation of the first 4 atomic layers as well as the reduction in nearest neighbouring atoms for these atomic layers. A result of this effect is the layer dependency for each of the segregation parameters (the activation energy (Q), pre-exponential factor (D_0), interaction parameter (Ω) and the segregation energy (ΔG)).

DFT calculations performed on the Fe(100) crystal orientation revealed a distinct layer dependence for each of the segregation parameters. The activation energy of diffusion in the bulk crystal had a value of 2.75 eV (265 kJ/mol), this value increased toward the surface with the exception of segregation from atomic layer 4-3 having a value of 2.71 eV (261 kJ/mol) and the segregation from atomic layer 2 to 1 having the smallest value of 1.39 eV (134 kJ/mol). The largest value was observed for the segregation of S from atomic layer 3 to 2 with a value of 2.97 eV (287 kJ/mol). Since this is the largest activation energy value for S segregation, it formed the rate limiting step for the segregation of S from the bulk towards the surface.

The segregation energy for S was observed to increase from the bulk towards the second atomic layer (0.21 eV (20.7 kJ/mol)) and then rapidly decreasing to a value of -1.93 eV (-186 kJ/mol) in the surface layer. This indicates that S segregation to the second atomic layer is unfavourable but favourable for segregation to the first atomic layer. This is confirmed by the negative interaction parameters obtained for all the atomic layers, with the largest value of -0.46 eV (-44.4 kJ/mol) for the surface layer.

These values obtained by DFT calculations were used in the MDM to obtain a fit onto the experimental data that could effectively describe the surface effect. From the fit of the MDM, values for the pre-exponential factor were extracted. Results showed the largest value is present in the bulk material, with atomic layer 2 having the smallest value. This was observed for both the segregation profiles obtained at the heating rates of respectively 0.005K/s and 0.0075K/s. In comparison to the conventional implementation of the MDM, a distinct difference was observed in the region attributed to the surface effect. The model incorporating the surface effect was capable of providing an accurate description of the complete segregation profile, whereas the conventional model failed to provide an accurate description. The surface effect was also observed in the Fe(111) orientation, and was more dramatic due to the greater degree of lattice relaxation for this orientation of Fe.

It can be concluded that there exists a surface effect in the crystal, which causes the segregation parameters to be layer dependant. In order to provide an accurate description of segregation by taking this effect into consideration, the MDM was used with the segregation parameters obtained by DFT calculations. In comparison to the conventional MDM, which considers only a single set of segregation parameters, the model considering the surface effect provided a more accurate description of the experimentally observed data.

The segregation profiles of the Fe(100) and Fe(111) were compared to one another at both the heating rate of 0.005K/s and 0.0075K/s respectively. Results confirmed the orientation dependence of the activation energy of diffusion, observed in chapter 6, but also showed that the equilibrium parameters, the segregation energy (ΔG) and the interaction parameter (Ω) are dependent on the surface orientation. For both of these parameters the surface orientation dependence was explained as being the result of S having different surface binding energies in the respective surface layers of Fe(100) and Fe(111).

This chapter provides conclusive evidence for the orientation dependence of the segregation parameters, Q, ΔG and Ω. Furthermore, it was shown that the surface plays an important role during surface segregation and gives rise to the effect, termed in this study, as the surface effect; an effect responsible for the layer dependence of all the segregation parameters in the system, extending from the surface layer to the 4th atomic layer.

7.5. References

[1]. X. Yuan, C. Song, X. Kong, Y. Xu, Q.F. Fang, C.S. Liu, Phys. B Phys. Condens. Matter 425 (2013) 42.
[2]. M. Gupta, R.P. Gupta, J. Phys. Condens. Matter 25 (2013) 415502.
[3]. P. E. Barnard, Experimental and computational study of S segregation in Fe, M.Sc. Dissertation, Bloemfontein, 2012.
[4]. P. Błoński, A. Kiejna, Vacuum 74 (2004) 179.
[5]. M. Spencer, A. Hung, I. Snook, I. Yarovsky, Surf. Sci. 513 (2002) 389.
[6]. P. Błoński, A. Kiejna, Surf. Sci. 601 (2007) 123.
[7]. Z. Q. Wang, Y. S. Li, F. Jona, P. M. Marcus, *Solid State Commun.* 61(1987) 623.
[8]. K. O. Legg, F. Jona, D. W. Jepsen, P.M. Marcus, *Surf. Sci.* 66 (1977) 25.
[9]. J. Sokolov, F. Jona, P.M. Marcus, Phys. Rev. B. 33 (1986) 1397.

[10]. S. Hong, A. Anderson, Phys. Rev. B 38 (1988) 9417.

[11]. A. Kiejna, E. Wachowicz, Phys. Rev. B 78 (2008) 113403.

[12]. J. du Plessis, Surface Segregation, Sci-Tech Publications, Bloemfontein, 1990.

[13]. C.H.P. Lupis, Chemical Thermodynamics of Materials, Elsevier Science Publishing Co., Inc., New York, 1983.

[14]. E.C. Viljoen, J. du Plessis, Surf. Sci. 468 (2000) 27.

[15]. J. Du Plessis, E.C. Viljoen, Surf. Sci. 358 (1996) 905.

[16]. G. Henkelman, B.P. Uberuaga, H. Jónsson, J. Chem. Phys. 113 (2000) 9901.

[17]. P. Giannozzi, et.al., J. Phys. Condens. Matter 21 (2009) 395502.

[18]. H.J. Grabke, H. Viefhaus, in:, P.A. Dowben, A. Miller (Eds.), Surf. Segreg. Phenom., CRC press, Boca Raton, 1990.

[19]. J. Philibert, Atom movements: Diffusion and mass transport in solids, Les éditions de physique, France, 1991.

[20]. H. Ding, S. Huang, G. Ghosh, P.K. Liaw, M. Asta, Scr. Mater. 67 (2012) 732.

[21]. H. D. Shih, F. Jona, D. W. Jepsen, and P. M. Marcus, Phys. Rev. Lett. 46 (1981) 731.

[22]. T.K. Yamada, H. Tamura, M. Shishido, T. Irisawa, T. Mizoguchi, Surf. Sci. 603 (2009) 315.

Chapter 8

Surface segregation of Cr in Fe(100) and Fe(100)-S alloys and the "surface effect"

8.1. Introduction

Iron (Fe)-based chromium (Cr) alloys has been the subject of interest in a number of research articles [1-12]. This is not surprising considering the many industrial and technological applications of these alloys. They are promising candidates for materials in fission reactors, with the ability to operate over long periods of time despite being exposed to high irradiation levels and temperatures [13, 14]. Furthermore, the presence of a thin Cr layer on the surface of a Fe-Cr alloy results in the formation of a protective Cr-oxide surface layer which prevents oxidation of the bulk material [4, 7]. This concept is utilised in the manufacturing of stainless steels, where Cr serves as an anti-corrosive agent protecting the material against conditions otherwise unsuitable for the alloy. These properties offered by Cr can only be harnessed if a Cr layer forms in the surface or on the surface of the alloy, which is achieved by segregation of Cr towards the surface. Surface segregation in Fe-Cr alloys has been the topic in many research papers, but despite these many efforts the question concerning Cr segregation in Fe remains largely an open question. Some researchers report the segregation of Cr in Fe while others report the unlikely possibility of Cr segregating in Fe.

First principle calculations were conducted by Kiejna et. Al. [4] to investigate the effect of bulk concentration and surface orientation on the ability of Cr to segregate. For low bulk concentrations, below 3 at %, segregation of Cr in the Fe(100), Fe(110),Fe(111) and Fe(210) orientations were observed to be unfavourable. Of these orientations, Fe(110) had the highest segregation energy of -0.001 eV in comparison to all the other orientations having a positive segregation energy. With the addition of another Cr atom into the 2×2 simulation cell, 1×2 for the (210) orientation, the segregation of Cr became more favourable, with all segregation energies being negative. These concentrations were less than 5 at. % in the crystal with the exception of the (210) orientation with a value of 5 at. %. In another first principle study performed by Geng [3], the segregation of Cr in Fe(100) was investigated for concentrations of 3.125 at. %, 6.25 at. %, 25 at. % and 50 at. %. All concentrations of Cr studied showed that Cr segregation does not occur. Based on these findings, Cr segregation in Fe does not occur, independent of the Cr concentration in the bulk of Fe. Ruban et. al. [15] performed first principle calculations to investigate the segregation of various transition metals solutes in the close-packed surfaces of transitional metal hosts. For segregation of Cr in Fe, a positive segregation energy was obtained, indicating unfavourable segregation of Cr in Fe. Contrary to these calculations a recent experimental study performed by Idczak et. al. [5] utilising X-Ray Photoelectron Spectroscopy (XPS), Cr segregation in Fe was observed. Fe-Cr alloys with a Cr concentration of 12 at. % in the bulk had a surface Cr concentration exceeding the Fe surface concentration when annealed at temperatures of up to 1000 K. Cr segregation in Fe was also observed by Suzuki et. al. [7] whom studied segregation for Cr concentrations of 13 at. % and 25 at. % in Fe using Angle Resolved Auger Electron Spectroscopy (AR-AES).

Yaun et. al. [8] performed first principle calculations in order to study the segregation of Cr in Fe(100) and considered the segregation energy of Cr to depend on the layer in which the Cr atom resides. It was observed that for Cr segregating to the first 5 atomic layers, all the segregation energies were positive. Indicating that the segregation of Cr in Fe(100) does not occur. The segregation energy was observed to increase monotonically from the bulk up to the second atomic layer, where it then decreased from 0.44 eV to a value of 0.1 eV in the surface layer. Similar findings was obtained by Gupta et al. [6] confirming a larger positive segregation energy for the second atomic layer as for the first. These results suggest a influence of the subsurface layers on the segregation of Cr to the surface of Fe.

It is interesting to note, that most of the theoretical work done on Cr segregation in Fe report that Cr is unlikely to segregate in Fe, while the majority of experimental work report the segregation of Cr in Fe. This suggests that there is a process occurring in real systems that is neglected by theoretical models. One possibility is the presence of other species in the system that could favour Cr segregation in Fe. This is confirmed by the findings of Schiffmann et. al. [16] whom observed that the non-metal impurities; N, C, S, and O are likely to cause Cr segregation in Fe in a process involving co-segregation of Cr with these non-metals. Similar findings were obtained by Clauberg et. al. [17] and Franchy et. al. [9] whom observed N and S co-segregation with Cr in Fe. These findings would provide an explanation for the discrepancies found between the experimental and theoretical work reported.

In this chapter, the segregation of Cr in bcc Fe is studied by a sequential multi-scale modelling approach in order to determine whether there exists a concentration dependence and temperature dependence on Cr segregation. The idea of a layer dependency on the segregation energy is taken further by considering all the segregation parameters (the segregation energy, the interaction parameters, the activation energy and pre-exponential factor) in the first 4 atomic layers to be dependent on the layer in which the Cr atom resides. Furthermore, the possibility of S causing the segregation of Cr in Fe in a co-segregation process is studied by considering the ternary alloy Fe-Cr-S.

The approach of a sequential multi-scale model allows for a comprehensive study of Cr in Fe over a length scale ranging from the atomistic description offered by Density Functional Theory (DFT) calculations to the macroscopic description of the Modified Darken Model (MDM). DFT is utilised to calculate each of the mentioned segregation parameters in Fe. These parameters are simulated by the MDM model for different bulk concentrations of Cr in Fe over a wide temperature range (525-1200K) using the linear programmed heating method [18].

8.2. Computational details

The computational details for the DFT calculations performed on the bcc Fe lattice has already been described in chapter 6, section 6.2.1. In order to perform calculations on the Fe-Cr system, the energy cut-off and the starting magnetisation were optimised for a single Cr atom in a 3×3×3 Fe simulation cell. The cut-off energy, E_{cut}, used was 844 eV while the starting magnetisation of Cr was chosen as -0.2 with Fe having a starting magnetisation value of 0.6. These parameters delivered the ground state energy of the 3×3×3 Fe-Cr simulation cell.

The theoretical concepts and mathematical equations used in the calculations presented in this chapter, is described in chapter 7, section 7.2. To avoid repetition, the calculation performed in this chapter refers to the applicable equations in chapter 7.

8.3. Results and discussion

8.3.1. Activation energy of diffusion, *Q*

In order for Cr to diffuse to a nearest neighbour vacancy, it requires an amount of energy equal to or exceeding the activation energy of diffusion, Q. This energy barrier is the sum of the migration energy and the vacancy formation energy terms as described by equation 6.2 in chapter 6. Vacancy formation energies for the first 5 atomic layers were calculated by equation 7.1 in chapter 7. To obtain the migration energy, the CI-NEB method was used to calculate the minimum energy path and consequently the migration energy barrier for these atomic layers. Figure 8.1 presents the migration energy as a function of the diffusion path length, L, as Cr segregates from the bulk material towards the surface layer. The vacancy formation energy, the migration energy and the activation energy of diffusion is presented in table 8.1.

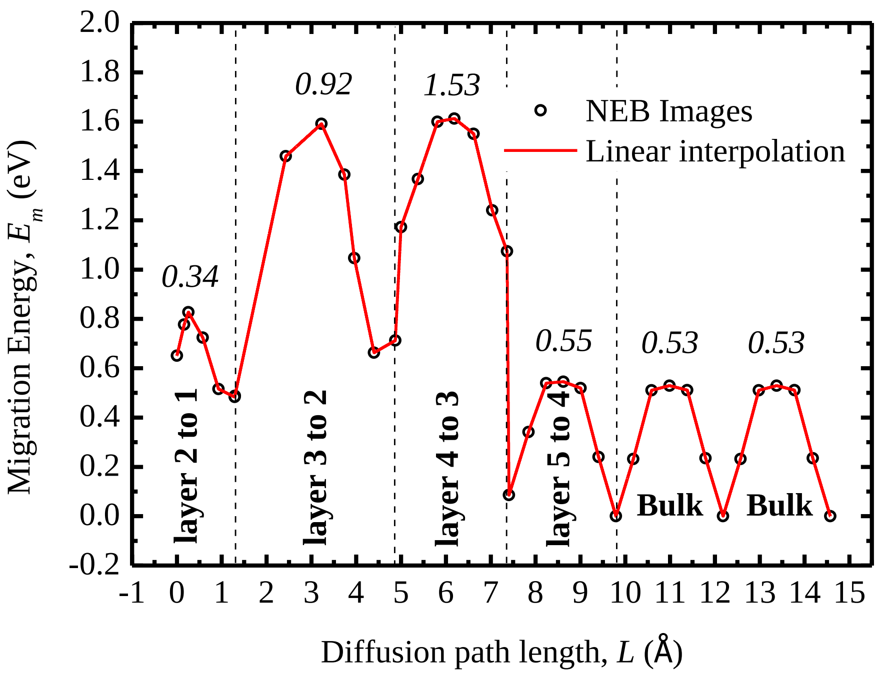

Figure 8.1: *Migration energy of Cr segregating from the bulk to the surface layer (atomic layer 1) in Fe(100).*

Table 8.1: *Vacancy formation energy (E_{vac}), migration energy (E_m) and activation energy of diffusion (Q) for Cr in teach of the first 5 atomic layers of Fe(100).*

Layer, *n*	**Vacancy formation Energy, E_{vac} (eV)**	**Migration Energy, E_m (eV)**	**Activation Energy, *Q* (eV)**	**Activation Energy, *Q* (kJ/mol)**
2→1	1.28	0.34	1.62	156
3→2	2.42	0.92	3.34	322
4→3	2.63	1.53	4.16	401
5→4	2.77	0.55	3.32	320
bulk	2.64	0.53	3.17	306

The results in table 8.1 indicate that very little energy is required to form a vacancy in the surface layer (first atomic layer). This is partially caused by the reduced coordination of atoms in the surface layer and consequently a weaker binding energy, but also due to relaxation of the surface. Relaxation of the surface further weakens the bond strength by expanding the inter-lattice spacing between the first two atomic layers in Fe(100) [19, 20].

A distinct difference is observed in the activation energy of the different atomic layers, with a non-monotonic increase from the surface into the bulk. The results in table 8.1 indicate that the diffusion of Cr in Fe(100) would be slow, with the exception of Cr diffusing from atomic layer 2 into atomic layer 1. This suggests that in comparison to the other layers, Cr segregation from atomic layer 2 to atomic layer 1 would be a rapid process, resulting in the almost immediate "dumping" of Cr from atomic layer 2 into atomic layer 1. With the highest energy barrier observed for the diffusion of Cr from atomic layer 4 to atomic layer 3. This activation energy barrier forms the rate limiting step for the segregation of Cr towards the surface layer.

8.3.2. Segregation energy, ΔG.

The segregation energy was defined by equation 7.3 as the total energy change occurring when a bulk impurity atom diffuses to one of the first 4 atomic layers. Therefore, the segregation energy can be considered as the binding energy difference between an impurity atom in the bulk as opposed to an impurity atom being bound in the surface or one of the near surface layers in the material. Figure 8.2 presents the variation of the segregation energy in the first 5 atomic layers of Fe(100), where atomic layer 5 is the first true bulk layer. The corresponding values are presented in table 8.2.

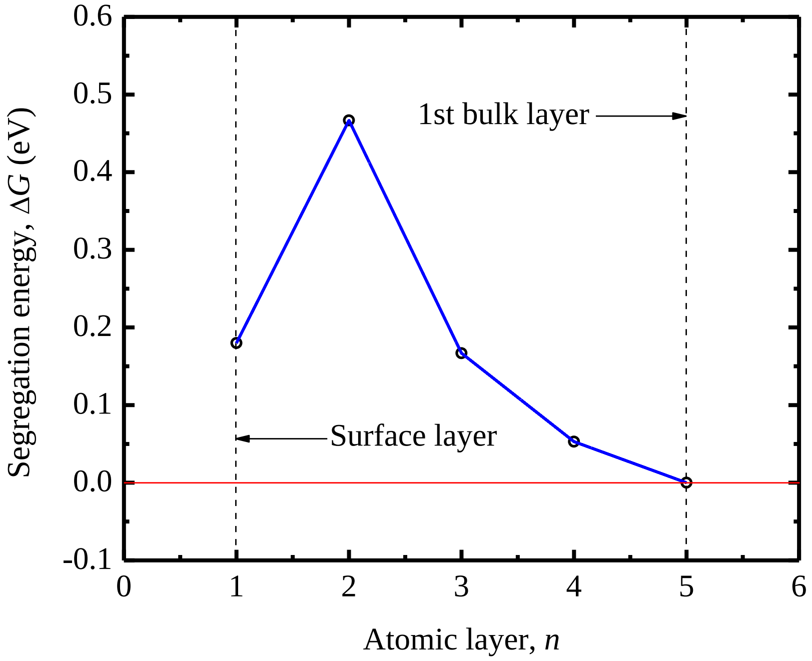

Figure 8.2: *Segregation energy for atomic layers 1 to 5, with 5 representing the bulk crystal. The segregation energy is observed to be monotonically increasing from the bulk up to atomic layer 2, where it then decreases for the surface layer, atomic layer 1. Positive segregation energies for all atomic layer indicate the unfavourable segregation of Cr in bcc Fe(100).*

Table 8.2: *Segregation energies for each of the surface layers in Fe(100) for Cr segregating towards the Fe(100) surface. Positive segregation energies indicate an endothermic process and the unfavourable segregation of Cr in bcc Fe(100).*

Layer, *n*	**Segregation energy of Cr in Fe, ΔG (eV)**	**Segregation energy of Cr in Fe, ΔG (kJ/mol)**
Bulk → 1(surface)	0.18	17.3
Bulk →2	0.47	45.3
Bulk →3	0.17	16.4
Bulk →4	0.05	4.82
Bulk →5	0.00	0.00

According to the results presented in figure 8.2 and table 8.2, the segregation of Cr towards the surface and near surface layers is unfavourable. The reaction is observed to be endothermic, as is evident in the positive segregation energy values. Atomic layer 2 shows the highest positive segregation energy value of 0.47 eV. The segregation energy values obtained in this study concurs with the values calculated by Yuan et. al. [8] and Gupta et. al. [6] (0.345 eV). They obtained segregation energy values for atomic layer 2 of respectively 0.44 eV and 0.345 eV. The slightly smaller value obtained by Gupta et. al. [6] was calculated for a simulation cell of dimensions $2a\times2a\times4a$, whereas the calculations performed by Yuan et al. as well as the calculations performed in this study was obtained for a simulation cell of dimensions $3a\times3a\times4a$. It has been found that the size of the simulation cell can influence the energetics of the Fe-Cr system due to the long range interactions of Cr with nearest neighbouring Cr atoms. Kiejna et. al. [4] obtained an energy difference of ~0.1 eV over the distance of $2a$ as a result of the Cr-Cr interaction.

8.3.3. Interaction parameter, Ω.

The interaction parameter in terms of the regular solution model [21, 22] describes the interaction of the various elements in the system as a pair-wise interaction [22]. Equation 7.4 was used to calculate the interaction parameter of Fe and Cr as a function of the atomic layer in which the Cr atom resides. Table 8.3 contains the results for the interaction energies and interaction parameter of Cr in the first 5 atomic layers of Fe(100).

Table 8.3: *Regular solution interaction parameter, Ω, and interaction energies, ε, of Fe-Cr in each of the first 5 atomic layers of Fe(100). The interaction energies for the pure components Fe and Cr is that of their respective bulk structures.*

Layer, *n*	ε_{Fe-Fe} (eV)	ε_{Cr-Cr} (eV)	ε_{Fe-Cr} (eV)	Ω_{Fe-Cr} (eV)	Ω_{Fe-Cr} (kJ/mol)
1	-	-	0.49	-0.36	-34.4
2	-	-	0.53	-0.06	-5.49
3	-	-	0.54	0.06	5.51
4	-	-	0.55	0.11	10.6
bulk	0.61	0.46	0.55	0.11	10.6

In the bulk as well as in the fourth and third atomic layers, a positive interaction parameter is obtained. This indicates that Cr and Fe are attracted towards one another in these layers which in turn predict that Cr segregation from these layers is unfavourable. Atomic layers 2 and 1 show a negative interaction parameter and predict the favourable segregation of Cr from these layers.

8.3.4. Pre-exponential factor, D_0.

This final segregation parameter is considered to be temperature independent and is described by equation 7.8. Taking the ratios of D_0 from for each atomic layer with respect to the bulk layer provides a more simplified expression, equation 8.1.

$$\frac{D_{0_i}}{D_{0bulk}} = \frac{\left[a^2 f\nu_0 \exp\left(\frac{\Delta S_v^f + \Delta S_m}{k_B}\right)\right]_i}{\left[a^2 f\nu_0 \exp\left(\frac{\Delta S_v^f + \Delta S_m}{k_B}\right)\right]_{bulk}}$$

$$D_{0_i} = D_{0bulk}\frac{a_i^2}{a_5^2} \qquad (8.1)$$

Equation 8.1 describes the ratio of the D_0 value for each of the first 4 atomic layers with respect to the bulk D_0 value. The value for D_0 in the bulk was obtained from tracer diffusion studies, delivering a value of 2.53×10^{-4} m^2/s [23]. Subsequently, the D_0 values for the first 4 atomic layers, constituting the surface region, were calculated by equation 8.1. In chapter 7 this approximation was observed to provide a good first approximation, but that a final answer should be obtained from other methods. Here equation 8.1 is used to provide the final answer for the D_0 values. This can be justified by considering that the kinetic of segregation is not the primary topic of interest, but rather the thermodynamics described by the interaction parameter and the segregation energy that are presented in the chemical potential term. Also, relative to one another different profiles using the same D_0 values would provide profiles that are comparable to one another, as is the case in this study. Table 8.4 presents the D_0 values for each of the first 5 atomic layers of the Fe(100) orientation.

Table 8.4: *Values for the pre-exponential terms of Cr segregating in the Fe(100) surface.*

Layer, *n*	**D_0 (m^2/s) × 10^{-4}**
1	2.12
2	2.57
3	2.52
4	2.57
bulk	2.53

Little variation is observed between the D_0 values of the different atomic layers, with only the surface layer showing a value slightly smaller than the rest, as a result of having less nearest neighbouring atoms. The above segregation parameters, Q, ΔG, Ω and D_0 describe the thermodynamics and kinetics at a specific concentration and temperature, 0 K where DFT is performed. In order to determine what the influence of temperature and the bulk concentration would be on the Fe-Cr system, these segregation parameters are used in the MDM to simulate the possible segregation profiles. The model describes the segregation of an element in terms of its chemical potential, μ. This quantity is capable of describing the state of the system at different concentrations and temperatures, if the segregation parameters ΔG and Ω of the system is known.

8.4. MDM Simulated segregation of Cr in Fe(100)

In the previous sections, the segregation parameters of Cr in bcc Fe(100) was obtained by DFT calculations. These results describe the microscopic behaviour of Cr in Fe, but does not provide a complete macroscopic picture of Cr segregation in the bcc Fe(100) lattice. These segregation parameters were also determined for the concentration of only one Cr atom in the simulation cell (1.2 at. %) and at the nominal DFT temperature of 0 K. To study the behaviour of Cr in Fe on the macroscopic scale, the DFT results formed part of a sequential multi-scale simulation approach, where the second part of the multi-scale model is composed of the MDM. This multi-scale approach offers the ability of studying the Fe-Cr system over different spatial scales, from the microscopic to the macroscopic regime. The use of the MDM allows for a complete study of the Fe-Cr alloy for a range of different concentrations and temperatures.

The segregation of Cr in bcc Fe(100) was simulated by the MDM for bulk concentrations of 0.1, 0.16, 0.5, 1, 2, 5, 10, 12, 15, 20 and 22.5 at% Cr in Fe(100) by allowing the temperature to increase linearly at a rate of 0.05K/s. The results for the linear programmed heating simulations are presented in figure 8.3.

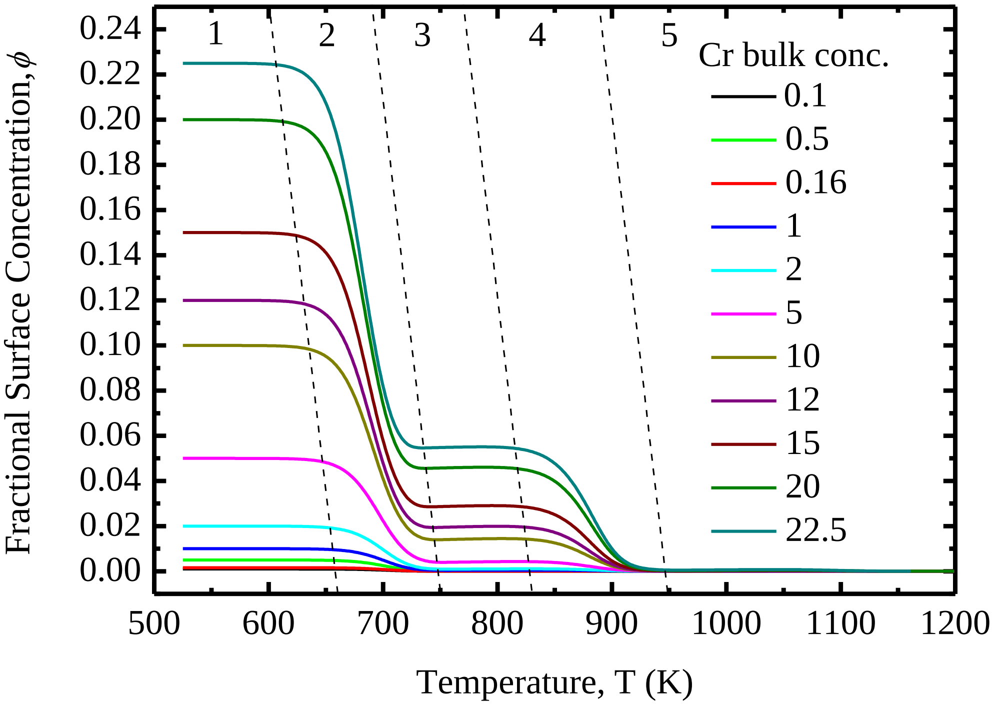

Figure 8.3: *Fractional surface concentration of Cr in the surface layer of Fe(100). Over the bulk concentration range of 0.1 – 22.5 at. % no segregation of Cr was observed, instead the desegregation of Cr into the subsurface layers is observed, with 5 different regions identifiable for the segregation process.*

The results in figure 8.3, shows a desegregation of Cr into the subsurface layers of Fe(100) for all concentrations in the range of 0.1 – 22.5 at. %. According to the work of Kiejna et. al. [4], the maximum Cr concentration in the Fe(100) surface is 25 at. %. This value was considered for all simulations. The different concentrations exhibit the same behaviour with 5 distinct regions visible in each of the profiles presented in figure 8.4. Region 1 shows little variation in the concentrations with a stable concentration region visible, indicating that the temperatures in this region is insufficient to cause diffusion of Cr in Fe(100). Region 2 is characterised by the rapid desegregation of Cr up to a certain temperature whereupon the Cr concentration in the surface layer reaches a plateau. This plateau region makes out region 3 of the profile. Once again a desegregation of Cr is observed in region 4, resulting in a zero Cr concentration in the surface layer, forming region 5 of the desegregation process.

Considering the layer dependence of the segregation parameters, the explanation of the Cr desegregation, should be evident in the subsurface atomic layers. Before an analysis of these layers are performed, consider the 3-dimensional surface plot of the Fe(100)-20%Cr alloy in figure 8.4.

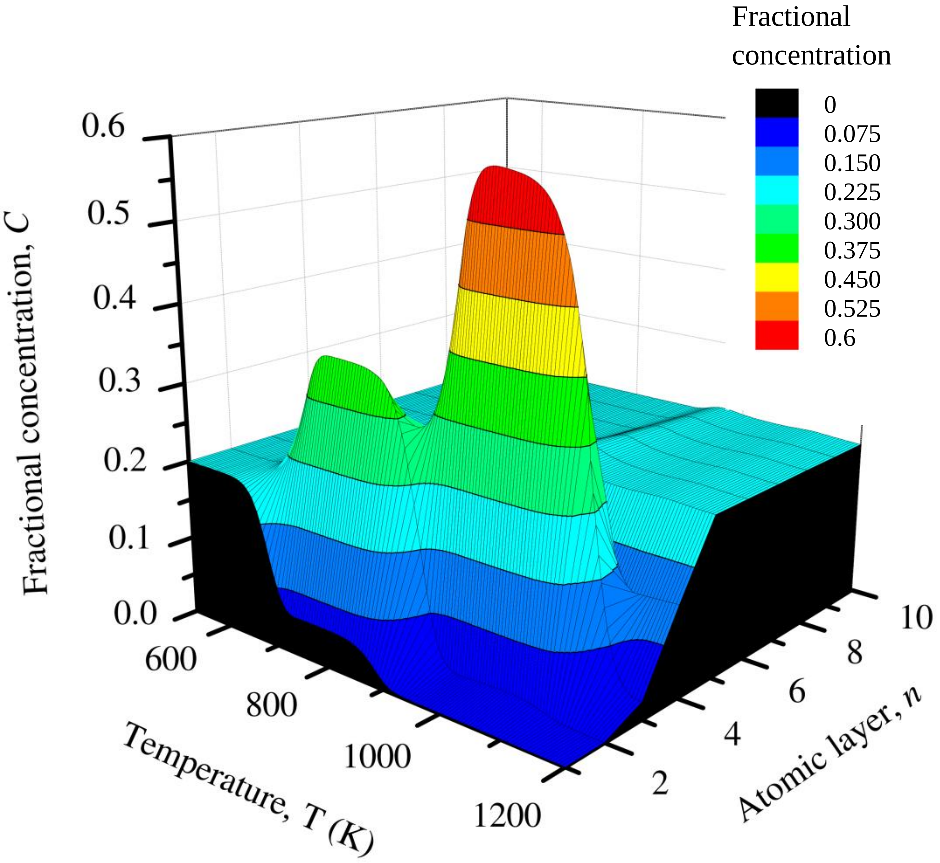

Figure 8.4: *3-dimensional plot describing the composition of the first 10 atomic layers of the Fe(100)-20%Cr alloy during a linear programmed heating segregation run from an initial temperature of 525 K to a final temperature of 1200 K, heated at a constant rate of 0.05K/s. A sharp increase in the concentrations of the 2nd and 3rd atomic layers is observed due to the desegregation of Cr from the surface layer into these two atomic layers.*

Figure 8.4 describes the composition of the Fe(100)-20%Cr alloy in each of the first 10 atomic layers as a function of temperature. The desegregation of Cr from the surface layer into the 2nd atomic layer and thereafter into the 3rd atomic layer is observed by the increase in the concentration of Cr in these two atomic layers. A 2-dimensional contour plot of figure 8.4 is provided in figure 8.5, showing the composition of the first 10 atomic layers in the Fe(100)-20%Cr alloy as a function of the temperature.

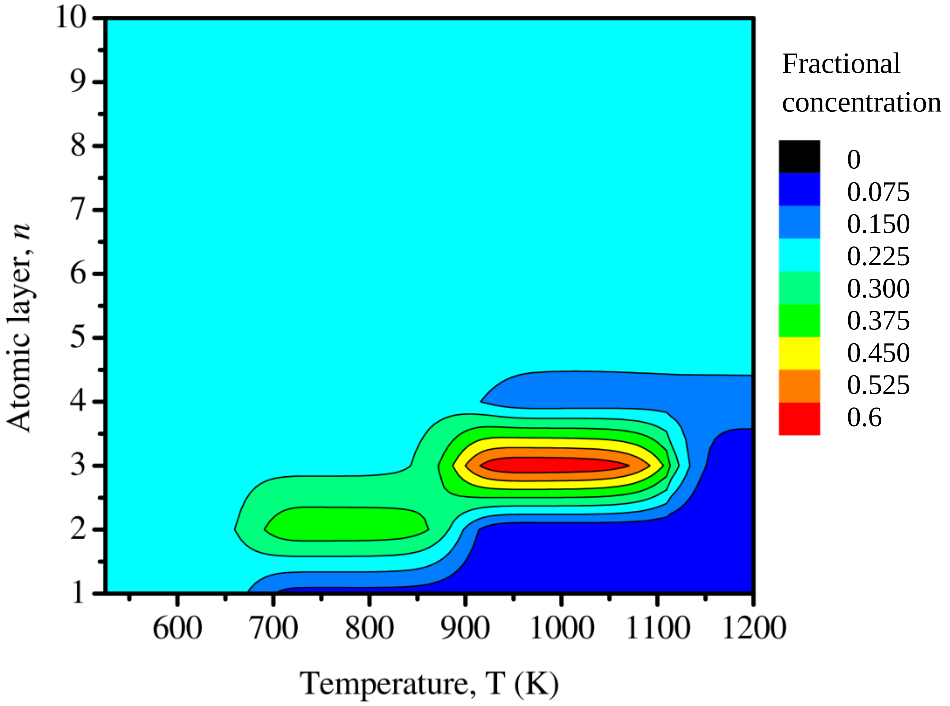

Figure 8.5: *2-dimensional contour plot of the Fe(100)-20%Cr describing the concentration of Cr in the first 10 atomic layers of the alloy as a function of temperature.*

The contour plot in figure 8.5 provided an overhead view of the Cr concentration in the first 10 atomic layers of the Fe(100)-20%Cr alloy. The increase in concentrations of atomic layers 2 and 3 is evident in figure 8.5, caused by the desegregation of Cr from atomic layer 1. Next, an analysis of the subsurface layers is performed in order to explain the observed desegregation of Cr in Fe(100), evident in figure 8.3 - 8.5. Figure 8.6 presents the concentration of atomic layers 1-10 as a function of temperature.

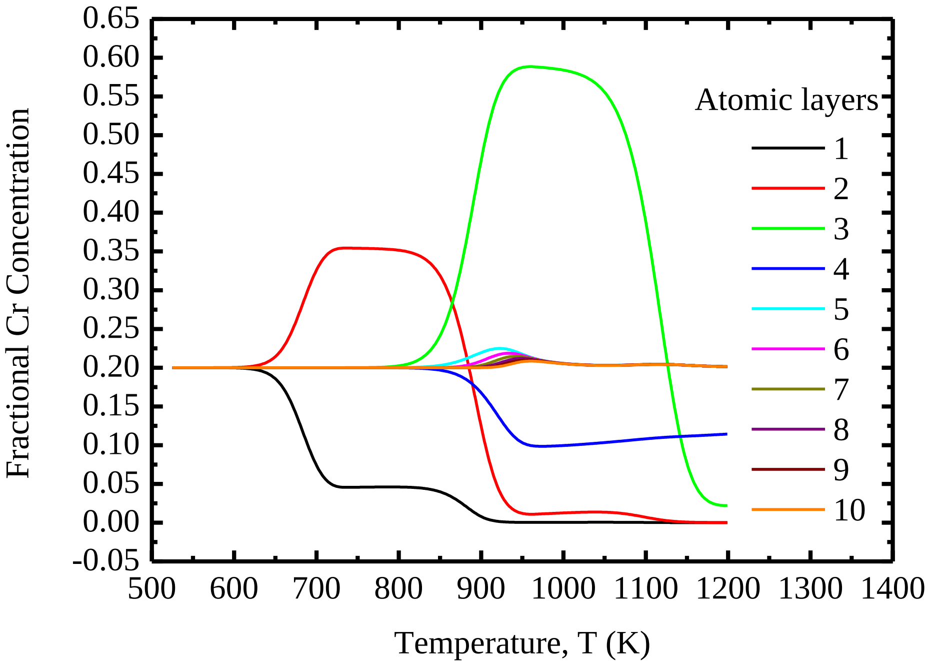

Figure 8.6: *Fractional concentration of Cr in atomic layers 1 to 10 of the Fe(100)-20% alloy as a function of temperature.*

Each of the observed regions in figure 8.3 can now be explained by considering the change in the subsurface layers. Region 1 is observed as the region where insufficient thermal energy is available for diffusion to occur. The desegregation of Cr in region 2 is observed to correspond to the increase in Cr concentration of the second atomic layer. In region 3, the surface concentration reaches a plateau region as a result of atomic layer 2 having reached a maximum concentration of 35 at. %. The concentration of atomic layer 2 increased up to a value of 35 at. %, where upon it starts to slowly desegregate, noted in a decreasing concentration. As Cr from the second atomic layer start to desegregate, the concentration of atomic layer 3 starts to increase. This flux of Cr atoms out of atomic layer 2 and into atomic layer 3 opens up the second atomic layer for more Cr from the first atomic layer to desegregate, as noted by the decreasing concentration of atomic layer 1 in region 4. As the surface concentration reaches a zero value region 5 is entered, characterised by the complete depletion of Cr in the surface layer. The 3rd atomic layer reaches a concentration of 58 at%, almost three times the initial bulk concentration, before it starts to decrease in concentration due to Cr desegregating into the bulk material. During the desegregation of Cr from the surface into the bulk, atomic layers 1-3 undergoes the most change. Atomic layer 4 is observed to decrease to half its initial concentration before increasing slowly. Atomic layers 5 and to 10 shows a slight increase and thereafter a gradual decrease to a new bulk concentration value, higher than the initial value.

Figure 8.3 combined with figure 8.4 provide a comprehensive view on the behaviour of Cr in the Fe-Cr alloys at elevated temperatures. Cr is observed to desegregate into the bulk, resulting in an increased bulk concentration of Cr in Fe. In order to understand the process in figure 8.4 and 8.6, in terms of the respective segregation parameters consider tables 8.1, 8.2 and 8.3. A large repulsive interaction parameter is observed for atomic layer 1, which combined with the positive segregation energy forces Cr from the first to the second atomic layer. Once there Cr experiences a segregation energy decrease into the bulk accompanied by a positive interaction energy, resulting in the further desegregation of Cr from atomic layer 2 into atomic layer 3 and eventually into the bulk.

The role of the activation energy is less visible, but it plays a role in the maximum allowed Cr concentrations in the respective atomic layers. The activation energy of diffusion for Cr from atomic layer 1 to 2 is small and therefore, Cr desegregates with relative ease from atomic layer 1 to 2. The activation energy is much higher for Cr diffusion from atomic layer 2 to 3 and Cr builds up in the 2nd atomic layer before desegregating into atomic layer 3. The largest activation energy is observed for Cr diffusion from atomic layer 3 to 4 and this is the reason for the large increase in the Cr concentration of atomic layer 3. Atomic layer 4 is also observed to decrease in concentration as a result of the high activation energy barrier for diffusion from atomic layer 4 to 3. This is accompanied by a positive interaction parameter and segregation energy resulting in the desegregation of Cr from atomic layer 4 into the bulk. Therefore, it is clear that the activation energy plays an important role in the kinetics of Cr desegregation, but the thermodynamics is completely determined by the interaction parameter and the segregation energy, which are both contained in the chemical potential, μ.

8.5. Segregation in the ternary Fe-Cr-S alloy

In the introduction section it was mentioned how the presence of the non-metal impurities C, N, O and S could potentially be responsible for the segregation of Cr as it co-segregates with these non-metal impurities in Fe. It was already shown that Cr does not segregate in Fe in the temperature range 500 - 1200 K, independent of the Cr concentration. Thus, to provide an answer to the observed segregation of Cr in Fe reported in literature, the co-segregation of S and Cr in Fe is investigated in this section by TOF-SIMS segregation measurements.

All the segregation parameters of S in Fe(100) and Cr in Fe(100) was already calculated in chapter 7 and in the preceding section of this chapter. If S is to be responsible for the co-segregation of Cr, then there should be a strong interaction between these two species. The interaction parameters between Cr and S in the Fe(100) lattice was calculated for each of the first 4 atomic layers as well as for the bulk crystal using DFT. Although the TOF-SIMS experiments were performed on a polycrystalline Fe sample, while the calculations were performed for the Fe(100) orientation, the bulk values will be the same. Also the surface layer values would be slightly different in magnitude as a result of the surface orientation dependence, but will have the same sign. Therefore the calculations presented for the Fe(100) can provide a qualitative explanation of the observed co-segregation of Cr and S measured by TOF-SIMS. Recalling equation 7.4 in chapter 7, which describes the interaction energy between two species, also presented here by equation 8.2

$$\Omega_{CrS}^{j} = Z^{j}\left[\varepsilon_{CrS}^{j} - \frac{1}{2}\left(\varepsilon_{Cr-Cr} + \varepsilon_{S-S}\right)\right]. \tag{8.2}$$

The interaction energies, ε, for the pure elements Cr and S were obtained from the calculations performed in chapter 7 and the preceding sections of this chapter, while the interaction energy for Cr-S was determined from the binding energy of a Cr-S bond in each of the first 4 atomic layers and the bulk of Fe(100). The results for the interaction energies and the interaction parameters for Cr-S in Fe(100) are presented in table 8.5.

Table 8.5: *Interaction energies for S and Cr in their respective pure forms and the interaction energies and regular solution interaction parameters for Cr-S in the Fe(100) lattice.*

Layer, *n*	ε_{S-S} (eV)	ε_{Cr-Cr} (eV)	ε_{Cr-S} (eV)	Ω_{Cr-S} (eV)	Ω_{Cr-S} (kJ/mol)
1	-	-	0.13	-1.13	-109
2	-	-	0.30	-0.91	-87.4
3	-	-	0.76	2.82	272
4	-	-	0.78	2.97	286
bulk	0.36	0.46	0.66	1.96	189

Strong interactions are observed between Cr and S, with positive values for the 3rd and 4th atomic layers as well as the bulk lattice, while negative values are obtained for atomic layer 1 and 2. The positive interaction parameters indicate that Cr and S are strongly attracted to one another and would form a strong bond. On the contrary, the negative interaction parameters of atomic layers 1 and 2 suggest a repulsive interaction between Cr and S and the formation of a bond is unlikely. TOF-SIMS segregation experiments were performed on a polycrystalline Fe sample, containing 5 ppm S and 0.16 at. % Cr to determine the segregation behaviour of S and Cr in Fe. The details of the segregation measurements has already been described in chapter 6, section 6.3.2, where S segregation in Fe was discussed. Figure 8.7 presents the segregation results obtained for the ternary Fe-Cr-S alloy.

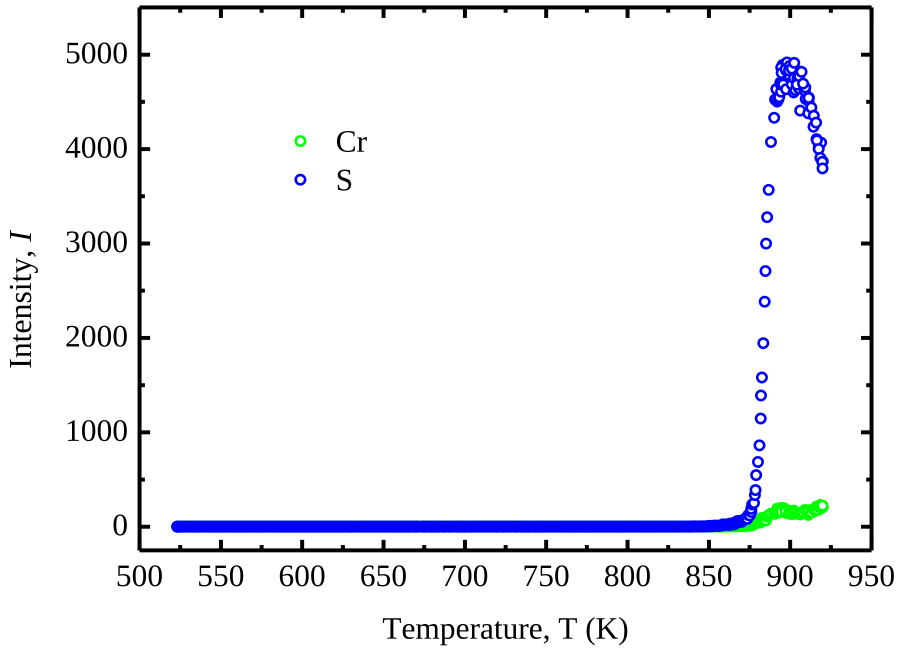

Figure 8.7: *Segregation profile of S and Cr in a polycrystalline Fe sample containing 5 ppm S and 0.16 at. % Cr. Analysis was performed by TOF-SIMS at a heating rate of 0.1 K/s in positive spectroscopy mode to allow the detection of the positive Cr ions.*

The segregation experiments were performed in the temperature range 525 K – 925 K, with 925 K being the maximum achievable temperature of the TOF-SIMS instrument. Segregation of S is observed at temperatures exceeding ~865 K as expected due to the negative interaction parameters and strong segregation energy of S in Fe(100) (chapter 7). However, contrary to the binary Fe-S alloy studied in chapter 7, S is observed to desegregate at temperatures exceeding ~900 K, an unexpected behaviour since S in Fe (Fe(100) and Fe(111)) was previously observed to dominate the surface once it has segregated. Cr segregating is also observed along with S and the two elements are said to co-segregate. In order to explained this unexpected behaviour of both S and Cr, consider the interaction parameters of Cr and S in table 8.5 calculated by DFT. In the bulk as well as for atomic layers 4 and 3, a strong positive (attractive) interaction is observed between Cr and S. Recalling that S is a strongly segregating element, it can be concluded that as a result of a strong attractive Cr –S interaction, S "draws" Cr from the Fe lattice towards the surface layer. This causes the co-segregation of Cr and S with an increase in surface concentration of both species observed. As the concentration of S increases, the negative interaction between Cr and S in atomic layers 1 and 2 becomes more dominant. Cr and S are now experiences a repulsive interaction towards one another, which causes the desegregation of S from the surface. The segregation energies of Cr and S are observed to have a lesser effect on the segregation behaviour and the system seems to be dominated by the large interactions parameters between Cr and S.

The co-segregation of S and Cr confirms that indeed experimentally Cr segregation is achievable. The desegregation of S into the bulk material, renders the effect thereof on Cr segregation impossible, especially at high temperatures where S is expected to be absent in the surface layer. Thus, for a ternary alloy Fe-Cr-S annealed at a high temperature for a sufficient amount of time, Cr is expected to dominate the surface concentration and it might be interpreted that Cr has segregated towards the surface while in fact S segregation caused the co-segregation of Cr. The fact that S is almost always present in Fe even for sample of high purity as used in this study, suggest that the interaction observed in this study in likely to be present in most Fe alloys. This result obtained in this study provides some clarity on the discrepancies that exist in literature concerning the segregation of Cr in Fe. It confirms both the segregation of Cr observed experimentally and the theoretical results which found Cr segregation to be unfavourable with the role of S being the “missing” link. Furthermore, the layer dependency of the interaction parameter and thus the segregation parameters is confirmed which presents conclusive evidence for the presence of the “surface effect”.

8.5. Summary

Segregation of Cr in different concentration of Fe(100)-Cr alloys were investigated by a sequential multi-scale modelling approach. The segregation parameters Q, ΔG and Ω were calculated by DFT. It was shown that each of these segregation parameters is dependent on the atomic layer in which the Cr atom resides. Subsequent simulations were performed by the Modified Darken Model in order to obtain a macroscopic description of Cr segregation in Fe(100). Results indicated that for all concentrations considered Cr does not segregate to the surface but instead desegregate into the subsurface atomic layers. A 3-dimensional analysis of the subsurface layers showed an increase in the second and third atomic layers which are in agreement with the observed desegregation of Cr in the surface layer.

Desegregation of Cr was explained in terms of the thermodynamic properties, the interaction parameter and the segregation energy, which constitutes the chemical potential term used in the Modified Darken Model. Therefore, it can be concluded that the desegregation of Cr in Fe(100) is determined by the thermodynamic properties of the system; the segregation energy and the interaction parameter. These two terms were found to complement one another in the desegregation of Cr in the subsurface layers of Fe(100). The kinetic properties of the system were found to be responsible for the build-up of Cr in the respective atomic layers as a result of the large activation energy barriers preventing diffusion of Cr. After sufficient thermal energy has been placed into the Fe-Cr alloys, at temperatures exceeding 1100 K, the surface layer has been depleted of Cr with a slight increase in the bulk concentration of Cr being observed. The results of this study confirm the calculations performed by other first principle studies, indicating that Cr does not segregate to the surface of Fe.

The observed segregation of Cr in Fe, reported in literature, was showed to be the likely results of S causing the segregating of Cr leading to co-segregation of Cr and S. These two species, Cr and S, was shown for the Fe(100) orientation to have a strong interaction in the 4th and 3rd atomic layers as well as in the bulk of Fe(100), which causes the co-segregation of Cr and S. In the surface layer and 2nd atomic layer Cr and S is observed to repel one another which causes the desegregation of S while Cr remains on the surface of Fe. TOF-SIMS data obtained for a polycrystalline Fe sample confirms the calculations obtained for the Fe(100) orientation. For the polycrystalline Fe sample, the bulk interactions are expected to be the same as for the Fe(100) orientation, also the surface layer values are expected to differ as a result of the orientation dependence of the interaction parameter, but the sign of the interaction is expected to be the same as that of the Fe(100) orientation. Therefore, the calculated interactions provide a qualitative explanation of the observed TOF-SIMS data for S and Cr co-segregation. These results presents possible explanations for the discrepancies that exist between the theoretical and experimental results reported in literature and furthermore confirm the layer dependency of the segregation parameters, the "surface effect" as described in this study.

8.6. References

[1]. B. Nonas, K. Wildberger, R. Zeller, P.H. Dederichs, Phys. Rev. Lett. 80 (1998) 4574.

[2]. M. Polak, C. Fadley, L. Rubinovich, Phys. Rev. B 65 (2002) 205404.

[3]. W.T. Geng, Phys. Rev. B 68 (2003) 233402.

[4]. A. Kiejna, E. Wachowicz, Phys. Rev. B 78 (2008) 113403.

[5]. R. Idczak, K. Idczak, R. Konieczny, J. Nucl. Mater. 452 (2014) 141.

[6]. M. Gupta, R.P. Gupta, J. Phys. Condens. Matter 25 (2013) 415502.

[7]. S. Suzuki, T. Kosaka, H. Inoue, M. Isshiki, Y. Waseda, Appl. Surf. Sci. 103 (1996) 495.

[8]. X. -S. Yuan, C. Song, X.-S. Kong, Y.-C. Xu, Q.F. Fang, C.S. Liu, Physica B 425 (2013) 42.

[9]. R. Franchy, J. Boysen, P. Gaßmann, C. Uebing, 119 (1997) 357.

[10]. P. Olsson, J. Nucl. Mater. 386-388 (2009) 86.

[11]. P. Olsson, I. Abrikosov, L. Vitos, J. Wallenius, J. Nucl. Mater. 321 (2003) 84.

[12]. E. Park, B. Hüning, M. Spiegel, Appl. Surf. Sci. 249 (2005) 127.

[13]. J. M. Sampedro, E. del Rio, M. J. Caturla, M. Victoria, J. M. Perlado, J. Nucl. Mater. 417 (2011) 1050.

[14]. F.A. Garner, M.B. Toloczko, B.H. Sencer, J. Nucl. Mater. 276 (2000) 123.

[15]. A.V. Ruban, H.L. Skriver, Comput. Mater. Sci. 15 (1999) 119.

[16]. B. Schiffmann, M. Polak, P.A. Dowben (eds.), A. Miller (eds.) Surface segregation phenomena, CRC Press Inc., Boca Raton, Florida, USA, 1990.

[17]. E. Clauberg, J. Janověc, C. Uebing, H. Viefhaus, H.J. Grabke, Appl. Surf. Sci. 161 (2000) 35.

[18]. E.C. Viljoen, J. du Plessis, Surf. Sci. 468 (2000) 27.

[19]. P. E. Barnard, Experimental and computational study of S segregation in Fe, M.Sc. Dissertation, Bloemfontein, 2012.

[20]. P. Błoński, A. Kiejna, Vacuum 74 (2004) 179.

[21]. J. du Plessis, Surface Segregation, Sci-Tech Publications, Bloemfontein, 1990.

[22]. C.H.P. Lupis, Chemical Thermodynamics of Materials, Elsevier Science Publishing Co., Inc., New York, 1983.

[23]. R.C. Weast (eds.), M. J. Astle (eds.), CRC Handbook of Chemistry and Physics, CRC Press Inc., Boca Raton, Florida, USA, 1982.

Conclusion

Surface segregation of S and Cr in bcc Fe was investigated with the focus being on determining the influence of the microscopic effect of the lattice on the segregation parameters. One of these effects includes the orientation dependence of the segregation parameters; the pre-exponential factor (D_0) the activation energy of diffusion (Q), the segregation energy (ΔG) and the interaction parameter, **Ω**. The other effects of the microscopic structure are constituted by the surface of the material. The surface layers relax and as a consequence have a layer dependency for each of the segregation parameters. The absence of second and third nearest neighbouring atoms to the atoms residing in the surface region of the crystal enhances this layer dependency of the segregation parameters. This effect brought about by the surface was termed the "surface effect" and was shown to extend up to the 4th atomic layer. The results obtained for the segregation parameters of S in Fe(100) as calculated by DFT is presented in the following two tables.

Layer, *n*	**D_0 (m^2/s)**	**ΔG (kJ/mol)**	**Ω_{Fe-S} (kJ/mol)**
1	26.33	-186	-44.4
2	5.00	20.7	-30.9
3	30.67	6.51	-22.2
4	31.04	-1.40	-25.1
bulk	40.00	0.00	-25.1

Layer, *n*	**Q (kJ/mol)**
2→1	134
3→2	287
4→3	261
5→4	279
bulk	265

The results obtained for the segregation parameters of Cr in Fe(100) is presented in the tables below.

Layer, *n*	**D_0 (m^2/s) × 10^{-4}**	**ΔG (kJ/mol)**	**Ω_{Fe-Cr} (kJ/mol)**
1	2.12	17.4	-34.4
2	2.57	45.3	-5.49
3	2.52	16.4	5.51
4	2.57	4.82	10.6
bulk	2.53	0.00	10.6

Layer, *n*	***Q* (kJ/mol)**
2→1	156
3→2	322
4→3	401
5→4	320
bulk	306

The segregation parameters of S in Fe(100) were fitted onto the experimental data using the Modified Darken Model (MDM). Results revealed that the surface effect provided an accurate description of the experimental data. Fitting of the conventional MDM failed to provide an accurate description of the measured data. The data was effectively described by a set of two kinetic parameters, one representing the bulk system and the other representing the surface. These parameters were respectively described by the bulk kinetic parameters and that of atomic layer 2. The surface effect in Fe(111) was described by the model of Fick in combination with the MDM. The results for the segregation parameters obtained by fitting of the MDM to the experimental data of Fe(100) and Fe(111) is presented in the table below;

Parameter	**Fe(100)**	**Fe(100)**	**Fe(111)**	**Fe(111)**	**Fe(100)**	**Fe(111)**
Rate (K/s)	0.005	0.0075	0.005	0.0075	**Average**	**Average**
Q^{Bulk} **(kJ/mol)**	265	265	190	190	265	190
Q^{Surf} **(kJ/mol)**	287	287	300	300	287	300
D_0^{Bulk} **(m^2/s)**	40.0	40.0	0.025	0.0025	40.0	0.0138
D_0^{Surf} **(m^2/s)**	5.00	0.75	27.5	45.0	2.88	36.3
ΔG^{Surf} **(kJ/mol)**	-186	-186	-154	-154	-186	-154
Ω^{Surf} **(kJ/mol)**	-44.4	-44.4	-35.0	-35.0	-44.4	-35.0

The segregation parameters of Cr were simulated in the MDM to obtain a macroscopic picture of Cr segregation. Results indicated that for all concentration in the range 0.01 – 20 at. % Cr desegregates into the bulk instead of segregating to the surface layer.

Cr segregation was observed in the Fe-Cr-S alloy as a result of a strong interaction with S, leading to Cr and S co-segregating. This effect was due to the positive (attractive interaction of Cr and S in the bulk, the 4th and 3rd atomic layers. Once a sufficient S concentration was reached on the surface, the negative interaction parameter of atomic layer 1 and 2 caused S to desegregate while Cr remained in the surface layer. These interactions between Cr and S of the first four atomic layers are tabulated below;

Layer, *n*	Ω_{Cr-S} **(kJ/mol)**
1	-109
2	-87.4
3	272
4	286
bulk	189

These results of Cr segregation in Fe-Cr-S present some clarification of the discrepancies found in literature between theoretical studies reporting that Cr does not segregate while experimental studies report the contrary. It is suggested that the Fe sample contains some impurities, such as S, which causes the co-segregation of Cr along with the impurities.

Appendix A

Computer Code

This appendix contains the computer code for the Modified Darken Model software developed during this study. The modified Darken Model, described in chapter 3, section 3.3.1, was coded in the C++ programming language implemented in the Linux (Ubuntu) operating system. The following section of code contains the main part of the program. Comments on the code are provided in blue as to provide the user with some explanation on the use of a specific line of code.

```
do //Main loop running temperatures
{
    timestep = timestep_Val_In;//timeStep = initial user input value

    #pragma omp parallel for default (shared) num_threads(cpu_cores) private (alfa, beta) //parallilize over for loop
    for (Equation = 0; Equation < Number_of_equations+1; Equation+=1)//for loop to iterate over number of equations
        {
            D[Equation] = D_0[Equation]*exp(-Q[Equation]/(R*T));//Calculate diffusion coefficient
            M[Equation] = D[Equation]/(R*T);//Calculate mobility using the Einstein relation

            C_plus_1[Element][Equation] = C[Element][Equation+1];//Concentration of the next layer
            C_minus_1[Element][Equation] = C[Element][Equation-1];//Concentration of the previous layer
            Layers_C[Element][Equation] = Equation;   //The number of the current layer

             C_at[Element][Equation] = C[Element][Equation];//Concentration of the current layer
            C_plus_1[1][Equation] = 1 - C_plus_1[0][Equation] ;//Calculate the +1 concentrations of the third element of the current equation

            C_minus_1[1][Equation] = 1 - C_minus_1[0][Equation];//Calculate the  -1 concentrations of the third element of the current equation

             C_at[1][Equation] = 1 - C_at[0][Equation] ;        //Calculate the concentrations of the third element of the current equation

            if (Equation == 0)//Forces concentrations to be zero
            {
                C_minus_1[1][Equation] = 0;
                C_minus_1[0][Equation] = 0;
            }
            U_plus_1[Element][Equation]  = Calculate_U_plus_1(Equation,Element);//delta chemical potential for layer +1



            if (Equation == 0) //Conditions for the 1st layer
```

```
{
        U_plus_1[Element][Equation] = U_plus_1[Element][Equation]  - DeltaG[0];
}
else if (Equation == 1)//Conditions for the 2nd layer
{
        U_plus_1[Element][Equation] = U_plus_1[Element][Equation]  - DeltaG[1];
}
else if (Equation == 2)//Conditions for the 3rd layer
{
        U_plus_1[Element][Equation] = U_plus_1[Element][Equation]  - DeltaG[2];
}
else if (Equation == 3)//Conditions for the 4th layer
{
        U_plus_1[Element][Equation] = U_plus_1[Element][Equation]  - DeltaG[3];
}
else
{
        U_minus_1[Element][Equation]  = Calculate_U_minus_1(Equation,Element);//delta chemical potential for layer-1
}
 if (U_plus_1[Element][Equation]  >= 0)//All If statement that follow contain temporary parameter for the correct direction
of diffusion
{
        alfa = C_plus_1[Element][Equation];
}
if (U_plus_1[Element][Equation]  < 0)
{
        alfa = C_at[Element][Equation];
}

if (U_minus_1[Element][Equation]  >= 0)
{
        beta = C_at[Element][Equation];
```

```
            }

            if (U_minus_1[Element][Equation]  < 0)
            {
                beta = C_minus_1[Element][Equation];
            }
            //Next section calculates the differential equation
            DIFF_dummy[Element][Equation] = (((M[Equation]*alfa)/(d[Equation]*d[Equation]))*U_plus_1[Element][Equation]);
            if (Equation == 0)
                DIFF[Element][Equation] = DIFF_dummy[Element][Equation];
            else if (Equation == 1)
                DIFF[Element][Equation] = ((M[Equation]*alfa)/(d[Equation]*d[Equation]))*U_plus_1[Element][Equation] -
DIFF_dummy[Element][Equation-1];
            else if (Equation == 2)
                DIFF[Element][Equation] = ((M[Equation]*alfa)/(d[Equation]*d[Equation]))*U_plus_1[Element][Equation] -
DIFF_dummy[Element][Equation-1];
            else if (Equation == 3)
                DIFF[Element][Equation] = ((M[Equation]*alfa)/(d[Equation]*d[Equation]))*U_plus_1[Element][Equation] -
DIFF_dummy[Element][Equation-1];
            else if (Equation == 4)
                DIFF[Element][Equation] = ((M[Equation]*alfa)/(d[Equation]*d[Equation]))*U_plus_1[Element][Equation] -
DIFF_dummy[Element][Equation-1];
            else
                DIFF[Element][Equation] = (((M[Equation]*alfa)/(d[Equation]*d[Equation]))*U_plus_1[Element][Equation] -
((M[Equation]*beta)/(d[Equation]*d[Equation]))*U_minus_1[Element][Equation]);
            timestep_Val = Calculate_Timestep_and_C(timestep, Tolerance, Element, Equation);//Calculate integration timestep
        }
        DIFF[Element][Number_of_equations] = 0;//Forces the last layer to be = 0, ensures correct use of boundary conditions
        timestep = timestep_Val;//assign timestep to calculated value
        Time = Time + timestep;//Compute total simulation real time
        T = T + (timestep * HeatingRate);//Perform linear heating
```

```
		#pragma omp parallel for default (shared) num_threads(cpu_cores) //parallelize over for loop
		for (Equation = 0; Equation < Number_of_equations+1; Equation+=1)//for loop to iterate over number of atomic layers to save the new concentration after integration
		{
			NewC[Element][Equation] = C[Element][Equation] + (timestep*DIFF[Element][Equation]); //Calculate new concentration by Euler integration
			C[Element][Equation] = NewC[Element][Equation];//Update concentrations by placing new value into old variable

		}
		if (Time <= SputterTime)//simulate the effect of sputtering on the surface
		{
			C[0][0] = C_bulk[0];
			T = T_start;
		}

		if (T > T_start + counter)//code to save the temperature and concentration every counter step
		{
			SaveC[0] = C[0][0];	//Variable for element i surface concentration
			SaveC[1] = C[0][1];
			SaveC[2] = C[0][2];
			SaveC[3] = C[0][3];
			SaveC[4] = C[0][4];
			SaveC[5] = C[0][5];
			SaveC[6] = C[0][6];
			SaveC[7] = C[0][7];
			SaveC[8] = C[0][8];
			SaveC[9] = C[0][9];
			SaveSurf_C(TotalWallTime, TotalCPUTime, timestep);//Save data into C, Temp, Time - format
			counter +=1;//index counting surface concentration entries
		}
```

```
        if (T > T_Save_Values)//code to save the temperature and conc every T_save_Values step
        {
                if (Equation < 20)
                        T_Save_Values = T + 0.25;
                else
                        T_Save_Values = T + 1;

                SaveTemp(Number_of_equations, TotalWallTime,  TotalCPUTime);
        }
}
while (T =< T_Stop); //This code in this loop will execute until the temperature is greater than the stop temperature T_Stop
```

```
#!/bin/bash  # linux .sh script file

NAME='# Name of the calculation'

if [ -x ./Darken ]; then                        # Script determines if there is a executable Darken else it terminates
        cat >$NAME.input.txt << EOF        # Create the Darken input file
                $NAME                                   # Name of calculation
                C_bulk1                                 # bulk concentration of segregant
                Q                                       # activation energy
                D_0                                     # pre-exponential factor
                DeltaG                                  # Segregation Energy
                inter12                                 # interaction parameter
                d_Bulk                                  # inter-lattice spacing
                HeatingRate                             # Heating rate of segregation run
                CoolingRate                             # cooling rate of segregation run
                T_start                                 # LPH start time
                T_Stop                                  # LPH start time
                Number_of_equations                     # Number of equations
                SputterTime                             # pre-sputter time
                Max_Surf_Conc                           # Maximum allowed concentration of segregand
                Tolerance                               # Tolerance for integration - typically E-3 to E-5
                timestep_Val_In                         # Maximum allowed timestep value
                cpu_cores                               # number of cpu cores for parallel execution
        EOF
                mkdir $NAME #make a directory in present working directory with name $NAME
                mv $NAME.input.txt $NAME #move darken input file to $NAME
                cd $NAME #direct to directory $NAME
                ../Darken_2C < $NAME.input.txt  #Run Darken application with input file
        echo " The Automation script for the Darken simulation has finished " #user output to terminal
else
        echo "no executable file was found, compile the program!!" #user output to terminal
fi
```

Appendix B: Conferences and publications

Conferences

New Method for the preparation of S doped Fe samples characterised by AES and TOF-SIMS depth profiling

P.E. Barnard, J.J. Terblans, H.C. Swart

European Conference on the Application of Surface and Interface Analysis (ECASIA), Sardinia, Italy, 2013

PHI systems and their modifications at KOVSIES

H.C. Swart, J.J. Terblans, E. Coetsee, W.D. Roos, O.M. Ntwaeaborwa, R.E. Kroon, S. Cronje, P.E. Barnard

PHI European User Meeting, Commundo Tagungs hotel, Ismaning (Munich), Germany, May 14 - 15, 2014 (invited talk)

Publications

P.E. Barnard, J.J. Terblans, H. C. Swart, **AES and TOF-SIMS measurements to confirm a new method for the preparation of S doped Fe samples**. Surf. Interface Anal. doi: 10.1002/sia.5448 (2014)